

# **EXPERIMENTAL STUDY OF AN ION CYCLOTRON RESONANCE ACCELERATOR**

by

Christopher T. Ramsell

A DISSERTATION

Submitted to:  
Michigan State University  
Department of Physics and Astronomy  
National Superconducting Cyclotron Laboratory

in partial fulfillment of the requirements  
for the degree of

DOCTOR OF PHILOSOPHY

2000

# **ABSTRACT**

## **EXPERIMENTAL STUDY OF AN ION CYCLOTRON RESONANCE ACCELERATOR**

by

Christopher T. Ramsell

The Ion Cyclotron Resonance Accelerator (ICRA) uses the operating principles of cyclotrons and gyrotrons. The novel geometry of the ICRA allows an ion beam to drift axially while being accelerated in the azimuthal direction. Previous work on electron cyclotron resonance acceleration used waveguide modes to accelerate an electron beam [5]. This research extends cyclotron resonance acceleration to ions by using a high field superconducting magnet and an rf driven magnetron operating at a harmonic of the cyclotron frequency. The superconducting solenoid provides an axial magnetic field for radial confinement and an rf driven magnetron provides azimuthal electric fields for acceleration. The intent of the ICRA concept is to create an ion accelerator which is simple, compact, lightweight, and inexpensive. Furthermore, injection and extraction are inherently simple since the beam drifts through the acceleration region. However, use of this convenient geometry leads to an accelerated beam with a large energy spread. Therefore, the ICRA will be most useful for applications which do not require a mono-energetic beam. An ICRA designed to accelerate protons to 10 MeV would be useful for the production of radioisotopes, or neutron beams, as well as for materials science applications.

As a first step toward producing an ICRA at useful energies, a low energy ICRA has been designed, built, and tested as a demonstration of the concept. Analytical theory and a full computer model have been developed for the ICRA. Beam measurements taken on the ICRA experiment have been compared with theory.

The ICRA computer model uses realistic fields of the solenoid, magnetron, and electrostatic bend. This code tracks single particle trajectories from the ion source through the entire system to a target face. A full emittance injected beam can be modeled by tracking many single particle trajectories.

The ICRA experiment is designed to accelerate a proton beam from 5 keV to 50 keV in 5 turns. A superconducting solenoid provides a 2.5 Tesla axial magnetic field. The accelerating structure built for the experiment operates at 152 MHz (4<sup>th</sup> harmonic) and provides 3 kV across 8 gaps. Measurements of the accelerated beam current vs. beam orbit radius indicate an energy distribution ranging from near zero to near the full design energy, with 7% of the beam current above 24 keV and 1% above 42 keV.

Energy distributions generated using the ICRA computer model show reasonable agreement with the experimental data. After a small correction of the bend voltage, the computer model shows good agreement with the magnitude and shape of the experimental data for a wide range of turn number.

Finally, a scheme for optimization of the basic ICRA design is given. Design parameters are identified which minimize cost and which maximize the accelerated beam current. Three 10 MeV proton designs are given which offer a compromise between low cost and a high quality beam.

# **DEDICATION**

To my beautiful wife, Katrina.

She gives me strength and makes life worth living.

# ACKNOWLEDGMENTS

I want to thank **Terry Grimm**. The ICRA concept was his idea, and I am thankful to Terry for giving me the opportunity to design and build an entire particle accelerator and gain the all the experience that comes with such a project. Terry is a very smart guy, and he has taught me most of what I know about accelerators.

I want to thank my advisor, **Richard York**, for being very fair and easy to talk to and for providing funding for this project. York is relentlessly practical and matter of fact. What I learned from him is best stated in his own words: “Don’t worry about the mysteries of the universe. Just get the damn thing working !”

A special thanks goes to **Felix Marti**. Felix was not originally involved in my project, however he had the knowledge and expertise that we needed, so he ended up getting sucked into it anyway.

Also thanks to **Chris Compton**, a good friend who has been here through most of the project. Over the years Chris helped on many things, including design of the support structure for the ICRA and taking data, just to mention a few.

I also want to acknowledge the contribution of each student who worked on this project for me. In chronological order they are:

**Scott Rice** built components of the rf cavity, and toiled with me through the magnetic mapping process. Thanks Scott !

**Erica Blobaume** and I built the ion source and Einzel lens together as an REU project. Thanks Erica !

**Nathan Pung** was very helpful with the experimental set up, building the support structure, alignment of components, and running the ICRA. His help enabled me to move ahead at a time when I really needed it. Thanks Nate !

**Joel Fields** worked on the setup and alignment as well as computer modeling of the 50 keV ICRA. Thanks Joel !

# TABLE OF CONTENTS

<b>LIST OF SYMBOLS AND ABBREVIATIONS</b> .....	ix
<b>LIST OF TABLES</b> .....	xii
<b>LIST OF FIGURES</b> .....	xiv
<b>1. INTRODUCTION</b> .....	1
1.1 Cyclotrons .....	2
1.2 Gyrotrons .....	4
1.3 The Magnetron .....	6
1.4 Ion Cyclotron Resonance Acceleration .....	7
1.5 Applications .....	10
<b>2. THEORY</b> .....	12
2.1 Magnetic Field .....	12
2.2 Vacuum .....	15
2.3 Ion Source .....	16
2.4 RF Cavity .....	17
2.4.1 Waveguides .....	18
2.4.2 Coaxial Quarter Wave Cavity .....	24
2.4.3 RF Driven Magnetron .....	34
2.4.4 Equivalent Circuit Representation .....	39
2.4.5 The Hybrid Quarter Wave – Magnetron Cavity .....	42
2.5 Analytical Model of the Beam Trajectory .....	46
2.5.1 Electrostatic Bend .....	51
2.5.2 Conservation of Magnetic Moment .....	53
2.5.3 Mirror Condition .....	58
2.5.4 Mass Spectrum of the Injected Beam .....	61
2.5.5 Number of Turns Through the Acceleration Region .....	64
2.5.6 Acceleration Region .....	65
2.5.7 RF Phase and Magnetic Field Flatness Criterion .....	70
2.5.8 Axial Turn Length in the Extraction Region .....	75

2.6	Computer Model of the Beam Trajectory	77
2.6.1	The Computer Code	79
2.6.2	Phase Dependence and Acceleration	81
2.6.3	Cavity End Field Effects	92
2.6.4	Magnetic Field and Phase	95
2.6.5	Complete Single Particle Trajectories	97
2.6.6	Acceptance Phase Space of the RF Driven Magnetron	112
2.6.7	Injected Beam Emittance	118
2.6.8	Energy Distribution of the Accelerated Beam	124
<b>3.</b>	<b>DESIGN</b>	<b>127</b>
3.1	Basic System Parameters	128
3.2	Components of the System	139
3.2.1	Superconducting Magnet	148
3.2.2	Vacuum System	148
3.2.3	Ion Source, Einzel lens, and Electrostatic Bend	151
3.2.4	RF Cavity	156
3.2.5	Beam Diagnostics	162
3.2.6	Mounting Structure	166
<b>4.</b>	<b>EXPERIMENTAL RESULTS</b>	<b>168</b>
4.1	Magnet Mapping	169
4.2	Ion Source	172
4.3	RF Cavity	174
4.3.1	Experimental Methods	174
4.3.2	Summary of RF Measurements	189
4.4	Alignment	190
4.5	Measurements of the Injected Beam	193
4.5.1	Ion Spectrum	194
4.5.2	Radius of Beam Orbit	200
4.5.3	Mirror Curve	201
4.5.4	Number of Turns Through the Acceleration Region	203
4.5.5	Injected Beam Emittance	211

4.6	Measurements of the Accelerated Beam	214
4.6.1	Energy Distributions	215
4.6.2	Resonance Width	226
<b>5.</b>	<b>DISCUSSION</b>	<b>228</b>
5.1	Discussion of Results	228
5.2	The Next Step for the ICRA	232
<b>6.</b>	<b>CONCLUSION</b>	<b>252</b>
<b>APPENDIX</b>		<b>254</b>
<b>REFERENCES</b>		<b>263</b>

## LIST OF SYMBOLS AND ABBREVIATIONS

a	radius of inner conductor of coaxial quarter wave cavity
b	radius of outer conductor of coaxial quarter wave cavity
c	speed of light
C	conductance for vacuum pumping [Liters/sec]
C	capacitance
$C_\ell$	capacitance of coaxial section of length $\ell$
$C_m$	capacitance of magnetron section
E	beam energy (also use K)
$\vec{E}$	electric field
FC	Faraday cup
$f_o$	resonant frequency
$f_c$	cyclotron frequency
$f_{rf}$	rf frequency
g	gap size between bending plates
ICRA	ion cyclotron resonance accelerator
ID	inner diameter
K	kinetic energy (also use E)
L	inductance
$\ell$	axial length
$\ell_{cav}$	axial length of the rf driven magnetron
$\ell_{eff}$	effective length of the bending plates in the direction of the beam.
NbTi	Niobium-Titanium, a material commonly used to make superconducting wire
NSCL	National Superconducting Cyclotron Laboratory
$N_{turns}$	number of orbits the beam goes through while traversing the cavity length
NWA	network analyzer
OD	outer diameter
P	pressure [Torr]
PET	positron emission tomography
$P_{Loss}$	power lost due to resistance in the rf cavity

$P_{rf}$	rf power
$p_{\parallel}$	component of momentum parallel to the local magnetic field
$p_{\perp}$	component of momentum perpendicular to the local magnetic field
$p_z$	axial component of momentum
Q	Quality factor of a resonant circuit or resonant cavity
Q	throughput [Torr Liter/sec]
rf	radio frequency
R	inner radius of magnetron cavity
$R_s$	shunt resistance
s	arc length
S	pumping speed of turbo pump [Liter/sec]
$T_c$	critical temperature of a superconducting material
TE	transverse electric
TEM	transverse electric and magnetic
TM	transverse magnetic
$V_{beam}$	initial voltage the beam is accelerated thru when extracted from the ion source
$V_{bend}$	voltage difference between the upper and lower electrostatic bending plates
x	horizontal position in the accelerator centered coordinate system
$x_s$	horizontal position in the coordinate system of the ion source
$x'$	slope $dx/dz$
y	vertical position in the accelerator centered coordinate system
$y_s$	vertical position in the coordinate system of the ion source
$y'$	slope $dy/dz$
z	axial position in the accelerator centered coordinate system
$Z_C$	characteristic impedance of a coaxial quarter wave cavity
$Z_0$	impedance of free space $Z_0 = \sqrt{\mu_0/\epsilon_0} = 377 \Omega$
$z_s$	axial position in the coordinate system of the ion source

#### Greek symbols

$\alpha$	shorthand notation for $(p_{\perp}/p_{\parallel})$
$\alpha_0$	$p_{\perp}/p_{\parallel}$ at the entrance to the acceleration region

$\delta$	skin depth
$\Delta z_{\text{turn}}$	axial turn length (section 2.5.8)
$\varepsilon$	beam emittance
$\varepsilon_0$	permittivity of free space $\varepsilon_0 = 8.85(10^{-12})$ C/Vm
$\gamma$	relativistic mass factor $\gamma = 1 + \frac{K}{mc^2}$ (assume $\gamma=1$ unless stated otherwise).
$\mu_0$	permeability of free space $\mu_0 = 4\pi(10^{-7})$ Tm/A
$\phi$	rf phase of the particle ( $\phi = \omega_{\text{rf}} t - n\theta$ )
$\theta$	azimuthal position of particle in the accelerator centered coordinate system
$\theta_{\text{bend}}$	angle the beam is bent by the electrostatic bending plates (see Figure 25)
$\rho$	radius of curvature through the electrostatic bend (see Figure 25)
$\tau$	phase of the rf ( $\tau = \omega_{\text{rf}} t$ )
$\omega_c$	cyclotron angular frequency [rad/s]
$\omega_0$	resonant frequency
$\omega_{\text{rf}}$	rf frequency

## LIST OF TABLES

- Table 1. Gap voltage in the rf cavity required for different turn numbers using equation 2.80 with injection energy of 5 keV and final energy of 50 keV. pg.130
- Table 2. Compare the cavity voltage ( $V_o$ ) calculated from the analytical model w/ the computer model. Notice that in the computer model, the reduced axial momentum causes an increased number of turns. The lower  $p_z$  and accurate electric field cause a significantly lower cavity voltage required. pg.132
- Table 3. Total phase drift over the acceleration region. Compares what we would expect analytically with the actual computer result (for optimum acceleration case). pg.135
- Table 4. Final system parameters for a 5 turn trajectory through the 50 keV ICRA. pg.138
- Table 5. A summary of the basic characteristics of each of the main 3 beam diagnostics. pg.163
- Table 6. Two points on the magnetic axis (relative to the axis of the magnet bore). Azimuthal variation for all z planes is less than 0.15% of the central field value ( $B_o = 2.5T$ ). pg.170
- Table 7. Approximate beam currents of each constituent in a typical beam used in the 50 keV ICRA. pg.172
- Table 8. Results of method 1: Parameters for the hybrid rf cavity. pg.181
- Table 9. Three voltage ratios measured by the low power calibration method. pg.186
- Table 10. Comparison between low power measurements made by method 1 and method 2. pg.187
- Table 11. Summary of rf cavity measurements. pg.189
- Table 12. Comparison between calculation and experimental data of the  $H^+$  beam orbit radius in the high B-field region. In each case the beam is just below mirroring ( $p_{\perp} \approx p_{total}$ ). pg.200
- Table 13.  $p_z$  and  $\Delta p_z$  as well as  $N_{turns}$  and  $\Delta N_{turns}$  of the injected beam calculated from experimental mirror data of Figure 91. pg.207

Table 14. Arc lengths observed visually on the extraction Faraday cup ( $V_{\text{Einzel}} = 2.8 \text{ kV}$ ).  
pg.209

Table 15. Rate of change of total number of turns (N) through the 50 keV ICRA.  
Visual observations compared with computer result (using  $V_{\text{mirror}} = 745 \text{ V}$  for trailing  
edge of image).  
pg.210

Table 16. Three different 10 MeV ICRA designs with  $\alpha = 2,4,8$ .  
pg.249

# LIST OF FIGURES

## **Chapter 1.**

- Figure 1. An example of a two dee cyclotron and the coordinate system used. pg.2
- Figure 2. Side view of a gyrotron. pg.4
- Figure 3. Cross section of the annular electron beam in a gyrotron. Copied from reference [4] pg.5
- Figure 4. Electric a) and magnetic b) fields in a magnetron structure with 8 oscillators. Copied from [8]. pg.6
- Figure 5. Hole and slot configuration of a single oscillator and its equivalent LC circuit. Copied from [9]. pg.7
- Figure 6. Basic components of an ICRA pg.9

## **Chapter 2.**

- Figure 7. An ion moving in a helical path in a constant axial B-field. pg.13
- Figure 8. Cross sections of a Helmholtz coil (left) and a solenoid (right) with equal coil dimensions pg.14
- Figure 9. Axial field profile for a Helmholtz coil (left) and a solenoid (right) with equal dimensions. pg.14
- Figure 10. Examples of waveguides. pg.20
- Figure 11. a) A TE field pattern in which E is transverse only, but B has transverse and axial components. b) A TM field pattern in which B is transverse only, but E has transverse and axial components. pg.21
- Figure 12. Cross section of a coaxial transmission line. pg.24
- Figure 13. Geometry of a quarter wave cavity. pg.27

Figure 14. Voltage and current profiles for the quarter wave cavity.	pg.27
Figure 15. A four gap magnetron structure showing the $\pi$ -mode at two different times The z axis points into the page.	pg.34
Figure 16. Geometry of a single oscillator and its equivalent circuit.	pg.35
Figure 17. Equivalent circuit for a four gap magnetron in the $\pi$ mode.	pg.36
Figure 18. A four gap magnetron made of hyperbolic vanes.	pg.38
Figure 19. The C  (R <sub>o</sub> +L) circuit which represents the frequency response of a resonant cavity.	pg.39
Figure 20. The parallel RLC circuit representation of a resonant cavity uses a fictitious shunt resistance (R <sub>s</sub> ).	pg.40
Figure 21. An extra capacitance added across the end of a foreshortened quarter wave cavity.	pg.42
Figure 22. Assumed voltage profile and lengths of the hybrid cavity for the 50 keV ICRA.	pg.43
Figure 23. Top and side view of the trajectory through an ICRA with trajectory shown in red, and magnetic field lines shown in blue. The axial magnetic field profile is plotted below.	pg.47
Figure 24. Beam orbit as seen looking in the axial direction as bend voltage is increased	pg.48
Figure 25. Geometry of the electrostatic bend.	pg.51
Figure 26. Geometry of conservation of magnetic moment (copied from reference 19).	pg.54
Figure 27. A comparison of the beam orbit radius through the injection region calculated using the analytical model and using ICRAcyclone. The magnetic field profile is shown in blue.	pg.55
Figure 28. Mirroring the beam is analogous to when a ball does not have enough kinetic energy to make it to the top of a hill.	pg.60

- Figure 29. Axial view of a beam containing three ions species. The bend voltage is fixed at the point for which the Argon orbit is centered around the z axis. pg.62
- Figure 30. An rf driven magnetron structure with  $n=4$  oscillating in the  $\pi$ -mode. pg.66
- Figure 31. Azimuthal component of the E-field vs azimuthal position. pg.66
- Figure 32. Lowest order term for the radial dependence of cavity voltage in an 8 gap magnetron. pg.68
- Figure 33. Beam orbit radius from spread sheet calculation plotted next to magnetron inner radius. pg.69
- Figure 34. Magnetic field profile for the 50 keV ICRA with flatness of  $\delta B/B_0 < 0.5\%$  over the 5 cm acceleration region. pg.73
- Figure 35. Axial turn length depends on beam radius (or energy) in the extraction region pg.76
- Figure 36. Equipotential lines in an 8 gap magnetron structure at entrance (left) and exit planes (right). Solution computed using RELAX3D. pg.80
- Figure 37. Final proton energy vs initial phase for single particle trajectories through the computer model of the 50 keV ICRA. The curve is repeated for three different rf cavity voltages. pg.82
- Figure 38. Cavity voltage required for “optimal acceleration” vs. number of turns through the acceleration region of the 50 keV ICRA. pg.83
- Figure 39. Final proton energy vs initial phase for fixed  $V_0$  in the 50 keV ICRA. As  $\alpha$  is increased, the beam gains more energy and eventually strikes the wall. Here  $\alpha_0$  indicates  $p_{\perp}/p_{\parallel}$  of the central ray. pg.85
- Figure 40. Beam orbit radius vs z position for the three trajectories in Figure 39 with  $\phi_0=68^\circ$  and  $\Delta\alpha/\alpha = (+2\%, 0, \text{ and } -2\%)$ . pg.86
- Figure 41. A snapshot in time of an ion (red dot) at the moment of peak electric field across the gap. Two cases are shown. On the left the ion lags the rf and on the right the ion leads the rf. pg.88
- Figure 42. Axial momentum through the acceleration region (rf on) for three different initial phases. pg.89

Figure 43. Three ions are started with different initial phases. Tracking their phase through the acceleration region reveals phase pulling toward  $90^\circ$ . Notice the red line goes through the greatest number of turns and the green line goes through the fewest turns. pg.90

Figure 44. The red line shows final vs. initial phase of protons accelerated through the magnetron. (50 keV ICRA design). The solid black line represents final phase equal to the initial phase. Dotted lines have been placed at  $\phi=90^\circ$  and  $\phi=(360^\circ+90^\circ)$  for comparison. pg.91

Figure 45. Final proton energy vs. initial phase for a fixed  $V_0$  in the 50 keV ICRA. The beam which passes through the end fields before entering the cavity shows a higher energy gain and a shift in optimum initial phase. pg.93

Figure 46. The ion with initial  $\phi > 90^\circ$  gets a decrease in  $p_z$  through end fields, but the ion with initial  $\phi < 90^\circ$  gets an increase in  $p_z$ . The particle moves left to right. The acceleration region is between the dashed lines. The entrance end fields are just to the left of the acceleration region. pg.94

Figure 47. Phase vs. axial position over the acceleration region. pg.96

Figure 48. Top and side view of a proton trajectory through the entire computer model for the 50 keV ICRA. Here  $\frac{1}{2}V_{\text{bend}} = 722$  Volts. The beam mirrors before reaching the accelerating cavity. pg.98

Figure 49. Top and side view of a proton trajectory through the entire computer model for the 50 keV ICRA. Here  $\frac{1}{2}V_{\text{bend}} = 718$  Volts. The beam is just below the mirror voltage. RF is off. pg.100

Figure 50. Axial view of the same trajectory as shown in Figure 49 except that the trajectory is only shown through the injection region.  $\frac{1}{2}V_{\text{bend}} = 718$  Volts. The beam is just below the mirror voltage. RF is off. pg.102

Figure 51. Top and side view of a proton trajectory through the entire computer model for the 50 keV ICRA. Here  $\frac{1}{2}V_{\text{bend}} = 710$  Volts, which gives  $N_{\text{turns}} = 11$  through the cavity length. RF is off. pg.104

Figure 52. Top and side view of a proton trajectory through the entire computer model for the 50 keV ICRA. Here  $\frac{1}{2}V_{\text{bend}} = 680$  Volts, which gives  $N_{\text{turns}} = 5$  through the cavity length. RF is off. pg.106

Figure 53. Top and side view of a proton trajectory through the entire computer model for the 50 keV ICRA. Again  $\frac{1}{2}V_{\text{bend}} = 680$  Volts, which gives  $N_{\text{turns}} = 5$  through the cavity length, but now the rf is on. pg.108

Figure 54. Axial view of the same proton trajectory that was shown in Figure 53 except that here the trajectory is shown only through the acceleration region so that the increase in radius can be seen. Again  $\frac{1}{2}V_{\text{bend}} = 680$  Volts,  $N_{\text{turns}} = 5$  through the cavity length, and the rf is on. pg.110

Figure 55. Initial particle coordinates at the ion source are expressed in a Cartesian coordinate system centered on the central ray, but the acceptance phase space at the entrance plane of the magnetron must be expressed in an accelerator-centered cylindrical coordinate system. pg.55

Figure 56. Two planes through the acceptance phase space at the entrance plane of the magnetron for a 1 MeV proton ICRA. Each data point represents a summation over all rf phases. pg.116

Figure 57. Final positions of protons shot forward from the ion source through the injection fringe fields and stopped at the entrance plane of the magnetron. The acceptance phase space from Figure 56 is outlined with dotted lines for comparison. pg.117

Figure 58. The emittance used at the ion source is a coupled phase space of  $3 \times 3 \times 3 = 81$  particles pg.118

Figure 59. Final x, y positions of protons on the extraction Faraday Cup after being shot from the ion source through the entire system. Here the bending voltage is high enough to give an arc length of more than  $360^\circ$ . pg.120

Figure 60. Final  $\theta$  position of protons on extraction Faraday Cup vs their axial momentum at  $z=0$ . pg.121

Figure 61. A mirror curve generated using ICRAcyclone. The fraction of particles, which reach the extraction Faraday cup without being mirrored, is plotted vs. bend voltage. pg.61

Figure 62. Mirror voltage of 81 protons vs. their axial momentum at  $z=0$  at  $V_{\text{bend}} = 690\text{V}$ . The solid line is included for visual comparison with linear. pg.123

Figure 63. An integrated Energy distribution for the 50 keV ICRA generated using the computer model. Emittance of the injected beam was  $2.2\pi$  mm mrad. pg.125

Figure 64. Scanning over cavity voltage shows a peak in the beam current accelerated above a given energy. Emittance of the injected beam was  $2.2\pi$  mm mrad. Data generated using the computer model for the 50 keV ICRA design. pg.126

### **Chapter 3.**

Figure 65. Beam radius vs. magnetic field for several beam energies. pg.129

Figure 66. Phase vs.  $z$  for trajectories started with different initial phases in the 50 keV ICRA. The red, blue, and green curves use the computer model with a solenoidal B-field, cavity end fields, and acceleration through the magnetron. The oscillation (once per turn) is caused by motion of the orbit center. The blue oscillating curve gives optimum acceleration. The smooth blue curve is the analytical calculation of phase based on equation 2.83 which assumes a centered beam and no phase pulling. Vertical dotted lines represent the ends of the acceleration region. Both blue curves have the same initial phase at the cavity entrance so the total phase change over the acceleration region can be compared. pg.134

Figure 67. Parallel and perpendicular momentum and beam radius calculated analytically through the injection region. pg.136

Figure 68. Side view of the 50 keV ICRA with the author added to give a sense of scale. The large blue dewar contains the superconducting solenoid. The ion source is on the left and the extraction end is on the right. The vertical tube leads up to the vacuum turbo pump which is just off the top of the photo. pg.140

Figure 69. A view looking down on the ion source. Notice the angle between the accelerator  $z$  axis and the source axis is because the source is aligned with a B-field line. The motion feed through mounted on the left side of the junction piece (red tape around it) is used for moving the injection Faraday cup into the beam. pg.141

Figure 70. A side view of the ion source assembly, which shows the four main components. From left to right, these are: the water cooling jacket, the insulating glass break, the electrical feed through, and the bellows which connects the source to the vacuum junction. The actual ion source is inside the water cooling jacket, and the Einzel lens can be seen through the glass break. The electrostatic bend is inside the vacuum junction. Compare this photo with the mechanical drawing of Figure 72. The source is mounted on two V-blocks which are rigidly connected by an aluminum plate. Pusher blocks on the sides of the V-blocks are used to adjust the position and angle of the source horizontally, and vertical bolts through the aluminum plate are used to adjust the position and angle of the source vertically. pg.142

Figure 71. The extraction end of the 50 keV ICRA. The rf accelerating cavity (aluminum tube) is mounted in the bore of the superconducting magnet (blue). The V-block below the cavity can be adjusted in order to align the rf cavity with the magnetic axis. The extraction port covers the extreme downstream end of the system and contains the extraction Faraday cup and viewports for observing the beam. The mechanical feedthrough on top of the extraction port is used to move the radial probe, in the radial direction (see Figure 73). pg.143

Figure 72. Top view of a cross section through the 50 keV ICRA. All major components are labeled, however the radial probe is not shown in this view (see Figure 73). B-field lines are shown in blue and a trajectory is shown in red. The magnetron section only is cut through two different planes in order to show the inner and outer vanes both. Figure 76 shows this more clearly. pg.144

Figure 73. Side view of a cross section through the 50 keV ICRA. All major components are labeled. B-field lines are shown in blue and a trajectory is shown in red. The magnetron section only is cut through two different planes in order to show the inner and outer vanes both. Figure 76 shows this more clearly. pg.146

Figure 74. Simple representation of the vacuum system showing typical pressures during high gas load into ion source. Conductances are calculated using formulas in [17]. pg.150

Figure 75. Schematic of the electronics for the 50 keV ICRA. pg.154

Figure 76. A cutaway view of the rf cavity. Notice that in the magnetron section only, the cross section has been taken through two different planes in order to show a cross section through an inner vane and an outer vane both. pg.159

Figure 77. Components of the magnetron section before assembly. pg.161

Figure 78. Components of the hybrid rf cavity. Here the magnetron is assembled. The magnetron, inner conductor, and shorting plate (all made of copper) are about to be inserted into the aluminum outer conductor. pg.161

Figure 79. A view of the fully assembled rf cavity looking into the extraction end. The 8 tapered magnetron vanes of the acceleration section can be seen inside the ID of the exit mounting ring. pg.162

Figure 80. Pivot points of the mounting structure. pg.167

#### **Chapter 4.**

Figure 81. Measured axial magnetic field at  $r = 0$ . Data has been centered axially and normalized. pg.171

Figure 82. Measured axial magnetic field in the acceleration region. The smooth line is a parabolic curve fit to the data. The flat field length for  $\Delta B/B_0 < 0.5\%$  is 2.1 inches = 5.3 cm. pg.171

Figure 83. Schematic drawing of the experimental setup for measurement of Q. The matched state is the condition used when running the cavity at full power and accelerating beam. However, measured Q approaches the true unloaded Q only in the unloaded state. pg.179

Figure 84. Transmission frequency response curves used for measurement of the Q. The matched state (top) gives  $f_o/\Delta f = 802$ , and the unloaded state (bottom) gives  $f_o/\Delta f = 1550$  pg.180

Figure 85. Experimental setup for the calibration of method 2. V is a voltage at a probe, and V' is a voltage at the end of a cable. pg.183

Figure 86. Geometry of the ion beam as one constituent clips on the entrance to the magntron. Here the bending voltage is turned high enough that the  $H_2^+$  beam (larger radius) has clipped on the entrance to the magntron and the beam with the  $H^+$  (smaller radius) is centered on the z axis. pg.196

Figure 87. Ion spectrum taken on the extraction FC. The solid black line shows experimental data. Theoretical values where each ion should clip have been calculated using equation 2.73 and are shown as vertical red dotted lines. From left to right:  $Ar^+$ ,  $N_2^+$ ,  $O_2^+$ ,  $C_2^+$ ,  $Ar^{+2}$ ,  $H_2O^+$ ,  $N^+$ ,  $O^+$ ,  $Ar^{+3}$ ,  $C^+$ ,  $H_3^+$ ,  $H_2^+$ , and  $H^+$ . The experimental value at which the  $H^+$  beam mirrors is shown as a blue dotted line. Using these calculated values, the expected theoretical curve is plotted as a solid red line. pg.197

Figure 88. Drawing of the beam image observed on the extraction Faraday cup. Here the bending voltage is high enough that both ion beams produce a full  $360^\circ$  ring. At lower bend voltages the image observed is less than  $360^\circ$  as will be described in section 4.5.4. pg.198

Figure 89. Experimental data. Black diamonds represent beam current measured on the radial probe which is shielded from electrons showers. Dotted lines mark the range of bend voltage where the  $H_2^+$  beam was observed to clip visually, and where the  $H^+$  beam mirrors. pg.199

Figure 90. Experimental mirror curve. Proton beam current on the radial probe vs. bend voltage for several different Einzel lens settings. pg.201

Figure 91. Experimental data. Proton beam current on the radial probe vs. bend voltage. The Einzel Lens setting is 3.0 kV. pg.202

Figure 92. Analytical calculation of  $p_z$  vs bend voltage compared with the result from the full computer model. The analytical calculation depends on the mirror voltage, therefore the two curves meet at the mirror point a-priori. pg.205

Figure 93. Analytical calculation of the spread in  $p_z$  vs bend voltage. pg.206

Figure 94. Drawing of the proton beam image observed on the extraction Faraday cup  
The arc length can only be measured for low bending voltages, where  $\Delta\theta < 360^\circ$ .pg.208

Figure 95. Comparison between computer generated mirror curves and experimental data. Experimental data (black diamonds) is normalized to its peak value (45 nA). The 5 solid lines represent computer generated mirror curves for 5 different injected emittances. pg.212

Figure 96. Arc length increases with bend voltage. The experimental data from Table 14 is plotted. The computer model is used to generate arc lengths for three different injected beam emittances:  $0.1\pi$ ,  $0.35\pi$ , and  $0.8\pi$  mm mrad (emittances are un-normalized). pg.213

Figure 97. Measured radial distribution with rf on and off (raw data). Beam current on the radial probe is plotted vs. radial position of the radial probe. Vertical dotted lines mark the calculated radius of the injected beam and maximum radius corresponding to the exit diameter of the magnetron. pg.215

Figure 98. Top graph: Raw data and corrected data are shown for rf on and off. The solid line shows a theoretical curve for the rf off case only. Bottom graph: The corrected data for rf on and off is shown on a log scale in order to show the accelerated data more clearly. pg.217

Figure 99. Drawing of visual observations on the extraction Faraday cup. This axial view shows the extraction Faraday cup which is located  $\approx 7''$  further down stream (into the page) than the radial probe. The radial probe casts a shadow at  $90^\circ$  rotation from the probe. The edge of the shadow moves inward as the radial probe is moved inward. pg.219

Figure 100. Measured energy distribution with rf on and off. Data is taken from the corrected radial distribution of Figure 98. Dotted lines mark the injection energy and peak design energy. pg.220

Figure 101. Comparison between corrected experimental data and the computer generated energy distribution. In each case:  $V_o = 1.7$  kV,  $\frac{1}{2}V_{\text{bend}} = 740$ V,  $V_{\text{Einzel}} = 2.5$  kV. The computer model uses a  $2.2\pi$  mm mrad injected beam emittance. pg.221

Figure 102. Measured energy distributions for several bending voltages. Cavity voltage is 1.4 kV,  $V_{\text{Einzel}} = 2.7$  kV, Mirror voltage ranges from 690 – 745 V. pg.222

Figure 103. Experimental data from Figure 102 is compared with the computer result. Here, bending voltages of 690 V and 710 V are used in the computer and experiment both. pg.223

Figure 104. Experimental data from Figure 102 is compared with the computer result. In the top graph the same bend voltage is used for computer and experiment. In the bottom graph, bending voltages in the computer model have been shifted lower to obtain matching energy distributions. pg.224

Figure 105. Experimental data showing the accelerated beam current vs. magnetic field. The position of the radial probe is 19.3 mm ( $E > 38$  keV), and  $\frac{1}{2}V_{\text{bend}} = 683$  V ( $N_{\text{turns}} \approx 5$ ). pg.226

Figure 106. Comparison between experimental data and the computer generated resonance width. The computer model uses:  $\frac{1}{2}V_{\text{bend}} = 683$  V,  $E > 38$  keV (for R-probe at 19.3 mm) and injected beam emittance of  $2.2 \pi$  mm mrad. pg.227

## **Chapter 5.**

Figure 107. Measured energy distribution of the proton beam with rf on and with rf off. pg.229

Figure 108. Comparison between measured energy distributions and computer generated energy distributions for two different bend voltages. pg.230

Figure 110. Cross section of a magnetron with two linear tapers used to approximate the square root shape of the acceleration trajectory. pg.233

Figure 111. The infinitesimal energy spread caused by an infinitesimal spread momentum spread is plotted vs.  $\alpha$  and for several values of  $n$ . pg.238

Figure 112. A graphical map of the basic design equations for the acceleration trajectory of the ICRA. Input parameters are  $E_0$ ,  $\alpha$ ,  $B_0$ ,  $n$ ,  $F$ ,  $E_{\text{gain}}$ , and the average radius fraction ( $r/R$ ). pg.241

Figure 113. Design equations for the resonant structure of the rf driven magnetron. Input parameters are:  $\ell_c$ ,  $n$ , and  $Q$ . Parameters taken from Figure 112 are:  $g$ ,  $\ell_{\text{cav}}$ ,  $f_{\text{rf}}$ , and  $V_0$ . pg.242

Figure 114. The dotted line shows the diameter required for resonators of the magnetron ( $n=4$ ) as a function of magnetic field. The solid line shows total diameter  $D = 2(r_{\text{beam}} + R_{\text{magnetron}})$  (for a 10 MeV beam) needed for the warm bore of the superconducting magnet. pg.247

# 1. INTRODUCTION

The Ion Cyclotron Resonance Accelerator (ICRA) is an ion accelerator which uses novel geometry. It combines the principles of cyclotrons and gyrotrons and uses an rf driven magnetron as the accelerating structure. The intent of the ICRA concept is to create an accelerator which is simple, compact, and lightweight. An ICRA designed to accelerate protons to 10 MeV would be useful for the production of radioisotopes, or neutrons, and may also have applications in materials science. The ICRA concept and 10 MeV design were first published in 1997 [1].

As a demonstration of the concept, a computer model has been developed to study particle trajectories in the ICRA, and a 50 keV proton ICRA has been built and tested. The first experimental results were published in April 1999 [2]. This thesis describes the theory that has been developed for the ICRA, then presents the design of the 50 keV prototype, and compares the experimental results with the theory. Finally it gives recommendations for future research, and presents an improved 10 MeV design.

This chapter begins by introducing the reader to cyclotrons, gyrotrons, and magnetrons. In section 1.4 an overview of the ion cyclotron resonance accelerator and its basic components are given. Section 1.5 discusses the applications for which the ICRA is the most well suited.

Chapter 2 covers the theory which has been developed for the ICRA, including both analytical and computer model. Chapter 3 then presents the specific design of the 50 keV experiment. Chapter 4 shows the experimental results, and compares with the theory. Chapter 5 then gives recommendations for future research, presents the design of a 10 MeV ICRA, and gives a conclusion.

## 1.1 Cyclotrons

In 1931 Ernest Lawrence demonstrated the cyclotron, by accelerating protons to an energy of 80 keV. This new tool for probing the nucleus fueled our understanding of the atom and led to the rise of nuclear and high energy physics. Today, synchrotrons achieve much higher energies than cyclotrons, however cyclotrons are still the leading choice in fields such as the production of radioisotopes for medical applications, proton and neutron beam therapy for treatment of cancer, as well as nuclear physics.

Cyclotrons use time varying electric fields to accelerate charged particles in the azimuthal ( $\theta$ ) direction, and an axial ( $z$ ) dc magnetic field to bend the particle beam into a closed orbit so that it will pass through the same accelerating structure many times. The geometry and coordinate system for a simple cyclotron are shown in Figure 1. The accelerating structure is a set of hollow conductors called “dees”, which serve the same function as drift tubes in a linear accelerator. As a particle passes through a dee, the voltage potential is changing with time, but is constant with respect to position so the electric field inside the dee is zero. However, since each adjacent dee has a different voltage, particles are accelerated by electric fields across the gaps between the dees.

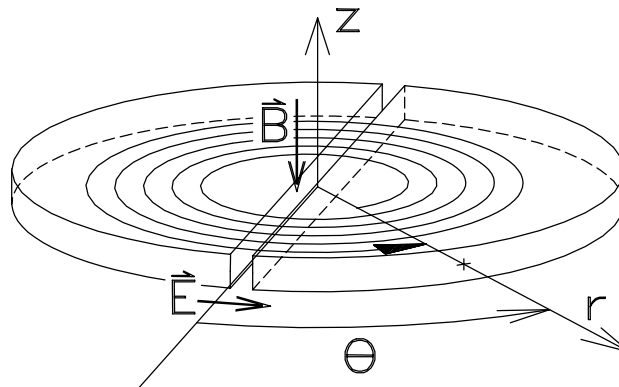


**Figure 1. An example of a two dee cyclotron and the coordinate system used.**

The voltage on the dees alternates at a constant rf frequency ( $f_{rf}$ ). In order to be continuously accelerated, the beam must cross each gap only at times when the E-field is pointing forward (azimuthally). Thus, the rf frequency must be a harmonic of the cyclotron orbital frequency ( $f_c$ ). This is the resonance condition required for acceleration.

Because of the “drift tube” nature of the dees, the beam will strike the inner surface of a dee if it is not kept in the median plane ( $z=0$ ). For this reason, weak axial focusing was used to confine ions. At higher energies relativistic effects prevented the use of weak focusing. Therefore, strong axial focusing was developed using steel pole tips to create an azimuthal variation in the magnetic field.

As the beam gains kinetic energy, its orbit radius in the magnetic field increases. Extraction is usually achieved by allowing the beam that reaches full radius to pass behind a thin septum into a region where a strong dc electric field pulls the beam in the radial direction. At large radius, the radial spacing between turns may become extremely small ( $r \propto \sqrt{E}$ ), in which case, some beam current will be lost by scraping on the septum. Beam current hitting the septum creates thermal and radiation issues which contribute to limiting the beam current in the cyclotron. An alternative extraction method is to accelerate a negative ion beam, then use a foil to strip ions to positive charge state which changes the radius of curvature of the beam. In either case, only the beam that reaches full radius is extracted, so the cyclotron has a relatively narrow energy spread in comparison with the ICRA which has no such constraint.

## 1.2 Gyrotrons

Gyrotrons are a source of high power coherent microwaves. Theoretical gyrotron research began in the late 1950's by Twiss in Australia, J. Schneider in the U.S. and A.Gaponov in the U.S.S.R., though experimental verification was not obtained until the mid 1960's [3]. Today gyrotrons are available from industry with average rf power levels of a megawatt and efficiencies greater than 50%.

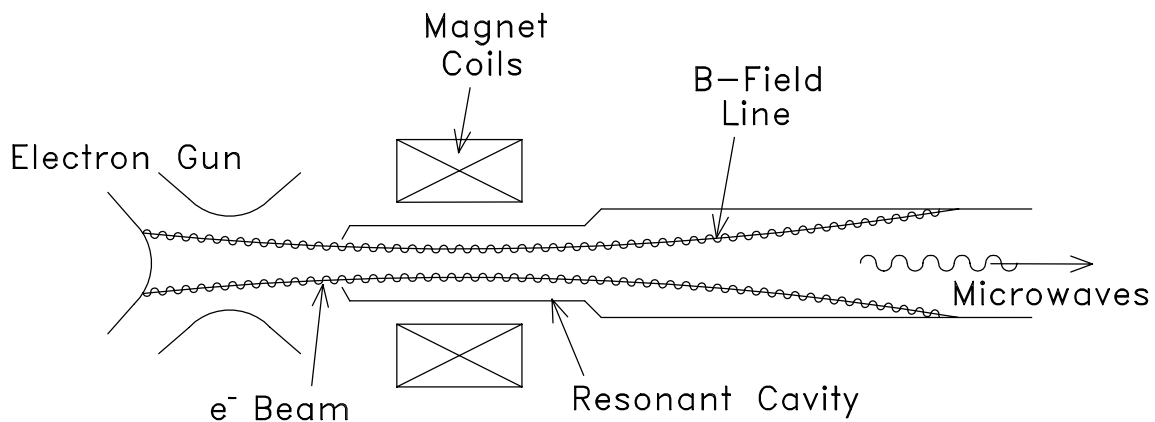


**Figure 2. Side view of a gyrotron.**

Gyrotrons convert the kinetic energy of a dc electron beam into high frequency electromagnetic fields by exciting waveguide modes in a cylindrical resonant cavity. A magnetic field in the direction of the cavity z axis, confines an annular electron beam to spiral around B-field lines. The e<sup>-</sup> beam is hollow in the center and contains many tiny beamlets around the circumference as shown in Figure 3.

The source of the electron beam is an electron gun located outside the resonant cavity in the fringe field region of the magnet. Here the velocity component parallel to

the B-field is set so that the beam will drift along field lines into the high field region of the resonant cavity where the interaction occurs. Inside the waveguide structure, the relativistic electron beam interacts with azimuthal electric fields which causes bunching within each beamlet. [4]

**Figure 3. Cross section of the annular electron beam in a gyrotron**  
Copied from reference [4]

Bunching and the transfer of energy from the electrons to the cavity fields both depend on a resonance between the cyclotron frequency of the electron orbits and the frequency of the cavity fields.

Even at the time that gyrotrons were being investigated as a source of microwaves, it was recognized that the inverse should also be possible, i.e. to accelerate electrons by driving a gyrotron structure with microwave power. This was demonstrated by Jory and Trivelpiece in 1968. Using electric fields from the  $TE_{11}$  mode of a circular waveguide, they accelerated a 10 mA electron beam and measured an energy gain of 460 keV [5].

### **1.3 The Magnetron**

Magnetrons, like gyrotrons, generate microwave radiation by converting the kinetic energy of an electron beam into electromagnetic fields in a resonant cavity which is immersed in an axial magnetic field [6]. Development of the magnetron in the late 1930's and early 1940's was instrumental in the successful use of radar during World War II [7]. Today magnetrons generate microwaves at 2.45 GHz in microwave ovens all over the world, and are so common that you can purchase a replacement tube for about \$50.

**Figure 4. Electric a) and magnetic b) fields in a magnetron structure with 8 oscillators.  
Copied from [8]**

The magnetron structure itself is a resonant cavity, but it is much different than the open waveguide structure of the gyrotron. The cavity is comprised of several coupled oscillators as shown in Figure 4. The hole and slot configuration of each oscillator means that the magnetron structure behaves like a lumped circuit with isolated inductance and

capacitance (Figure 5). The additional inductance and capacitance lowers the resonant frequency and allows the magnetron to be much smaller than a wavelength. Our interest in the magnetron is as an accelerating structure because an rf driven magnetron can be used to generate electric fields in the azimuthal direction.

**Figure 5. Hole and slot configuration of a single oscillator and its equivalent LC circuit.  
Copied from [9].**

#### **1.4 Ion Cyclotron Resonance Acceleration**

The ion cyclotron resonance accelerator (ICRA) combines the principles of cyclotrons and gyrotrons. Like the cyclotron, ions are confined radially ( $r$ ) while being accelerated in the azimuthal ( $\theta$ ) direction. However, in the axial ( $z$ ) direction, the beam is not confined. Instead, the beam is allowed to drift through the accelerating structure just as the electron beam drifts through the waveguide of a gyrotron. For this reason, an appropriate name for the ICRA is an “axial drift cyclotron”.

As mentioned previously, Jory and Trivelpiece demonstrated cyclotron resonance acceleration by accelerating an axially drifting electron beam in a waveguide. The research documented here extends cyclotron resonance acceleration to ions for the first time. The waveguide structures used in gyrotrons are on the order of a wavelength and would be too large at the low frequencies required to accelerate ions. However, by using an rf driven magnetron operating at a harmonic of the cyclotron frequency, together with a high field superconducting magnet, the accelerating structure becomes small enough to fit into the bore of a common superconducting magnet. This means that a magnet which is available from industry can be used.

The main components of an ICRA are shown in Figure 6. These are the superconducting magnet, ion source, electrostatic bend, accelerating structure, and the target. A dc ion beam is extracted from the ion source directly along a B-field line so that the  $\vec{v} \times \vec{B}$  force on the beam is zero. The electrostatic bend deflects the beam so that it has a component of momentum perpendicular to the B-field which causes it to orbit around field lines. The remaining momentum parallel to the B-field causes the beam to spiral axially into the high field region. At the acceleration region, the B-field is relatively flat and the beam drifts axially through the magnetron structure. While inside the magnetron, rf electric fields accelerate the beam in the azimuthal direction so that the radius of the beam orbit increases. Upon exit from the magnetron, the beam spirals into the lower field of the extraction region, until striking a target downstream. A detailed description of the beam trajectory is given in section 2.5.

**Figure 6. Basic components of an ICRA**

This acceleration scheme is inherently simple, compact, and inexpensive. In principle, the rf driven magnetron can be cut out of a single piece of copper. Superconducting magnets of the proper size are available from industry. The high magnetic field means the machine is very compact. Furthermore, because of the lack of axial focusing, no steel is needed to shape magnetic fields so the entire machine is lightweight. Since an ICRA would be compact and lightweight, it might be designed to be portable which could open up some field applications for accelerators. Beam extraction is inherently simple because nearly all of the beam drifts through the accelerating cavity to the target region where it can be isolated from the accelerator mitigating maintenance and radiation shielding issues.

As we will see, the penalty for all of these advantages is that the beam accelerated by the ICRA contains a large energy spread. In fact the extracted beam will contain energies ranging from near zero to the full design energy. This is caused by three

factors. 1) For simplicity the injected beam is dc, therefore the part of the beam which is in phase with the rf is accelerated, while the rest of the beam is decelerated. 2) Any spread in the axial momentum through the acceleration can cause a difference in the number of kicks an ion receives. 3) A radial dependence of the accelerating fields in the rf driven magnetron causes radial defocusing. The large energy spread simply means that the ICRA will be most useful for applications in which an energy spread does not matter, such as the production of radioisotopes, or neutron beams.

## **1.5 Applications**

Today proton and heavier ion beams at energies below a few MeV are typically produced by electrostatic accelerators or radio frequency quadrupoles. Beams above a few MeV are typically produced by cyclotrons, or linacs, with the highest energies being attained by synchrotrons. In principle, an ICRA could be designed to accelerate any ion to any energy range. However, for the purpose of limiting the scope of this discussion, we will concentrate on a particular energy regime from 3 to 12 MeV. In particular, an ICRA designed to accelerate protons or deuterons to 10 MeV would be useful for many applications. Three areas for which the ICRA is the most well suited are 1) production of short lived radioisotopes, 2) as an accelerator based neutron source, and 3) for materials science applications.

The use of radioisotopes in medicine and industry has experienced steady growth over the past two decades. Medium energy accelerators ( $10 < E < 30$  MeV) are used in commercial production of radioisotopes with half lives long enough for shipment. Lower

energy machines ( $E < 10$  MeV) are used in hospitals for on site production of relatively short lived isotopes. The most common of these are the positron emitters:  $^{11}\text{C}$ ,  $^{13}\text{N}$ ,  $^{15}\text{O}$ , and  $^{18}\text{F}$  which are used for positron emission tomography (PET) [10,11]. A 10 or 12 MeV ICRA delivering 10 to 50  $\mu\text{A}$  of protons to the upper half of the energy range would be useful for production of these PET isotopes. If that ICRA were designed to be portable, it could be shared by several institutions.

Applications for neutron beams include thermal neutron radiography, fast neutron radiography, fast neutron analysis, and neutron activation analysis. Of these, fast neutron analysis has recently gained attention as a method for rapidly identifying materials in applications such as bomb/drug/weapon detection for airport security. A more common application of neutron beams, thermal neutron radiography, is used to produce an image of the internal components of an object by passing neutrons through the object and imaging the neutrons on film. The majority of neutron radiographs are made at nuclear reactors where high neutron fluxes are available. The disadvantage here is that equipment to be radiographed must be brought to the reactor site. Accelerator based neutron sources produce somewhat lower neutron fluxes than reactors, but offer the possibility of being portable and therefore would be more useful for field applications. A 10 MeV ICRA producing only 10 $\mu\text{A}$  of protons (upper half of  $\Delta E$ ) would produce a neutron rate useful for neutron radiography or as a research tool for fast neutron analysis.

Finally there are numerous materials science applications for which a 10 MeV ICRA would also be useful including: ion implantation, charged particle activation analysis, and radiation damage studies.

## 2. THEORY

This chapter covers the theory needed to understand and design an ion cyclotron resonance accelerator (ICRA). Sections 2.1, 2.2, and 2.3 explain basic considerations for the magnetic field, vacuum, and ion source. Section 2.4 covers the theory of resonant rf cavities. The last two sections comprise the majority of the chapter. Section 2.5 covers all aspects of the beam trajectory that can be calculated analytically. Section 2.6 covers those aspects of the beam trajectory which can only be calculated using a full computer model.

### 2.1 Magnetic Field

Consider a positive ion with charge ( $q$ ) and mass ( $m$ ) in a region of constant magnetic field,  $B$ . If the ion has some momentum in a direction perpendicular to the B-field ( $p_{\perp}$ ), then the  $\vec{v} \times \vec{B}$  term of the Lorentz force equation provides a centripetal force which causes the ion to move in a circular path. The radius ( $r$ ) of this orbit is given by:

$$p_{\perp} = qBr \quad (2.1)$$

The angular frequency, called the cyclotron frequency, is given by:

$$\omega_c = \frac{qB}{\gamma m} \quad (2.2)$$

where  $\gamma$  is the relativistic mass factor. Notice that for  $\gamma=1$  the cyclotron frequency depends on the B-field and on  $\frac{m}{q}$  of the ion, but does not depend on the ion velocity.

In the direction parallel to magnetic field lines, force on the ion is zero and the ion

will simply drift ( $p_{\parallel} = \text{constant}$ ). Therefore in a region of constant magnetic field, an ion with momentum  $\vec{p} = (\vec{p}_{\perp} + \vec{p}_{\parallel})$  will move in a helical path.

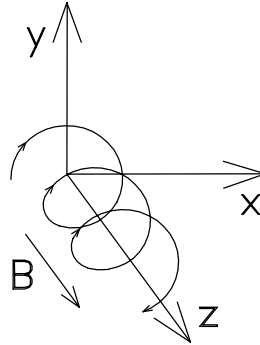


**Figure 7. An ion moving in a helical path in a constant axial B-field.**

As in the cyclotron, acceleration in the ICRA requires a resonance between the rf accelerating fields and a harmonic of the cyclotron frequency, (section 2.5.6). However, since ions in the ICRA will also drift along B-field lines (z direction), the magnetic field must be nearly constant over the axial (z) length of the acceleration region (for  $\gamma \cong 1$ ). At higher energies, the cyclotron frequency will decrease as  $\gamma$  becomes greater than 1. In this case it will be necessary to add a slope ( $dB/dz$ ) to the B-field, which matches the increase in  $\gamma$ , in order to maintain resonance. Since the focus of this work is a low energy 50 keV proton accelerator, the reader should assume that  $\gamma = 1$ , for the remainder of this document unless stated otherwise.

A Helmholtz coil pair provides a longer axial flat field length than a solenoid of equal coil radius ( $R_c$ ) and axial length ( $z_c$ ). However, either coil geometry will work.

The B-field on the z axis ( $r=0$ ), of a single current loop is given by:

$$B_z(z) = B_0 \frac{R_c^3}{(R_c^2 + z^2)^{\frac{3}{2}}} \quad (2.3)$$

where the field has been normalized to the central field value  $B_0$ . This equation can be used to calculate the fields on the axis of a Helmholtz coil or a solenoid by simply placing coils at appropriate locations and then superimposing the B-field of each coil. Solving for the magnetic field off axis ( $r \neq 0$ ) is more difficult (see section 2.6.1). Figure 8 shows the geometry of a Helmholtz coil and a solenoid coil. Figure 9 shows the axial profile of each B-field. Notice the Helmholtz coil provides a significantly longer flat field length.

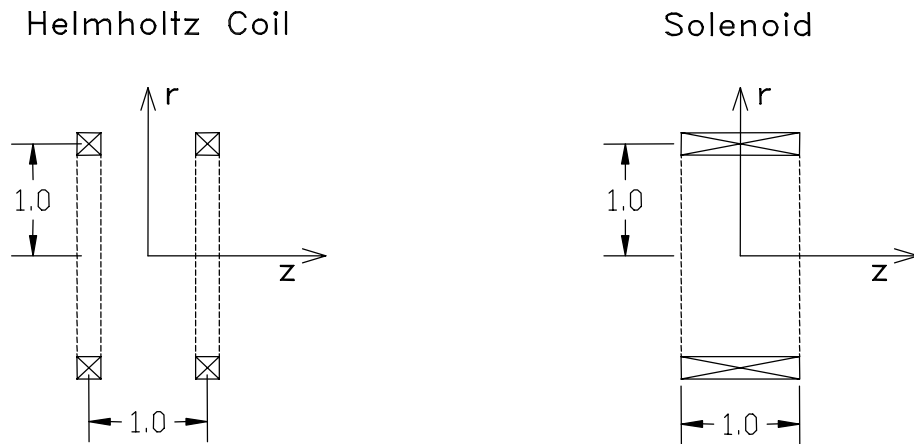


**Figure 8. Cross sections of a Helmholtz coil (left) and a solenoid (right) with equal coil dimensions**

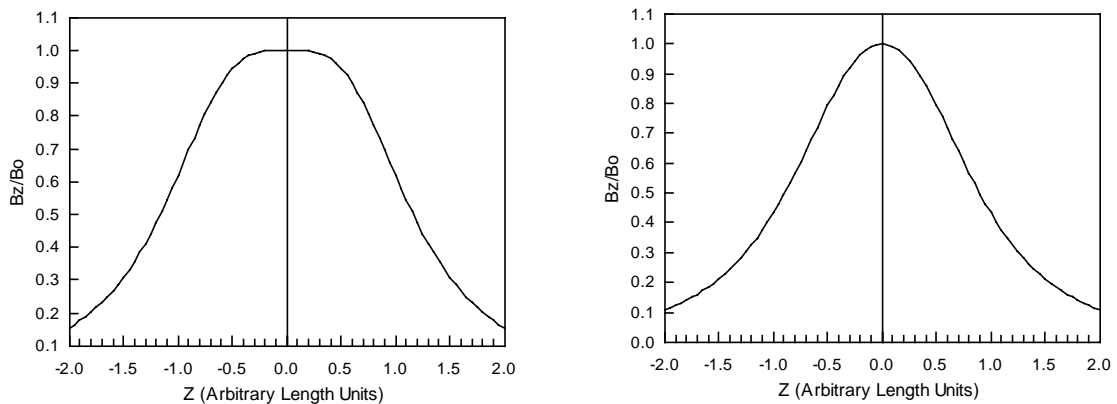


**Figure 9. Axial field profile for a Helmholtz coil (left) and a solenoid (right) with equal dimensions.**

For the ICRA, the choice of B-field profile is an important consideration because: 1) the flat field length limits the axial length available for acceleration, and 2) the ion source must be able to operate in the chosen fringe field region. Furthermore we will see in section 2.5.2 that the ratio of field at the acceleration region to field at the source is involved in determining the increase in the transverse momentum spread of the beam.

## **2.2 Vacuum**

Preferably the vacuum system for any accelerator should maintain a complete absence of atoms. In reality, the pressure in the ICRA will be dominated by the mass flow of gas fed into the ion source, and to a smaller extent by outgassing from materials inside the vacuum chamber. The mean free path ( $\lambda$ ) is the average distance that a particle travels before colliding with another particle. For this experiment, it is sufficient to have a mean free path longer than the path of the beam. Details of the vacuum system are given in section 3.2.2.

### **2.3 Ion Source**

A wide variety of ion sources are adequate to supply the beam for an ICRA. The only requirement is that the source must operate in the fringe field of the magnet at the chosen location. However, a high brightness source is preferred because the acceptance phase space of the rf driven magnetron together with the brightness of the injected beam are crucial parameters which determine the final accelerated beam current.

In most ion sources, the energy spread in the extracted beam is small, because all ions are accelerated through nearly the same potential from the extraction aperture to the puller electrode. However, the beam will have some finite spread in transverse and longitudinal position and momentum. These beam dimensions occupy a 6 dimensional volume in phase space. The transverse spread in position and momentum is normally described in terms of two dimensional areas called the beam emittance. The computer model of the injected beam emittance is discussed in section 2.6.7 of this chapter.

In chapter 3, we will see that the ion source chosen for the 50 keV ICRA is a simple electron impact ion source. Electrons emitted from a hot filament are accelerated through approximately 100 volts toward an anode. The electrons impact and ionize H<sub>2</sub> gas creating H<sup>+</sup> and H<sub>2</sub><sup>+</sup>. An ion beam is extracted from the source at 5 - 10 keV. The energy spread in this type of source is due to both the temperature of the ions and variations in the potential at which the ion was created. The maximum energy spread is still small. The computer model of section 2.6 uses the assumption that  $\Delta E = 0$ .

The source chosen for the 50 keV ICRA also includes an Einzel lens for focusing the beam before injection into the ICRA. This electrostatic lens provides azimuthally symmetric electric fields, which are effective for focusing the low velocity beam, and

also has an adjustable focal length. For the purposes of this chapter on theory, the Einzel lens should be thought of as part of the ion source apparatus. Details of the ion source and the Einzel lens are given in section 3.2.3 of the chapter on design.

## **2.4 RF Cavity**

Initial designs for the ICRA used an rf driven magnetron in an 8 Tesla axial dc magnetic field [1]. In chapter 3 on the design of the 50 keV ICRA we will see that the availability of a 2.5 Tesla superconducting magnet created the opportunity to build a proof of principle device at very low cost. The disadvantage of this lower magnetic field is that a pure magnetron would not fit into the bore of the available magnet. The solution was to build a hybrid coaxial - magnetron cavity.

This section covers the electromagnetic theory needed to design the rf accelerating structure of the ICRA. The theory is well known and is given here as background. Section 2.4.1 begins with plane waves, then reviews waveguide TE and TM modes. Section 2.4.2 covers TEM waves in a coaxial cavity, then the fields in a coaxial quarter wave cavity are derived. Section 2.4.3 gives the fields in the central region of the magnetron structure. Section 2.4.4 simplifies the theory by representing a resonant cavity as an equivalent lumped circuit. Finally, the method used to describe the hybrid cavity is given in section 2.4.5.

### 2.4.1 Waveguides

We begin with the time harmonic form of Maxwell's equations in a source free region of empty space.

$$\vec{\nabla} \times \vec{E} = -i\omega\vec{B} \quad (2.4)$$

$$\vec{\nabla} \times \vec{B} = \frac{i\omega}{c^2} \vec{E} \quad (2.5)$$

$$\vec{\nabla} \cdot \vec{E} = 0 \quad (2.6)$$

$$\vec{\nabla} \cdot \vec{B} = 0 \quad (2.7)$$

In this form, oscillatory time dependence is assumed. Therefore it is only necessary to solve for the spatial dependence,  $\vec{E}(\vec{r})$ , then the full time dependent solution is recovered by multiplying by an oscillatory factor:  $\vec{E}(\vec{r}, t) = \vec{E}(\vec{r})e^{-i\omega t}$ . This approach is correct in general because any non-oscillatory time dependence can be constructed with a Fourier series. However, for this work we are only interested in oscillatory solutions.

Taking the curl of equation 2.4 and substituting equations 2.5 and 2.6 gives:

$$\vec{\nabla} \times \vec{\nabla} \times \vec{E} = -i\omega(\vec{\nabla} \times \vec{B})$$

$$\vec{\nabla}(\vec{\nabla} \cdot \vec{E}) - \vec{\nabla}^2 \vec{E} = -i\omega\left(\frac{i\omega}{c^2} \vec{E}\right)$$

$$\vec{\nabla}^2 \vec{E} = -\frac{\omega^2}{c^2} \vec{E}$$

Where the total wave vector is defined as:

$$|\vec{k}| = \frac{\omega}{c}$$

This gives the vector Helmholtz wave equation:

$$\boxed{(\nabla^2 + k^2)\vec{E} = 0} \quad (2.8)$$

Similarly for the magnetic field:  $\boxed{(\nabla^2 + k^2)\vec{B} = 0}$  (2.9)

Where each vector equation actually represents three scalar wave equations. An important solution of the wave equation in open space (no boundary conditions) is the plane wave. The electric field for a plane wave can be expressed in the form:

$$\vec{E}(\vec{r}, t) = \vec{E}_0 e^{i(\vec{k} \cdot \vec{r} - \omega t)} \quad (2.10)$$

The direction that the wave propagates is given by the wave vector,  $\vec{k}$ , but the direction of the actual electric field is given by  $\vec{E}_0$ . The velocity of propagation is  $v = \frac{\omega}{k} = c$ .

Notice that imposing  $\vec{\nabla} \cdot \vec{E} = 0$  on equation 2.10 gives  $\vec{k} \cdot \vec{E}_0 = 0$ . This means that the E-field cannot point in the direction of propagation [12, 13]. Furthermore, Using equation 2.4 to solve for the magnetic field leads to:

$$\vec{B}(\vec{r}, t) = \frac{1}{\omega} [\vec{k} \times \vec{E}(\vec{r}, t)] \quad (2.11)$$

Evidently the magnetic part of the wave has the same form, but points in a direction perpendicular to the direction of propagation and to the electric field. For this reason plane waves are referred to as transverse electric and magnetic or TEM waves. For example, if the wave propagates in the z direction, then  $\vec{k} \cdot \vec{r} = kz$  and  $\vec{E}_0 = \hat{x}E_x + \hat{y}E_y$  so the plane wave would be written as:

$$\vec{E}(\vec{r}, t) = (\hat{x}E_x + \hat{y}E_y) e^{i(kz - \omega t)}$$

and the B-field would be:

$$\vec{B}(\vec{r}, t) = \frac{k}{\omega} (\hat{y}E_x - \hat{x}E_y) e^{i(kz - \omega t)}$$

### Waveguides

Waveguides are hollow conductors with cross section of any shape that remain constant along their axial (z) length. Examples are shown in Figure 10. Of course electrostatic fields cannot exist inside a waveguide because the metal walls all have the same potential. However, if plane waves are introduced into a waveguide the waves will reflect off of the conducting walls. The incident and reflected waves superimpose to create a standing wave pattern along the transverse dimensions, and a travelling wave along the axial dimension as shown in Figure 11.

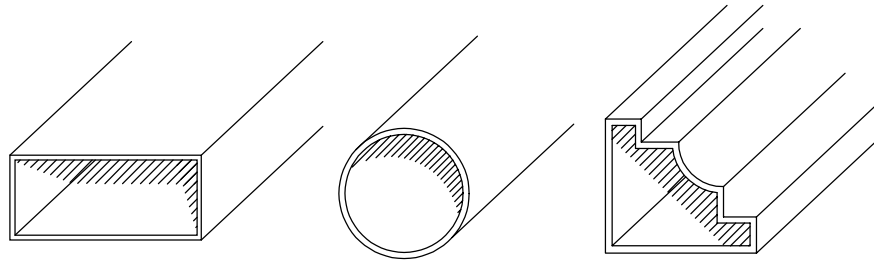


**Figure 10. Examples of waveguides**

Since the wave pattern must satisfy the boundary conditions at the conducting walls, either  $\vec{E}$  or  $\vec{B}$  must have a component in the direction of propagation. Thus fields in a waveguide are either TE (transverse electric) or TM (transverse magnetic), but waveguides do not support TEM waves. Notice that whether the waves are TE or TM depends on the initial polarization of the wave (or the orientation of the driving probe).

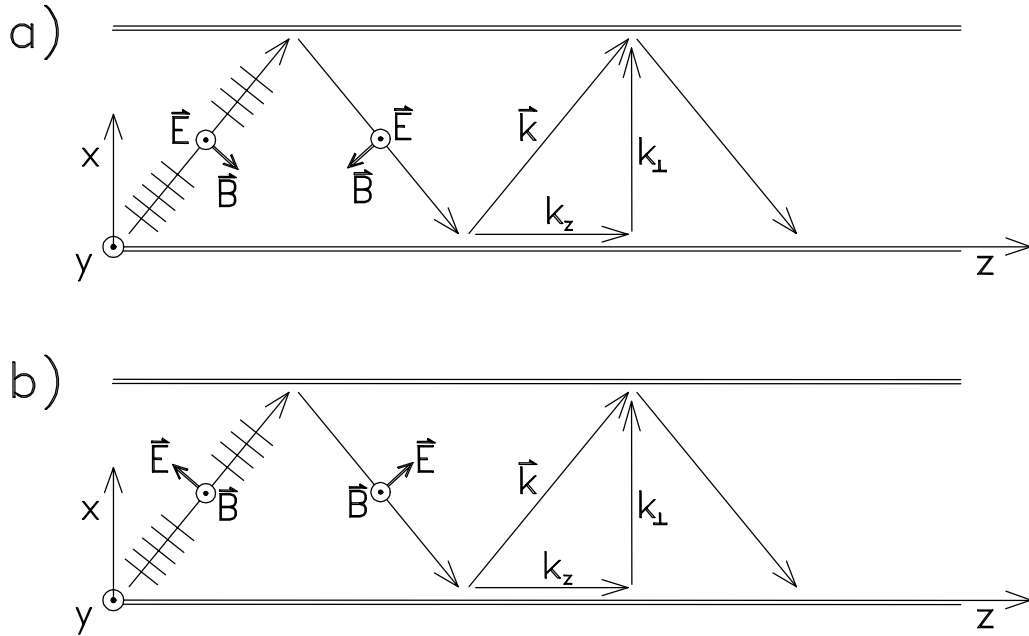


**Figure 11**

- a) A TE field pattern in which E is transverse only, but B has transverse and axial components.  
b) A TM field pattern in which B is transverse only, but E has transverse and axial components.

In the usual treatment of waveguides [12, 13] the fields are separated into transverse and axial dependence using separation of variables.

Assume that any of the six components  $E_x$ ,  $E_y$ ,  $E_z$ ,  $B_x$ ,  $B_y$ , or  $B_z$  can be written as:

$$\Psi(\vec{r}) = f(x, y)g(z) \quad (2.12)$$

The wave equation can be broken into:

$$(\nabla_{\perp}^2 + k_{\perp}^2)f(x, y) = 0 \quad \text{and} \quad \left(\frac{\partial^2}{\partial z^2} + k_z^2\right)g(z) = 0$$

where  $k_z^2 = k^2 - k_{\perp}^2$  (2.13)

If  $k_z$  is real, the solution for  $g(z)$  is oscillatory, so the electric and magnetic fields are both of the form:

$$\vec{E}(\vec{r}, t) = \vec{E}(x, y) e^{i(k_z z - \omega t)} \quad (2.14)$$

Where  $\vec{E}(x, y)$  could have components in both the transverse ( $\hat{\perp}$ ) and longitudinal ( $\hat{z}$ ) directions. When solving for the fields in a specific waveguide geometry, forcing  $\vec{E}(x, y)$  to satisfy the boundary conditions leads to an expression for  $k_{\perp}$  in terms of the transverse waveguide dimensions.

Obviously, propagation down the waveguide depends on  $k_z$  being real, but notice the implication of equation 2.13. The wave vectors,  $k$ ,  $k_{\perp}$ , and  $k_z$ , are related by a triangle equality (see Figure 11). Therefore, if  $k$  depends on frequency of the wave ( $k=\omega/c$ ), and  $k_{\perp}$  is fixed by the cross sectional dimensions of the waveguide, then  $k_z$  is simply the remaining side of the triangle. The result is that, if the frequency (or  $k$ ) becomes small enough,  $k_z$  will become imaginary and the wave will not propagate through the waveguide.

For this reason, waveguides have a cut off frequency, below which waves introduced into the waveguide will not propagate along the length. The cut off frequency occurs when  $k = k_{\perp}$ , and depends exclusively on the transverse dimensions of the waveguide being used.

$$f_c = \frac{c k_{\perp}}{2\pi}$$

Since the  $z$  dependence is only in the exponential factor, we can write

$$\vec{\nabla} = (\vec{\nabla}_{\perp} - i k_z \hat{z}) \quad (2.15)$$

where:  $\vec{\nabla}_{\perp} = \hat{x} \frac{\partial}{\partial x} + \hat{y} \frac{\partial}{\partial y}$  for Cartesian coordinates.

This allows field components to be separated into transverse and longitudinal directions. Substituting equation 2.14 into equation 2.4 and then using 2.15 to separate terms in the transverse and longitudinal directions gives :

$$\textbf{Longitudinal:} \quad (\vec{\nabla}_{\perp} \times \vec{E}_{\perp}) = -i\omega B_z \hat{z} \quad (2.16)$$

$$\textbf{Transverse:} \quad (\vec{\nabla}_{\perp} \times \hat{z} E_z) - ik_z (\hat{z} \times \vec{E}_{\perp}) = -i\omega B_{\perp} \hat{\perp} \quad (2.17)$$

Where two analogous equations come from substituting  $B(r,t)$  into (2.5). Equations 2.16 and 2.17 relate the transverse and longitudinal components of the fields in a waveguide. Notice that equation 2.16 says that the longitudinal magnetic flux through the cross sectional area of the waveguide causes a transverse electric field.

Now consider the special case of a TEM wave by letting  $E_z$  and  $B_z$  both go to zero. Equations 2.16 and 2.17 reduce to:

$$(\vec{\nabla}_{\perp} \times \vec{E}_{\perp}) = 0 \quad (2.18)$$

$$B_{\perp} = \frac{k}{\omega} (\hat{z} \times \vec{E}_{\perp}) \quad (2.19)$$

Where we have let  $k_z = k$  since  $k_{\perp}$  will be zero. From equation 2.18 we see that without any magnetic flux through the cross sectional area of the waveguide, the transverse field ( $\vec{E}_{\perp}$ ) can only be caused by an electrostatic potential ( $\vec{E}_{\perp} = -\vec{\nabla}\Phi$ ). In other words TEM waves cannot exist inside a waveguide, unless there is a voltage difference between the walls to support a transverse electric field. Notice that equation 2.19 is the same result as for TEM plane waves in equation 2.11.

Since the conducting walls of a waveguide are all at the same potential, TEM waves cannot exist in waveguides. However, a transmission line with a voltage

difference between two separate conductors can support TEM waves. In the next section we begin by studying one example of a two conductor transmission line, called the coaxial transmission line.

### **2.4.2 Coaxial Quarter Wave Cavity**

TEM waves can exist in transmission lines which have two conductors. An example is the coaxial transmission line. The cross section of a coaxial line is shown in Figure 12. Where the radius of the inner conductor is “a” and the radius of the outer conductor is “b”.

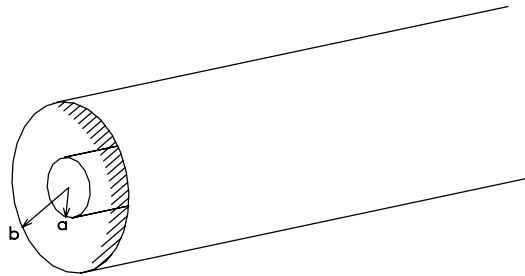


**Figure 12. Cross section of a coaxial transmission line**

Recall that the solution of the wave equation is separable into transverse and longitudinal dependence (equation 2.12), and that the fields of a TEM wave can be derived from an electrostatic potential (equation 2.18). This means that we can solve the Laplace equation for the electrostatic potential, and the transverse electric field, then multiply by the  $z$  dependence ( $e^{\pm ikz}$ ) and the time dependence ( $e^{-i\omega t}$ ) to obtain a complete solution.

Solving the Laplace equation for the transverse dependence only gives:

$$\nabla^2 \Phi = 0$$

$$\Phi(r) = V_0 \frac{\ln(r/b)}{\ln(a/b)}$$

Differentiating gives the electric field:

$$\vec{E} = -\nabla_{\perp} \Phi(r)$$

$$\vec{E}(r) = \frac{V_0}{\ln(a/b)} \frac{\hat{r}}{r} \quad (2.20)$$

and the magnetic field can be found using equation 2.19.

$$\vec{B}(r) = \frac{V_0}{c \ln(a/b)} \frac{\hat{\theta}}{r} \quad (2.21)$$

The surface current ( $J_s$ ) can be found using the boundary condition which comes from

Ampere's law: 
$$\vec{J}_s = \frac{1}{\mu_0} (\hat{n} \times \vec{B}) \quad (2.22)$$

where  $\hat{n}$  is a unit vector normal to the surface. For the inner conductor ( $\hat{n} = \hat{r}$ ) the

surface current is:

$$\vec{J}_s = \frac{1}{Z_0} \frac{V_0}{a \ln(b/a)} \hat{z}$$

Where  $Z_0 = \sqrt{\mu_0/\epsilon_0} = 377 \Omega$  is called the "impedance of free space".

Integrating around the circumference of the inner conductor gives the total current in terms of the voltage.

$$I = 2\pi a J_s$$

$$I_0 = \frac{1}{Z_0} \frac{2\pi V_0}{\ln(b/a)}$$

Therefore, we can solve for the ratio of the voltage to the current.

$$Z_c = \frac{V_o}{I_o} = \frac{Z_o}{2\pi} \ln(b/a) \quad (2.23)$$

$Z_c$  is known as the characteristic impedance of a coaxial transmission line.  $Z_c$  relates the peak voltage to the peak current (or the E-field to the B-field) and depends only on geometry of the transmission line.

### The Quarter Wave Cavity

Now consider a coaxial quarter wave cavity, i.e. a section of a coaxial transmission line whose length ( $\ell$ ) is one quarter of a wavelength ( $\frac{1}{4}\lambda$ ). A shorting plate at one end connects the inner and outer conductors while the other end is left open, as shown in Figure 13. The short forces the voltage difference between the inner and outer conductors to be zero at all times, but the open end can oscillate between  $\pm V_o$ . Therefore, we expect the voltage profile to look like a quarter of a wave as shown in Figure 14.

As with any electromagnetic oscillator, stored energy is transferred back and forth between the electric and magnetic fields. It is useful to think of charge as bouncing back and forth between the inner and the outer conductor, where the shorting plate provides a path for current to flow between the two. At the moment of maximum charge separation, the voltage difference is maximum and the electric field points in the radial direction. One quarter of a cycle later, charge flowing along the conductors and across the shorting plate causes a magnetic field in the azimuthal direction. The expected current profile is also shown in Figure 14. Obviously the magnetic field is largest at the short, and the electric field is largest at the open end.

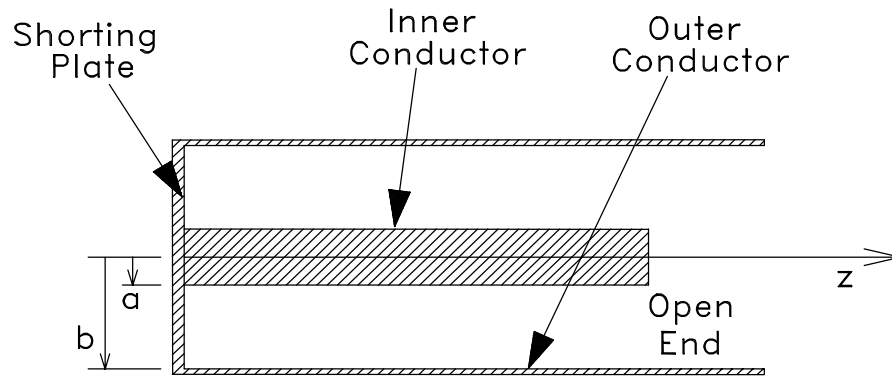


Figure 13. Geometry of a quarter wave cavity.

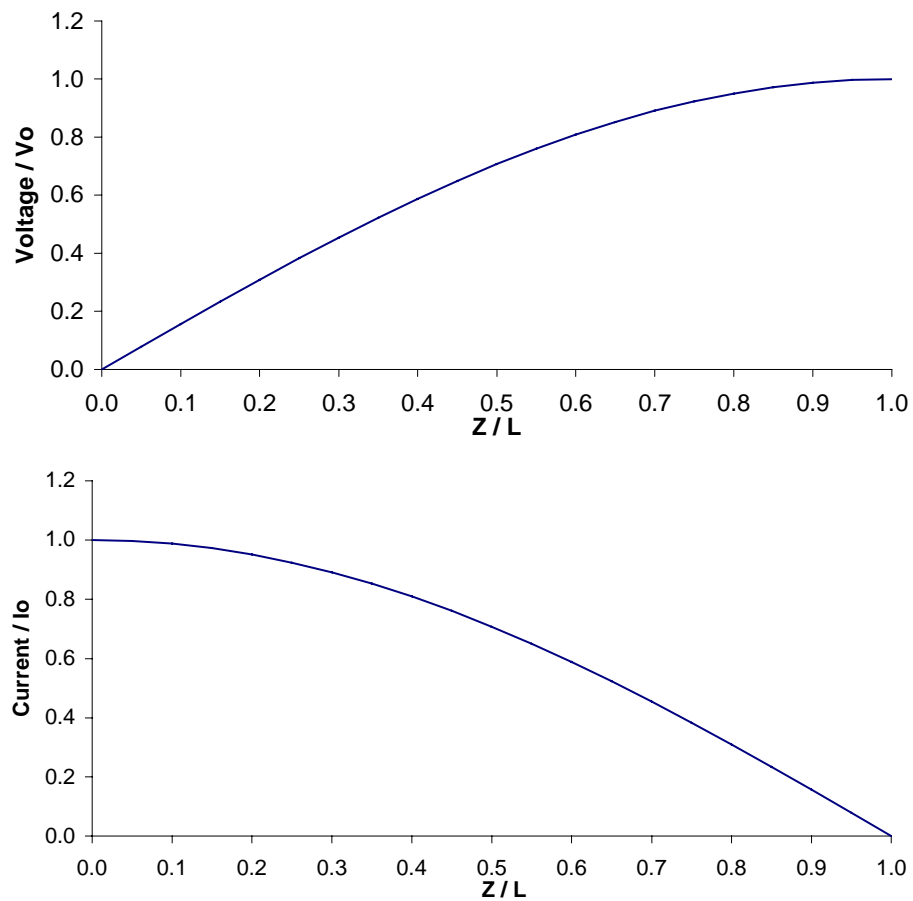


Figure 14. Voltage and current profiles for the quarter wave cavity

Since fields in the quarter wave cavity are TEM, they satisfy an electrostatic solution. Thus, we can solve for the transverse electrostatic fields, then add on the z dependence and time dependence last. The axial dependence can be found by superimposing the left and right moving waves.

$$V(z) = Ae^{ikz} + Be^{-ikz}$$

$$I(z) = Ce^{ikz} - De^{-ikz}$$

Where voltages add, but currents moving in opposite directions subtract. Applying boundary conditions ( $V = 0$  at  $z = 0$ ) at the shorted end, and ( $V = V_0$  at  $z = \ell$ ) at the open end gives:

$$V(z) = V_0 \sin\left(\frac{\pi z}{2\ell}\right) \quad (2.24)$$

Similarly, maximum current ( $I_0$ ) flows on the short, and  $I = 0$  at the open end.

$$I(z) = I_0 \cos\left(\frac{\pi z}{2\ell}\right) \quad (2.25)$$

Combining the radial, and the axial dependence, together with the time dependence, the electric field becomes.

$$\vec{E}_r(r, z) = \frac{V_0}{\ln(a/b)} \frac{1}{r} \sin\left(\frac{\pi z}{2\ell}\right) e^{-i\omega t} \hat{r} \quad (2.26)$$

Notice that this electric field is entirely in the radial direction, thus it does not account for fringe fields at the open end of the quarter wave cavity. Similarly the magnetic field is:

$$\vec{B}_\theta(r, z) = \frac{V_0}{c \ln(a/b)} \frac{1}{r} \cos\left(\frac{\pi z}{2\ell}\right) e^{-i\omega t} \hat{\theta} \quad (2.27)$$

When calculating the capacitance ( $C$ ), we must account for the axial profile. It can be found from the total energy stored in the electric field ( $U_E$ ).

$$U_E = \frac{1}{2} CV_0^2$$

Where the stored energy is:

$$U_E = \frac{1}{2} \epsilon_0 \int |\bar{E}|^2 d^3r$$

Substituting equation 2.26 and integrating gives:

$$U_E = \frac{1}{2} \left( \frac{\pi \epsilon_0 \ell}{\ln(b/a)} \right) V_0^2$$

Therefore the total capacitance of a quarter wave coaxial cavity is:

$$\boxed{C = \frac{\pi \epsilon_0 \ell}{\ln(b/a)}} \quad (2.28)$$

The inductance (L) is more difficult to calculate. Although equation 2.25 correctly accounts for the axial current distribution on the inner and outer conductors, the current which flows on the shorting plate (at  $z = 0$ ) also makes a significant contribution to the magnetic field near  $z = 0$ . A much simpler method is to use the relationship between wavelength and frequency  $\lambda_0 = c/f_0$  and the fact that the resonant frequency of the cavity ( $f_0$ ) is related to the inductance and capacitance by:

$$f_0 = \frac{1}{2\pi\sqrt{LC}}$$

Thus the total inductance is:

$$\boxed{L = \frac{4\mu_0 \ell}{\pi^3} \ln(b/a)} \quad (2.29)$$

The Quality factor, or the “Q” is defined as:

$$Q = \frac{\omega_0 \times (\text{energy stored in cavity fields})}{\text{time averaged power loss}}$$

or

$$\boxed{Q = \frac{\omega_0 U}{P_{\text{loss}}}} \quad (2.30)$$

The full analytical expression for the Q of a coaxial quarter wave cavity can be obtained by first calculating the time averaged power loss caused by surface currents flowing on the conductors.

The surface current ( $J_s$ ) on the inner conductor is obtained from equation (2.22):

$$\vec{J}_s = \frac{1}{\mu_o} (\hat{n} \times \vec{B}|_{r=a})$$

Substituting the B-field of equation 2.27 gives:

$$\vec{J}_s = \frac{V_o}{Z_o a \ln(b/a)} \cos\left(\frac{\pi z}{2\ell}\right) e^{-i\omega t} \hat{z} \quad (2.31)$$

The general expression for power loss due to current flowing through a resistive material is:

$$P_{\text{loss}} = \int_{\text{vol}} \vec{J} \cdot \vec{E} d^3r$$

where  $\vec{J}$  is the current density and  $d^3r$  is a differential element of volume. Ohm's law can be used to express the electric field in terms of  $\vec{J}$ .

$$\vec{J} = \sigma \vec{E}$$

$$P_{\text{loss}} = \int_{\text{vol}} \frac{J^2}{\sigma} d^3r \quad (2.32)$$

where  $\sigma$  is the conductivity of the metal. The power loss on the inner conductor is obtained by assuming that the current flows with uniform density over a depth of one skin depth ( $\delta$ ).

$$\delta = \frac{1}{\sqrt{\pi f \mu_o \sigma}} \quad (2.33)$$

Using  $\vec{J} = \vec{J}_s / \delta$  for case of the inner conductor, equation 2.32 reduces to:

$$P_{\text{inner}} = \frac{2\pi a}{\delta} \int_0^{\ell} J_s^2 dz$$

Substituting equation 2.31, then integrating, and taking the time average gives:

$$\begin{aligned} \langle P_{\text{inner}} \rangle &= \frac{2\pi}{a} \frac{V_o^2}{\delta \sigma (\ln b/a)^2 Z_o^2} \int_0^{\ell} \cos^2\left(\frac{\pi z}{2\ell}\right) dz \frac{1}{T} \int_0^T \sin^2(\omega t) dt \\ \langle P_{\text{inner}} \rangle &= \frac{V_o^2}{4\pi\sigma\delta Z_c^2} \left(\frac{\ell}{2a}\right) \end{aligned} \quad (2.34)$$

where  $Z_c$  is the characteristic impedance from equation 2.23.

Similarly the power loss due to current on the outer conductor is:

$$\langle P_{\text{outer}} \rangle = \frac{V_o^2}{4\pi\sigma\delta Z_c^2} \left(\frac{\ell}{2b}\right) \quad (2.35)$$

Since maximum current flows at the  $z=0$  end of the cavity, we must also account for power loss on the shorting plate. Again, using equation 2.22 for  $z=0$ :

$$\vec{J}_s = \frac{1}{\mu_o} (\hat{n} \times \vec{B}|_{z=0})$$

Substituting the magnetic field from equation (2.27) gives:

$$J_s = \frac{V_o}{Z_o \ln(b/a)} \hat{r} e^{-i\omega t} \quad (2.36)$$

As before, the power loss is calculated assuming the current has uniform density over one skin depth ( $\delta$ ). For the shorting plate the general expression for power loss reduces to:

$$P_{\text{short}} = \frac{2\pi}{\delta\sigma} \int_a^b J_s^2 r dr$$

Substituting equation 2.36 for the surface current, then integrating, and taking the time average gives:

$$\langle P_{\text{short}} \rangle = \frac{V_o^2}{4\pi\sigma\delta Z_c^2} \ln(b/a) \quad (2.37)$$

The total power loss is then:

$$\langle P_{\text{loss}} \rangle = \langle P_{\text{inner}} \rangle + \langle P_{\text{outer}} \rangle + \langle P_{\text{short}} \rangle$$

Substituting equations 2.34, 2.35, and 2.37 yields:

$$\langle P_{\text{loss}} \rangle = \frac{V_o^2}{4\pi\sigma\delta Z_c^2} \frac{\ell}{2} \left[ \frac{1}{a} + \frac{1}{b} + \frac{2}{\ell} \ln(b/a) \right] \quad (2.38)$$

Finally we can calculate an analytical expression for the Q using

$$Q = \frac{\omega_o U_E}{P_{\text{loss}}}$$

Where  $U_E = \frac{1}{2} C V_o^2$ , and the capacitance was given in equation 2.28. After significant

rearrangement we arrive at:

$$Q = \frac{2 \ln(b/a)}{\delta \left[ \frac{1}{a} + \frac{1}{b} + \frac{2}{\ell} \ln(b/a) \right]} \quad (2.39)$$

When using equations 2.38 and 2.39 one should be aware that in real resonant cavities, the conductivity of most conductors is significantly reduced from that of the pure metal [14]. Machining, cutting, and bending metal create crystalline defects that reduce the conductivity of metal [15]. Furthermore the conductivity of metal decreases as the operating temperature of the cavity increases.

Finally, it is useful to consider the ratio of  $R_s/Q$ , where  $R_s$  is the shunt resistance. In section 2.4.4 the shunt resistance is defined in terms of the power loss and the peak cavity voltage by the expression:

$$P_{\text{loss}} = \frac{V_o^2}{2R_s} \quad (2.40)$$

Thus, the  $(R_s/Q)$  becomes:

$$\frac{R_s}{Q} = \frac{V_o^2}{2(QP_{\text{loss}})}$$

Substituting equations 2.38 and 2.39 and rearranging, we find that the conductivity cancels and  $R_s/Q$  depends only on the geometrical factors a and b.

$$\frac{R_s}{Q} = \frac{2}{\pi^2} Z_o \ln(b/a) \quad (2.41)$$

Using equations 2.28 and 2.29 it is easy to show that  $\sqrt{\frac{L}{C}}$  gives the same result.

Therefore:

$$\frac{R_s}{Q} = \sqrt{\frac{L}{C}} \quad (2.42)$$

Although equation 2.41 is specific for the geometry of the quarter wave cavity, in general  $R_s/Q$  depends only on geometry. This is useful because although the effective conductivity is difficult to determine, the power loss can still be calculated very simply by measuring the Q, and either measuring or calculating  $\sqrt{\frac{L}{C}}$ , to determine  $R_s$ .

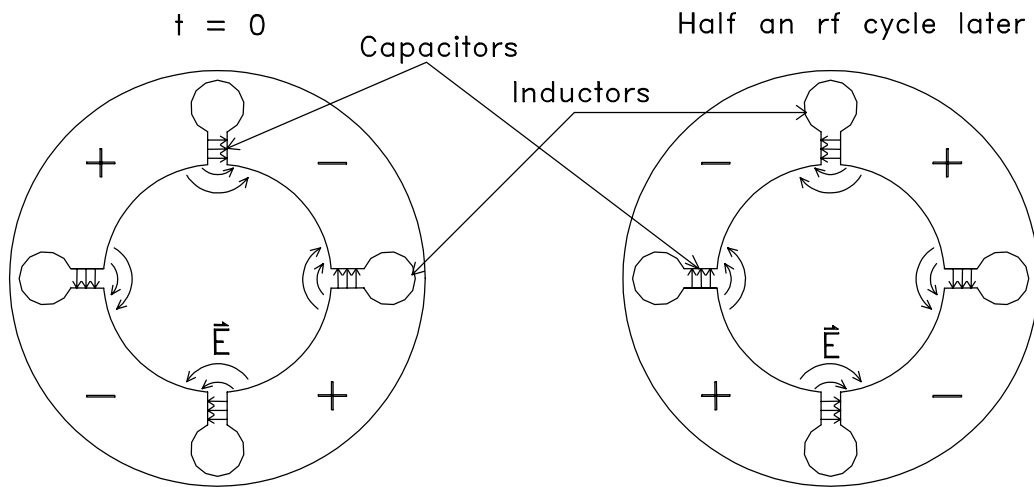
$$R_s = Q\sqrt{\frac{L}{C}}$$

Once  $R_s$  is known, equation 2.40 can be used to calculate the power loss for any cavity voltage.

### 2.4.3 RF Driven Magnetron

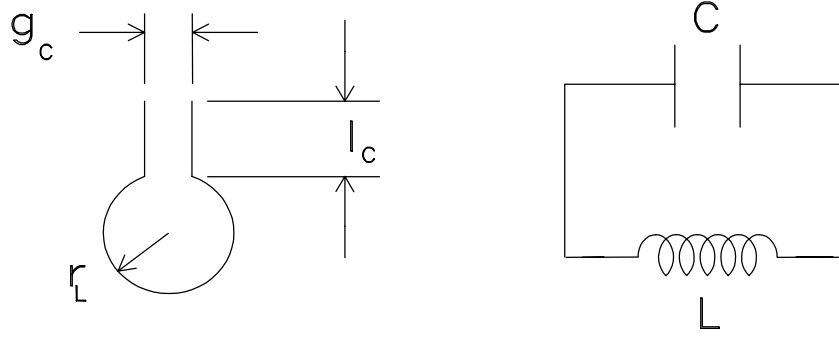
As explained in section 1.3, the magnetron structure is normally used to generate microwave power, by converting the kinetic energy of an electron beam into oscillating electromagnetic fields in the resonant cavity. However, the inverse is also possible. RF power can be used to drive oscillating electric and magnetic fields in a magnetron structure. We wish to use those fields to accelerate an ion beam.

Figure 15 shows an example of a four gap magnetron structure. The fields in a magnetron are most easily understood if one thinks of the charge which bounces back and forth from one side of an oscillator to the other. At the moment of maximum charge difference across a slot (+/-), the electric field in the slot is maximum. However, when charge is flowing from one side to the other, the current around the hole creates a magnetic field which points into the page. Thus the slot acts like a capacitor and the hole acts like an inductor.



**Figure 15. A four gap magnetron structure showing the  $\pi$ -mode at two different times**

**The z axis points into the page.**



**Figure 16. Geometry of a single oscillator and its equivalent circuit**

In this example, the magnetron structure is a set of four coupled harmonic oscillators. There are four modes of oscillation, however only the  $\pi$ -mode is of interest here. Strapping can be used to eliminate unwanted modes [6]. Figure 15 illustrates the  $\pi$ -mode in which the charge on each adjacent electrode is opposite. In other words each oscillator is  $180^\circ$  out of phase with the one next to it, hence the name “ $\pi$ -mode”.

Each oscillator behaves like an LC circuit. The geometry and equivalent circuit for a single oscillator are shown in Figure 16. A good estimate for the inductance and capacitance of a single oscillator can be calculated from the geometry alone.

$$C = \epsilon_o \frac{l_c l_{cav}}{g_c} \quad (2.43)$$

Where  $l_{cav}$  is the cavity length into the page.

$$L = \mu_o \frac{\pi r_L^2}{l_{cav}} \quad (2.44)$$

The resonant frequency of a single oscillator is evidently:

$$\omega_o = \frac{1}{\sqrt{LC}} = \frac{c}{r_L} \sqrt{\frac{g_c}{\pi l_c}} \quad (2.45)$$

where little  $c$  is the speed of light and all other geometrical parameters are defined in Figure 16.

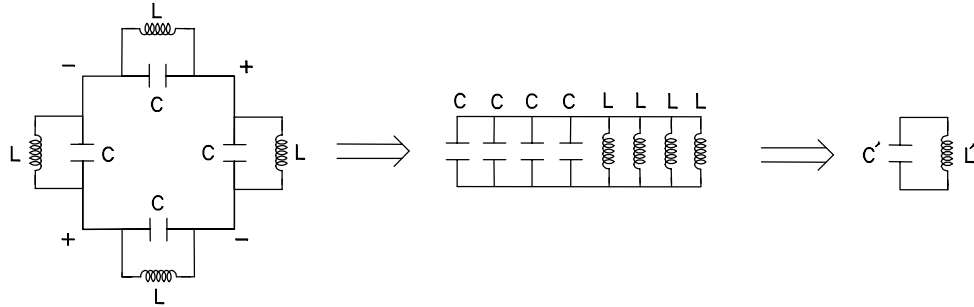


**Figure 17. Equivalent circuit for a four gap magnetron in the  $\pi$  mode.**

Figure 17 shows the equivalent circuit for the entire magnetron operating in the  $\pi$ -mode. The total inductance,  $L'$ , is:

$$L' = \frac{L}{4}$$

and the total capacitance,  $C'$ , is:

$$C' = 4C$$

$$\omega'_o = \frac{1}{\sqrt{L'C'}} = \frac{1}{\sqrt{LC}} = \omega_o$$

Thus, in the  $\pi$ -mode, the resonant frequency of the entire magnetron is the same as the resonant frequency of a single oscillator.

We are interested in the electric fields in the central region because they will be used to acceleration ions. The magnetic fields in the central region are negligible therefore  $\nabla \times \vec{E} = 0$  so the electric fields can be solved in terms of an electrostatic potential. The voltage potential is a solution to the Laplace equation in cylindrical

coordinates with radial and azimuthal dependence only. Matching to the boundary conditions, leads to a Fourier series in  $\theta$ .

$$V(r, \theta, t) = V_o \left[ A_n \left(\frac{r}{R}\right)^n \sin(n\theta) + A_{2n} \left(\frac{r}{R}\right)^{2n} \sin(2n\theta) + A_{3n} \left(\frac{r}{R}\right)^{3n} \sin(3n\theta) + \dots \right] e^{i\omega_{rf} t}$$

Where: 
$$A_{mn} = \frac{8}{\pi^2 f} \left( \frac{1}{m^2} \right) \sin\left(\frac{m\pi f}{2}\right) \quad \text{for: } m = 1, 2, 3, \dots$$

Here  $n$  is the harmonic number and  $f$  is a fraction which defines the gap width in terms of the angle subtended by a gap ( $\theta_g$ ) and the angle subtended by the remaining wall ( $\theta_w$ ) at  $r = R$  (see Figure 15).

$$f \equiv \frac{\theta_g}{\theta_w + \theta_g} = \frac{\theta_g}{2\pi / N_{\text{gaps}}}$$

Or written more compactly

$$V(r, \theta, t) = V_o \frac{8}{\pi^2 f} \sum_{m=1}^{\infty} \left[ \frac{1}{m^2} \sin\left(\frac{m\pi f}{2}\right) \left(\frac{r}{R}\right)^{mn} \sin(mn\theta) \right] e^{i\omega_{rf} t} \quad (2.46)$$

A good estimate of the voltage can be obtained by using only the lowest order term. For  $m = 1$  only:

$$V(r, \theta, t) = V_o \left(\frac{r}{R}\right)^n \sin(n\theta) e^{i\omega_{rf} t} \quad (2.47)$$

This expression represents the voltage due to hyperbolic vanes as shown in Figure 18

The azimuthal electric fields and energy gain of an ion accelerating through the electric field will be derived in section 2.5.6.

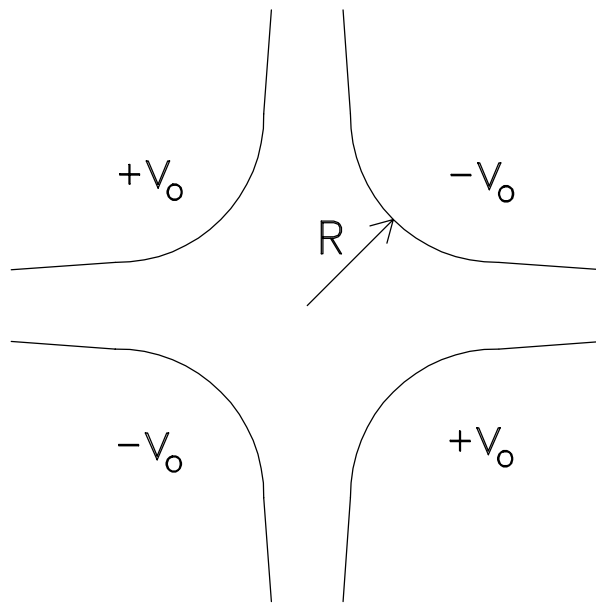


**Figure 18. A four gap magnetron made of hyperbolic vanes**

#### **2.4.4 Equivalent Circuit Representation**

Generally resonant cavities have electric and magnetic fields which exist in the same volume, therefore their inductance and capacitance are distributed. On the other hand, a lumped LC circuit has inductance and capacitance which are separated spatially. In spite of this difference, the frequency response of any resonant cavity can be accurately represented by an equivalent lumped LRC circuit, at least in the region near resonance.

The equivalent circuit representation is important because it presents the theory in terms of gross quantities such as L, R, C, and Q which can be measured. This section draws these quantities together and presents a simpler scheme for the theory of resonant cavities.

The circuit which most accurately represents the frequency response of a resonant cavity is the parallel-series combination shown in Figure 19. However, this circuit is complicated mathematically, and the series resistance ( $R_o$ ) is difficult to measure directly. The common practice among rf engineers is to use the parallel circuit of Figure 20. This circuit is much simpler to solve, and although the shunt resistance ( $R_s$ ) is a fictitious quantity,  $R_s$  can be measured directly. The two circuits are equivalent at resonance if we choose  $R_s = Q^2 R_o$ .

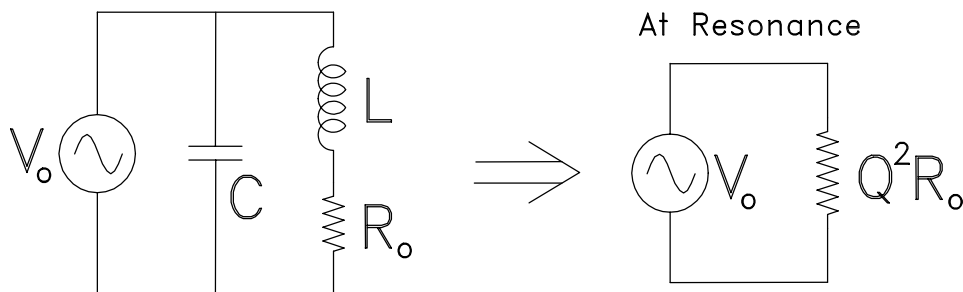


**Figure 19. The  $C \parallel (R_o + L)$  circuit which represents the frequency response of a resonant cavity**

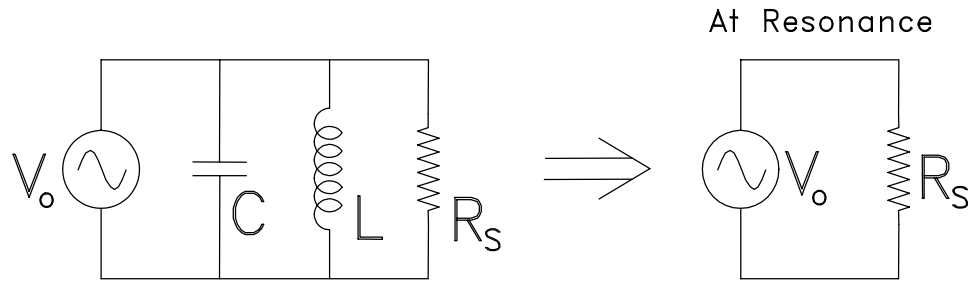


**Figure 20. The parallel RLC circuit representation of a resonant cavity uses a fictitious shunt resistance ( $R_s$ )**

First consider the impedance ( $Z_{LC}$ ) of only the parallel LC combination from the circuit of Figure 20.

$$Z_{LC} = \frac{1}{i\omega C + \frac{1}{i\omega L}} = \frac{i\omega L}{1 - \frac{\omega^2}{\omega_0^2}}$$

Where the resonant frequency is:

$$\omega_0 = \frac{1}{\sqrt{LC}}$$

The impedance of the parallel LC combination becomes infinite when ( $\omega \rightarrow \omega_0$ ).

Therefore, at resonance the parallel circuit reduces to  $R_s$  in series with  $V_o$ , as shown in Figure 20. This means that the power loss at resonance is due to the current through the shunt resistance only.

$$P_{\text{loss}} = \frac{V_o^2}{2R_s} \quad (2.48)$$

In the full parallel  $R_sLC$  combination, the voltage across the capacitor is the same as the voltage across the resistor. Therefore, the Q can be found using  $U_E = \frac{1}{2} CV_o^2$  and equation 2.48 for the power loss.

Substituting these into: 
$$Q = \frac{\omega_o U_E}{P_{\text{loss}}}$$

gives three useful expressions for the Q

$$\boxed{Q = \omega_o R_s C} \quad (2.49)$$

using  $\omega_o = \frac{1}{\sqrt{LC}}$ :

$$\boxed{Q = \frac{R_s}{\omega_o L}} \quad (2.50)$$

or eliminating  $\omega_o$ :

$$\boxed{Q = R_s \sqrt{\frac{C}{L}}} \quad (2.51)$$

Recall that this same relationship was found for the quarter wave cavity (equation 2.42).

Thus the power loss can be calculated using two simple equations:

$$\boxed{P_{\text{loss}} = \frac{V_o^2}{2R_s}} \quad \text{where} \quad \boxed{R_s = Q \sqrt{\frac{L}{C}}} \quad (2.52)$$

When designing a resonant cavity to be used as an accelerating structure, the bottom line is usually “how much power does it take to generate a voltage  $V_o$  ?”.

Therefore the shunt resistance is an important quantity to know. For experimental measurements it is useful to think of the shunt resistance as the Q times  $\sqrt{L/C}$ .

The Q depends on the resistivity of the metal and on cavity geometry both [16], but can be measured directly from the frequency response of the cavity.  $\sqrt{L/C}$  depends only on the cavity geometry and usually can be calculated (equations 2.28, 2.29 or 2.43, 2.44).

If expressed in terms of the resonant frequency, then  $f_o$  can be measured and only one of L or C must be calculated.

$$\sqrt{\frac{L}{C}} = \frac{1}{2\pi f_o C}$$

### **2.4.5 The Hybrid Coaxial – Magnetron Cavity**

Section 2.4 mentioned that the rf cavity used for the 50 keV ICRA is a hybrid between a coaxial quarter wave cavity and a magnetron structure. The chosen rf frequency of 152 MHz meant that the inductors of a pure magnetron would extend too far in the radial direction to fit into the warm bore of the available 2.5 Tesla superconducting magnet. The solution was to attach the vanes of a magnetron to the open end of a quarter wave cavity. In this way the vanes of the magnetron supply the electric fields needed for acceleration and the quarter wave cavity acts as the resonant structure needed for rf oscillation.

The specific geometry of this hybrid cavity will be shown in section 3.2.4. For the rf theory it is only necessary to know that adding the vanes of the magnetron adds a large capacitance to the end of the coaxial cavity as shown in Figure 21. The additional capacitance means that the coaxial cavity must be shortened to less than  $\lambda/4$ .

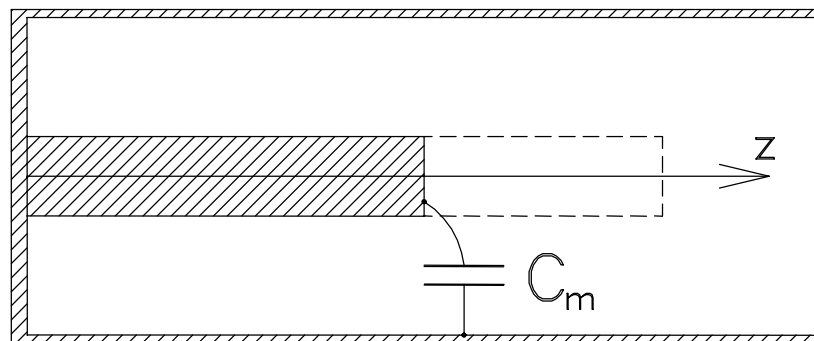


**Figure 21. An extra capacitance added across the end of a foreshortened quarter wave cavity**

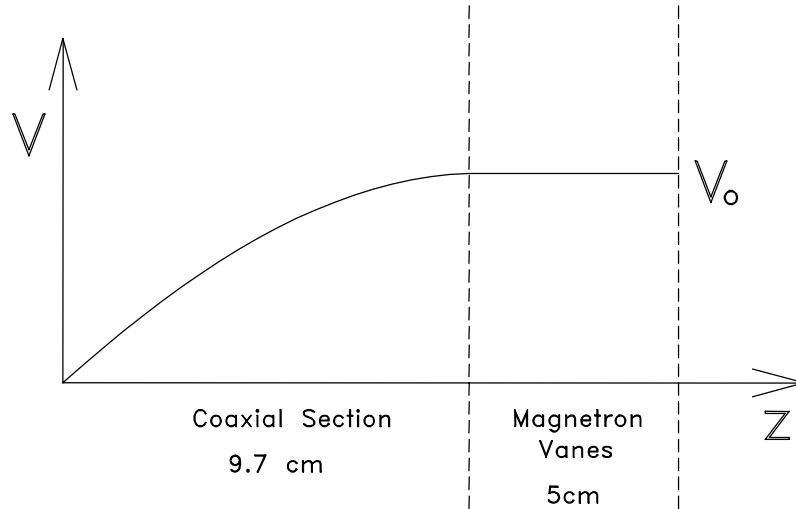


**Figure 22. Assumed voltage profile and lengths of the hybrid cavity for the 50 keV ICRA**

The capacitance of the magnetron section ( $C_m$ ) is large compared to the remaining capacitance of the coaxial section ( $C_v$ ). The approach used here is to assume that the inductance of the magnetron vanes is negligible since they are in the low magnetic field region. Under this assumption the voltage profile would be as shown in Figure 22.

The new length of the coaxial section can be found from the desired resonant frequency.

$$\omega_o = \frac{1}{\sqrt{LC}}$$

or 
$$LC = \frac{1}{\omega_o^2} = \text{fixed}$$

where both L and C are proportional to the length of the coaxial section, but  $C_m$  is a constant. Thus the length ( $\ell$ ) can be found by solving the quadratic equation:

$$(L'\ell)(C'\ell + C_m) = \frac{1}{\omega_o^2} = \text{fixed} \quad (2.53)$$

In order to calculate the power needed to generate the voltage  $V_o$ , we need to know the shunt resistance  $R_s = Q\sqrt{\frac{L}{C}}$ . Then the power can be calculated using equation (2.48)  $P_{\text{loss}} = \frac{V_o^2}{2R_s}$ . Thus we need to know the change in  $\sqrt{\frac{L}{C}}$  and in the  $Q$  caused by the additional capacitance ( $C_{\lambda/4} \rightarrow C_\ell + C_m$ ).

The change in  $R_s$  is dominated by the new  $\sqrt{\frac{L}{C}}$ . Luckily this is simple to calculate.

$$\sqrt{\frac{L}{C}} = \frac{1}{2\pi f_o C_{\lambda/4}} \rightarrow \frac{1}{2\pi f_o (C_\ell + C_m)} \quad (2.54)$$

The new theoretical  $Q$  can be calculated by repeating the procedure of section 2.4.2 with two changes. First, the integrals over currents on the inner and outer conductors will be taken over the new shorter length of the coaxial section and second, the current must be scaled up due to the additional capacitance. Since the charge on a capacitor at any time is:  $q = CV$ ,

differentiating gives: 
$$I = \frac{dq}{dt} = C \frac{dV}{dt} = \omega CV$$

Thus the current is proportional to the capacitance, so the new current is simply:

$$I_o \rightarrow I_o \left( \frac{C_\ell + C_m}{C_{\lambda/4}} \right)$$

Although the theoretical expression for the  $Q$  is straight forward to derive, it is of little use because the  $Q$  depends on the conductivity ( $\sigma$ ). In practice the conductivity of the cavity depends on the resistance of joints, connections, and surface oxidation on the conductors. The conductivity of the pure conductor is almost never achieved.

Furthermore, the  $Q$  can be measured from the frequency response curve of the actual cavity.

The method used to determine the power loss and  $V_o$  in the hybrid cavity is to measure  $f_o$ , measure the  $Q$ , and measure  $C_m$ . then calculate the remaining capacitance of the coaxial section. With these quantities known, the shunt resistance can be calculated so that the power required to generate  $V_o$  is known (equation 2.52). These measurements are given in chapter 4.

## **Printing Instructions**

Document must be saved first.

Print all pages, 12-45

Then delete both graphs in Figure 14 pg 27 and re-print page 14 (solenoid and Helm coil)

Close, but don't save

## **2.5 Analytical Model of the Beam Trajectory**

**See Chap2B.doc**

MOVE TO CHAPTER 3

### **Vacuum**

The mean free path ( $\lambda$ ) is the average distance that a particle travels before colliding with another particle. A useful rule of thumb is that for air at 20°C [17]:

$$\lambda[\text{cm}] = \frac{5}{P[\text{mTorr}]}$$

For this experiment, it is sufficient to have a mean free path longer than the path of the beam. The beam in the 50 keV ICRA will travel about 3 meters. Therefore, for a mean free path of at least  $\lambda = 5$  meters, the pressure should be below of  $P = 10^{-5}$  Torr.

### **2.3 Ion Source (old version)**

For this chapter on theory, the ion source should be thought of as a black box with a hole in the front which supplies a beam of ions. All ions are accelerated through the same initial voltage potential ( $V_{\text{beam}}$ ) from the source aperture to the puller electrode, where  $V_{\text{beam}}$  is in the range of 5 – 50 kV. Any variation in energy, due to temperature of the ions inside the source, is small. Therefore, it is a good approximation to assume that all ions, in the initial beam supplied by the ion source, have the same kinetic energy ( $E = qV_{\text{beam}}$ ).

However, the beam does have some finite spread in transverse and longitudinal position and momentum. These beam dimensions occupy a 6 dimensional volume in phase space. The transverse spread in position and momentum is normally described in terms of two dimensional areas called the beam emittance. The computer model of the beam emittance is discussed in section 2.6.7 of this chapter. Specifics of the ion source design are given in section 3.2.3.

## **2.5 Analytical Model of the Beam Trajectory**

This section covers all aspects of the beam trajectory that can be calculated analytically. The analytical model describes only the central ray through the system, i.e. a beam of zero emittance. Multi-particle trajectories are dealt with using the computer model in section 2.6. Limitations of the analytical model are discussed in the beginning of section 2.6.

We begin with a detailed overview of the beam trajectory which includes some motivation for each sub-section below. Figure 23 shows a top and side view of the entire beam trajectory through the ICRA. The basic components of the ICRA are the ion source, electrostatic bend, superconducting magnet, rf driven magnetron, and a target. Notice that the trajectory is divided into three distinct regions: the injection region, the acceleration region, and the extraction region.

A superconducting magnet provides a B-field which is constant in time. The ion beam is extracted from the source directly along a B-field line so that the  $\vec{v} \times \vec{B}$  force on the beam is zero. We will see in chapter 4, that this beam actually contains multiple ion species. The beam passes between a pair of electrostatic bending plates which are located at some radius away from the z axis. All ion species in the beam are deflected to the same angle  $\theta_{\text{bend}}$  (section 2.5.1). After the beam is deflected, it will have momentum components perpendicular ( $p_{\perp}$ ) and parallel ( $p_{\parallel}$ ) to the local magnetic field.

$$p_{\perp} = p_{\text{total}} \sin(\theta_{\text{bend}}) \quad p_{\parallel} = p_{\text{total}} \cos(\theta_{\text{bend}})$$

The perpendicular component causes the beam to orbit at radius  $r = p_{\perp}/qB$ , and the parallel component will cause the beam to move in the axial direction toward the high B-field region as shown in Figure 23.

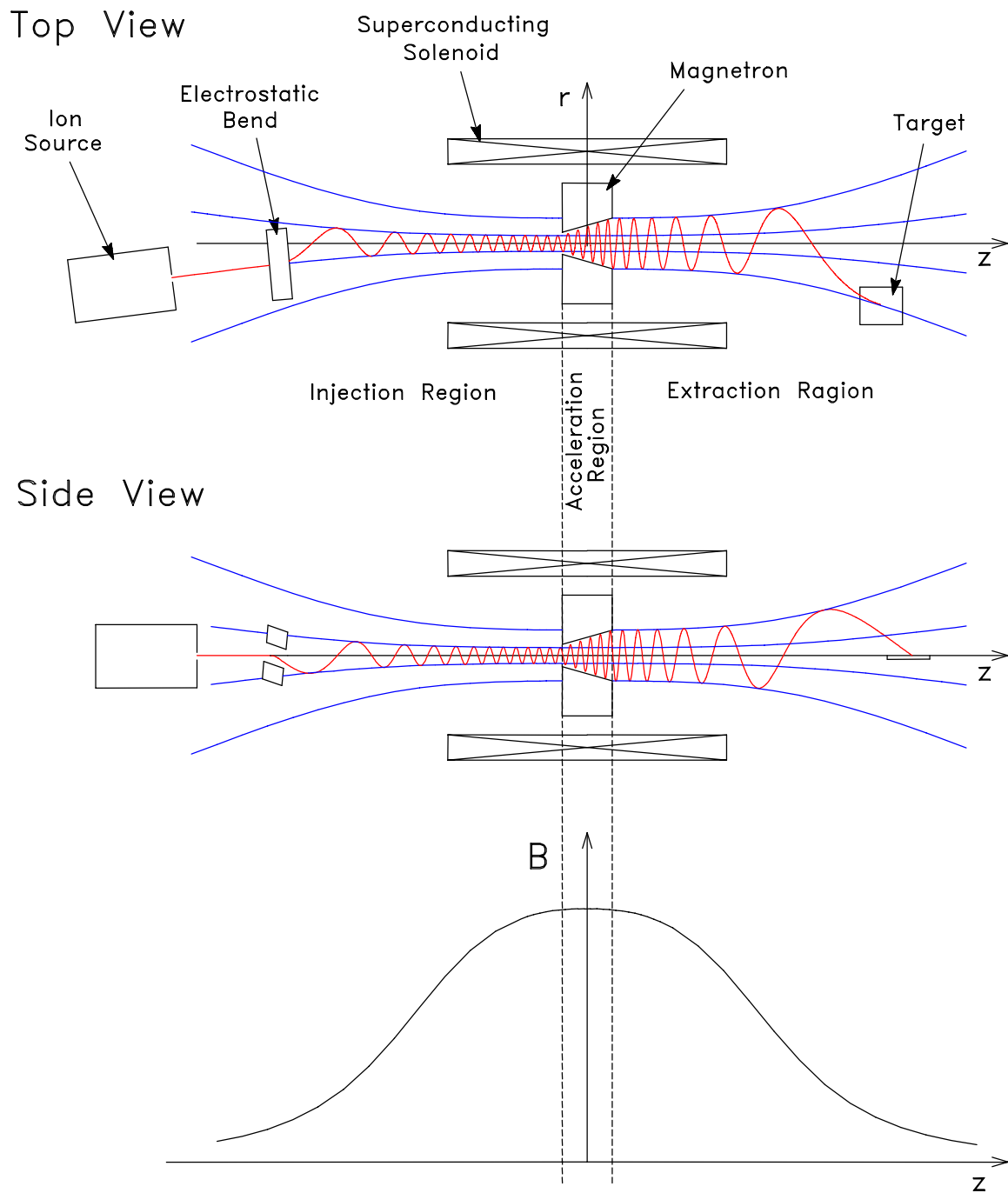


**Figure 23. Top and side view of the trajectory through an ICRA with trajectory shown in red, and magnetic field lines shown in blue. The axial magnetic field profile is plotted below.**

Imagine for a moment what happens if we begin with zero voltage on the bending plates and then gradually turn up the bend voltage. Obviously the bend angle will increase, which increases  $p_{\perp}$  and decreases  $p_{\parallel}$ . Since  $p_{\perp}$  increases, the radius of the beam orbit will grow. Figure 24 shows that if we look in the axial direction, we see that the point on the orbit where the beam initially passed through the bending plates is a fixed point. As the orbit radius increases, the center of the orbit shifts over in a direction perpendicular to the direction of the kick given by the electrostatic bend. We want the beam to be centered around the z axis so that it will be centered in the magnetron when it arrives at the acceleration region, and there is only one bending voltage (or bend angle) for which the beam is centered around the z axis. Therefore, the initial field line with which the ion source is aligned must be at the proper radial distance away from the z axis so that the beam will be centered when the desired ratio of  $(p_{\perp}/p_{\parallel})$  is reached.

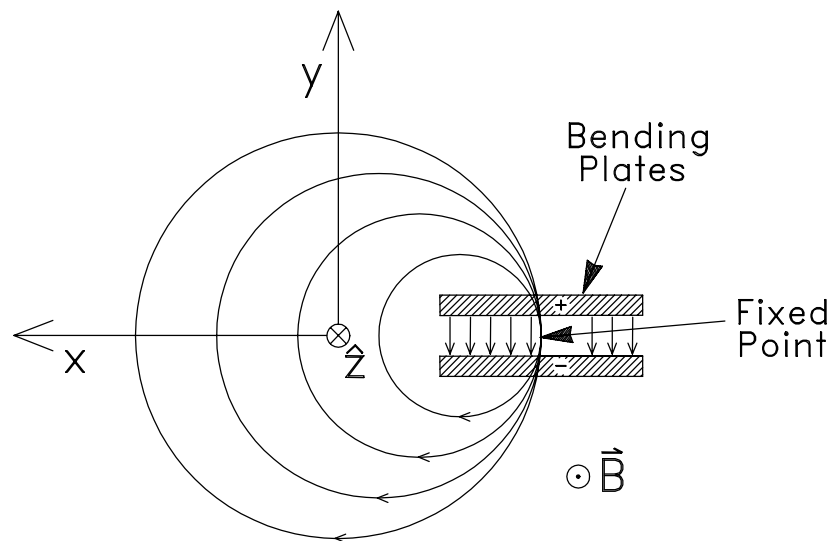


**Figure 24. Beam orbit as seen looking in the axial direction as bend voltage is increased**

As the beam spirals into the high B-field region, the orbit radius follows magnetic field lines. This means that  $r$  and  $p_{\parallel}$  decrease, but  $p_{\perp}$  increases. Section 2.5.2 shows that assuming conservation of magnetic moment, these three parameters can be easily calculated at any point in the injection trajectory if the magnetic field profile is known. If the peak B-field is high enough to drive the axial momentum ( $p_z$ ) to zero, the beam will mirror (section 2.5.3). This condition is important because it gives an experimental reference point from which we can determine the axial momentum. As mentioned above, the beam actually contains multiple ion species, however we are only interested in accelerating the  $H^+$  (proton) portion of the beam. Section 2.5.4 shows how the injection region of the ICRA can be used as a mass spectrometer to measure the constituents in the beam and to eliminate all but the  $H^+$  for injection into the acceleration region.

After traveling through the injection region, the ratio of  $p_{\perp}/p_{\parallel}$  has been transformed so that the proton beam arrives at the entrance to the acceleration region with the desired radius and axial momentum. The B-field is relatively constant through the acceleration region, so  $p_z$  can be assumed to be constant. The axial velocity determines the number of turns the beam goes through while traversing the cavity length (section 2.5.5). Inside the magnetron rf electric fields accelerate the beam in the azimuthal ( $\theta$ ) direction. If the cyclotron frequency remains in resonance with the rf frequency, the beam is accelerated across every gap in the magnetron. This causes the orbit radius to increase while the beam continues to drift axially. Because of the radial dependence of the E-field, the inner diameter of the magnetron should be tapered ( $dR/dz$ ) for maximum energy gain (section 2.5.6). The acceleration trajectory is ideal when the ion skims along the inner diameter of the cavity.

When the beam exits the magnetron it continues to drift axially into the extraction region. Since the extracted beam has a large energy spread from nearly zero to the full design energy, the beam in the extraction region should be thought of as a solid rotating cylinder of ions with high kinetic energies at large radius and the lowest energy at the center ( $E \sim r^2$ ).

The equations of section 2.5.2 that were used for the injection region, can now be applied to each energy component of the beam in the extraction region. As the B-field drops off, the beam follows field lines. The perpendicular momentum decreases while the parallel component and the orbit radius grow. The axial length between turns is calculated in section 2.5.8. This is important to consider when designing a target or beam diagnostics in the extraction region.

### 2.5.1 Electrostatic Bend

Let us derive the bending equation for an electrostatic bend in a region with no magnetic field. The electrostatic bend is essentially two flat plates which are separated by a gap,  $g$ , and with voltage difference  $V_{\text{bend}}$ . Using the bending geometry illustrated in Figure 25, we assume that the beam will follow a curved path with radius of curvature  $\rho$ , and that the electric field always points radially toward the center of this curvature.

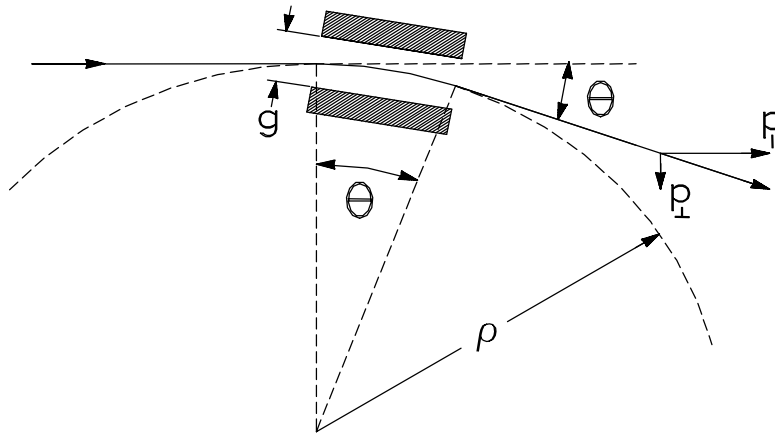


Figure 25. Geometry of the electrostatic bend

Equating the centripetal force with the electric force supplied by the E-field between the bending plates gives:

$$\vec{F} = q\vec{E}_{\text{bend}} = m\frac{v^2}{\rho}\hat{\rho}$$

where  $q$ ,  $m$  and  $v$  are the charge, mass and velocity of ions in the beam passing between the bend plates. The electric field between the bend plates is approximately

$$|\vec{E}_{\text{bend}}| = \frac{V_{\text{bend}}}{g} \text{ and the beam from the ion source has kinetic energy } K = \frac{1}{2}mv^2 = qV_{\text{beam}}$$

therefore, we can write:

$$q\frac{V_{\text{bend}}}{g} = \frac{2qV_{\text{beam}}}{\rho}$$

so the bending radius is:

$$\rho = 2g \frac{V_{\text{beam}}}{V_{\text{bend}}}$$

We can solve for the bend angle in radians:

$$\theta_{\text{bend}} = \frac{s}{\rho} = \frac{\frac{1}{2} V_{\text{bend}}}{V_{\text{beam}}} \left( \frac{\ell_{\text{eff}}}{g} \right) \text{ [radians]} \quad (2.55)$$

where a change in notation has been introduced from the arc length ( $s$ ) to the effective length of the bending plates ( $\ell_{\text{eff}}$ ). There are two important points to notice about equation 2.55. First, the bend angle does not depend on the mass or charge of the ion. Therefore, different ion species are all bent to the same angle. Second, the bend angle ( $\theta_{\text{bend}}$ ) is proportional to the bend voltage  $V_{\text{bend}}$ . This will be useful when calculating the trajectory through the injection region. In practice we do not need to know  $\ell_{\text{eff}}$  because as we will see in section 2.5.3, the mirror condition can be used to solve for this constant (see equation 2.69).

Of course a real electrostatic bend has fringe fields and edge effects that focus the beam. Since the analytical model deals only with the central ray, these higher order effects are not dealt with analytically, but will be accounted for in the computer model.

## 2.5.2 Conservation of Magnetic Moment

After the beam leaves the electrostatic bend, it has momentum perpendicular ( $p_{\perp}$ ) and parallel ( $p_{\parallel}$ ) to the magnetic field. The perpendicular component causes the beam to orbit around the B-field lines at radius  $r = \frac{p_{\perp}}{qB}$ , and the component parallel to the B-field causes the beam to move axially into the high field region. In order to calculate the trajectory of a single ion through the fringe field of the solenoid, we use the fact that the magnetic moment ( $\mu_{\text{mag}}$ ) is conserved in slowly varying magnetic fields [18, 19].

That is:

$$\mu_{\text{mag}} = \text{constant} \quad (2.56)$$

The magnetic moment is the current (I) times the area (A) encircled by an orbit.

$$\mu_{\text{mag}} = IA \quad (2.57)$$

Using  $I = qf_c$ , and  $p_{\perp} = qBr$ , this can be expressed as

$$\mu_{\text{mag}} = \frac{p_{\perp}^2}{2mB} = \frac{E_{\perp}}{B}$$

Or substituting directly into equation 2.57.

$$\mu_{\text{mag}} = IA = qf_c A = q \left( \frac{qB}{2\pi m} \right) \pi r^2$$

This means that the magnetic flux ( $\Phi_{\text{mag}}$ ) is also conserved.

$$\Phi_{\text{mag}} = BA = \text{constant} \quad (2.58)$$

Thus, the beam orbit follows magnetic field lines as shown in Figure 26.

Therefore:

$$B_1 r_1^2 = B_2 r_2^2$$

$$\boxed{\frac{r_2}{r_1} = \sqrt{\frac{B_1}{B_2}}} \quad (2.59)$$

**Figure 26. Geometry of conservation of magnetic moment (copied from reference 19).**

This means that if we know the radius of the orbit ( $r_1$ ) in the low field region ( $B_1$ ), then the radius ( $r_2$ ) in the high field region ( $B_2$ ) will be reduced by the square root of the ratio of the B-fields. Similarly we can calculate the perpendicular momentum by substituting:  $p_{\perp} = qBr$  for  $r$ .

$$\boxed{\frac{p_{\perp_2}}{p_{\perp_1}} = \sqrt{\frac{B_2}{B_1}}} \quad (2.60)$$

Notice that  $p_{\perp}$  increases as the square root of the B-field ratio. Finally we can calculate  $p_{\parallel}$  using the fact that kinetic energy of the beam is conserved in magnetic fields.

Therefore: 
$$p_{\parallel_2}^2 = p_{\text{total}}^2 - p_{\perp_2}^2 \quad (2.61)$$

$$\boxed{p_{\parallel_2} = \sqrt{p_{\text{total}}^2 - p_{\perp_1}^2 \left( \frac{B_2}{B_1} \right)}} \quad (2.62)$$

Since  $p_{\perp}$  increases while spiraling into the high field, and the total momentum remains constant, then  $p_{\parallel}$  must decrease.

As a check of the accuracy of this approximation, Figure 27 shows the analytical calculation of the orbit radius through the injection trajectory. The result is compared with data from the computer model of section 2.6. The computer model contains no approximations of this kind and should be considered completely accurate for the purposes of this comparison. The two calculations were started at the same radius in the high B-field region and then calculated backwards through the injection region so that the error can be seen in the region of large radius. The error in the analytical approximation (relative to computer model) grows to 1.5 % for the magnetic field profile shown. The error will be greater for a field which drops off faster or for a trajectory which is relatively more parallel (fewer turns).

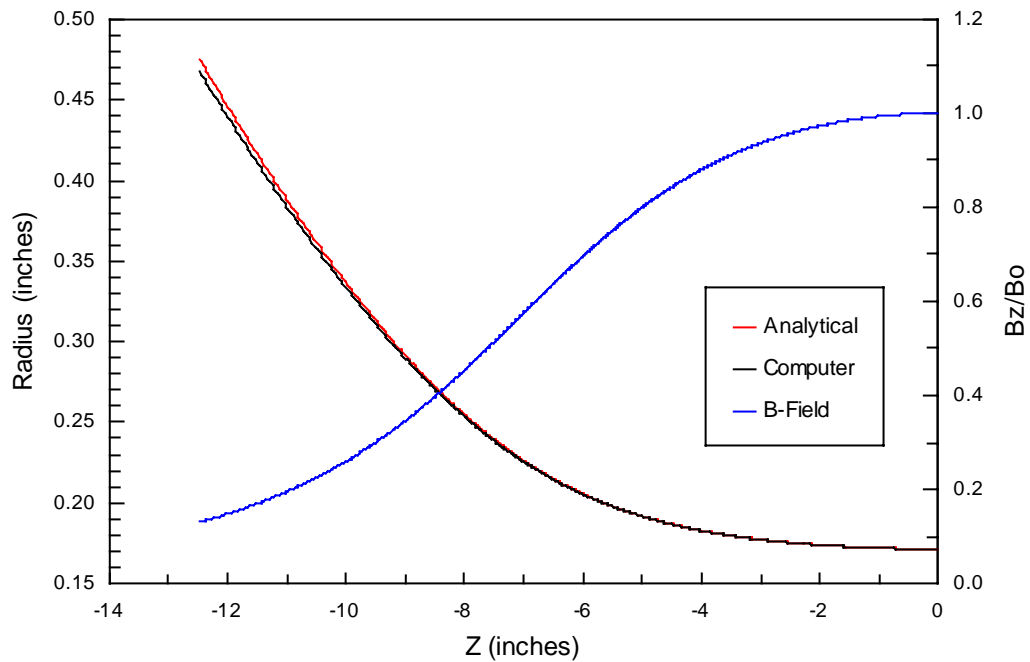


**Figure 27. A comparison of the beam orbit radius through the injection region calculated using the analytical model and using ICRAcyclone. The magnetic field profile is shown in blue.**

At the beginning of section 2.5 we said that the analytical model of the beam trajectory deals only with the central ray through the system, i.e. a beam of zero emittance. However, conservation of magnetic moment has some implications on how the spreads in the beam radius and momentum change. Therefore we will diverge briefly to discuss these here.

Imagine that a real beam entering the solenoidal fringe fields contains a spread in beam radius,  $\Delta r$ . From the geometry of the field lines alone, it is easy to see that the radial spread in the beam will decrease as the beam spirals into the high field (Figure 23). This can also be seen by differentiating equation 2.59.

$$\boxed{\Delta r_2 = \Delta r_1 \sqrt{\frac{B_1}{B_2}}} \quad (2.63)$$

So the radial spread ( $\Delta r_2$ ) in the high field region ( $B_2$ ) is less than the radial spread ( $\Delta r_1$ ) in the low field region ( $B_1$ ) by a factor of  $\sqrt{\frac{B_1}{B_2}}$ .

The spread in the perpendicular momentum is found by differentiating equation 2.60.

$$\boxed{\Delta p_{\perp 2} = \Delta p_{\perp 1} \sqrt{\frac{B_2}{B_1}}} \quad (2.64)$$

Hence, the spread in  $p_{\perp}$  increases by a factor of  $\sqrt{\frac{B_2}{B_1}}$ .

There is no simple form for  $\Delta p_{\parallel}$ . However, if we use 2.60 to express 2.61 in terms of parallel momentums only:

$$p_{\parallel 2}^2 = p_{\parallel 1}^2 \left( \frac{B_2}{B_1} \right) - p_{\text{tot}}^2 \left( \frac{B_2 - B_1}{B_1} \right)$$

then differentiating gives:

$$\Delta p_{\parallel 2} = \Delta p_{\parallel 1} \left( \frac{B_2}{B_1} \right) \left( \frac{p_{\parallel 1}}{p_{\parallel 2}} \right) \quad (2.65)$$

Although the actual parallel momentum decreases while spiraling into the high field region, both  $(B_2/B_1)$  and  $(p_{\parallel 1}/p_{\parallel 2})$  are greater than 1, so the spread in  $p_{\parallel}$  increases.

### 2.5.3 Mirror Condition

As discussed in section 2.5.2, when the beam goes from a region of low magnetic field to a region of high field adiabatically, the perpendicular momentum increases by the root of the B-field, and the parallel momentum decreases such that the kinetic energy of the beam is conserved. If the magnetic field becomes high enough, eventually the parallel momentum goes to zero and all of the momentum will be perpendicular to the B-field. At this point, the axial motion of the beam has come to a stop, but the axial force on the beam ( $\vec{F} = -qv_{\theta}B_r\hat{z}$ ) is still in the negative z direction (see Figure 26), so the beam will be reflected. This is referred to as “mirroring”.

In the case of the injection region of the ICRA, we want to determine what conditions, back in the low field region at the electrostatic bend, will lead to a beam which mirrors when it reaches the high field region. Here, we take  $B_1$  to be the low field and  $B_2$  to be the high field. Since we know the conditions at  $B_2$  for mirroring, we simply need to impose the mirror condition ( $p_{\parallel 2} \rightarrow 0$ ), and then solve for the conditions at  $B_1$  in terms of those at  $B_2$ . Begin by conserving kinetic energy between region (1) and (2).

$$\begin{aligned} |\vec{p}_1|^2 &= |\vec{p}_2|^2 \\ p_{\parallel 1}^2 + p_{\perp 1}^2 &= p_{\parallel 2}^2 + p_{\perp 2}^2 \end{aligned}$$

Now impose the mirror condition ( $p_{\parallel 2} \rightarrow 0$ ).

$$p_{\parallel 1}^2 + p_{\perp 1}^2 = 0 + p_{\perp 2}^2$$

Use (2.60) to express the  $p_{\perp}$  in the high field region in terms of  $p_{\perp}$  back at the bend.

$$p_{\parallel 1}^2 = p_{\perp 1}^2 \left( \frac{B_2}{B_1} - 1 \right)$$

We are interested in the bend angle which causes mirroring, so solve for the ratio of

perpendicular to parallel momentum, then use:  $\tan(\theta_{\text{bend}}) = \frac{p_{\perp 1}}{p_{\parallel 1}}$

$$\boxed{\frac{p_{\perp 1}}{p_{\parallel 1}} \Big|_{\text{mirror}} = \sqrt{\frac{B_1}{B_2 - B_1}}} \quad (2.66)$$

so that: 
$$\theta_{\text{mirror}} = \tan^{-1} \left( \sqrt{\frac{B_1}{B_2 - B_1}} \right) \quad (2.67)$$

Notice that the momentum ratio at the electrostatic bend, which leads to mirroring at the high field region, is known from the magnetic fields alone. This is the form that is most useful for the ICRA. However, this result can be understood intuitively if we invert and square equation (2.66) to obtain a kinetic energy ratio.

$$\frac{K_{\parallel 1}}{K_{\perp 1}} \Big|_{\text{mirror}} = \frac{B_2 - B_1}{B_1} \quad (2.68)$$

The ratio of parallel to perpendicular energy needed to reach the high B-field region ( $B_2$ ) is simply the fractional increase in the B-field. In fact this expression is exactly analogous to what one would derive for a golf ball rolling up a hill (zero rotational energy), in which the ratio of initial kinetic energy (K) to potential energy (U) is simply the fractional increase in height (h).

$$K_1 + U_1 = 0 + U_2$$

$$\frac{K_1}{U_1} = \frac{h_2 - h_1}{h_1}$$

This analogy occurs because in the process of rolling up the hill, K is converted into U (just as  $K_{\parallel}$  is converted into  $K_{\perp}$ ) while the total energy is conserved, and because U

changes linearly with  $h$  (just as  $K_{\perp}$  changes linearly with  $B$  (eqn 2.53) ). Therefore, if one is willing to think of  $K_{\perp}$  as a potential energy that is stored in the radius of the beam, and of  $K_{\parallel}$  as the kinetic part of the energy, then equation 2.68 says that the kinetic energy needed to reach the top of the hill is simply the potential energy times the fractional increase in the B-field.

The mirror condition provides a simple way to solve for the constants in bending equation 2.55. The mirror voltage ( $V_{\text{mirror}}$ ) will be measured experimentally (section 4.5.3), and the mirror angle is easily calculated from the B-field. Therefore, since the bend angle ( $\theta_{\text{bend}}$ ) scales linearly with bend voltage ( $V_{\text{bend}}$ ) equation 2.55 can be expressed as:

$$\theta_{\text{bend}} = \theta_{\text{mirror}} \left( \frac{V_{\text{bend}}}{V_{\text{mirror}}} \right) \quad (2.69)$$

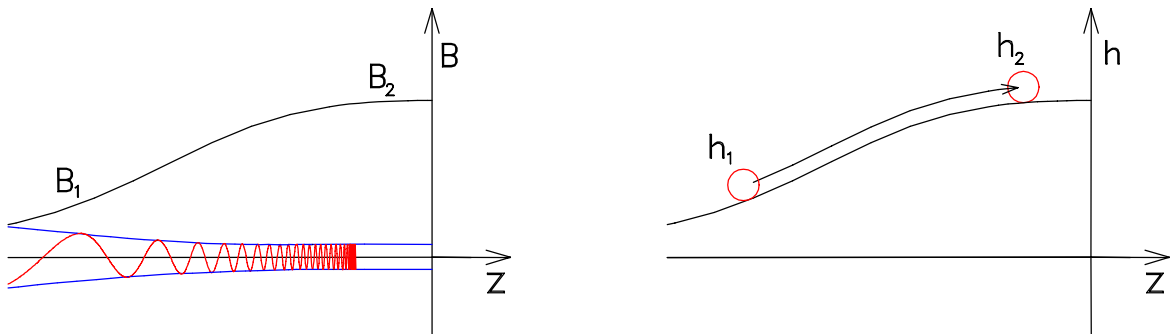


**Figure 28. Mirroring the beam is analogous to when a ball does not have enough kinetic energy to make it to the top of a hill.**

### 2.5.4 Mass Spectrum of the Injected Beam

In the ICRA, beam is extracted from the ion source along a B-field line so that the  $\vec{v} \times \vec{B}$  force on the beam is zero. All ions are accelerated through the same voltage ( $V_{\text{beam}}$ ) from the ion source aperture to the puller. However, because different ions may have different charge or different masses, different ions will have different total momentum.

$$p_{\text{total}} = \sqrt{2mE} = \sqrt{2mqV_{\text{beam}}} \quad (2.70)$$

When entering the electrostatic bend, the beam is parallel to the B-field,  $p_{\perp} = 0$ , and  $p_{\parallel} = p_{\text{total}}$ . In section 2.5.1 we showed that the electrostatic bend will bend all ions to the same angle ( $\theta_{\text{bend}}$ ) regardless of their mass or charge (equation 2.55). Refer to Figure 25 to see that:

$$p_{\perp} = p_{\text{total}} \sin(\theta_{\text{bend}}) \quad (2.71)$$

As soon as the beam obtains a component of momentum perpendicular to the B-field, ions will experience a  $\vec{v} \times \vec{B}$  force tending to make them orbit around a gyro center with a radius of:

$$r = \frac{p_{\perp}}{qB}$$

This can be expressed in terms of the bend angle, and beam energy using equations (2.70) and (2.71)

$$r = \frac{p_{\text{total}} \sin(\theta_{\text{bend}})}{qB} = \frac{\sqrt{2mqV_{\text{beam}}}}{qB} \sin(\theta_{\text{bend}})$$

Therefore:

$$r = \sqrt{\frac{2mV_{\text{beam}}}{qB^2}} \sin(\theta_{\text{bend}}) \quad (2.72)$$

Equation 2.72 gives the radius of the orbit immediately after the beam exits the electrostatic bend. Next, let the beam spiral from the bend ( $B_1$ ) to the high B-field region ( $B_2$ ). Using equation (2.59) gives:

$$r_2 = r_1 \sqrt{\frac{B_1}{B_2}} = \sqrt{\frac{2mV_{\text{beam}}}{qB_1B_2}} \sin(\theta_{\text{bend}}) \quad (2.73)$$

The important thing to notice here is that the radius of each different ion beam is proportional to the root of its mass to charge ratio, but the radius of all ions will increase as we increase the bend angle. Figure 29 shows the relative sizes of each constituent in an ion beam containing  $H^+$ ,  $H_2^+$  and  $Ar^+$  ions for a fixed bend angle.

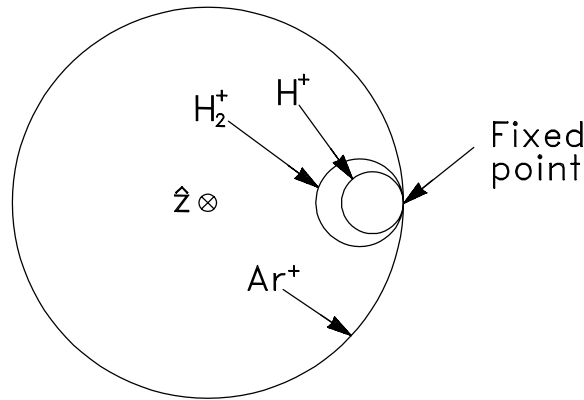


**Figure 29. Axial view of a beam containing three ions species.**

**The bend voltage is fixed at the point for which the Argon orbit is centered around the z axis.**

In the 50 keV ICRA, the narrowest aperture for the orbiting beam in the entire system is at the entrance to the magnetron. Experimentally we can turn up  $V_{\text{bend}}$  while measuring the beam current on a Faraday Cup at the extraction end. As each ion beam clips on the entrance to the magnetron, the current will drop at discrete bend voltages.

The resulting graph of beam current vs. bend voltage gives a spectrum of each ion species in the beam.

The voltages where each constituent in the beam clips can be calculated from equation 2.73. First we simplify by lumping all the known constants into a constant C.

$$r_2 = C \sqrt{\frac{m}{q}} \sin(\theta_{\text{bend}})$$

Setting  $r_2$  equal to the radius at which the beam will clip and solving for the bend angle we obtain:

$$\theta_{\text{bend}} = \sin^{-1} \left( \frac{r_{\text{clip}}}{C} \sqrt{\frac{q}{m}} \right) \quad (2.74)$$

Finally, the bend angle can be converted to the bend voltage using equation (2.55 or 2.69). Section 4.5.1 shows an ion spectrum measured experimentally and compares with the theoretical results using equation 2.7.4.

### 2.5.5 Number of Turns Through the Acceleration Region

After spiraling through the injection region, the beam arrives at the entrance to the acceleration region with  $r$ ,  $p_{\perp}$ , and  $p_{\parallel}$  which have been transformed according to the equations in section 2.5.2. We now wish to calculate the number of turns ( $N_{\text{turns}}$ ) that the beam goes through as it traverses the axial length of the cavity ( $\ell_{\text{cav}}$ ).

The magnetic field must be relatively constant over the length of the accelerating region in order to maintain resonance. Therefore, it is a very good approximation to assume the field is constant in the analytical model. The number of turns through the acceleration region is simply the ratio of the total time spent traversing the cavity length to the period for one revolution.

$$N_{\text{turns}} = \frac{t_{\text{cav}}}{T_c}$$

The total time spent in the cavity depends on the axial velocity ( $v_z = \frac{\ell_{\text{cav}}}{t_{\text{cav}}}$ ) and the

period for one revolution is related to the cyclotron frequency by:  $\frac{1}{T_c} = f_c = \frac{qB}{2\pi m}$ .

So the number of turns becomes:

$$\boxed{N_{\text{turns}} = f_c \frac{\ell_{\text{cav}}}{v_z} = \frac{qB \ell_{\text{cav}}}{2\pi p_z}} \quad (2.75)$$

When using this formula, one should be aware that equation 2.75 gives the number of turns through the length of the acceleration region only when the rf is off (no acceleration). When the rf is turned on, axial components of the electric field (caused by the tapered inner diameter of the magnetron) lead to an axial momentum change which depends on the phase of the beam. This effect is explained in section 2.6.2.

### 2.5.6 Acceleration Region

Section 2.4.3 showed that the electric fields in the central region of the rf driven magnetron can be written as a Fourier series in the azimuthal dependence. The lowest order contribution is for the case of hyperbolic vanes (refer to equation 2.47 and Figure 18). Using this first order term gives a good approximation of the cavity voltage and is useful for illustrating the important aspects of acceleration through the magnetron.

The lowest order term in the voltage, as a function of radius ( $r$ ) azimuthal position ( $\theta$ ) and time ( $t$ ), is given by:

$$V(r, \theta, t) = V_o \left(\frac{r}{R}\right)^n \sin(n\theta) e^{i\omega_{rf}t} \quad (2.76)$$

Here  $R$  is the inner radius of the cavity,  $V_o$  is the voltage on the cavity wall and  $n$  is the azimuthal mode number of the cavity, which comes from the number of gaps ( $N_{\text{gaps}}$ )

$$N_{\text{gaps}} = 2n$$

The azimuthal component of electric field is found by differentiating equation (2.76).

$$\vec{E} = -\vec{\nabla}V$$

$$E_{\theta} = -\frac{nV_o}{R} \left(\frac{r}{R}\right)^{n-1} \cos(n\theta) e^{i\omega_{rf}t} \quad (2.77)$$

Consider an 8 gap magnetron structure as shown in Figure 30. For this case  $n = 4$ . The azimuthal electric field ( $E_{\theta}$ ) is plotted as a function of  $\theta$  in Figure 31. The dc magnetic field points out of the page, so ions orbit in a counter-clockwise direction at

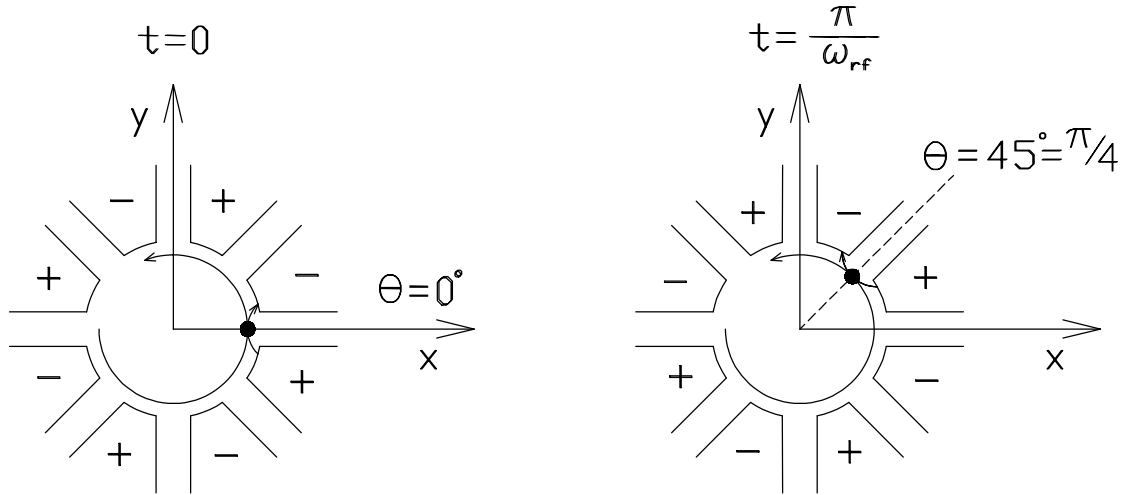


Figure 30. An rf driven magnetron structure with  $n=4$  oscillating in the  $\pi$ -mode.

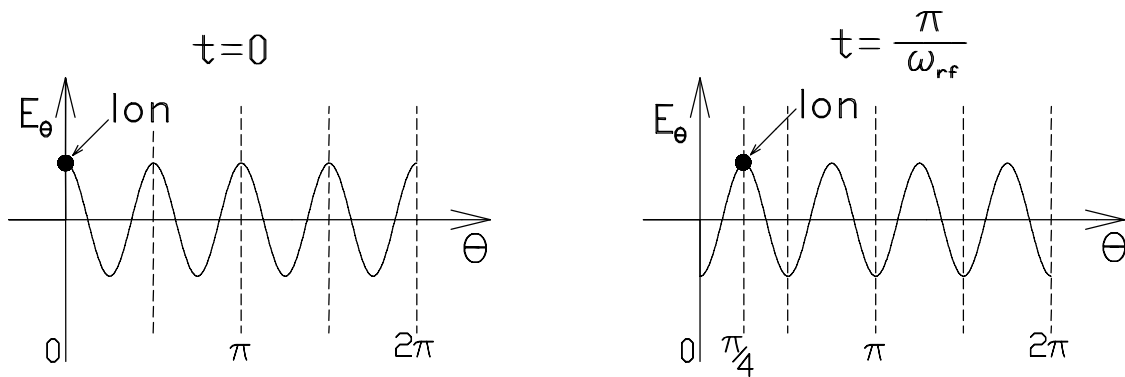


Figure 31. Azimuthal component of the E-field vs azimuthal position.

the cyclotron frequency  $\omega_c = \frac{qB}{m}$  (for  $\gamma = 1$ ). The phase of the rf signal is defined as:

$$\tau = \omega_{rf} t$$

and assuming the orbit is perfectly centered, the azimuthal position is:

$$\theta = \omega_c t.$$

If an ion crosses the first gap ( $\theta = 0$ ) at time  $t = 0$ , the electric field is maximum and the ion will be accelerated in the forward ( $\theta$ ) direction. If the cyclotron frequency is such that the ion arrives at the second gap ( $\theta = 45^\circ$ ) at the time when the rf phase has changed by half a cycle ( $\tau = 180^\circ$ ) then the electric field points forward and the ion is accelerated again. Setting the time to travel between gaps ( $t = \frac{2\pi}{N_{\text{gaps}} \omega_c}$ ) equal to the time for one half of an rf cycle ( $t = \frac{\pi}{\omega_{\text{rf}}}$ ), leads to the resonance condition required for acceleration.

$$\boxed{\omega_{\text{rf}} = n \omega_c} \quad (2.78)$$

The kinetic energy gained in crossing a single gap can be found by integrating along a path at constant radius.

$$K_{\text{gap}} = \int \vec{F} \cdot d\vec{s}$$

$$K_{\text{gap}} = -q n V_o \left(\frac{r}{R}\right)^n \int_{-\frac{\pi}{2n}}^{\frac{\pi}{2n}} \cos(n\theta) e^{i\omega_{\text{rf}} t} d\theta$$

$$K_{\text{gap}} = \frac{\pi}{2} q V_o \left(\frac{r}{R}\right)^n$$

If we define the total voltage difference across a gap as  $V_{\text{gap}} = 2V_o$ , the energy gained across a single gap becomes

$$\boxed{K_{\text{gap}} = \frac{\pi}{4} q V_{\text{gap}} \left(\frac{r}{R}\right)^n} \quad (2.79)$$

where  $\pi/4 = 0.79$  is the transit time factor.

Notice that the multipole nature of the magnetron, leads to an  $r^n$  radial dependence in the energy gain. This radial dependence is plotted in Figure 32 for  $n=4$ .

The beam will gain maximum energy if it remains as close as possible to the cavity wall ( $r \approx R$ ) throughout the acceleration trajectory. For this reason the inner diameter of magnetron should be tapered with  $z$  so that the beam will remain close to the cavity wall as its orbit radius increases. For this research, a linear taper was chosen ( $dR/dz = \text{constant}$ ), so that the actual magnetron would be simple to manufacture.

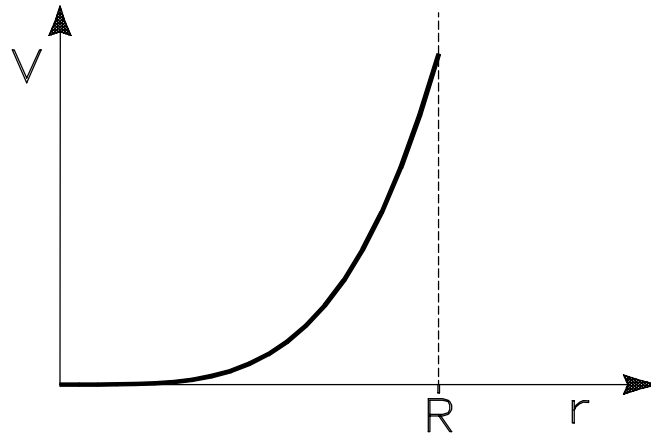


**Figure 32. Lowest order term for the radial dependence of cavity voltage in an 8 gap magnetron.**

Equation 2.79 can be used to calculate the orbit radius and energy gain through the acceleration region. One method is to choose the cavity slope ( $dR/dz$ ), initial radius fraction ( $r/R$ ), and axial momentum ( $p_z$ ), then let the particle gain energy  $K_{\text{gap}}$  across the first gap, then recalculate:  $r$ ,  $z$ , and  $R$ , so that  $K_{\text{gap}}$  can be calculated for the second gap. Continue this iteration until the cavity length has been traversed. If this is done as a simple spread sheet calculation, then the cavity voltage ( $V_o$ ) can be adjusted until an ideal trajectory is obtained. Figure 33 shows a calculation of orbit radius using this method.

A quicker estimate of the total energy gain can be made by estimating the average radius fraction throughout the acceleration trajectory  $\left\langle \frac{r}{R} \right\rangle$  and assuming that the

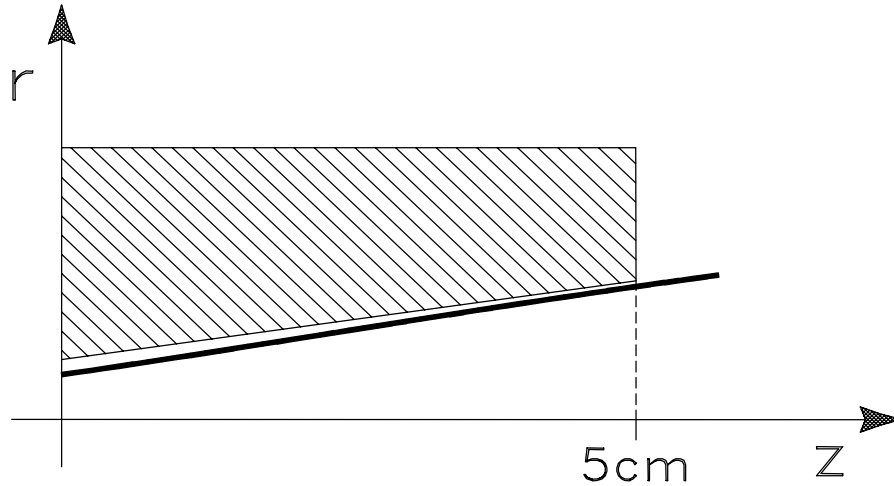


Figure 33. Beam orbit radius from spread sheet calculation plotted next to magnetron inner radius

energy gained across each gap remains constant throughout the trajectory. In this case using the number of gaps per turn ( $N_{\text{gaps}} = 2n$ ) and the total number of turns, ( $N_{\text{turns}}$ ), the total energy gain is simply:

$$K_{\text{gain}} = \frac{\pi}{4} q V_{\text{gap}} \left\langle \frac{r}{R} \right\rangle^n 2n N_{\text{turns}} \quad (2.80)$$

Finally, note that in this discussion the radial component of the E-field has been completely neglected (see Figure 15). This is a valid approximation because when averaged over time,  $E_r$  does not cause any net acceleration. Furthermore, the tapered inner diameter of the magnetron will cause a component of electric field in the z direction. Similarly the end fields, resulting from the finite axial length of the magnetron, will certainly have components in the z direction. For the most part these effects have been found to be small, however they will be discussed in sections 2.6.2 and 2.6.3. The full 3 dimensional solution of the electric field in the magnetron is accounted for in the computer model (see section 2.6).

### 2.5.7 RF Phase and Magnetic Field Flatness Criterion

The analytical model of the beam trajectory does not account for any variation in rf phase. In fact, the discussion and the timing arguments of section 2.5.6 describe the case in which the phase of the ion is constant relative to the rf ( $\omega_{rf} = n \omega_c$ ). Furthermore the derivation of the energy gain across a gap (equation 2.79) uses the assumption that the phase relative to the rf is  $\phi = 90^\circ$  so that the ion crosses a gap when the cavity voltage is at its maximum. However, in section 2.6.2 we will see that the computer model shows that the ICRA exhibits significant phase bunching. Also the experimental results show a resonance width that is much wider than expected (section 4.6.2). Therefore, it is necessary to derive analytical expressions for phase changes, as a basis for comparison.

This section first gives an introduction to rf phase and then covers phase changes caused by detuning of the magnetic field. Next the magnetic field flatness criterion is defined and an equation is found for the phase change caused by the magnetic field profile over the acceleration region .

The general equation which describes the phase of a particle during acceleration is:

$$\phi(t) = (\phi_o + \omega_{rf} t - n\theta)$$

or simply

$$\Delta\phi(t) = (\omega_{rf} t - n\theta) \tag{2.81}$$

If the beam orbit is centered, then the azimuthal position is:

$$\theta = \omega_c t.$$

so that:

$$\Delta\phi(t) = (\omega_{rf} - n\omega_c) t \quad (2.82)$$

In this form it is easy to see that the phase equation is simply a comparison of two rates.

At resonance ( $\omega_{rf} = n\omega_c$ ), the phase will remain constant at its initial value ( $\phi_0$ ).

However, if  $\omega_{rf} \neq n\omega_c$  then the phase will drift over time.

The time dependence of the rf signal is taken to be  $\sin(\omega_{rf} t)$ , therefore we expect optimum acceleration across any gap to occur when  $\phi = 90^\circ$ . We wish to determine how far the phase will drift through the acceleration region if the magnetic field is not at resonance.

### Phase Change Caused by Magnetic Field Detuning

Consider the case where the rf frequency is fixed at  $\omega_{rf} = n\omega_{co}$ , but the B-field (constant with respect to z) is detuned away from  $B_0$  by an amount  $\Delta B$ . In this case equation 2.82 becomes:

$$\Delta\phi(t) = [n\omega_{co} - n(\omega_{co} + \Delta\omega_c)]t$$

Where  $\omega_{co} = \frac{qB_0}{m}$ , and the zero subscript indicates the B-field required for resonance with the rf. In terms of the fractional change in the B-field this becomes:

$$\Delta\phi(t) = -n\omega_{co} \frac{\Delta B}{B_0} t \quad (2.83)$$

Here  $\Delta\phi$  is the total change in phase over the time, t, caused by  $\Delta B$ . This equation is valid for any time (t). However, if we want the phase change over the time the ion

spends in the accelerating cavity, it is useful to express  $\Delta\phi$  in terms of the number of turns in the cavity length. Using:

$$N_{\text{turns}} = \frac{t_{\text{cav}}}{\tau_{\text{co}}} = f_{\text{co}} t_{\text{cav}}$$

we obtain:

$$\Delta\phi_{\text{cav}} = -2\pi n \frac{\Delta B}{B_o} N_{\text{turns}} \quad \text{in radians} \quad (2.84)$$

or:

$$\Delta\phi_{\text{cav}} = -360^\circ n \frac{\Delta B}{B_o} N_{\text{turns}} \quad \text{in degrees} \quad (2.85)$$

These equations describe the phase change that occurs through the cavity length if the B-field is constant (no z dependence), but is detuned away from resonance with the rf frequency. These equations are valid only if acceleration does not cause a phase change. However, in section 2.6.2 we will see that electric fields in the rf driven the magnetron do cause a phase shift.

### Phase Change Caused by Magnetic Field Profile

The characteristics of Helmholtz and solenoidal fields were shown in section 2.1. The ideal magnetic field for the ICRA would be perfectly flat over the acceleration region in order to maintain resonance. However, this is not possible for any real coil. Therefore, it is useful to characterize the magnetic field flatness in terms of the percent drop off ( $\delta B/B_o$ ) at the ends of the acceleration region. The geometry is shown in Figure 34.

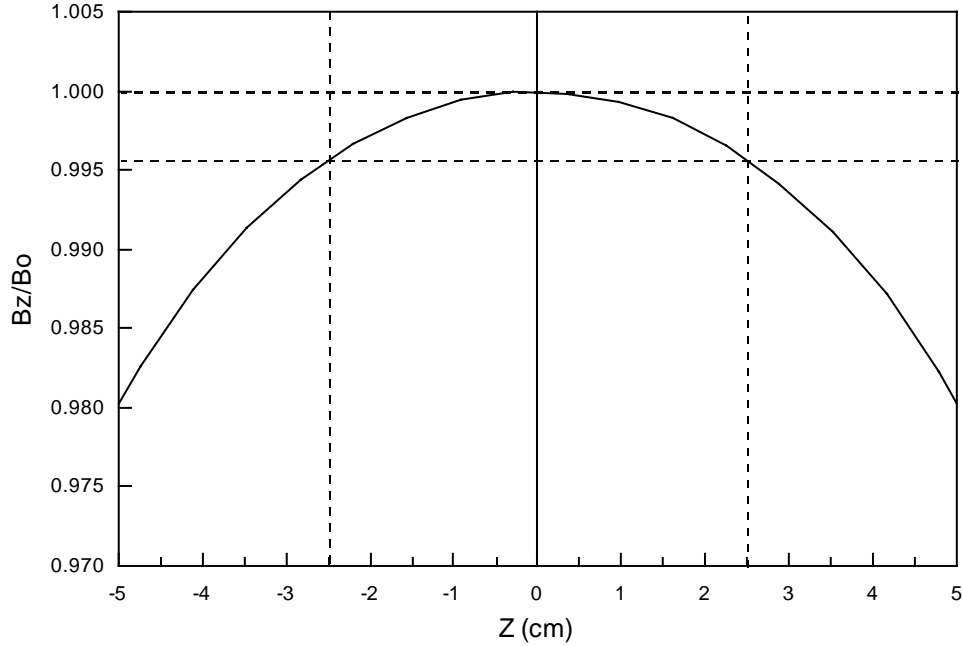


**Figure 34. Magnetic field profile for the 50 keV ICRA with flatness of  $\delta B/B_0 < 0.5\%$  over the 5 cm acceleration region**

Assume that the central value of the B-field ( $B_0$ ) is at resonance with the rf. Therefore, the subscript ‘zero’ will now indicate both the central field value and resonance. In this case,  $\Delta B$  is a function of  $z$ . Therefore, the total phase change requires integration. Using equation 2.83.

$$\Delta\phi(t) = - \int n\omega_{co} \frac{\Delta B(z)}{B_0} dt$$

The equation can be converted to an integration over  $z$ , by assuming that the axial velocity ( $v_z$ ) is constant.

$$\Delta\phi(t) = -\frac{n\omega_{co}}{B_o v_z} \int \Delta B(z) dz$$

The B-field profile of any coil over this central region can be closely approximated as a parabola.

$$B(z) = B_o - \delta B \frac{z^2}{(\frac{1}{2} \ell_{cav})^2}$$

Now integrating over this B-field profile from  $-\frac{1}{2} \ell_{cav}$  to  $+\frac{1}{2} \ell_{cav}$  and simplifying gives:

$$\Delta\phi_{cav} = -\frac{1}{3} n \omega_{co} \frac{\delta B}{B_o} t_{cav}$$

Once again, expressing this in terms of  $N_{turns}$ , gives the same result as equation 2.85 but reduced by a factor of 1/3.

$$\boxed{\Delta\phi_{cav} = -\frac{1}{3} 2\pi n \frac{\delta B}{B_o} N_{turns}} \quad \text{in radians} \quad (2.86)$$

$$\boxed{\Delta\phi_{cav} = -\frac{1}{3} 360^\circ n \frac{\delta B}{B_o} N_{turns}} \quad \text{in degrees} \quad (2.87)$$

Keep in mind that these equations are for when the central field value ( $B_o$ ) is matched for resonance with the rf. Certainly  $\Delta\phi$  over the acceleration region can be further reduced by increasing the central field ( $B_o$ ) so that resonance occurs at some compromise between  $B_o$  and ( $B_o - \delta B$ ). Again, equations 2.86 and 2.87 are valid only if acceleration does not cause the phase to change, however in section 2.6.2 we will see that electric fields in the rf driven the magnetron do cause a phase shift.

### 2.5.8 Axial Turn Length in the Extraction Region

Once the beam exits the acceleration region it spirals into the lower B-field region of the target. This is the extraction trajectory (refer to Figure 23). An important quantity to know in this region is the axial distance between turns, or the axial turn length. The axial turn length ( $\Delta z_{\text{turn}}$ ) can be calculated by multiplying the axial velocity ( $v_z$ ) times the time for a single turn.

$$\Delta z_{\text{turn}} = v_z \tau_c$$

Using the cyclotron frequency ( $f_c = \frac{1}{\tau_c}$ ) and expressing  $v_z$  in terms of the axial momentum, we obtain a convenient expression:

$$\boxed{\Delta z_{\text{turn}} = 2\pi \frac{p_z}{qB}} \quad (2.88)$$

Where,  $B = B_z(z)$  and  $p_z$  are both local variables, and  $p_z$  can be calculated using the adiabatic approximation discussed in section 2.5.2. Recall that as the B-field drops off through the extraction region,  $p_{\perp}$  is converted into  $p_{\parallel}$ , and therefore  $p_z$  increases.

Immediately after acceleration, nearly all of the energy is in  $p_{\perp}$ , ( $p_{\perp}/p_{\parallel}$  is large so  $p_{\parallel}$  is negligible). Therefore, in a region far enough downstream that the B-field has dropped off significantly, the value of  $p_z$  depends almost entirely on what has been converted from  $p_{\perp}$  to  $p_{\parallel}$ . Thus  $p_z$  will depend strongly on the total energy of the beam. The result is that in the extraction region, the beam at large radius has a larger axial turn length than the beam near the center. In fact after  $p_z$  has grown significantly,  $\Delta z_{\text{turn}}$  goes roughly as the root of the beam energy and therefore is roughly linear with radius. The analytical calculation plotted in Figure 35 shows the axial turn length vs. beam orbit radius for  $B/B_0 = 0.34$  in the 50 keV ICRA.

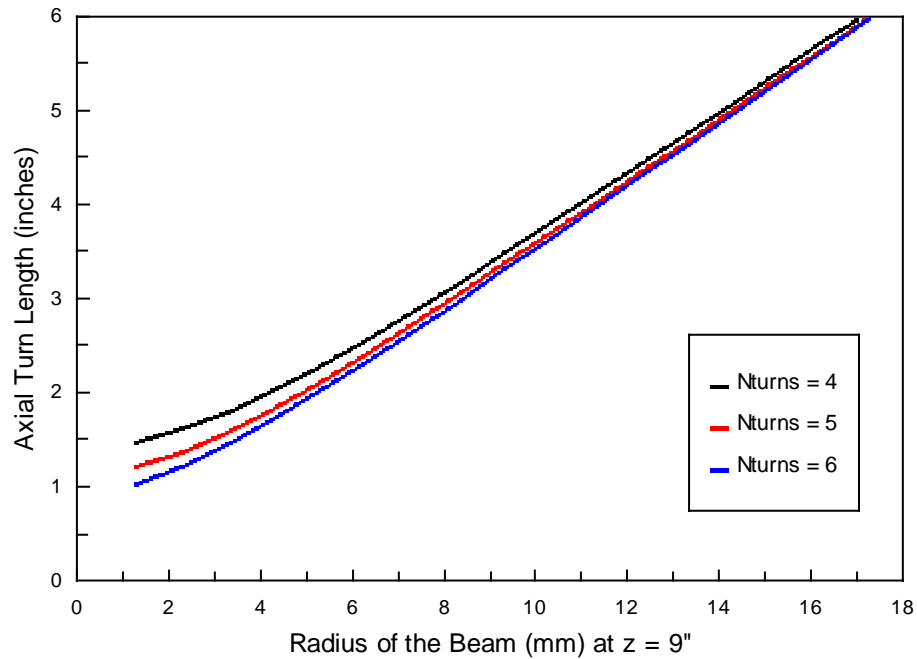


**Figure 35. Axial turn length depends on beam radius (or energy) in the extraction region**

It is important to understand the axial turn length when designing a target or a beam diagnostic for measurement of the extracted beam. In fact this result will be used for the corrections to the radial probe data in sections 3.2.5 and 4.6.1.

One should also be aware that equation 2.88 gives only the instantaneous value of the axial turn length. The actual length of a turn in the extraction region depends on the value of the B-field at every point throughout the orbit. This means that if there is a large change in B-field over a single turn, then the axial turn length will grow significantly and equation 2.88 will give a poor estimate of the actual length of a turn.

## **2.6 Computer Model of the Beam Trajectory**

See Chap2C.doc

$\delta B$

$l_{\text{cav}}$

NOT USED

### **2.5.6 Summary of Injected Beam Equations**

The point is that in the analytical model, the entire beam trajectory can be specified in terms of 2 parameters:  $N_{\text{turns}} \rightarrow p_z$  and  $(r/R) \rightarrow p_{\perp}$ .

Take this opportunity to make it clear that if  $N_{\text{turns}}$  is known, then  $p_z$  (at cav entrance) is known. They are inversely proportional. so we will use the two quantities interchangeably.

## **2.6 Computer Model of the Beam Trajectory**

This section covers the computer model used to study the beam trajectory through the ICRA. A complete computer model is necessary for two reasons:

1) There are several effects which are not accounted for in the analytical model (listed below) and 2) the computer model allows the capability to simulate a beam of finite emittance by running thousands of single particle trajectories, each with slightly different initial conditions. Modeling a full emittance beam is the ultimate goal of the computer model because this allows the accelerated beam current to be estimated.

The analytical model discussed in section 2.5 gives a good estimate of the trajectory, but there are several approximations made which limit the accuracy, especially in the acceleration region. In the analytical model, the beam is assumed to remain centered on the  $z$  axis and it would be difficult to accurately account for an off centered beam. During acceleration, ions are assumed to remain in phase with the rf (at  $\phi = 90^\circ$ ). In reality, acceleration at each gap causes motion of the orbit center, and whenever the beam is off center there is a corresponding oscillation in the phase (section 2.6.4). Most importantly, the analytical model cannot accurately predict  $(r/R)$  at every step through the acceleration trajectory and this ratio has major impact on the cavity voltage needed for optimum acceleration because the slope of voltage vs. position is so steep (Figure 32). For this reason, the average  $r/R$  in equation 2.80 is useful only as a first approximation. The computer model makes no assumptions of this sort and all of the effects mentioned above are accounted for. Accuracy of the computer model is limited mainly by the accuracy of the electric and magnetic fields that are input into the code.

Section 2.6.1 below describes the computer model. This section then begins with the simple case of acceleration through the magnetron in a flat magnetic field. Each section thereafter adds realistic effects, until the entire system is accounted for. Section 2.6.2 shows the dependence of final energy on the initial phase. End fields of the magnetron are added in section 2.6.3. A realistic magnetic field is added in section 2.6.4. At this point, the beam can be launched from the location of the ion source and pass through the entire system using realistic fields. Section 2.6.5 shows several views of single particle trajectories through the entire system.

Multi-particle trajectories begin in section 2.6.6. Here, initial conditions of each particle are adjusted in order to map out the acceptance phase space of the rf driven magnetron. Next a full emittance beam is launched from the ion source and characteristics of the injected beam (rf off) are discussed in section 2.6.7. Finally, the full emittance beam is accelerated and the energy distribution is obtained in section 2.6.8.

### 2.6.1 The Computer Code

A complete computer model has been developed for the ICRA. This model uses three computer codes: ICRAcyclone, RELAX3D, and BRZcoil.

ICRAcyclone is a modified version of Z3CYCLONE which was developed here at the NSCL and has been used for many years to model particle trajectories in cyclotrons at this lab [20, 21]. ICRAcyclone uses 4<sup>th</sup> order Runge Kutta integration to step an ion through its complete trajectory in three dimensions. An ion can be started from the ion source, then passed through the electrostatic bend, through the injection, acceleration, and extraction regions, until it stops at the target face. This code handles only single particle trajectories. However, a beam of finite emittance can be simulated using many single particle trajectories. Space charge forces are not accounted for.

The complete off axis analytical solution of the magnetic field [12 pg.177] is calculated using a code named BRZcoil [22, 23]. These Helmholtz, or solenoidal magnetic fields are two dimensional (azimuthal symmetry). BRZcoil calculates the magnetic field arrays for  $B_r$  and  $B_z$  over the entire volume of interest, including injection, acceleration, and extraction regions. These arrays are then imported by ICRAcyclone.

The full three dimensional solution for voltage potentials in the magnetron and the electrostatic bend are computed using RELAX3D, a code developed at TRIUMF in Vancouver, Canada [24]. RELAX3D uses successive overrelaxation to solve the Laplace equation for electrostatic potentials. The voltage arrays are imported to ICRAcyclone where electric fields are obtained by numerical differentiation.

The electric field of the electrostatic bend is constant in time. However, when modeling the electric fields in the magnetron, the electrostatic voltages are scaled by

$\sin(\omega_{rf} t)$ . Using an electrostatic solution to model the fields in the magnetron is valid because only the central region is modeled where electric fields are dominant. The time varying magnetic fields of the magnetron are negligible in the central region which means that  $\nabla \times \vec{E} = 0$ . Therefore, the fields can be derived from an electrostatic potential. Furthermore, the lumped circuit nature of the magnetron allows the cavity to be much smaller than a wavelength. Figure 36 below shows the RELAX3D solution of voltage potentials for a tapered magnetron with 8 gaps.

**Figure 36. Equipotential lines in an 8 gap magnetron structure at entrance (left) and exit planes (right). Solution computed using RELAX3D.**

## 2.6.2 Phase Dependence and Acceleration

This section deals only with acceleration through the rf driven magnetron. All trajectories through the magnetron use a flat B-field so that the effects discussed here can be isolated. In this section, graphs of final energy vs. initial phase are used to illustrate two topics which are very central to understanding acceleration in the ICRA. The first is the dependence on two operating parameters: cavity voltage and number of turns. The second, is a look ahead at the why the spread in  $(p_{\perp}/p_{\parallel})$  of the injected beam has important implications on the amount of beam current that can be accelerated. This section then covers two unique effects caused by acceleration through a magnetron structure. These are: 1) a change in axial momentum which is phase dependent, and 2) a change in phase which tends to bunch the beam.

Recall from section 2.5.7, that the general equation which describes the phase of a particle during acceleration is given by:

$$\phi(t) = (\phi_o + \omega_{rf} t - n\theta)$$

or simply

$$\Delta\phi(t) = (\omega_{rf} t - n\theta) \quad (2.89)$$

Since the time dependence of the rf signal is  $\sin(\omega_{rf} t)$ , optimum acceleration across any gap occurs for  $\phi = 90^\circ$ . If  $\phi > 90^\circ$  the ion lags the rf (arrives at the gap late), but if  $\phi < 90^\circ$  the ion leads the rf (arrives at the gap early).

Figure 37 shows a graph which is very important for understanding the characteristics of the ICRA. Ions are started from the cavity entrance plane and accelerated through the magnetron. The initial phase ( $\phi_o$ ) of each ion is varied, and the

final energies are plotted. As expected, ions that enter the magnetron with initial phase near  $90^\circ$  are accelerated across every gap and continue to gain energy until they leave the acceleration region. Ions with initial phase near  $270^\circ$  are decelerated. Note that deceleration is less effective than acceleration because if ions lose energy, their radius decreases and they fall toward the central region where cavity voltages go to zero.

Now consider the three different curves in Figure 37. Obviously as the cavity voltage increases, the beam gains more energy until it eventually strikes the wall. Remember that at every point throughout the acceleration region, the maximum orbit radius of the beam is limited by the inner radius of the magnetron. Any beam that goes beyond this boundary is lost.

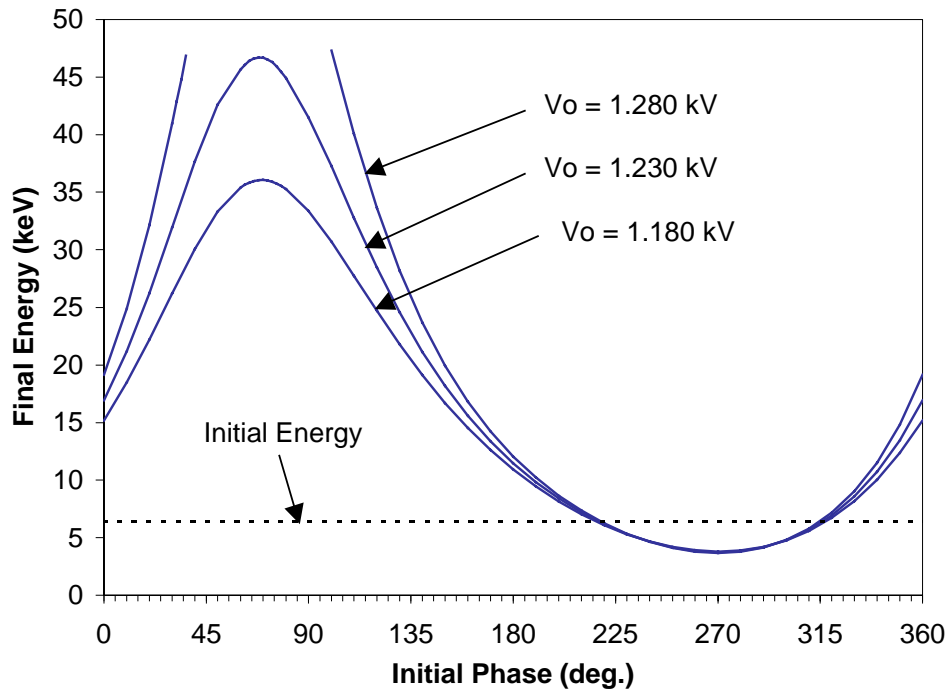


**Figure 37. Final proton energy vs initial phase for single particle trajectories through the computer model of the 50 keV ICRA. The curve is repeated for three different rf cavity voltages.**

Next consider what would happen if the axial momentum ( $p_z$ ) is increased. The voltage required for the beam to strike the wall would be higher because the beam goes through fewer turns in the cavity. This means that there is a one to one correspondence between  $V_o$  and  $N_{\text{turns}}$  (or between  $V_o$  and  $p_z$ ). In order to proceed, it is necessary to have a reference point which defines how to set the cavity voltage. Therefore, let us define “optimum acceleration” as the single particle trajectory at the peak of the  $E-\phi$  curve which reaches maximum final energy without striking the cavity wall. Figure 38 shows the cavity voltage required for optimum acceleration, vs.  $N_{\text{turns}}$  (or  $1/p_z$ ). This is just the same inverse relationship between  $V_o$  and  $N_{\text{turns}}$  that is evident in equation 2.80 for a fixed final energy.

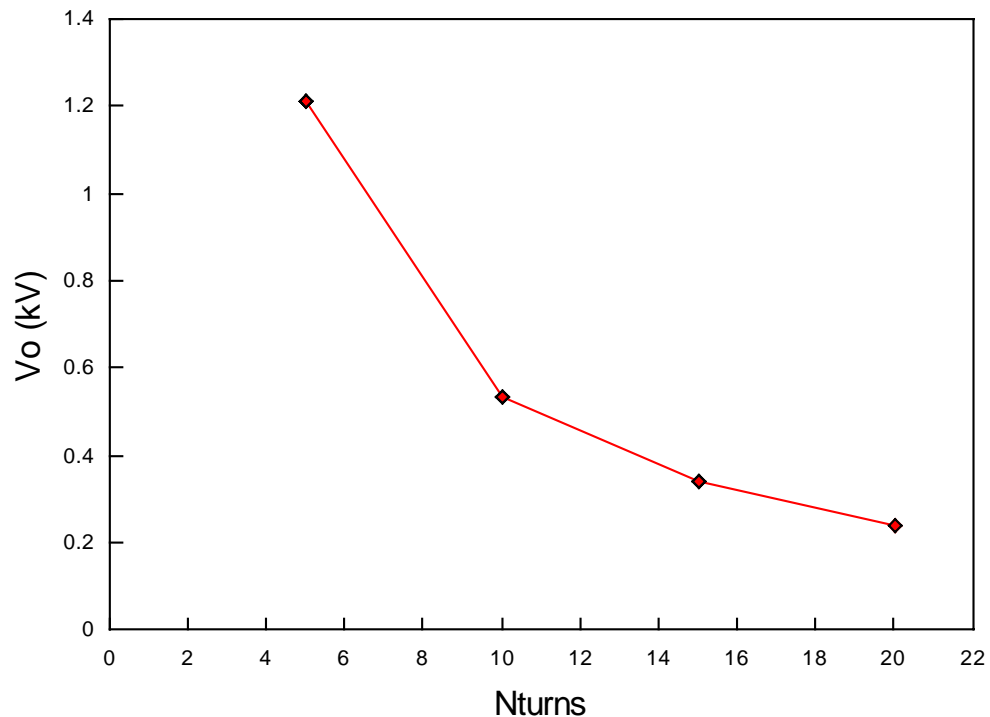


**Figure 38. Cavity voltage required for “optimal acceleration” vs. number of turns through the acceleration region of the 50 keV ICRA**

Keep in mind that since  $N_{\text{turns}} \propto 1/p_z$ , the information in Figure 38 could also be presented as  $V_o$  vs.  $p_z$ .  $N_{\text{turns}}$  was chosen here, only because the graph seems more intuitive. Figure 38 is a map of the operating parameters,  $V_o$  and  $p_z$ . Notice that for any operating point which is below the curve, the beam will not be fully accelerated. For any operating point above the curve, some portion of the beam will strike the wall.

The width of the peak of the  $E-\phi$  curve in Figure 37 has direct impact on how much beam current is accelerated by the ICRA. For an actual device using a dc injected beam, ions will enter the acceleration region at all phases. In the limit that the beam emittance goes to zero (central ray only), the fraction of the beam which is accelerated is simply the width of the  $E-\phi$  curve (above some chosen cutoff energy) divided by the full  $360^\circ$  range. For this reason, time is an important parameter in the beam phase space for determining what fraction of the beam is accelerated (see section 2.6.6).

At this point we must focus on a point that is more subtle, but also very central for understanding the ICRA. While the  $E-\phi$  curve does contain information about gross operating parameters, such as the cavity voltage ( $V_o$ ) and the  $N_{\text{turns}}$  setting, it also contains important implications on the full emittance beam which can be accelerated. Specifically, the range of  $(p_\perp/p_\parallel)$  must be small in order for significant current to be accelerated. To see why, consider the  $E-\phi$  curve shown in Figure 39 below. This time the cavity voltage ( $V_o$ ) is held constant and the initial ratio of  $(p_\perp/p_\parallel)$  is varied. Here we use the notation:

$$\alpha \equiv \frac{p_\perp}{p_\parallel} \quad (2.75)$$

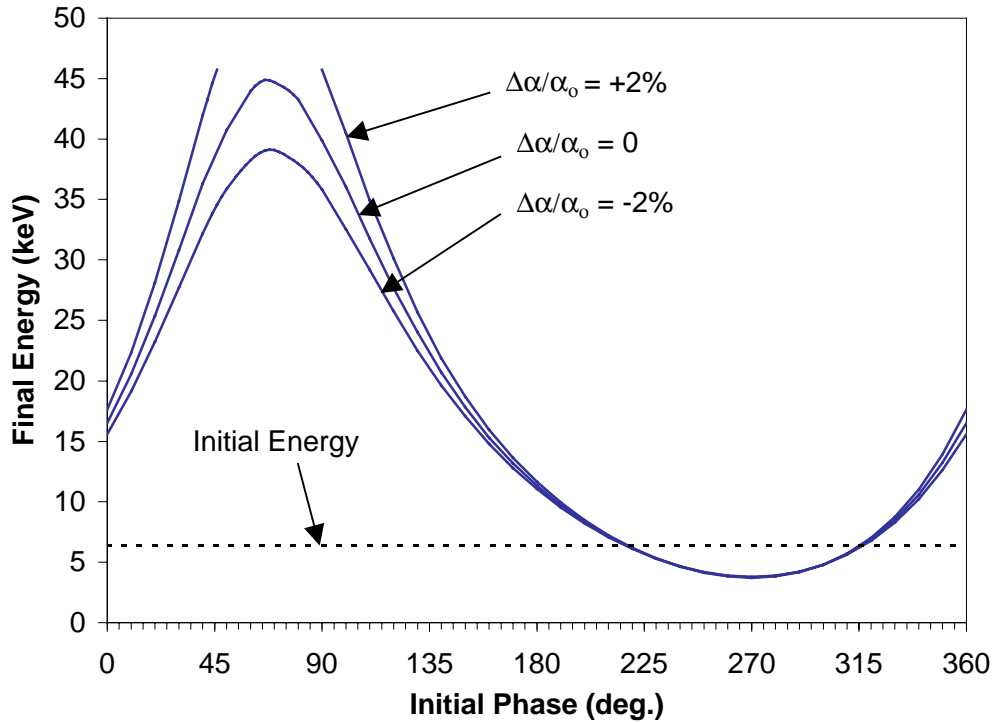


**Figure 39. Final proton energy vs initial phase for fixed  $V_0$  in the 50 keV ICRA. As  $\alpha$  is increased, the beam gains more energy and eventually strikes the wall. Here  $\alpha_0$  indicates  $p_{\perp}/p_{\parallel}$  of the central ray.**

Figure 39 clearly shows that as the initial ratio of  $\alpha$  is increased, the beam is accelerated to higher energies until it eventually strikes the wall. Recall that in the computer model all ions are injected at the same initial energy.

$$|\vec{p}|^2 = p_r^2 + p_{\theta}^2 + p_z^2 = \text{constant for all ions}$$

Therefore, increasing  $p_{\theta}$  decreases  $p_z$ , and vice versa. Here we see that acceleration in an rf driven magnetron causes radial defocusing. Any initial spread in  $\alpha$  leads to a radial spread and therefore a corresponding energy spread. To understand the source of the spread, consider two effects which determine how much energy the beam gains. Obviously, the beam will gain more energy if  $N_{\text{turns}}$  is high ( $p_z$  low) and less if  $N_{\text{turns}}$  is low ( $p_z$  high). This effect is then compounded by the radial dependence of the cavity

voltage. Throughout the trajectory, the ion whose radius fraction ( $r/R$ ) is high (large  $p_{\perp}$ ), sees a higher cavity voltage and moves to a higher ( $r/R$ ). On the other hand the ion with a lower radius fraction (smaller  $p_{\perp}$ ) sees a relatively lower cavity voltage, therefore it moves to a smaller ( $r/R$ ) relative to the first ion. These two coupled effects work together to cause the beam to gain more energy if  $(p_{\perp}/p_{\parallel})$  is high, and less energy if  $(p_{\perp}/p_{\parallel})$  is low. The result is that, the ICRA will accelerate maximum beam current to full energy when the beam entering the acceleration region has the minimum spread in  $(p_{\perp}/p_{\parallel})$ .

The radial defocusing is seen more clearly in Figure 40 below. Here the beam radius vs. axial position is plotted for the same three trajectories at the peak of the  $E-\phi$  curve in Figure 39 above. The ion with initial  $\Delta\alpha/\alpha_0 = +2\%$  strikes the wall, while the ion with initial  $\Delta\alpha/\alpha_0 = -2\%$  is not fully accelerated.

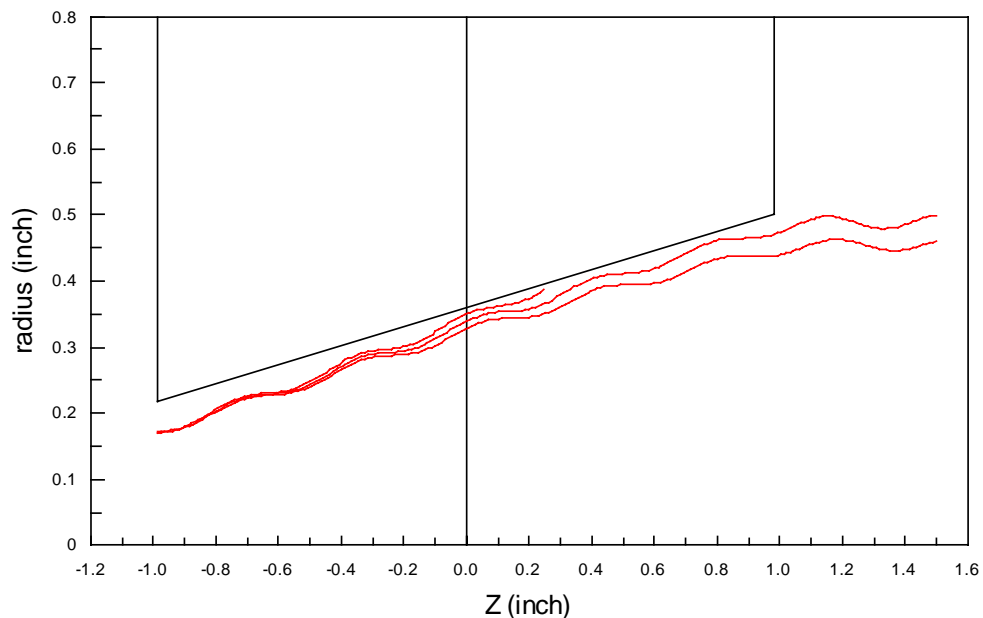


**Figure 40. Beam orbit radius vs z position for the three trajectories in Figure 39**

**with  $\phi_0=68^\circ$  and  $\Delta\alpha/\alpha = (+2\%, 0, \text{ and } -2\%)$ .**

### Phase Dependent Axial Momentum Change

In sections 2.5.5 and 2.5.6 of the analytical model, the axial momentum ( $p_z$ ) was assumed to remain constant through the acceleration region. In the absence of any axial forces, this would be the case. However, notice that in Figure 39 the maximum energy gain actually occurs at  $\phi_0 = 68^\circ$ , rather than  $\phi_0 = 90^\circ$ . This occurs because the taper of the cavity inner radius causes a change in the axial velocity which depends on phase. The beam which slows down axially, goes through more turns and therefore gains more energy.

It is not critically important for the reader to understand this effect because in practice we do not care which phase of the beam gets accelerated. However, since the magnitude of this effect does depend on the cavity slope, it is conceivable that this could place a limit on the maximum slope used. Therefore the effect is explained here.

Consider an ion orbiting in the counter clockwise ( $+\hat{\theta}$ ) direction as shown in Figure 41 below. For acceleration in the  $+\hat{\theta}$  direction the ion will always pass through an E-field just before each gap which has a component in the  $+\hat{z}$  direction, and an E-field just after each gap which has a component in the  $-\hat{z}$  direction. If the ion is in phase with the rf ( $\phi = 90^\circ$ ), then it receives an axial kick forward just before each gap, and backwards just after each gap, and the net change in the axial momentum is zero. However, if the ion lags the rf ( $\phi > 90^\circ$ ), then it will experience the maximum electric field just before passing the gap. Hence, its net change in axial momentum will be positive. Likewise, if an ion leads the rf ( $\phi < 90^\circ$ ), it will experience maximum electric field just after passing the gap, so it will have a net decrease in axial momentum. Figure 41 shows a schematic drawing which aids in visualizing the geometry. The decreased

axial momentum causes the ion which leads the rf to go through more turns and gain more energy. Obviously if the ion leads the rf by too much (for example  $\phi \rightarrow 0^\circ$ ), then the energy gain across each gap is reduced. The phase for peak energy gain ( $\phi = 68^\circ$  in this case) occurs for an optimum gain in  $N_{\text{turns}}$ , yet an insignificant degradation in  $K_{\text{gap}}$ .

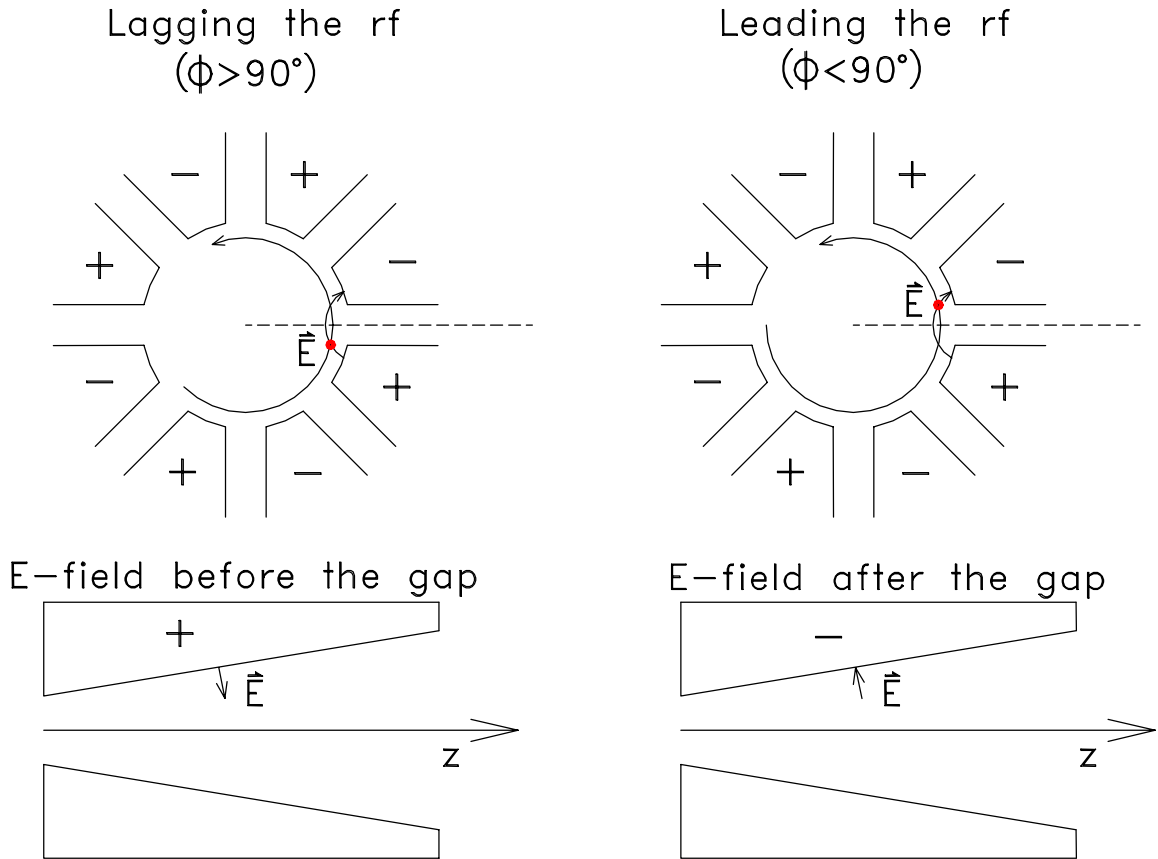


**Figure 41.** A snapshot in time of an ion (red dot) at the moment of peak electric field across the gap. Two cases are shown. On the left the ion lags the rf and on the right the ion leads the rf.

Figure 42 shows the evolution of the axial momentum through the acceleration region for three ions with initial phases  $\phi_0 = 60^\circ$ ,  $90^\circ$ , and  $120^\circ$ . The ion which leads the rf shows reduced  $p_z$  and the ion which lags the rf shows an increase in  $p_z$ . The magnetron cavity used here had 8 gaps. The small oscillations within each curve occur because the ion gets pushed forward then backward 8 times per turn.

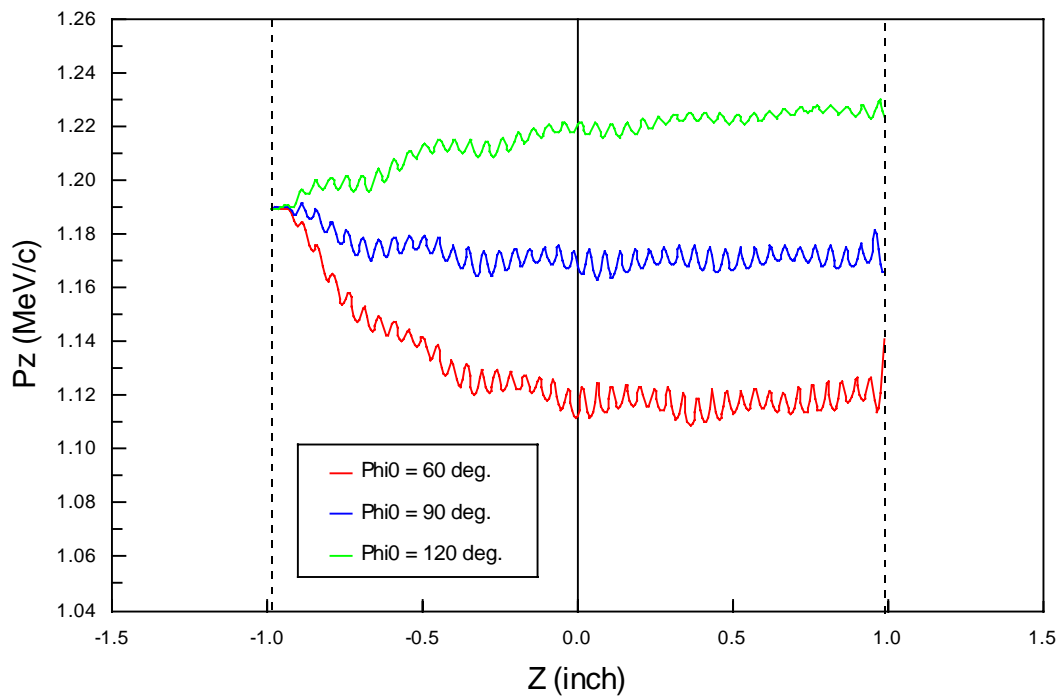


**Figure 42. Axial momentum through the acceleration region (rf on) for three different initial phases.**

## Phase Bunching

Using the computer model to track the phase through the acceleration region reveals a phase change which tends to bunch the beam near  $\phi = 90^\circ$ . The source of the phase shift is the radial component of electric field in the magnetron which causes a rotation in the motion of the orbit center. Figure 43 shows an example in which three ions started at three different phases each migrate towards  $\phi = 90^\circ$ . The oscillation in the phase occurs whenever the beam is off center from the accelerator center (acceleration always shifts the orbit center). Notice that the general trend is to bunch the beam near  $90^\circ$ . An additional view of the phase bunching with all computer modeling effects present can be seen in Figure 66 of chapter 3

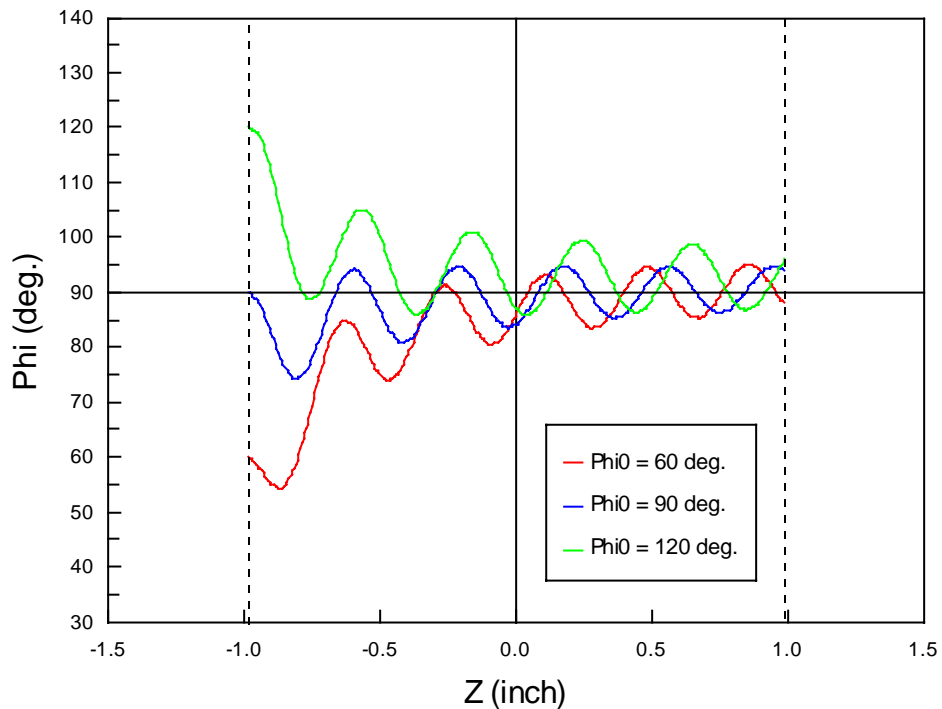


**Figure 43. Three ions are started with different initial phases. Tracking their phase through the acceleration region reveals phase pulling toward  $90^\circ$ . Notice the red line goes through the greatest number of turns and the green line goes through the fewest turns.**

A more global view of this effect can be seen by plotting the final phase after acceleration vs. the initial phase when entering the cavity for the full range of initial phases. Figure 44 shows the result. If no phase bunching occurred, then the final phase would be equal to the initial phase. A black line with slope = 1 has been plotted to show this case. However, results using the computer model (red line) show that a wide range of initial phases migrate toward  $\phi = 90^\circ$ .

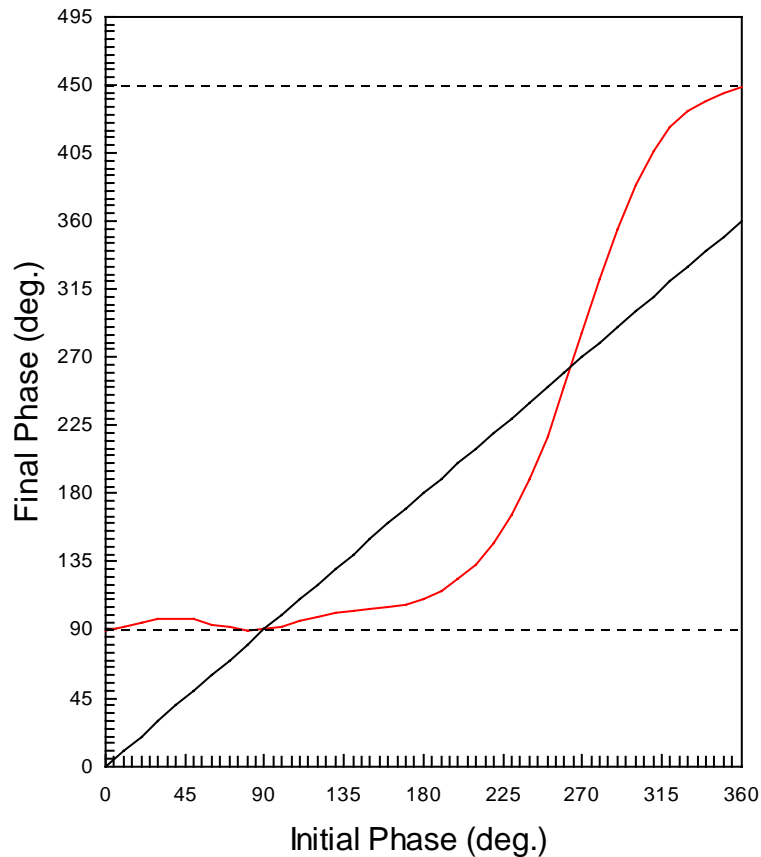


**Figure 44. The red line shows final vs. initial phase of protons accelerated through the magnetron. (50 keV ICRA design). The solid black line represents final phase equal to the initial phase. Dotted lines have been placed at  $\phi=90^\circ$  and  $\phi=(360^\circ+90^\circ)$  for comparison.**

### 2.6.3 Cavity End Field Effects

Just before entering the acceleration region, the injected beam will pass through the electric end fields of the magnetron. These end fields are accounted for in the computer model because in the 3D solution of the electric fields (using RELAX3D) the magnetron has finite axial length, and ground plates are placed one cm away from each end. Allowing an ion to travel through the end fields before entering the acceleration region causes two effects. Both effects are relatively insignificant. They are mentioned here for completeness. All trajectories in this section use a constant magnetic field so that the effects of the end fields can be isolated.

The first effect is a small additional energy gain through the end field region. This causes the beam to enter the magnetron at a slightly higher energy. Therefore, since the peak energy is limited by the inner diameter of the accelerating cavity, the voltage must be decreased so that the ion does not hit the wall. Figure 45 shows an  $E-\phi$  curve which compares a beam that has passed through the end fields, with the beam that did not pass through the end fields. The cavity voltage was held constant in each case, so the small additional energy gain through the end fields sets the beam on a different trajectory towards a much higher energy gain.

The second effect is a shift in the optimum initial phase. This occurs because the end fields, just before entering the magnetron, have large  $z$  components. If an ion lags the rf ( $\phi > 90^\circ$ ), then the ion will experience the peak electric field just before it passes the gap. On the other hand if the ion leads the rf ( $\phi < 90^\circ$ ) then it will experience the peak electric field just after passing the gap (review Figure 41). In the end field region, the electric field just before the gap has an axial component in the  $-z$  direction,

but the E-field just after the gap has an axial component in the  $+\hat{z}$  direction. Therefore, the ion which lags the rf ( $\phi > 90^\circ$ ) will have a net decrease in axial momentum ( $p_z$ ) and therefore gains more energy than the ion which leads the rf.

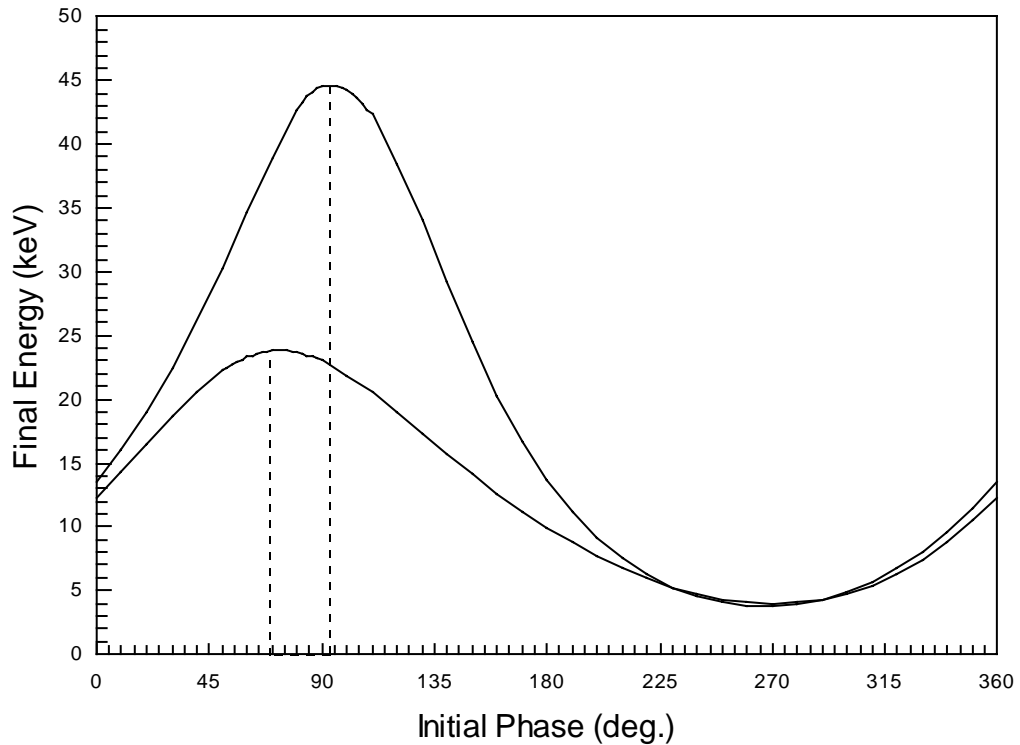


**Figure 45. Final proton energy vs. initial phase for a fixed  $V_0$  in the 50 keV ICRA.**

**The beam which passes through the end fields before entering the cavity shows a higher energy gain and a shift in optimum initial phase.**

Figure 46 shows the change in axial momentum through the end fields and acceleration region. The acceleration region is between the dotted lines. The particle moves from left to right so the entrance end fields are in the region to the left of the acceleration region. Although the ion with  $\phi_0 = 60^\circ$  has decreasing  $p_z$  in the acceleration

region, it is the ion with  $\phi_0 = 120^\circ$  which has decreased axial momentum through the entrance end fields.

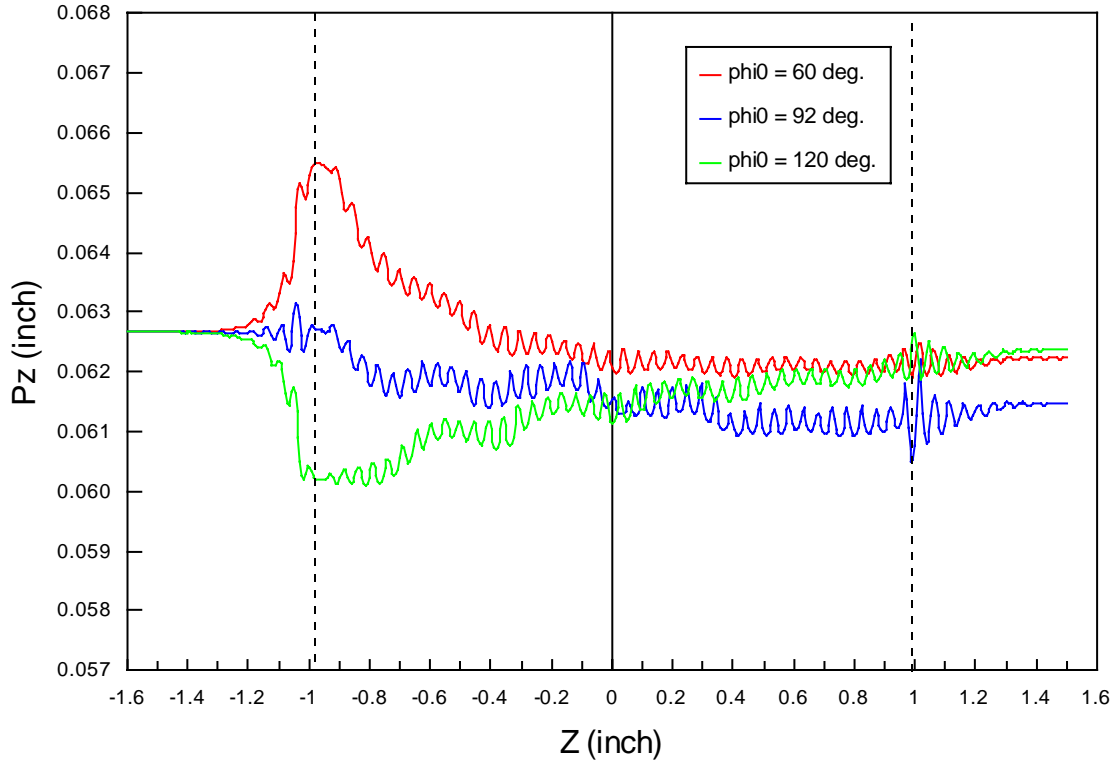


**Figure 46.** The ion with initial  $\phi > 90^\circ$  gets a decrease in  $p_z$  through end fields, but the ion with initial  $\phi < 90^\circ$  gets an increase in  $p_z$ . The particle moves left to right. The acceleration region is between the dashed lines. The entrance end fields are just to the left of the acceleration region.

End fields at the exit side of the acceleration region cause a similar additional energy gain, however the effect is less significant since the beam is now at high energy.

Notice the large oscillation in  $p_z$  caused by the exit fields in Figure 46. The net axial momentum change ( $\Delta p_z$ ) caused by the exit end fields is not significant because phase bunching (section 2.6.2) through the acceleration region causes ions to have phase near  $90^\circ$ .

## 2.6.4 Magnetic Field and Phase

From this point forward in this chapter, a realistic magnetic field is used in the computer model (either solenoidal or Helmholtz). This section discusses phase changes caused by the B-field profile over the acceleration region. The characteristics of Helmholtz and solenoidal fields were discussed in section 2.1. The full off axis solution of magnetic fields was discussed in section 2.6.

Recall that the magnetic field flatness is characterized in terms of the drop at the ends of the acceleration region ( $\delta B$ ). B-field flatness criterion was defined in section 2.5.7, and the field profile over the acceleration region of the 50 keV ICRA was shown in Figure 34.

Using a realistic field introduces a phase drift anywhere where  $n\omega_c \neq \omega_{rf}$ . In the ICRA it is useful to plot phase vs. axial position. Figure 47 shows  $\phi$  vs.  $z$  as the ion accelerates through the magnetron. Notice that the oscillation in phase has one cycle per turn. This occurs because acceleration at each gap pushes the center of the beam around, and whenever the beam is off center there is a corresponding oscillation in the phase. This effect is well known in cyclotrons. The phase oscillation is of no great consequence, although it should be minimized by centering the beam.

More important is the overall phase drift caused by regions where the B-field is not in resonance with the rf frequency. Whenever the B-field is low ( $n\omega_c < \omega_{rf}$ ), equation 2.81 (section 2.5.7) predicts that the phase will increase in time. The reader should compare the phase diagram in Figure 47 with the B-field profile shown in Figure 34 to see that the phase drift past the ends of the cavity makes sense.

**Figure 47. Phase vs. axial position over the acceleration region.**

Phase graphs like the one in Figure 47 are useful for checking that the beam remains in resonance and will be particularly important when designing an ICRA with a sloped B-field for acceleration to relativistic energies.

The addition of the realistic magnetic field over the entire volume of the accelerator allows particles to be shot through the entire system from ion source to target. A set of complete single particle trajectories is shown in the following section.

## 2.6.5 Complete Single Particle Trajectories

The previous three sub-sections (2.6.2 – 2.6.4) covered the complete computer model, starting from acceleration through the magnetron in a flat magnetic field, and then adding end fields of the magnetron and a realistic solenoid. Section 2.6.6 will begin discussion of multi-particle trajectories used to model a beam of finite emittance. However, before leaving single particle trajectories, we wish to show a series of views of the beam. In this section the electrostatic bending plates have been added, so that all realistic fields are now in place. The figures which follow show several examples of single particle trajectories shot through the entire system using the ICRA computer model.

List of views:

Fig 48. top and side view - mirroring beam – rf off

Fig 49. top and side view - Nturns =  $\infty$  – rf off

Fig 50. Axial view - Nturns =  $\infty$  – rf off

Fig 51. top and side view – Nturns = 20 – rf off

Fig 52. top and side view – Nturns = 5 – rf off

Fig 53. top and side view – Nturns = 5 – rf ON

Fig 54. Axial view – acceleration region only – rf ON

Total of 14 pages required for 7 captions and 7 Figures

Caption for Figure 48 goes here

Figure 48 goes here

Caption for Figure 49 goes here

Figure 49 goes here

Caption for Figure 50 goes here

Figure 50 goes here

Caption for Figure 51 goes here

Figure 51 goes here

Caption for Figure 52 goes here

Figure 52 goes here

Caption for Figure 53 goes here

Figure 53 goes here

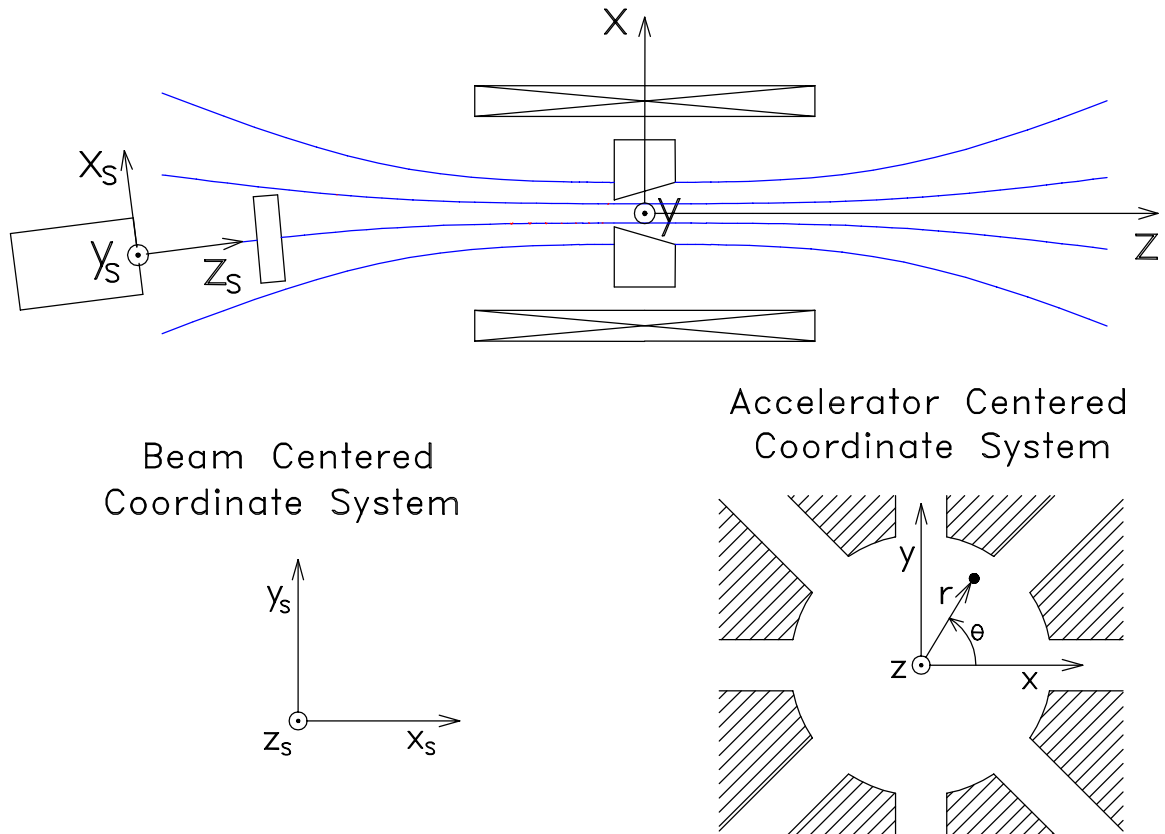
Caption for Figure 54 goes here

Figure 54 goes here

### 2.6.6 Acceptance Phase Space of the RF Driven Magnetron

Any serious analysis of the maximum amount of current that could be accelerated by an ICRA, must be based on an understanding of the acceptance phase space of the acceleration region used. The acceptance phase space can be mapped out by using ICRAcyclone to start particles at the entrance plane of the magnetron, then accelerating each particle, and tabulating their final energies. The initial conditions of each trajectory are varied over some range in order to map out the boundaries of the phase space of the beam which is accelerated to the desired energy. Since the ICRA accelerates beam to some large energy spread, a cutoff energy must be chosen as a criterion for an acceptably accelerated beam. Obviously if you choose  $E_{\text{cut}} = 0.9 E_{\text{max}}$  the acceptance phase space will be smaller than if you choose  $E_{\text{cut}} = 0.5 E_{\text{max}}$ .

It may be tempting to describe this phase space in terms of Cartesian variables ( $x, y, z, p_x, p_y, p_z, t$ ), but attempts at this have proven to be futile. The natural coordinate system for the magnetron cavity in an axial B-field is cylindrical. Therefore, the acceptance phase space must be mapped in  $(r, \theta, z, p_r, p_\theta, p_z, t)$  using a coordinate system whose origin is at the center of the magnetron. This “accelerator-centered coordinate system” is shown in Figure 55. To see why this is true, imagine that you have just run the trajectory for some chosen central ray, then you change the initial position of the particle by  $\Delta y$  to see the effect on the final energy. In doing this, the initial conditions of the particle have actually changed, by  $r$  and  $\theta$  both. As we will see, the acceptance phase space does depend on  $r$  but it does not depend on  $\theta$ , therefore in changing  $y$ , you have missed the azimuthal symmetry.



**Figure 55. Initial particle coordinates at the ion source are expressed in a Cartesian coordinate system centered on the central ray, but the acceptance phase space at the entrance plane of the magnetron must be expressed in an accelerator-centered cylindrical coordinate system.**

Before proceeding, four cautionary statements are given here:

- 1) Once the initial acceptance phase space of the magnetron has been mapped out, that does not necessarily mean that a beam can be produced to fill that space. In fact a large source of optimization for the ICRA is in tailoring a beam to fill the desired phase space as much as possible.
- 2) The method used here to relate the injected beam to the acceptance at the entrance plane of the magnetron, was to choose an emittance back at the ion source, then shoot each particle from the ion source, forward through the fringe fields, and stop the beam at the entrance plane of the magnetron. When doing this, the initial coordinates of each

particle at the ion source should be expressed in a Cartesian coordinate system with the origin at the central ray of the beam as shown in Figure 55. The coordinates of each particle can then be expressed in the cylindrical accelerator-centered system so that the beam can be shot forward, then stopped at the entrance plane of the magnetron, and compared with the acceptance plots to determine the fraction of particles that landed inside the acceptance phase space.

3) And finally, notice that it is not necessary to map out the acceptance phase space.

It is only a tool for comparing what beam the injection region produces with what beam the magnetron could accelerate if that beam could be produced. The accelerated fraction of the beam can also be determined by completely bypassing this pit stop and simply running particle trajectories through the entire system.

#### Results of the analysis of the acceptance phase space.

In order to map out a 7 dimensional coupled phase space ( $r, \theta, z, p_r, p_\theta, p_z, t$ ) we first scan over one variable at a time to see its effect. Those parameters whose effects are negligible are then dropped. Three variables can be eliminated. The effect of  $\theta$  is negligible, and  $z$  was chosen to be constant at the entrance plane of the magnetron.

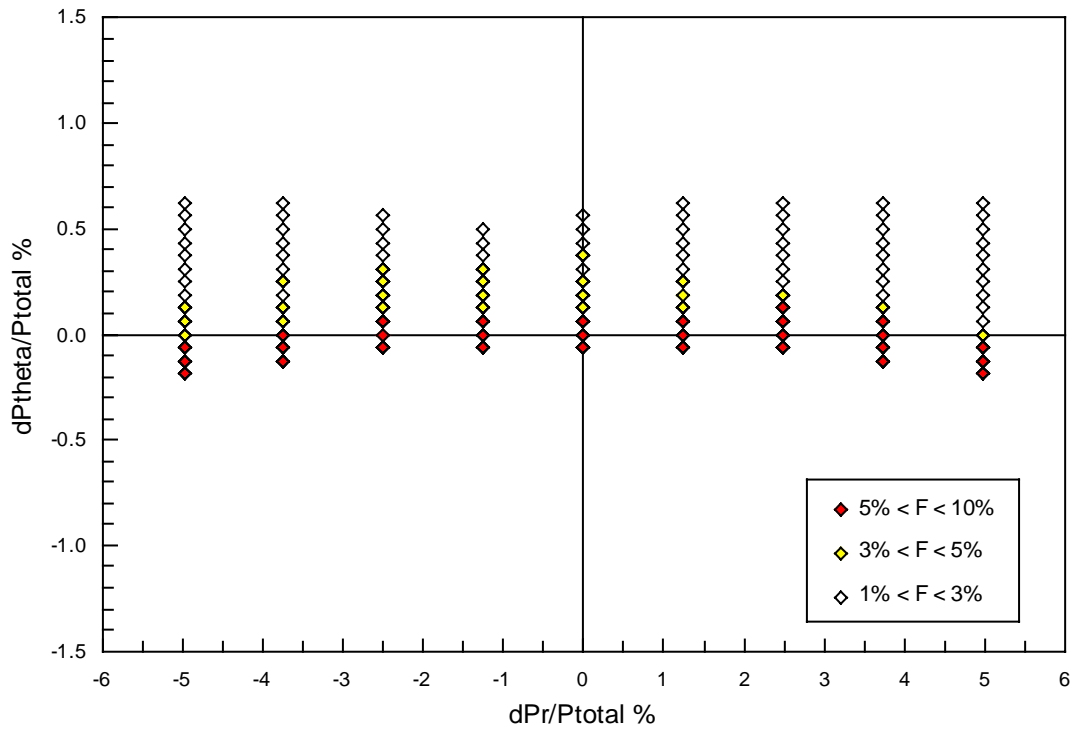
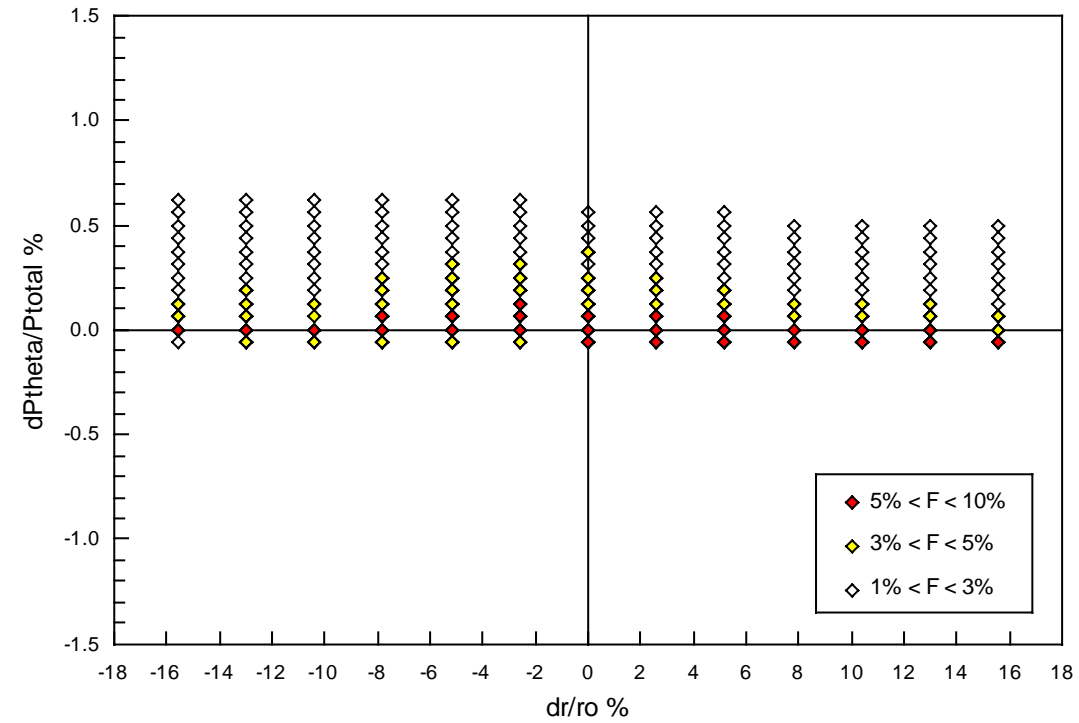
One momentum can be eliminated because all ions in the computer model begin with the same energy, therefore  $p_z, p_\theta$  and  $p_r$  are not independent. Thus mapping all three would be redundant. The arbitrary choice was made to drop  $p_z$ , therefore the relevant phase space parameters become:  $r, p_r, p_\theta$ , and time (or  $\phi_0$ ). We already know that the accelerated beam depends on rf phase (review section 2.6.2) and we must sum over the

full  $0^\circ - 360^\circ$  phase range because the injected dc beam will contain all phases. Scanning each of the remaining three parameters independently shows that the acceptance phase space is very sensitive to  $p_\theta$ , and only moderately sensitive to  $r$  and  $p_r$ . Recall the discussion of the spread in  $(p_\perp/p_\parallel)$  in section 2.6.2

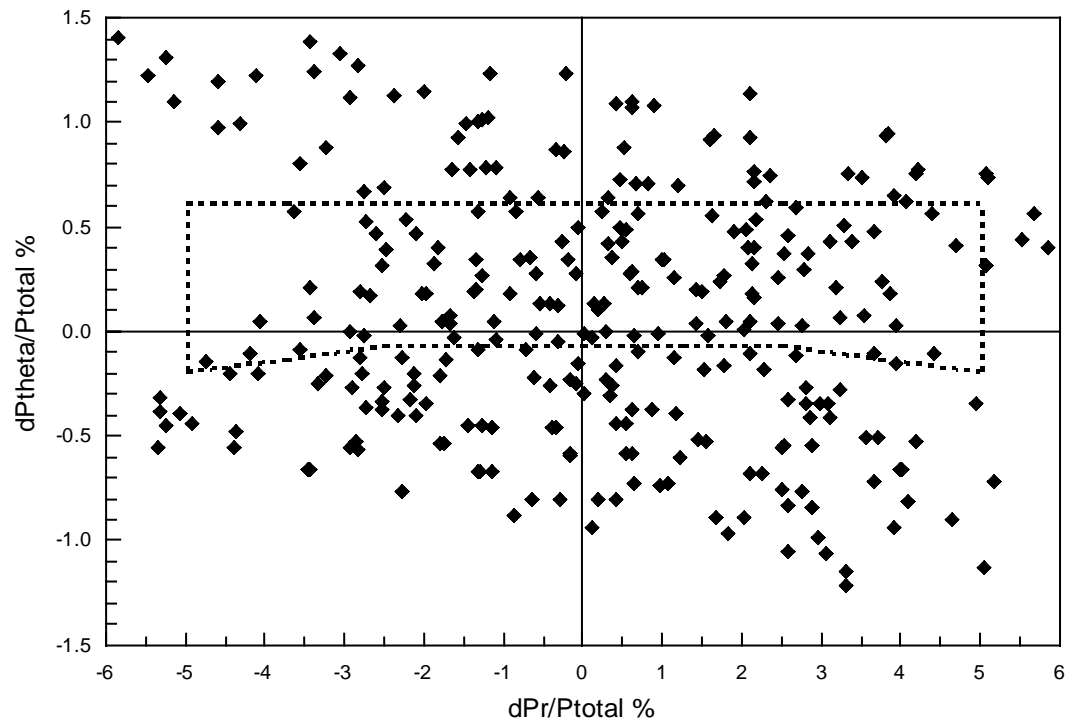
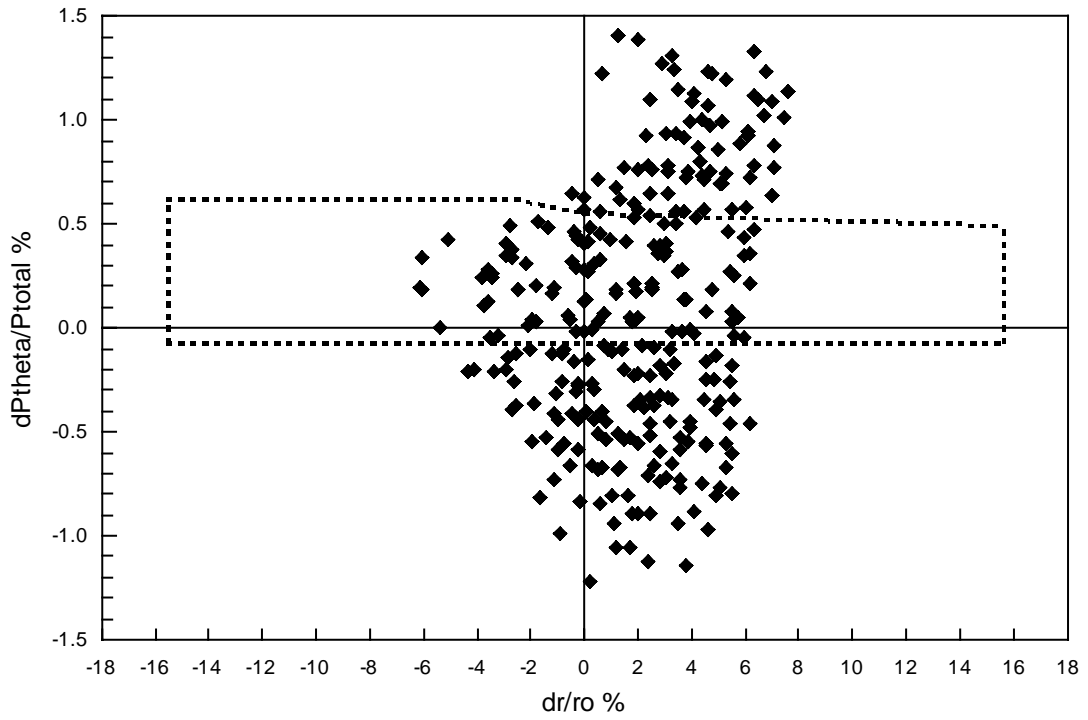
Figure 56 shows the results of scans over two planes through the remaining three dimensional phase space volume. These are  $\Delta p_\theta$ , vs.  $\Delta r$ , and  $\Delta p_\theta$ , vs.  $\Delta p_r$ . Here  $\Delta$  indicates a change relative to the central ray. Each data point on the graph includes a summation over all rf phases. In other words each point represents the width of the  $E-\phi$  curve of Figure 39 for a cutoff energy of  $E > 0.9 E_{\text{design}}$ . Thus if a beam of zero emittance was placed at one of the red data points, then the fraction accelerated would be between 5% - 10 % (see the legend of Figure 56).

Figure 57 shows the final positions of particles tracked from the ion source, forward through the injection region, and stopped at the entrance plane of the acceleration region. For comparison, the boundary of the acceptance phase space is outlined with a dotted line in Figure 57. The beam outside this boundary is not accelerated above the cutoff energy. Notice that the injected beam has a wider  $p_\theta$  spread, and a narrower radial spread, than what the magnetron will accept. This tendency occurs because the injection trajectory causes a decrease in the radial spread of the beam, and an increase in the momentum spreads ( $\Delta p_\theta$ , and  $\Delta p_z$ ). This is explained at the end of section 2.5.2.

This particular result was for an 8 Tesla, 1 MeV proton design. The injected beam had an emittance of  $2\pi$  mm mrad (unnormalized) and the fraction accelerated above 0.9 MeV was 1.9 %.



**Figure 56. Two planes through the acceptance phase space at the entrance plane of the magnetron for a 1 MeV proton ICRA. Each data point represents a summation over all rf phases.**



**Figure 57. Final positions of protons shot forward from the ion source through the injection fringe fields and stopped at the entrance plane of the magnetron.**

The acceptance phase space from Figure 56 is outlined with dotted lines for comparison.

### 2.6.7 Injected Beam Emittance

This section deals with characteristics of the injected beam only. Although the beam will pass through the injection, acceleration, and extraction regions, the rf power in the accelerating cavity is off for all cases. All trajectories in this section are tracked from the ion source, through the electrostatic bend, and through the realistic magnetic field.

A beam of some finite emittance can be modeled by using ICRAyclone to run many single particle trajectories, one after another. Recall that ICRAyclone does not account for space charge effects (section 2.6.1). Initial conditions for each particle back at the ion source are expressed in a Cartesian coordinate system with the origin at the central ray of the beam (see Figure 55 section 2.6.6). The 4 transverse phase space dimensions are  $x_s, x'_s, y_s, y'_s$ , where  $x'_s = p_{xs}/p_{total}$  is simply the slope of a particular ray relative to the central ray. In the plots which follow, the injected beam emittance was modeled by a fully coupled set of  $3 \times 3 \times 3 \times 3 = 81$  particles. The  $(x_s, x'_s)$  and  $(y_s, y'_s)$  planes are shown in Figure 58.

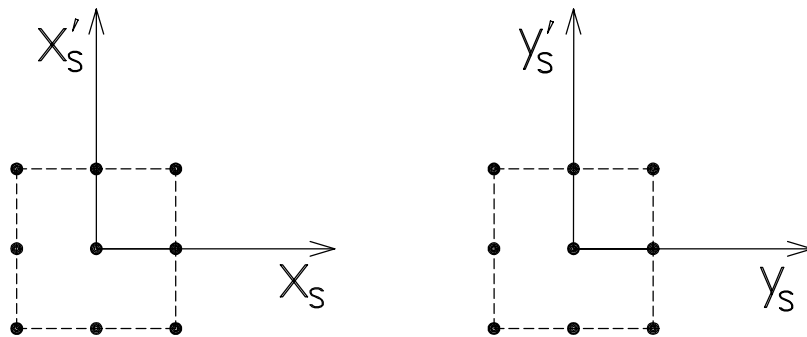


Figure 58. The emittance used at the ion source is a coupled phase space of  $3 \times 3 \times 3 \times 3 = 81$  particles

In section 4.5.3 we will see that the axial momentum spread of the beam ( $\Delta p_z$ ) can be measured experimentally in two ways; the arc length at the extraction end, and the mirror curve (both discussed below). These measurements can be reproduced using the computer code and used to determine whether the beam emittance has been chosen correctly.

#### Arc Length at the Extraction Faraday Cup

The extraction Faraday Cup (EXFC) is a phosphor screen that is used for viewing the beam at the far downstream extraction end of the 50 keV experiment. The EXFC is oriented perpendicular to the z axis so the image seen is in an x-y plane. The reader may want to look ahead to Figure 72 in Section 3.2. If the beam were a single particle trajectory, one would expect to see the beam hit at a single point on the extraction Faraday cup. However, for a real beam, any spread in the axial momentum causes the image on the extraction Faraday cup to spread in the  $\theta$  direction. This spread ( $\Delta\theta$ ) is referred to here as the “arc length”.

In order to check the arc length in the computer model, the full emittance of 81 particles was tracked from the ion source, through the entire system, to the z plane of the extraction Faraday cup. The x-y positions are then plotted. An example is shown in Figure 59.

It is simple to see how a spread in axial velocity causes the image of the beam to smear out in  $\theta$  if the magnetic field were constant. However, the solenoidal fringe fields in the extraction region of the ICRA are certainly not constant. Therefore, it is necessary to check whether the arc length is a good measure of the spread in axial momentum at  $z=0$ . This was done by using the computer code to track the full emittance beam from the

ion source, through the entire system, to the extraction Faraday cup. The axial momentum of each ion was obtained at  $z=0$  as the ion passed through the center of the system. Then the final angle of each ion on the extraction Faraday cup is plotted vs.  $1/p_z$ . The results in Figure 60 below show that the relation between  $1/p_z$  and  $\theta$  is extremely linear even with the solenoidal field. Therefore, the arc length is a direct measure of  $\Delta p_z$ .

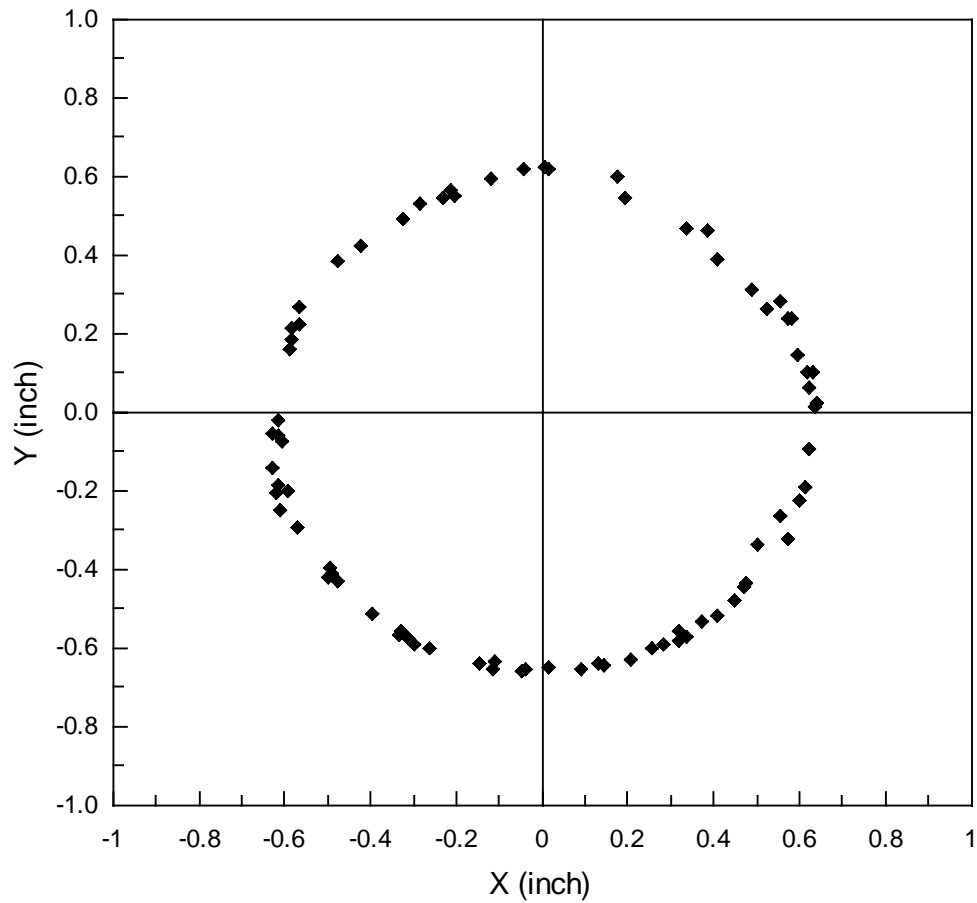


**Figure 59. Final x, y positions of protons on the extraction Faraday Cup after being shot from the ion source through the entire system.**

**Here the bending voltage is high enough to give an arc length of more than 360°.**

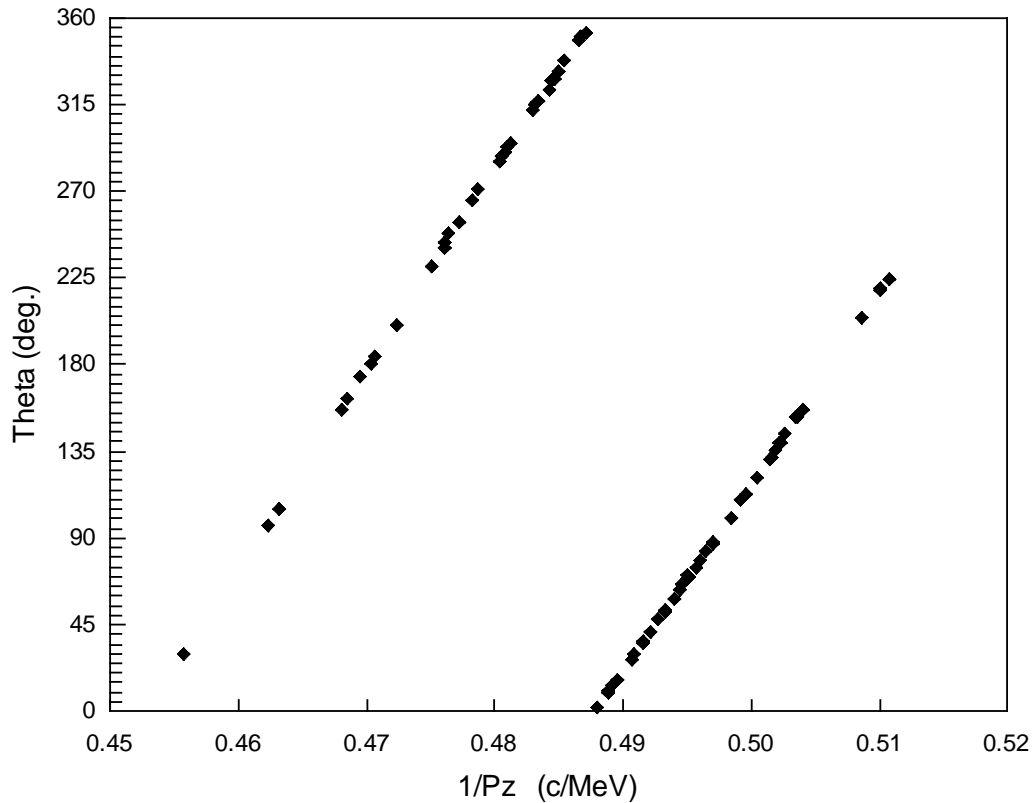


**Figure 60.** Final  $\theta$  position of protons on extraction Faraday Cup vs their axial momentum at  $z=0$ .

### Mirror Curve

The second useful experimental measurement of  $\Delta p_z$  is the mirror curve. Experimentally, beam current on the extraction Faraday cup is measured while the bending voltage is increased. If the spread in  $p_z$  were zero, then the axial momentum would continue to decrease until the mirror angle is reached at which point the current reaching the extraction end would instantly drop to zero (section 2.5.3). On the other hand, if the beam contains a spread in  $p_z$ , then different components of the beam will mirror at different bend voltages. This causes the beam current to drop over some finite range of bending voltage. The plot of current vs. bend voltage is called a “mirror curve”

The mirror curve can be reproduced with the computer model by first selecting an injection emittance, then tracking all particles through the entire system. The number of ions which arrive at the extraction Faraday cup are plotted as a function of bend voltage. An example is shown in Figure 61.

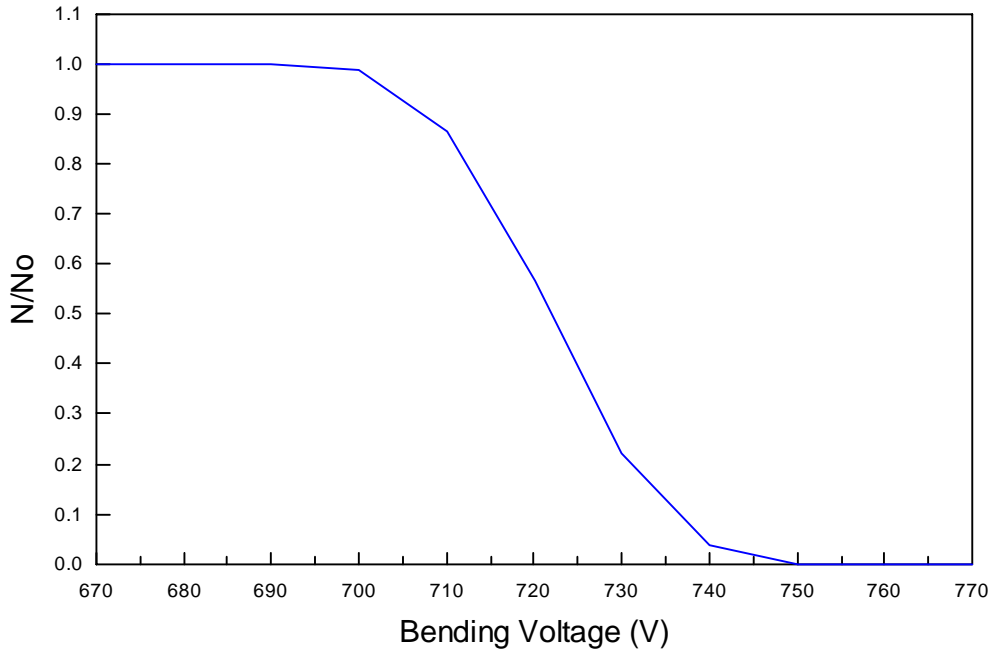


**Figure 61. A mirror curve generated using ICRAcyclone. The fraction of particles, which reach the extraction Faraday cup without being mirrored, is plotted vs. bend voltage.**

In order to check whether the mirror voltage is a good measure of axial momentum at  $z=0$ , an entire emittance was tracked through the system for one constant bend voltage, and the value of  $p_z$  for each particle is obtained as it passes  $z=0$ . Then the mirror voltage of each particle is obtained and plotted vs.  $p_z$  at  $z=0$ . Figure 62 shows that the result is fairly linear, indicating that mirror voltage also is a good measure of the axial momentum at  $z = 0$ .

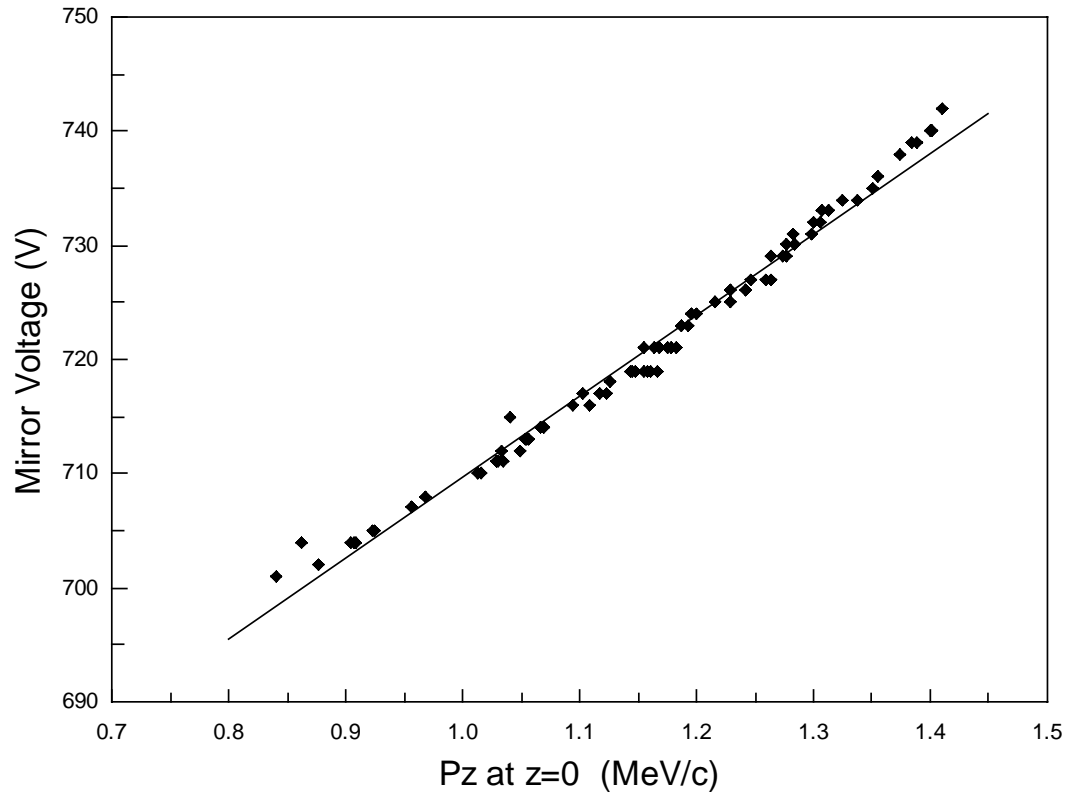


**Figure 62. Mirror voltage of 81 protons vs. their axial momentum at  $z=0$  at  $V_{\text{bend}} = 690$  V.**  
**The solid line is included for visual comparison with linear.**

## 2.6.8 Energy Distribution of the Accelerated Beam

All trajectories in this section are tracked from the ion source through the entire system with rf on. The injected beam emittance used is the one shown in section 2.6.7.

A fully coupled emittance of  $3 \times 3 \times 3 \times 3 = 81$  particles is shot through the system for every 2 degrees in phase. After the full emittance beam is accelerated, the number of particles at each energy are counted and the percent of particles is plotted vs. energy. Figure 63 shows the result. Here  $V_{\text{bend}} = 700\text{V}$  which corresponds to  $N_{\text{turns}} \cong 11$ .

The large energy spread is a basic characteristic of the ICRA because nearly all of the beam (except what strikes the wall) drifts through the accelerating cavity whether it is accelerated or not. Specifically two factors cause the spread. First, since the dc injected beam contains ions over the full range of rf phase, even part of the beam near  $\phi = 270^\circ$  which is decelerated still contributes to the energy distribution curve. Second, the radial defocusing discussed in section 2.6.2 causes an energy spread in the accelerated portion of the beam.

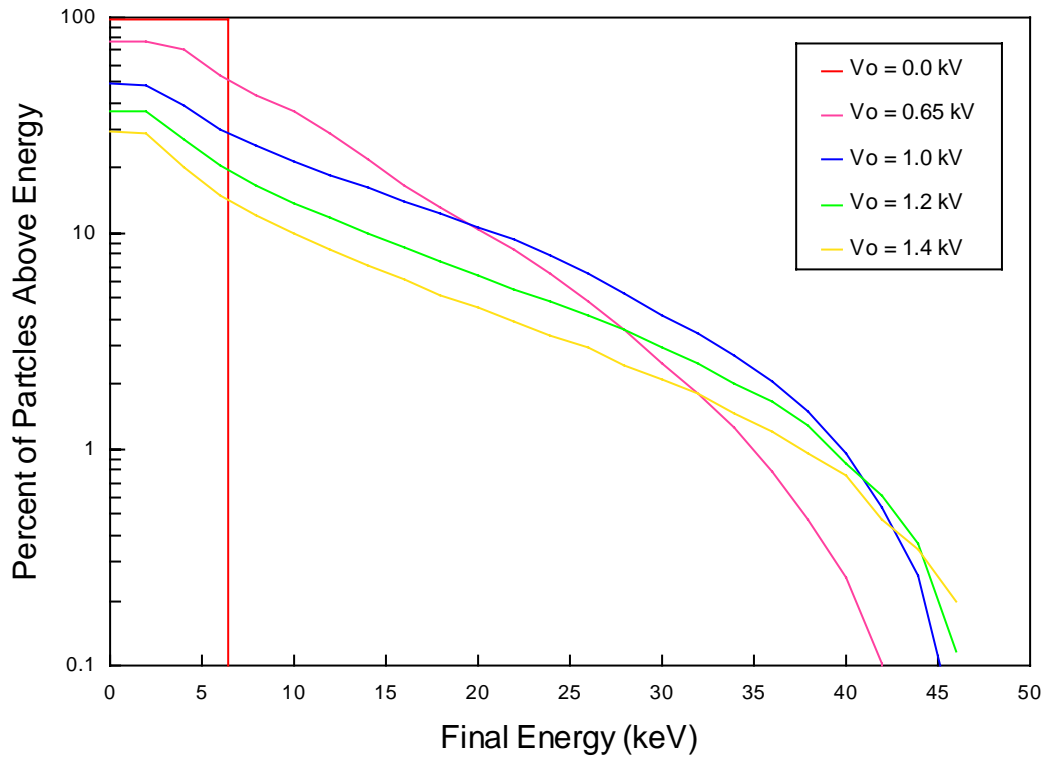


**Figure 63. An integrated Energy distribution for the 50 keV ICRA generated using the computer model. Emittance of the injected beam was  $2.2\pi$  mm mrad.**

Figure 63 is an integrated distribution, meaning that any point on the curve represents the percentage of particles accelerated above a given energy. Thus, if zero particles hit the wall, then the number of particles above  $E = 0$  would be 100%. Notice where the curves intersect the percent particles axis ( $E = 0$ ). Figure 63 shows that for  $V_o = 1.0$  kV, the current above  $E=0$  has dropped to 50%, meaning that 50% of the particles were intercepted by the cavity wall. As the cavity voltage is increased, the beam current at high energy increases (right hand side increases), but also more of the beam strikes the wall (left hand side of the curve drops). Thus, for any cutoff energy

chosen, the beam current will pass through a maximum. The curve in Figure 64 shows the peak in the current for ions accelerated above 42 keV.

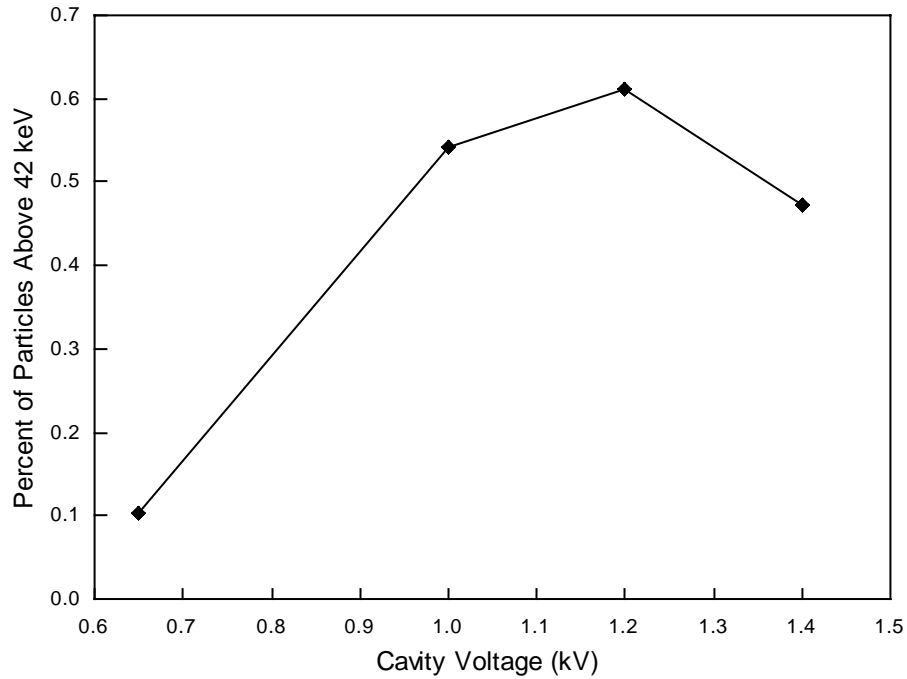


**Figure 64.** Scanning over cavity voltage shows a peak in the beam current accelerated above a given energy. Emittance of the injected beam was  $2.2\pi$  mm mrad. Data generated using the computer model for the 50 keV ICRA design .

## NEED THIS FOR RESONANCE WIDTH

Notice that if  $\omega_{rf} = n\omega_c$  the phase will remain constant at all times, however if  $\omega_{rf} \neq n\omega_c$  then the phase will drift with time.

Consider the case where the rf frequency is fixed at  $\omega_{rf} = n\omega_{co}$  but the B-field (constant with respect to z) is allowed to change by  $\Delta B$ , then equation XXX gives:

$$\Delta\phi(t) = [n\omega_{co} - n(\omega_{co} + \Delta\omega_c)]t$$

In terms of the variation in B-field this becomes:

$$\Delta\phi(t) = n\omega_{co} \frac{\Delta B}{B} t$$

Here  $\Delta\phi$  is the total change in phase over the time, t, caused by  $\Delta B$ . This equation is valid for any time (t). However, if we want the phase change over the time the ion spends in the accelerating cavity, it is useful to express  $\Delta\phi$  in terms of the number of turns in the cavity length. Using:

$$N_{\text{turns}} = \frac{t_{\text{cav}}}{\tau_{\text{co}}} = f_{\text{co}} t_{\text{cav}}$$

we obtain:

$$\Delta\phi(t) = 2\pi n \frac{\Delta B}{B} N_{\text{turns}} \quad \text{in radians}$$

or:

$$\Delta\phi(t) = 360^\circ n \frac{\Delta B}{B} N_{\text{turns}} \quad \text{in degrees}$$

These equations describe the phase change that occurs if the B-field is constant (no z dependence), but is de-tuned away from resonance with the rf frequency. And for the case where acceleration does not cause phase pulling. At the end of this section we will

see that acceleration in the magnetron does cause phase pulling. These equations are also needed for section XXX on resonance width.

Some beam hits  
the wall

Beam not fully  
Accelerated

With End Fields

Without End Fields

Move this to chapter 3

Recall that the magnetic field flatness is characterized in terms of the percent drop at the ends of the acceleration region ( $\delta B$ ). B-field flatness criterion defined was defined in section 2.5.7, and the field profile over the acceleration region was shown in Figure 34. For the case of a 1 MeV design, the computer model was used to study several values of B-field variation and it was found that for  $N_{\text{turns}} = 10$ ,  $\delta B < 0.5\%$  induced an insignificant degradation in the final energy of the beam. Obviously for a higher number of turns the B-field flatness criterion will be more stringent.

From the energy distribution section

**I need to vary the resolution of each variable to see which ones make a difference. Maybe phase does not need to be every 2 degrees. or maybe I get different results if I increase x from 3 particles to 10. I should use the resolution that gives consistent results.**

### **Not used**

After we add realistic B-field the phase will slip all the way through the injection region, therefore the value of the initial phase becomes meaningless.

### Centering Effect

It seems intuitive that the radial dependence of the cavity voltage would cause a centering effect. This is because if the beam is initially off center, it receives a biggest kick where it passes closest to the wall and a smaller kick where it passes further from the wall. Since each kick shifts the orbit center in the  $\vec{E} \times \vec{B}$  direction, the net force should push the orbit center toward the center of the cavity. In other words, since the cavity voltage is maximum at the cavity wall ( $r = R$ ) and goes to zero at the center ( $r = 0$ ), the voltage profile effectively acts like a potential well. In fact, a simple spread sheet model for a two gap magnetron ( $n = 1$ ) can be made which tracks the orbit center as it oscillates back and forth in one dimension only. This simple model shows that the magnetron does exhibit the centering effect as expected. However, if a magnetron has more than 2 gaps, the centering effect is destroyed. The additional gaps, in the direction perpendicular to the direction that the beam is off center, have a radial electric field which pushes the orbit center back to its original location. Hence, for magnetrons with 4, 6, 8... gaps the

centering effect is nulled out. Results from the computer model for the 50 keV ICRA ( $n = 4$ ) show no significant centering effect. Except for some small oscillations, the orbit center remains pretty much frozen to magnetic field lines at its original location.

The computer model shows that acceleration through the rf driven magnetron causes a centering effect which pushes orbit centers toward the z axis. Consider an ion moving in an orbit which is centered on the z axis. The orbit radius in terms of energy is:

$$r = \frac{p_{\perp}}{qB} = \frac{\sqrt{2mE}}{qB}$$

If the ion receives an instantaneous kick in the  $\hat{\theta}$  direction, the orbit radius will increase

by:

$$\Delta r = \frac{\sqrt{2m}}{2qB} \frac{\Delta E}{\sqrt{E}}$$

or simply

$$\frac{\Delta r}{r} = \frac{\Delta E}{E} = \frac{K_{\text{gap}}}{K}$$

Therefore the orbit center has shifted by  $\Delta r$  in a direction  $\frac{\vec{E} \times \vec{B}}{|\vec{E} \times \vec{B}|}$

If the orbit is off center, the ion will pass closer to the wall on one side of its orbit than on the other side. The radial dependence of the cavity voltage (Figure 68) means that the ion will receive a larger kick when it passes closer to the wall, and a smaller kick when it is further from the wall. The net effect is to push the orbit center back toward the z axis.

Thus, the orbit center experiences a restoring force which pushes the orbit center toward the accelerator z axis.

A simple spread sheet can be made to calculate the change in center position for each kick, and track the x position of a particle back and forth iteratively. The result shows that the magnitude of the centering effect depends on the radial dependence of the cavity voltage.

### 3. DESIGN

From the outset of this research, the intent was to build an operating device as a demonstration of the ICRA concept. Initial designs for a 1 MeV demonstration ICRA used a 488 MHz magnetron operating in an 8 Tesla Helmholtz coil with a 10 cm flat field length. Although this Helmholtz coil is available from industry, it would have been the single most expensive component in the system (~ \$100K). However, a superconducting solenoid available at the NSCL made it possible to perform this research at very low cost. This solenoid has an operating magnetic field of 2.5 Tesla and a flat field length of 5 cm. In order to use this solenoid for the ICRA experiment, the beam energy was scaled down to 50 keV to accommodate the lower B-field and the shorter acceleration region, and the rf cavity was redesigned to operate at 152 MHz.

This chapter details the design of the 50 keV proton ICRA. Section 3.1 walks the reader through the choice of all basic system parameters. Section 3.2 begins with an overview of the actual components and then discusses the main components in greater detail in sub-sections. Section 3.2.1 covers the superconducting magnet. Section 3.2.2 covers the vacuum system. Section 3.2.3 covers the ion source, the Einzel lens, and the electrostatic bend. Design of the rf cavity is given in section 3.2.4. Section 3.2.5 discusses the beam diagnostics used to determine the location of the beam and make beam measurements. Finally, section 3.2.6 covers the mounting structure used to position and align all components.

### **3.1 Basic System Parameters**

This section gives a brief account of how the basic system parameters were chosen for the 50 keV ICRA. The discussion is primarily meant to be a guide to how one would design any ICRA. Unfortunately, during the building process some experimental realities (chapter 4) forced changes in the final system parameters. In these cases, the explanation has been given in footnotes so as not to confuse the continuity of the main discussion. If the reader is interested only in how to design an ICRA, these footnotes should be ignored. Table 4 lists the final system parameters which may differ slightly from those initial values in the discussion.

The design process begins at the exit plane of the acceleration region and works backwards to the ion source. Figure 65 shows a useful graph of proton orbit radius vs. magnetic field for a range of energies. The choice of 50 keV at 2.5 Tesla<sup>1</sup> means that the final  $r = 1.3$  cm, easily fits inside the 8" bore of the solenoid (section 3.2.1). The ICRA is capable of operating over a wide range of  $N_{\text{turns}}$  (review Figure 38). For example 5 – 15 turns is a reasonable choice for the 50 keV ICRA. Since the fewest  $N_{\text{turns}}$  requires the highest  $V_o$ , we use  $N_{\text{turns}} = 5$  to check the E-field in the cavity for vacuum sparking across a chosen gap width.

The choice of injection energy limits the cavity gap width. For example, if we choose  $E_{\perp o} = 5$  keV, the orbit radius at the cavity entrance is:  $r_o = 0.41$  cm. Using the computer model, an initial radius fraction of  $r_o/R_o \approx 0.75$  works well and allows the

1) The original design used an 8 gap magnetron operating at 154 MHz in  $B_o = 2.53$  Tesla, however the final resonant frequency of the rf cavity is 152 MHz, thus  $B_o = 2.49$  Tesla. Since the rf cavity was already built with exit radius  $R = 1.27$ cm, this small drop in B-field restricts the final energy to 48 keV.

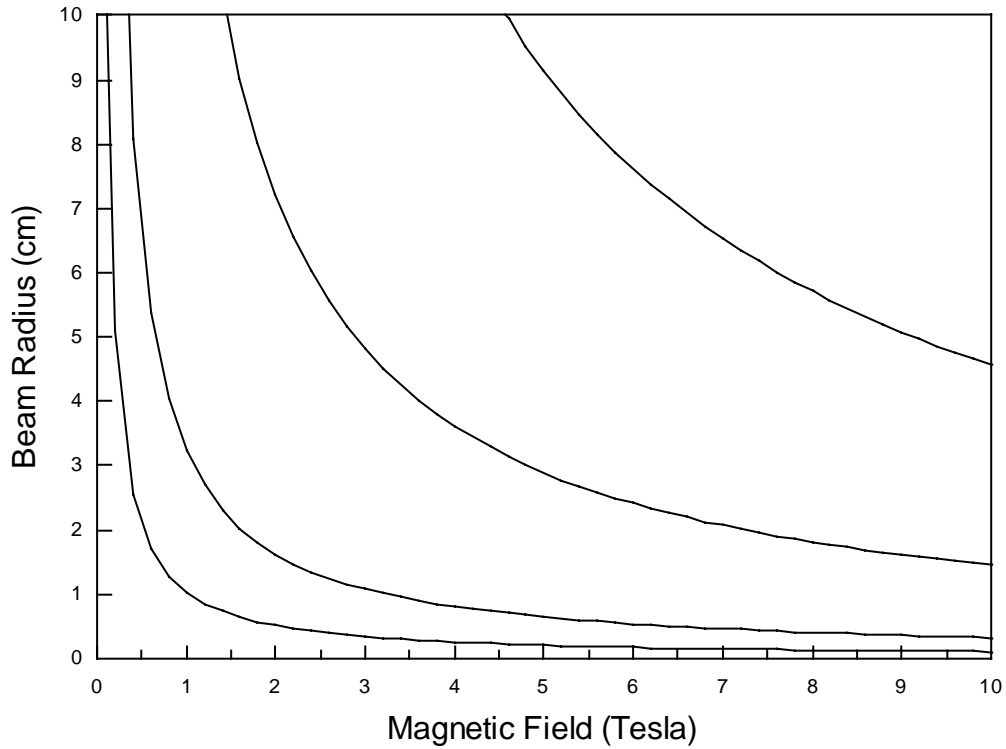


**Figure 65. Beam radius vs. magnetic field for several beam energies.**

curved acceleration trajectory to come close to the linear taper of the magnetron yet exit near  $r/R = 0.98$  for full energy gain. So the cavity radius at the entrance plane is chosen

to be:  $R_o = \frac{r_o}{0.75} = 0.55 \text{ cm}$ . At the entrance plane, assume that the gap between

magnetron vanes is the same as the width of the vane. Thus, the gap width for an 8 gap magnetron follows from the circumference<sup>2</sup>.

$$g = \frac{2\pi R_o}{2N_{\text{gaps}}} = 0.216 \text{ cm}.$$

2) Note that since  $g$  can increase with  $R_o$ , this means that the maximum cavity voltage (limited by vacuum sparking) increases with the injection energy.

Now check the electric field for this choice of  $N_{\text{turns}}$  and gap width. Using equation 2.75, the parallel injection energy for 5 turns is  $E_{\parallel 0} = 0.8 \text{ keV}$ , so the total injection energy<sup>3</sup> is  $E_0 = 5.8 \text{ keV}$ . The total energy gain is:  $E_{\text{gain}} = (50 - 5.8 \text{ keV}) = 44.2 \text{ keV}$  and the energy gain across a single gap is about 1.1 keV. The average radius fraction throughout the acceleration region can be estimated by:

$$\left\langle \frac{r}{R} \right\rangle = \frac{0.75 + 0.98}{2} = 0.87$$

Using equation 2.80 for the energy gain gives  $V_0 = 2.5 \text{ kV}$  across a gap<sup>4</sup>. Therefore, the E-field is  $|\vec{E}| \approx V_0/g = 12 \text{ kV/cm}$ . Even after field enhancement (due to sharp corners) this is far below the Kilpatrick criterion for vacuum sparking which is  $|\vec{E}| = 100 \text{ kV/cm}$  for dc, and several times higher for rf E-fields [25]. For higher turn numbers the cavity voltage will be less of course. Table 1 lists  $V_0$  for several  $N_{\text{turns}}$ .

**Table 1. Gap voltage in the rf cavity required for different turn numbers using equation 2.80 with injection energy of 5 keV and final energy of 50 keV.**

$N_{\text{turns}}$	$V_0$
5	2.5 kV
10	1.2 kV
15	0.8 kV

3) While running the experiment the total injection energy was increased to 6.4 keV in order to clip the  $\text{H}_2^+$  beam (section 4.5.1). However the cavity was initially designed based on  $E_{\perp} = 5 \text{ keV}$  ( $E_{\text{total}} = 5.8 \text{ keV}$ ).

4) Notice that when using equation 2.80 we set  $V_{\text{gap}} = V_0$ , rather than  $V_{\text{gap}} = 2V_0$ . This is because the outer conductor (and the outer vanes) of the hybrid rf cavity remain at ground so the total gap voltage is  $V_0$ , as opposed to a pure magnetron, where all vanes would go to  $\pm V_0$ , giving a total of  $2V_0$  across a gap.

The procedure above uses the analytical model to calculate the basic design parameters. One parameter that requires more attention is the rf cavity voltage ( $V_o$ ). Table 2 below shows a comparison between  $V_o$  calculated by four different methods with increasing accuracy from left to right. In each case the injection energy is  $E_o = 6.4$  keV, and the initial axial momentum is set for 5 turns.

The first column in Table 2 uses the analytical expression for the energy gain (equation 2.80) which assumes a constant radius fraction ( $r/R$ ) throughout the trajectory. The second column uses the spread sheet method discussed in section 2.5.6. Here the orbit radius and energy gain (equation 2.79) are recalculated at every gap so that  $r/R$  varies naturally throughout the trajectory. Both of these two analytical methods use only the first term in the Fourier series to approximate the radial dependence of the cavity voltage. On the other hand the computer model uses the complete electric field and allows  $r/R$  to vary naturally. Furthermore, the computer model accounts for the change in  $p_z$  caused by the cavity taper (section 2.6.2). The third column gives  $V_o$  using the computer model with a flat magnetic field. Notice that the accurate electric field and variable  $p_z$  cause significant reduction in  $V_o$ . The fourth column uses the computer model, but this time a realistic magnetic field profile over the acceleration region is used and the beam passes through the end fields at entrance and exit. On the surface one might think that the cavity voltage should be higher in this case to account for phase drift where the B-field is not perfectly in resonance with the rf. However, the small additional energy gain, caused by the end fields at the entrance, means that the cavity voltage must be decreased. Furthermore, the decreased B-field at the end of the cavity causes a slight increase in the axial momentum and leads to a curvature in the trajectory so that the beam

cannot reach full radius at exit without striking the wall at an earlier point in the cavity. The net effect of adding the realistic B-field over the acceleration region is to degrade the final energy by 6% to 45 keV. This small loss in final energy could be regained by simply increasing the cavity inner radius. The choice of magnetic field profile over the acceleration region is discussed on the following page.

**Table 2. Comparison of the cavity voltage ( $V_0$ ) calculated from the analytical model with that from the computer model. Notice that in the computer model, the reduced axial momentum causes an increased number of turns. The lower  $p_z$  and accurate electric field cause a significantly lower cavity voltage required**

	<b>Analytical w/ constant r/R</b>	<b>Analytical w/ variable r/R</b>	<b>Computer w/ flat B-Field</b>	<b>Computer w/ <math>\delta B/B_0 &lt; 0.5\%</math> and end fields</b>
<b><math>E_0</math></b>	6.4 keV	6.4 keV	6.4 keV	6.4 keV
<b>Initial <math>p_z</math></b>	1.19 MeV/c	1.19 MeV/c	1.19 MeV/c	1.21 MeV/c
<b>Final <math>p_z</math></b>	1.19 MeV/c	1.19 MeV/c	1.11 MeV/c	1.28 MeV/c
<b>Nturns</b>	5.0	5.0	5.23	5.0
<b><math>V_0</math></b>	2.16 kV	1.94 kV	1.23 kV	1.08 keV
<b><math>E_{final}</math></b>	48 keV	48 keV	48 keV	45 keV

### Magnetic Field Flatness

At this point it is necessary to choose the magnetic field flatness over the acceleration region (defined in Figure 34). Of course the smaller the field variation ( $\delta B$ ), the more expensive the superconducting magnet will be. Thus the largest B-field variation should be chosen which does not significantly degrade acceleration. Magnetic field flatness can be chosen by considering the phase drift caused by the B-field profile over the acceleration region. The analytical expression was derived in section 2.5.7. Since the phase drift depends on the number of turns (equation 2.87), trajectories with  $N_{\text{turns}} \cong 15$  are used here as a worst case situation.

Comparing the phase drift through the acceleration region with what one would calculate analytically is not straight forward because, since acceleration causes phase bunching, the total phase change of any trajectory depends on the initial phase. However, we can choose the initial phase which gives optimum acceleration (peak of the  $E-\phi_0$  curve) for comparison with analytical.

Figure 66 shows phase vs.  $z$  for particles started at three different initial phases. The red, blue, and green curves (oscillating once per turn) have been calculated using the computer model. Each trajectory uses the full solenoidal magnetic field (Figure 34), and travels through end fields, and through the acceleration region. Vertical dotted lines mark the ends of the acceleration region. Even with all effects present, acceleration does cause phase bunching (review Figure 43).

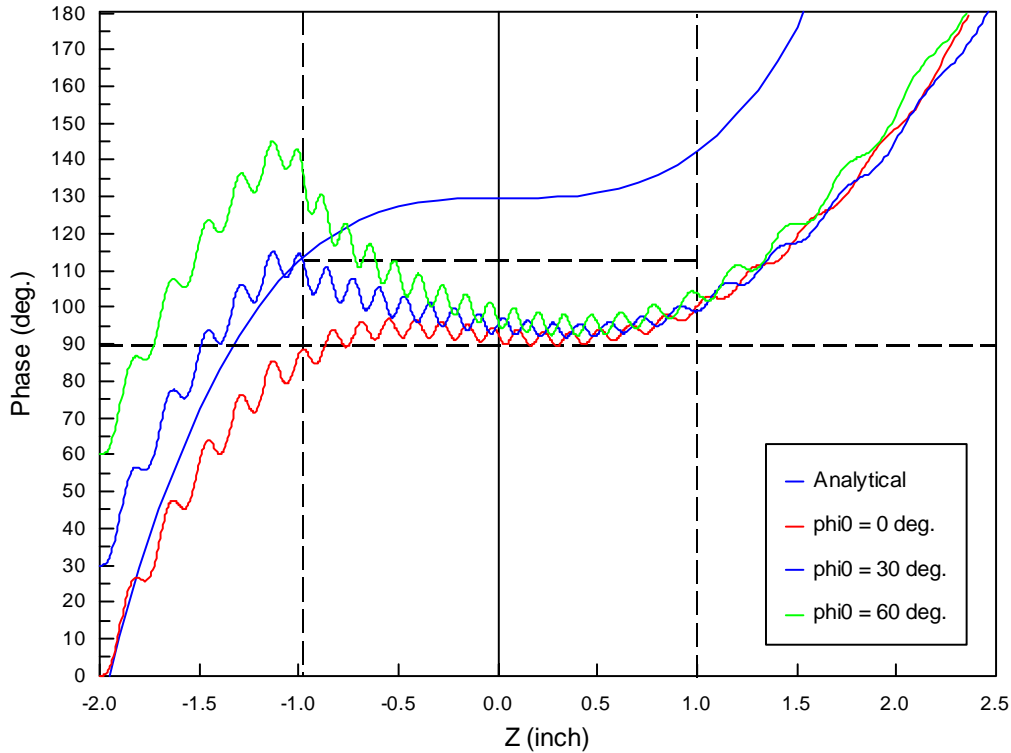


**Figure 66. Phase vs.  $z$  for trajectories started with different initial phases in the 50 keV ICRA. The red, blue, and green curves use the computer model with a solenoidal B-field, cavity end fields, and acceleration through the magnetron. The oscillation (once per turn) is caused by motion of the orbit center. The blue oscillating curve gives optimum acceleration. The smooth blue curve is the analytical calculation of phase based on equation 2.83 which assumes a centered beam and no phase pulling. Vertical dotted lines represent the ends of the acceleration region. Both blue curves have the same initial phase at the cavity entrance so the total phase change over the acceleration region can be compared.**

Now consider only the two blue curves shown in Figure 66. These two curves provide a comparison between the analytical calculation and the computer model (for the B-field profile of Figure 34). The smooth blue curve was calculated using equation 2.83 which assumes a centered beam and no phase pulling. The blue curve which oscillates once per turn is the computer result. These two curves start with the same phase at the entrance to the acceleration region so that the total phase change over the acceleration region can be compared. Table 3 below summarizes the result.

**Table 3. Total phase drift over the acceleration region. Compares what we would expect analytically with the actual computer result (for optimum acceleration case).**

	$\Delta\phi$	$V/V_o = \sin(90^\circ + \Delta\phi)$
Analytical Calculation	+ 30°	0.87
Computer Model	- 15°	0.97

Based on the B-field profile only (analytically) we would expect the phase to drift forward, yet the computer model shows that phase bunching dominates and actually causes the phase to decrease. Since the computer model gives a phase change which is much less than expected, the analytical result might be taken as the worst case prediction. However, an accurate determination of the total phase change certainly requires the full computer model.

For the 50 keV the B-field flatness was chosen to be  $\delta B < 0.5\%$  based on the analytical calculation. This choice does cause a 6% degradation in final energy (of a single particle trajectory) as shown in Table 2. Yet, based on phase change alone, Figure 66 and Table 3 indicate that this field flatness may be more stringent than was necessary. In fact the degradation in final energy is caused by an increase in axial momentum near the cavity exit. This causes a slight increase in the axial momentum and leads to a curvature in the trajectory so that the beam cannot reach full radius at exit without striking the wall at an earlier point in the cavity. The final design energy could be regained by simply increasing the inner radius of the cavity or changing the cavity slope to allow for the additional curvature in the trajectory.

Complete magnetic field mapping results are given in section 4.1.

## Injection Region

Once the magnetic field profile is known, (See Figure 81 in section 4.1) the trajectory through the injection region can be completely specified in terms of  $N_{\text{turns}}$  and  $r_o/R_o$  at the cavity entrance. First let's review what we know about the conditions at the entrance plane

- Perpendicular: For  $r_o = 0.41 \text{ cm} \rightarrow p_{\perp o} = 3.1 \text{ MeV/c}$  (equation 2.1)
- Parallel : For  $N_{\text{turns}} = 5 \rightarrow p_{\parallel o} = 1.2 \text{ MeV/c}$  (equation 2.75)

Now ( $r$ ,  $p_{\perp}$ ,  $p_{\parallel}$ , and  $\Delta z_{\text{turn}}$ ) can be found at any axial position in the lower B-field of the injection region using equations 2.59, 2.60, 2.62, and 2.88. Figure 67 shows the result.

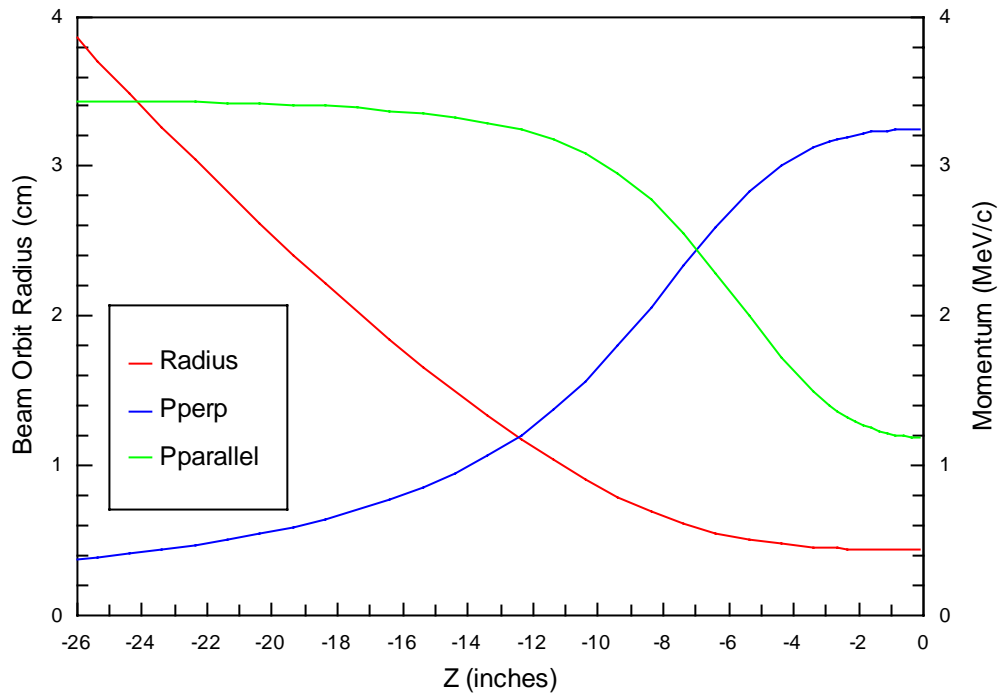


**Figure 67. Parallel and perpendicular momentum and beam radius calculated analytically through the injection region.**

### Location of the Electrostatic Bend

We want the electrostatic bend to approach an instantaneous kick so that the beam turns through only a small fraction of an orbit while traversing the bend plates. ( $\ell_{\text{eff}} \ll \Delta z_{\text{turn}}$ ). However, a short axial length of the bend plates requires a high  $V_{\text{bend}}$ . Moving back to a lower B-field causes a higher induced momentum spread (section 2.5.2), but  $\theta_{\text{bend}}$  is lower so  $V_{\text{bend}}$  will also be lower. Furthermore, the bend plates should be at a convenient location (inside the magnet bore would be difficult). At  $z = -12''$ ,  $B = 0.35$  Tesla, so the bend angle is only  $\theta_{\text{bend}} = \tan^{-1}(p_{\perp}/p_{\parallel}) \approx 20^{\circ}$ . Using equation 2.55, with  $\ell_{\text{eff}} = 2$  cm and  $g = 0.8$  cm, gives  $\frac{1}{2}V_{\text{bend}}$  below  $\pm 1$  kV. This allows a convenient power supply to be used.

### Location of the Ion Source

The source should be as close as possible to the high field region in order to minimize the induced momentum spread. However the ion source assembly was made of standard components to keep the cost low. The minimum length for the basic components needed (section 3.2.3) pushed the source aperture back to 12.9'' behind the E-static bend. Hence, the source location is  $z = -26.2''$  where the B-field is 0.030 Tesla. Equation 2.59 can be used to follow the field line back further and place the source aperture at a radius of  $r = 3.66''$ .

The proceeding discussion gives a procedure for designing an ICRA. As mentioned in the beginning of this section, certain experimental realities force small changes in the design (see footnotes). The final parameters for the 50 keV ICRA are listed in Table 4 below.

**Table 4. Final system parameters for a 5 turn trajectory through the 50 keV ICRA. The values given here differ slightly from those in the text to account for changes made during the experiment.**

See footnotes on the previous three pages for explanation.

<b>Ion Source Aperture</b>	
Ion:	protons
z =	-26.2''
B/B <sub>o</sub> =	0.013
radial position: r =	3.88 cm
extraction voltage V <sub>beam</sub> =	6.4 keV
<b>Electrostatic Bend</b>	
z =	-12.25''
B/B <sub>o</sub> =	0.141
orbit radius: r =	1.16 cm
p <sub>⊥</sub> /p <sub>∥</sub> =	0.37
θ <sub>bend</sub> =	20°
ℓ =	2 cm
g =	0.8 cm
V <sub>bend</sub> =	~ ±700 V
<b>Cavity Entrance</b>	
p <sub>⊥</sub> /p <sub>∥</sub> =	2.74
orbit radius: r =	0.436 cm
cavity radius: R =	0.55 cm
p <sub>z</sub> =	1.19 MeV/c
<b>Acceleration Region</b>	
B <sub>o</sub> =	2.493 Tesla
field flatness: δB/B <sub>o</sub> <	0.5 %
n =	4
f <sub>rf</sub> =	152 MHz
rf off: N <sub>turns</sub> =	5
rf on: N <sub>turns</sub> =	5.23
V <sub>o</sub> =	1.08 kV
cavity length ℓ <sub>cav</sub> =	5 cm
g =	0.216 cm
peak cavity voltage: V <sub>o</sub> =	3 kV @100W input
<b>Cavity Exit</b>	
cavity radius: R =	1.27 cm
orbit radius: r =	1.22 cm
E <sub>final</sub> =	45 keV

The design presented here is based purely on single particle trajectories. Knowledge of the accelerated beam current requires tracking many single particle trajectories as discussed in section 2.6.8, and also involves knowledge of the emittance of the beam extracted from the ion source. Theoretical and experimental injected beam emittance and accelerated beam currents are presented in sections 4.5 and 4.6.

### **3.2 Components of the System**

We begin with an overview of the system, then the sub-sections below will cover each of the major components in greater detail. Figure 68 shows a photo of the 50 keV ICRA. The large blue dewar is the superconducting solenoid. The ion source is on the left and the extraction end on the right. The source is at high voltage, so it is covered with a clear box made of polycarbonate. The entire system is approximately 5 feet long and 6 feet tall. The vacuum turbo pump is just off the top of the photo on top of the

vertical tube. The ion source can be seen more clearly in Figure 69. In this photo the source is aligned with a B-field line, so the angle between the accelerator z axis and the source axis can be clearly seen. Figure 70 shows a close up of the ion source and the vacuum junction which connects source to the rf cavity and the turbo pump. Figure 71 shows the extraction end of the system. This view shows the rf cavity mounted inside the magnet bore. The extraction port, which covers the far downstream end, has view ports for observing the accelerated beam, and a mechanical feed through on top for moving the radial probe (section. 3.2.5).

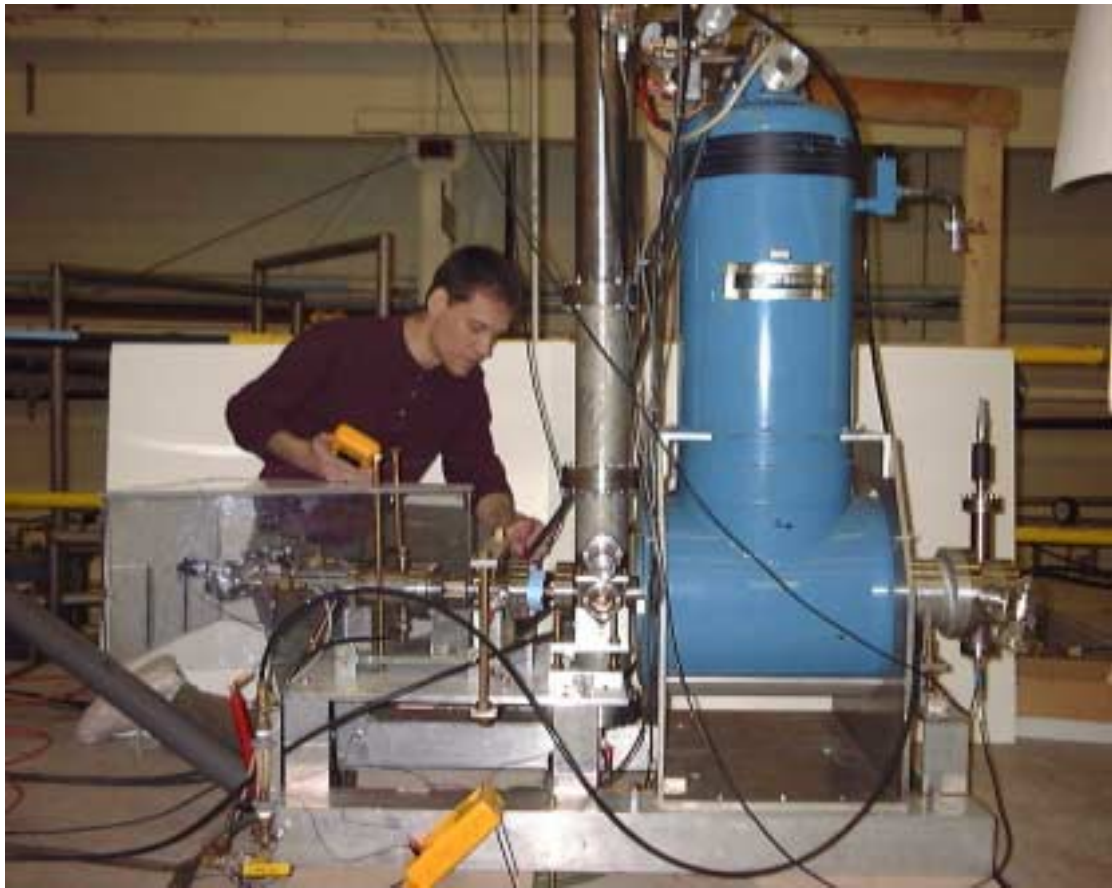


**Figure 68. Side view of the 50 keV ICRA with the author added to give a sense of scale. The large blue dewar contains the superconducting solenoid. The ion source is on the left and the extraction end is on the right. The vertical tube leads up to the vacuum turbo pump which is just off the top of the photo.**

The mechanical drawing in Figure 72 shows a top view of a cross section through the 50 keV ICRA. The major components are labeled. The proton beam is shown in red and B-field lines are shown in blue. Figure 73 shows a side view cross section.

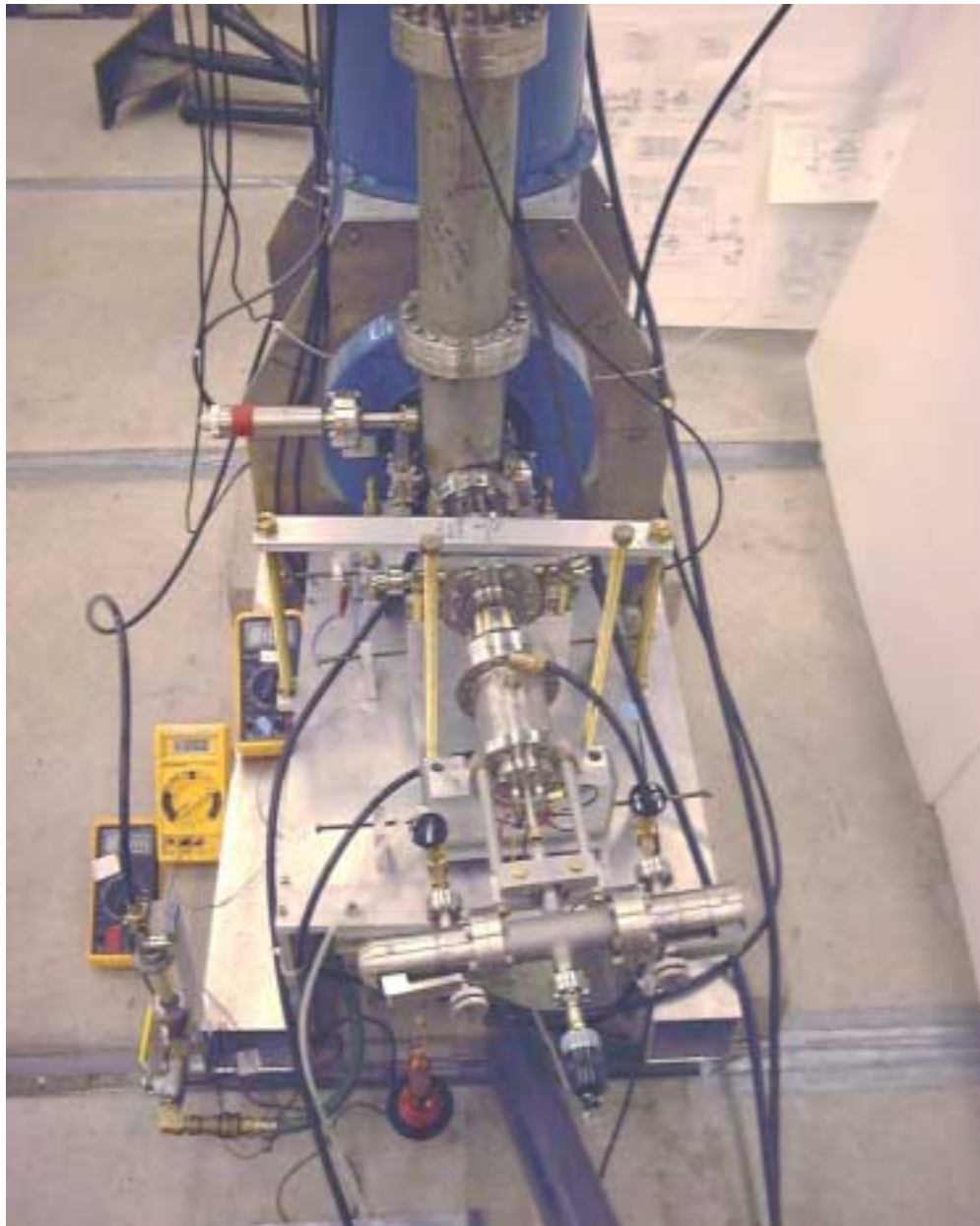


**Figure 69.** A view looking down on the ion source. Notice the angle between the accelerator z axis and the source axis is because the source is aligned with a B-field line. The motion feed through mounted on the left side of the junction piece (red tape around it) is used for moving the injection Faraday cup into the beam.

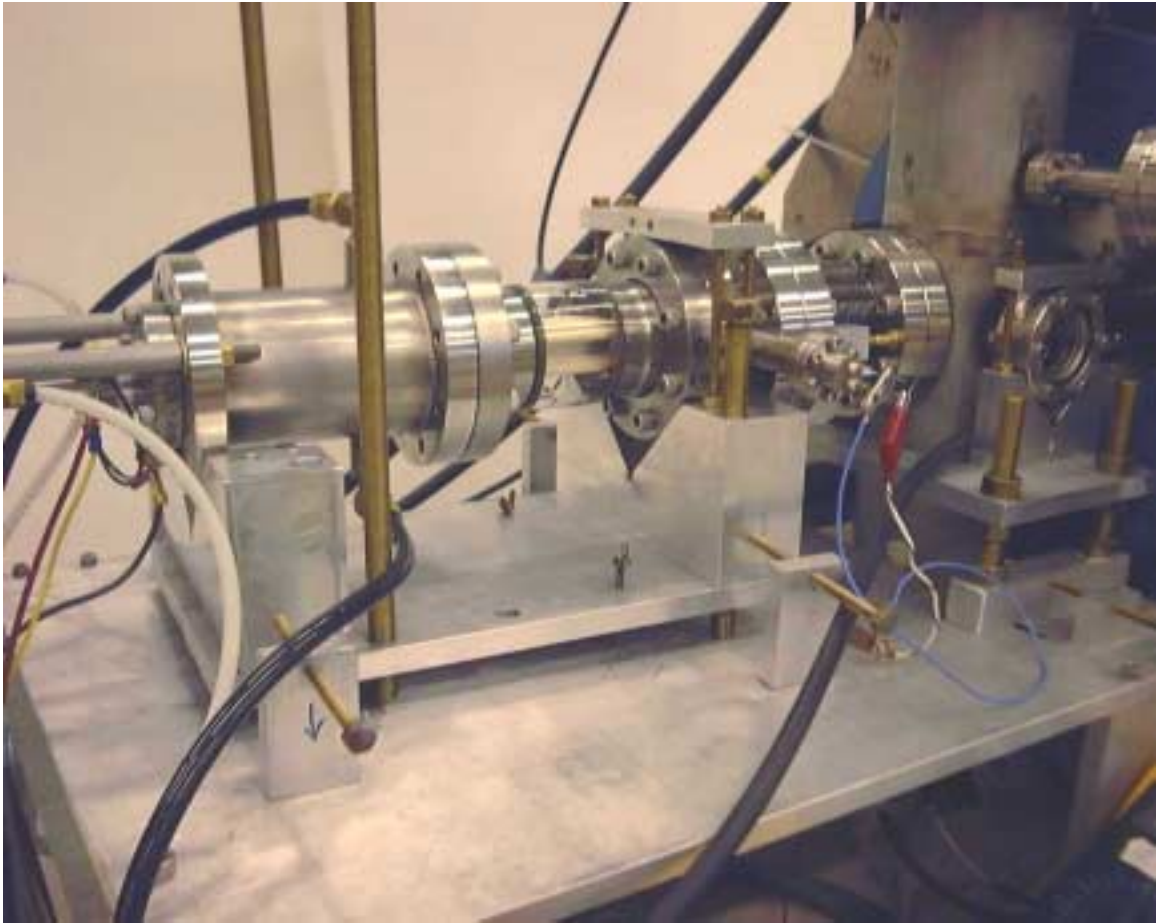


**Figure 70. A side view of the ion source assembly, which shows the four main components. From left to right, these are: the water cooling jacket, the insulating glass break, the electrical feed through, and the bellows which connects the source to the vacuum junction. The actual ion source is inside the water cooling jacket, and the Einzel lens can be seen through the glass break. The electrostatic bend is inside the vacuum junction. Compare this photo with the mechanical drawing of Figure 72. The source is mounted on two V-blocks which are rigidly connected by an aluminum plate. Pusher blocks on the sides of the V-blocks are used to adjust the position and angle of the source horizontally, and vertical bolts through the aluminum plate are used to adjust the position and angle of the source vertically.**



**Figure 71. The extraction end of the 50 keV ICRA. The rf accelerating cavity (aluminum tube) is mounted in the bore of the superconducting magnet (blue). The V-block below the cavity can be adjusted in order to align the rf cavity with the magnetic axis. The extraction port covers the extreme downstream end of the system and contains the extraction Faraday cup and viewports for observing the beam. The mechanical feedthrough on top of the extraction port is used to move the radial probe, in the radial direction (see Figure 73).**

**Figure 72. Top view of a cross section through the 50 keV ICRA. All major components are labeled, however the radial probe is not shown in this view (see Figure 73). B-field lines are shown in blue and a trajectory is shown in red. The magnetron section only is cut through two different planes in order to show the inner and outer vanes both. Figure 76 shows this more clearly.**

Top view cross section goes here

**Figure 73. Side view of a cross section through the 50 keV ICRA. All major components are labeled. B-field lines are shown in blue and a trajectory is shown in red. The magnetron section only is cut through two different planes in order to show the inner and outer vanes both. Figure 76 shows this more clearly.**

Side view cross section goes here

### **3.2.1 Superconducting Magnet**

The magnet used is a superconducting solenoid made in the 1970's by Intermagnetics General Corporation. This solenoid has an 8" diameter warm bore and a flat field length of 5 cm for a field variation of less than 0.5%. The NbTi coil is rated at 3.5 Tesla for 125 Amps. However, due to the age of the solenoid, it was decided to run the field at 2.5 Tesla (89 Amps). The superconducting solenoid is inside the large blue dewar which can be seen in Figure 68. The 8" warm bore can be seen in Figure 71. Magnetic field mapping results are given in section 4.1. The axial field profile is shown in Figure 81.

### **3.2.2 Vacuum System**

The vacuum system consists of a turbo pump, a rough pump, and the vacuum walls of 5 main components: the ion source, vacuum junction, vertical extension tube, the outer conductor of the rf cavity, and the extraction port. The system was simplified by using the aluminum outer conductor of the rf cavity as a vacuum wall. All vacuum seals have conflat knife edges and use OFE copper gaskets, except the two seals to the aluminum outer conductor of the rf cavity which use viton O-rings. The turbo pump is mounted on top of the vertical extension tube (~ one meter long) so that the fan blades are in a magnetic field below 50 Gauss.

A simple representation of the vacuum system is shown in Figure 74. The system was initially designed for a throughput of  $Q = 10^{-4}$  Torr Liter/sec, however higher pressure was required in the ion source to ignite the hydrogen plasma. Therefore,  $Q = 10^{-3}$  Torr Liter/sec is representative of actual operating conditions. Pressure in the system is dominated by the gas flow into the ion source. The poor conductance of the long vertical tube reduces the pumping speed from 500 L/s at the turbo pump to 85 L/s at the vacuum junction. The conductance of the injection components further reduces the pumping speed to 30 L/s near the ion source aperture. For conductance formulas see reference [17].

Typical operating pressure at the junction is  $P_2 = 1(10^{-5})$  Torr and a typical pressure near the ion source is  $P_3 = 3(10^{-5})$  Torr. A calculation of the mean free path ( $\lambda$ ), using the cross section ( $\sigma$ ) for electron capture by an incident proton [26], can be expressed in terms of the pressure (P).

$$\lambda = \frac{1}{n\sigma} = \frac{3 \text{ mTorr meter}}{P}$$

Thus, for an average pressure along the beam path of about  $2(10^{-5})$  Torr, the mean free path is:

$$\lambda = 150 \text{ meters}$$

The accelerated beam in the 50 keV ICRA has a total path length ( $\ell$ ) of 3 meters, so the beam lost by charge exchange with gas in the system can be estimated using:

$$I = I_0 e^{-\frac{\ell}{\lambda}}$$

This gives:  $I/I_0 = 98 \%$ , therefore about 2 % of the beam is lost to recombination.

This calculation shows that the vacuum system is marginal. However, it is adequate for the purposes of the ICRA experiment. While running the experiment, care was taken not to raise pressures higher than those stated here.

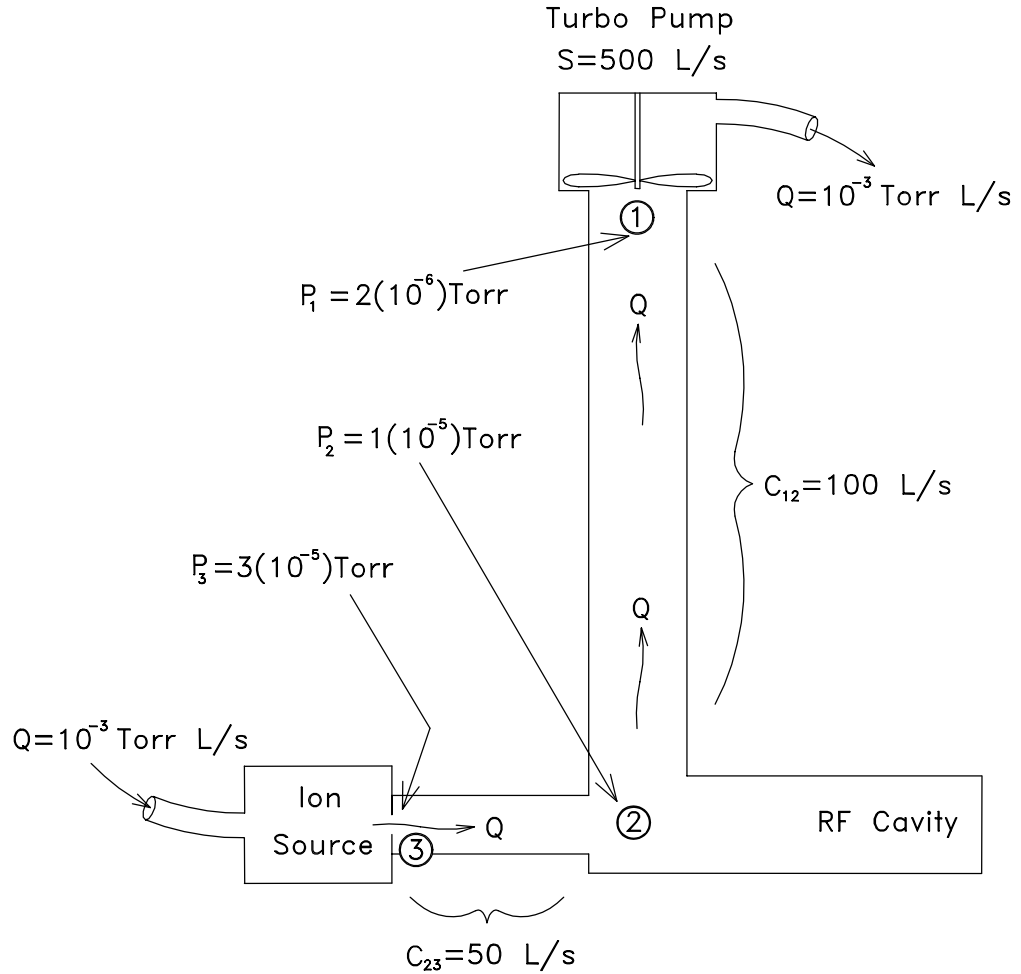


**Figure 74. Simple representation of the vacuum system showing typical pressures during high gas load into ion source. Conductances are calculated using formulas in [17].**

### 3.2.3 Ion Source, Einzel Lens, and Electrostatic Bend

This section covers all components of the injection region. The major external components of the ion source assembly can be seen in Figure 70. These are the water cooling jacket, the glass break, the electrical feed through, and the bellows, which connects the entire source assembly to the vacuum junction. The major internal components can be seen in Figure 72. The ion source itself is mounted inside the water cooling jacket, the Einzel lens is mounted inside the glass break, and the electrostatic bend is mounted inside the vacuum junction. These three components are discussed below.

#### Ion Source

The actual ion source is a simple electron filament source purchased from Colutron Research Corp. This component includes the filament, anode, and electrical and gas feedthroughs. A dc current heats the filament so that electrons are emitted. Electrons are then accelerated through ~ 100 volts toward the anode. Gas is leaked in through the rear of the source and ionized by the electron beam. Ions are extracted through a 0.020" diameter aperture in the anode. The gas pressure inside the source needed to light a plasma ranges from 30 mTorr for Argon to over 1000 mTorr for pure Hydrogen. The 0.020" aperture is small enough to keep high pressure in the source, yet allow low pressure in the beam line. However, gas flow through the aperture is the major gas load to the vacuum system.

An electrical schematic is shown in Figure 75. The power supplies for the filament and anode are isolated by an isolation transformer and floated at high voltage

(5 – 10kV) so that the ion source can be maintained at high voltage. The source aperture (at high voltage) and the puller (at ground) are separated by a 6 mm gap. The strong electric field across this gap extracts the ion beam from the source and accelerates it to the injection energy ( $qV_{\text{beam}}$ ). The glass break electrically isolates the water cooling jacket from the rest of the beam line which is grounded. A clear box made of polycarbonate covers the water cooling jacket for safety, and a plywood and acrylic box covers the power supplies. Dials on the power supplies have been replaced by long plastic rods so that the source can be adjusted while the beam is on.

### Einzel Lens

The Einzel Lens consists of three coaxial drift tubes called the “puller”, the “mid tube”, and the “exit tube”. The tubes are held on the same axis by being trapped between 4 ceramic rods. The 4 ceramic rods are held in place by mounting rings at the entrance and the exit. Set screws in the mounting rings allow alignment of the puller aperture with the source aperture. The puller aperture is  $D = 0.070''$ , after which the inner diameter of all three tubes opens to  $D = \frac{1}{4}''$ . All three drift tubes are electrically isolated so that the beam current hitting each tube can be monitored. The mid tube is normally placed at high positive voltage (2-3kV) while the other two tubes are kept at ground. Fringe fields in the gaps between the drift tubes focus the beam. The focal length can be adjusted by adjusting the voltage of the mid tube ( $V_{\text{Einzel}}$ ). Einzel lenses are well understood, therefore minimal detail is given here [27].

### Electrostatic Bend

The electrostatic bend is made of two flat copper plates separated by an 8 mm gap. The bend angle for the injected beam is about  $20^\circ$ , therefore the bend plates are tilted at  $10^\circ$ . See the geometry of Figure 25. The bend plates are also rotated about the y (vertical) axis by 4.7 degrees so that the upstream face of the plates is perpendicular to the oncoming beam. Voltage used on the bend plates is less than 800 volts each.

**Figure 75. Schematic of the electronics for the 50 keV ICRA.**

Electrical Schematic goes here

### 3.2.4 RF Cavity

At an operating magnetic field of 2.5 Tesla, the cyclotron frequency for protons is 38 MHz. Therefore, a magnetron operating at the 4<sup>th</sup> harmonic (8 gaps) would have an rf frequency of 152 MHz. At this frequency a pure magnetron will not fit into the 8” warm bore of the superconducting solenoid because the inductors extend too far in the radial direction. The solution was to replace the inductors of the pure magnetron with some inductance which extends in the axial direction where space is not limited. A coaxial quarter wave cavity has the geometry needed to move the inductance axially. Therefore the vanes of the magnetron which are mostly capacitive, have been mounted across the open end of a coaxial section which provides the inductance needed. The result is the “hybrid coaxial – magnetron cavity” shown in Figure 76.

The structure can be difficult to visualize. Start by considering Figure 15 which shows an example of a 4 gap magnetron operating in the  $\pi$  mode. Notice that in the  $\pi$  mode (frozen in time), the charge difference between each vane alternates, + - + - . Thus, every other vane should be connected to the inner conductor of the coaxial section, while the remaining half of the vanes should be connected to the outer conductor. The cutaway view of Figure 76 is taken in two different planes (magnetron section only) in order to show a cross section through an inner vane which is electrically connected only to the inner conductor, and an outer vane which is electrically connected only to the outer conductor. Ceramic insulators allow all vanes to be mechanically connected. This configuration has one additional benefit. While a pure magnetron is a set of coupled oscillators with  $2n-1$  possible modes of oscillation, the hybrid cavity is naturally strapped to allow oscillation only in the  $\pi$  mode.

The vanes of the rf cavity were made by electron discharge machining (EDM). Figure 77 shows the individual components of the magnetron section. Figure 78 shows the magnetron and the inner conductor and the shorting plate assembled together just before being inserted into the aluminum outer conductor. Figure 79 shows a view looking into the fully assembled rf cavity from the extraction end.

The rf cavity has two coupling loops. The large loop is for coupling power into the cavity, and the small loop is a pickup loop which gives a voltage signal that is proportional to the cavity voltage ( $V_o$ ). Inductive coupling was chosen because high B-fields at the shorting plate are accessible but the high rf voltage end at the magnetron is at the center of the superconducting solenoid and so would be difficult to access. During construction of the cavity, the area of the drive loop was adjusted in order to obtain an impedance match with the  $50\Omega$  cables used. The area of the pickup loop was adjusted to obtain an output signal in a convenient voltage range ( $V \leq 1$  volt). Both final loops are rigid (cannot be adjusted). Furthermore the rf cavity has no tuning mechanism. The resonant frequency is fixed at 152 MHz, therefore the resonance required for acceleration is hit by adjusting the magnet current.

The rf cavity is designed to generate 3 kV across the gaps of the magnetron for an input power of less than 100 Watts (review section 2.4.5). The experimental results are given in section 4.3. The input rf signal is generated by a Hewlett Packard 8660B signal generator and then amplified by a TE Systems 1546RA rf amp. This narrow band rf amplifier has an operating window from 150 – 160 MHz, and a gain of 40 dB (100W output for 10mW input). Power output of the rf amp is measured with a Bird 43 watt meter before going to the drive loop of the rf cavity. The signal from the cavity pickup

loop is read on an oscilloscope. This pickup voltage is then used to calculate the voltage across the magnetron vanes ( $V_o$ ).

**Figure 76. A cutaway view of the rf cavity. Notice that in the magnetron section only, the cross section has been taken through two different planes in order to show a cross section through an inner vane and an outer vane both.**

Cut away view of rf cavity goes here



**Figure 77. Components of the magnetron section before assembly.**



**Figure 78. Components of the hybrid rf cavity. Here the magnetron is assembled. The magnetron, inner conductor, and shorting plate (all made of copper) are about to be inserted into the aluminum outer conductor.**



**Figure 79.** A view of the fully assembled rf cavity looking into the extraction end. The 8 tapered magnetron vanes of the acceleration section can be seen inside the ID of the exit mounting ring.

### **3.2.5 Beam Diagnostics**

Beam diagnostics are the tools used to determine the location of the beam and make measurements of the beam. This section will discuss the three main beam diagnostics used. These are: the injection Faraday cup, the radial probe, and the extraction Faraday cup (below).

Other diagnostics include the bend plates and an aperture on the downstream side of the bend plates. The top and bottom bend plates and the aperture are all 3 electrically isolated so that the beam current hitting them can be monitored. Furthermore, the top and bottom bend plates and the aperture all have phosphor coating (KBr). This is used to determine visually if the beam is too high, or too low, or too far left, or too far right.

What follows is a description of the three main diagnostic tools mentioned above. The three most important characteristics of each tool are summarized in Table 5.

**Table 5. A summary of the basic characteristics of each of the 3 main beam diagnostics.**

	<b>Electrically Isolated</b>	<b>Phosphor Coating</b>	<b>Moveable</b>
<b>Injection F.C.</b>	yes	yes	yes
<b>Radial Probe</b>	yes	-	yes
<b>Extraction F.C.</b>	yes	yes	-

### Injection Faraday Cup and Viewer

The injection Faraday cup is an aluminum plate that is mounted on a motion feed through. It is electrically isolated so that the beam current hitting it can be measured, and it has a phosphor coating (KBr) which allows an image of the beam to be seen. The injection Faraday cup can be moved into the beam at a point immediately upstream of the electrostatic bend. It is shown in two positions on Figure 72. This tool is useful for aligning the ion source with a B-field line. Since the beam actually contains 3 different ion species, a misalignment with the B-field causes the beam to split, so that three separate beam spots are seen on the injection Faraday cup. By adjusting the angle of the ion source, the three beam spots can be brought together at one point. (In section 4.5.5 we will see that the computer model shows that the point at which the three beams come

together is actually about  $0.5^\circ$  away from a B-field line. However, this condition is reproducible, and therefore it is useful.)

### Radial Probe

The radial probe is a Faraday cup which can be moved radially into the extracted beam. Geometry of the radial probe is shown in Figure 73. The mechanical feedthrough which moves the probe can be seen in the photo of Figure 71. The radial probe is used to measure the radial distribution of the accelerated beam (beam current vs. radius). Recall that the extracted beam is a rotating cylinder of ions all centered around the z axis but orbiting at different radii because they have different energies ( $E \propto r^2$ ). The energy distribution obtained from the computer model was shown in Figure 63. The radial probe is designed for experimental measurement of this same curve so that a comparison between theory and experiment can be made (see section 4.6.1).

The radial probe has an electron blocker mounted along the upstream edge which prevents electrons from reaching the Faraday cup portion of the probe. The electron blocker works on the fact that electrons orbit around B-field lines at such a small radius that  $r$  can be neglected ( $\sim 0.1$  mm). Hence, electrons effectively move along magnetic field lines and therefore the electron blocker casts a shadow that electrons cannot reach. The Faraday cup resides in this electron shadow. However, protons orbit at much larger radius ( $r \leq 2$ cm), and therefore can pass behind the  $e^-$  blocker and strike the Faraday cup. A small portion of the proton beam does strike the electron blocker. This effect on radial probe data will be accounted for with a mathematical correction.

Figure 73 shows that the inner edge of the radial probe is sloped ( $dy/dz$ ). Since the proton beam in the extraction region follows B-field lines (section 2.5.2), and since the radial probe has some axial length ( $\Delta z$ ), the slope of the inner edge of the probe must match the local field line in order for the current at any single energy to be measured correctly. However, field lines at large radius have a steep slope, while the slope goes to zero at the z axis. Therefore, the radial probe has the correct slope only for one energy. This was chosen to be the full accelerated beam energy (50 keV). Measurements at any lower energies will require a mathematical correction.

Finally, for some conditions, the radial probe is not long enough in the axial direction to catch all of the beam (see section 2.5.8). This will require a third mathematical correction. These three mathematical corrections to the radial probe data are discussed in section 4.6.1 and details are given in Appendix A.

### Extraction Faraday Cup and Viewer

The extraction Faraday cup is a round aluminum plate that is mounted at the far downstream end of the 50 keV ICRA. See Figure 72. It is electrically isolated for measurement of beam current, but more importantly it has a phosphor coating (KBr) which allows an image of the beam to be seen through a viewport. The information obtained from visualizing the beam on the extraction Faraday cup has been instrumental in understanding much of the behavior of the beam in the ICRA. The extraction Faraday cup allows measurement of the beam arc length (section 2.6.7 and 4.5.4), it is useful for understanding the ion spectrum (section 2.5.4 and 4.5.1) and it provided proof that the accelerated beam consists of ions orbiting around the z axis at large radius (section 4.6.1).

### 3.2.6 Mounting Structure

The purpose of the mounting structure is to hold all components in place and allow adjustments so that the components can be aligned relative to each other.

Alignment consists of the following four criteria.

- The axis of the rf cavity must coincide with the magnetic axis.
- The magnetron must be in the center of the magnet axially so that the acceleration region is in the region of flattest B-field.
- The ion source must be at the correct location relative to the rf cavity so that the spiraling beam will be centered (x,y) when entering the rf cavity.
- The axis of the ion source should be aligned with the local B-field line.

Four pivot points were chosen which satisfy these criteria and yet can be implemented in a simple structure. The rf cavity and the vacuum junction (contains the bend plates) are connected together as one rigid piece. The entire ion source assembly is also one rigid piece. However, a bellows between the source and the vacuum junction allows the ion source to move relative to the rf cavity and the electrostatic bend. The rf cavity/junction assembly has a pivot point at each end. Similarly, the ion source assembly has a pivot point at each end. All four pivot points allow vertical and horizontal motion. The location of each pivot point is shown in Figure 80. Notice that one pivot point is located at the exit of the Einzel lens and another pivot point is located at the electrostatic bend. This allows these two points to be held stationary while the other end of a component is moved. Pusher blocks are used for horizontal motion and threaded rod is used for vertical motion. Examples can be seen in Figure 70 and 71.

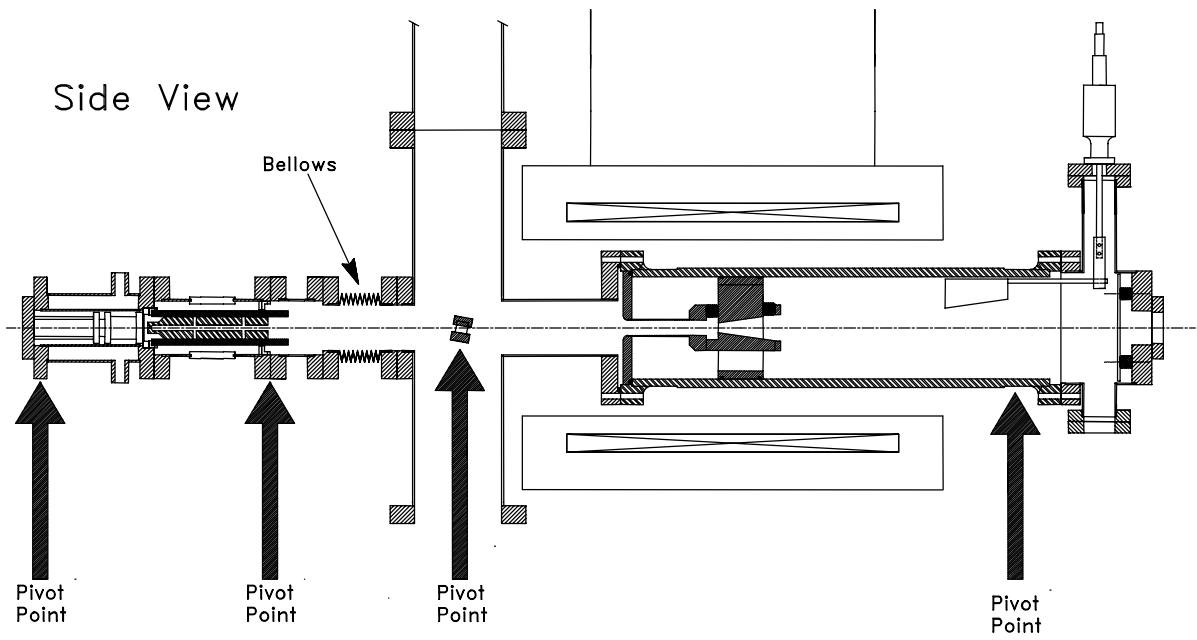


**Figure 80. Pivot points of the mounting structure**

## **4. EXPERIMENTAL RESULTS**

The major components of the 50 keV ICRA were assembled and aligned during December of 1998. Accelerated beam was first obtained in January of 1999. This chapter covers the experimental results and discusses comparisons with the theory. Section 4.1 summarizes the results of mapping the magnetic field of the superconducting solenoid. Section 4.2 covers the ion source. Section 4.3 covers the rf cavity experimental methods (4.3.1) and has a separate summary of results section (4.3.2). Finally, the beam measurements are divided into two sections. Section 4.4 covers measurements of the injected beam (rf off), and section 4.5 covers measurements of the accelerated beam (rf on).

## **4.1 Magnet Mapping**

It was necessary to map the magnetic field of the superconducting magnet before the design of the 50 keV ICRA could be finalized. This section gives a summary of the magnetic field mapping results.

The purpose of mapping the magnetic field was to accomplish four main goals.

### **1) Locate the magnetic axis of the magnet.**

The magnet coil is mounted inside the dewar, but is not necessarily coaxial with the dewar bore.

### **2) Locate the axial position of the magnetic center.**

The magnetron should be placed at the correct axial location which provides the flattest magnetic field over the length of the acceleration region.

### **3) Obtain the full axial magnetic field profile.**

The field profile is needed to calculate the trajectory, and choose locations for the ion source and electrostatic bend. The axial field profile also provides all information needed to calculate B-field arrays for the computer model.

### **4) Determine the flat field length for $\Delta B/B_0 = -0.5\%$ .**

The resonance condition requires that the axial length of the acceleration region be limited to this flat field length.

The magnetic field was mapped using a two-axis Hall probe ( $B_z$ ,  $B_r$ ). The Hall probe is mounted inside an acrylic tube, and two mounting rings hold the acrylic tube

inside the magnet bore. The Hall probe can be mounted at several discrete radial positions inside the acrylic tube, and the mounting rings allow the acrylic tube to move azimuthally and axially relative to the dewar. Therefore, the mapping apparatus provides motion of the Hall probe in all three dimensions of the cylindrical coordinate system of the acrylic tube ( $r, \theta, z$ ). Position errors are estimated to be less than 1 mm (0.040"). Furthermore, the two mounting rings which hold the acrylic tube inside the magnet bore are adjustable. This allows the position of the entire mapping apparatus to be adjusted relative to the magnet bore until the mapper axis is aligned with the magnetic axis.

The magnetic axis was located by scanning  $B_r$  and  $B_z$  vs.  $\theta$  for several different  $z$  planes, and then adjusting the position of the mapper until a location was found which gives minimal azimuthal variation in the field. Table 6 below gives the location of the magnetic axis relative to the magnet bore.

**Table 6. Two points on the magnetic axis (relative to the axis of the magnet bore). Azimuthal variation for all  $z$  planes is less than 0.15% of the central field value ( $B_0 = 2.5T$ ).**

at $z = +8.25''$	at $z = -8.25''$
$x = +0.064''$	$x = +0.046''$
$y = -0.186''$	$y = -0.119''$

The location of the axial center was calculated from three different field profiles. The average is  $z_{\text{center}} = +0.35''$ , with a standard deviation of  $0.02''$ . Figure 81 shows the full magnetic field profile which has been centered in  $z$  and normalized to the central field value. Figure 82 below shows the measured B-field over the central field region.

A parabola has been fit to the data so that the flat field length can be calculated. The flat field length is 5.3 cm for  $\Delta B/B_0 < 0.5\%$ .

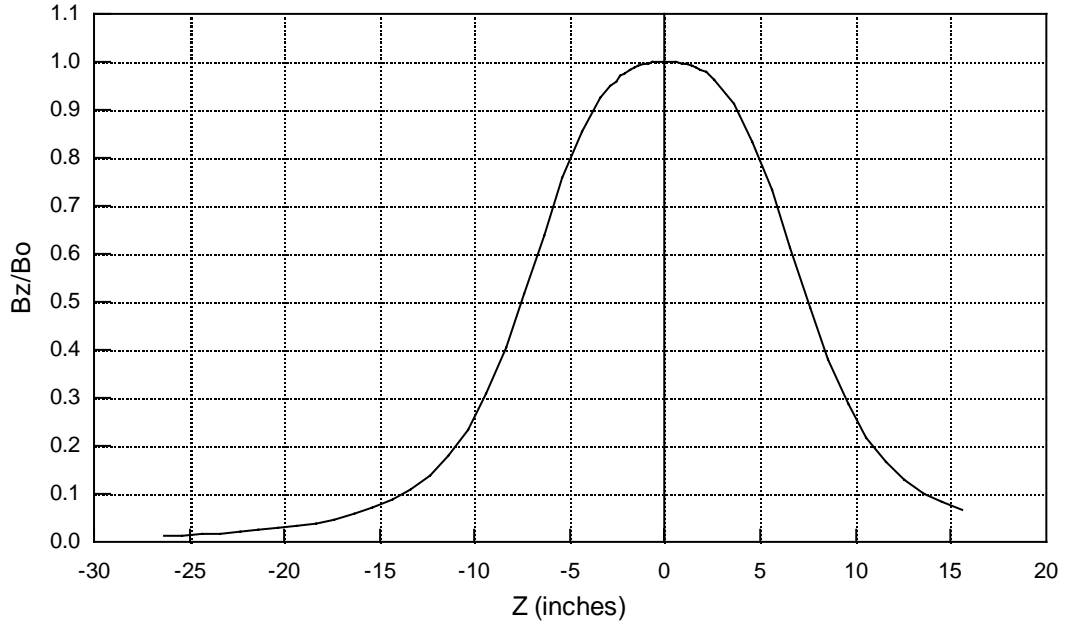


**Figure 81.** Measured axial magnetic field at  $r = 0$ . Data has been centered axially and normalized.

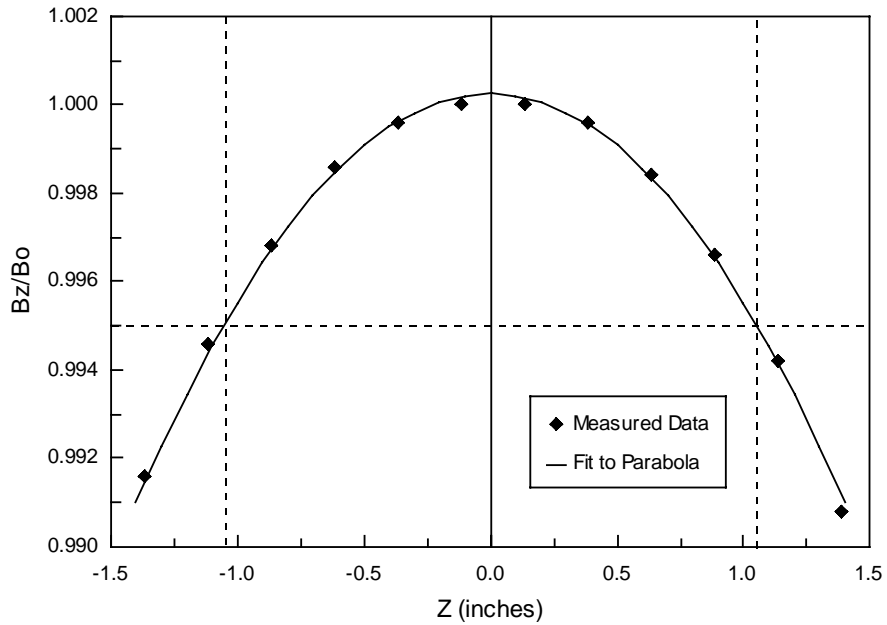


**Figure 82.** Measured axial magnetic field in the acceleration region. The smooth line is a parabolic curve fit to the data. The flat field length for  $\Delta B/B_0 < 0.5\%$  is 2.1 inches = 5.3 cm

## **4.2 Ion Source**

The design of the ion source was discussed in section 3.2.3. The filament supplies electrons which ionize the gas inside the source, however significant ion beam current is extracted only when the source pressure becomes high enough to ignite a plasma. The pressure at which a plasma will ignite depends on the properties of the particular gas used. Pure Argon will ignite with gas pressure inside the source as low as 40 mTorr. However, pure H<sub>2</sub> gas requires about 2000 mTorr. In order to keep pressure in the rest of the vacuum system below 10<sup>-5</sup> Torr it was necessary to use Argon as a support gas. This combination of H<sub>2</sub>+Ar allows a reasonable proton beam with a source pressure of 500 mTorr.

With pure Argon in the source, a beam of up to 10 μA can be extracted. However, with pure H<sub>2</sub> gas in the source, the majority of the beam is H<sub>2</sub><sup>+</sup>, and only a small fraction is H<sup>+</sup>. This small fraction of H<sup>+</sup> produced is exacerbated by the pressure limitations explained above. Between these two effects, a typical beam used for measurements in the 50 keV ICRA contains only about 5 – 50 nA of protons, rather than the 1 - 10 μA originally expected. Table 7 shows typical beam currents for the ion source running in this H<sub>2</sub>+Ar mode. Section 4.5.1 explains the ion spectrum in greater detail.

**Table 7.**

**Approximate beam currents of each constituent in typical beams used in the 50 keV ICRA.**

<b>Ion</b>	<b>Beam Current</b>
Ar <sup>+</sup>	1 – 10 μA
H <sub>2</sub> <sup>+</sup>	50 –500 nA
H <sup>+</sup>	5 – 50 nA

Operating the ion source in a magnetic field creates many concerns such as: the ability to ignite a plasma, and to extract a beam from the source, the performance of the Einzel lens, etc. The magnetic field at the source is about 300 Gauss. However, electrons in the source are pulled along the z axis of the source, and the source is aligned with the local magnetic field. Experimental results show that operating the source in this magnetic field is not a problem. In fact the beam appeared to be more stable with the B-field on, than with the B-field off. Furthermore, the Einzel lens provided a wide range of focusing capability and whether the B-field was on or off caused no discernable change in performance.

A major disadvantage of this particular source design is that each filament only lasts for about 50 - 100 hours, and replacing a filament requires complete disassembly of the source. After replacing the filament, re-assembly of the source requires re-alignment of the Einzel Lens and connection to the ICRA vacuum system.

### **4.3 RF Cavity**

The purpose of the rf cavity measurements is to determine the gap voltage ( $V_o$ ) for a given input power ( $P_{in}$ ). The rf cavity is a hybrid magnetron / coaxial cavity. The design was discussed in section 3.2.4 and a drawing of a cross section through the cavity was shown in Figure 76. The theory was explained in section 2.4.5. Section 4.3.1 covers the rf measurement techniques used, and presents the experimental results. A summary of the results is given in section 4.3.2.

#### **4.3.1 Experimental Methods**

The rf cavity gap voltage ( $V_o$ )\* cannot be measured by attaching a probe directly across the open end of the cavity because any measurement, which couples significant power out of the cavity, changes the power loss and results in an incorrect measurement of  $V_o$ . Even when using probes with impedance as high as 1 M $\Omega$  and capacitance as low as 1.5 pF, the additional capacitance increases the losses in the cavity and gives an erroneous measurement.

\* A pure magnetron would have  $V_{gap} = 2V_o$ . However the hybrid cavity has  $V_{gap} = V_o$ .

The method used here is to determine  $V_o$  indirectly by two independent low power methods. Recall from section 2.4.5 that the power loss (P) can be expressed in terms of the shunt resistance ( $R_s$ ):

$$P = \frac{V_o^2}{2R_s} \quad (4.1)$$

Where:

$$R_s = Q\sqrt{\frac{L}{C}} = \frac{Q}{2\pi f_o (C_\ell + C_m)} \quad (4.2)$$

If  $R_s$  is known, then the cavity voltage is known for a given input power.

Method 1 is to measure  $Q$ ,  $f_o$ , and the capacitance of the magnetron section ( $C_m$ ), then calculate the capacitance of the coaxial section ( $C_\ell$ ). From these,  $R_s$  can be calculated so that  $V_o$  is known for a given input power. The results of method 1 are summarized in Table 8 below.

Method 2 is a calibration of the pickup and drive loops. Rather than driving the cavity from the drive loop and attempting to measure  $V_o$  across the open end. The cavity is driven from the open end so that  $V_o$  is known, and the voltage at the drive loop is measured. The results of method 2 are summarized in Table 9.

### **Method 1 (Measurement of Cavity Parameters)**

If the shunt resistance ( $R_s$ ) is known, equation 4.1 can be used to calculate the cavity voltage ( $V_o$ ) for a given input power ( $P$ ). The shunt resistance can be calculated from  $Q$ ,  $L$ , and  $C$ . However, the inductance ( $L$ ) is difficult to measure, while the resonant frequency ( $f_o$ ) is easy to measure. Therefore, it is convenient to express  $R_s$  in terms of  $Q$ ,  $f_o$  and the capacitance.

$$R_s = Q \left( \frac{R_s}{Q} \right) = Q \sqrt{\frac{L}{C}} = \frac{Q}{2\pi f_o (C_\ell + C_m)}$$

The inner and outer vanes of the magnetron are electrically isolated, therefore the capacitance of the magnetron section ( $C_m$ ) can be measured with a simple capacitance meter. On the other hand, the capacitance of the coaxial section ( $C_\ell$ ) must be calculated using equation 2.28, which accounts for a  $\sin(z)$  voltage profile along the length of the coaxial section ( $\ell$ ). The resonant frequency is easily found as the peak in the transmission curve on a network analyzer. However, accurate measurement of the  $Q$  takes more care.

### **Measurement of the Unloaded Q**

Measurements of the  $Q$  were made using a Hewlett Packard 8714C network analyzer (NWA). A brief account of the method is given here. The signal generator inside the NWA scans over frequency and the output signal is transmitted through the rf cavity in order to obtain a frequency response curve for the cavity. The  $Q$  is then

calculated from the peak in the transmission curve using  $Q = f_o/\Delta f$ , where  $f_o$  is the center frequency of the peak and  $\Delta f$  is the full width at half of the maximum power.

The Q must be calculated from a peak in the transmitted signal, not from the dip in the reflected signal. The reason for this becomes obvious if one considers the meaning of each curve. A dip in the reflection curve means that power was sent toward the cavity, but did not return to the NWA for whatever reason. On the other hand the peak in a transmission curve means that power was successfully coupled into the cavity which excited rf fields in the cavity, then a small portion of that signal was coupled out by the pickup probe and transmitted back to the NWA. Obviously a transmission measurement is representative of the actual frequency response of the rf cavity, but a reflection curve is not necessarily.

Obtaining a true transmission curve also depends on placement of the drive and pickup probes inside the cavity. The purpose of the pickup probe is to obtain a voltage which is proportional to the cavity fields. Therefore it is important that the pickup probe be located far enough away from the drive probe that it couples only to the cavity fields but does not couple any power from evanescent waves emitted directly from the drive probe.

The actual Q of the resonant cavity (defined in equation 2.30) is called the “unloaded Q” or  $Q_o$ . If any power is coupled into or out of the cavity then the cavity becomes loaded and the measured Q will be less than  $Q_o$ . In other words the loaded Q is always less than the unloaded Q ( $Q_L < Q_o$ ). Since measurement of the Q requires transmitting rf power through the cavity, it is not possible to measure the true  $Q_o$ . However, the measured Q ( $Q_m$ ) does approach  $Q_o$  asymptotically as coupling to the

cavity becomes very weak. For the specific case that the drive loop is matched to the input line (no reflection, so all power flows into the cavity) the half power theorem says that  $\frac{1}{2}$  of the power will be dissipated in the cavity and  $\frac{1}{2}$  of the power will be dissipated in the external circuit. In this case the measured Q is  $\frac{1}{2}$  of the unloaded Q [16].

$$Q_m = \frac{Q_o}{2}$$

In order to confirm that the Q is being measured correctly, transmission curves should be taken for both a matched condition and for a weakly coupled condition. If the ratio of these two Q measurements approaches 2, then the correct  $Q_o$  has been found.

Figure 83 shows a schematic drawing of two experimental conditions used for measurement of Q. In the matched state the drive loop is matched to the  $50 \Omega$  characteristic impedance of the input coaxial line so that all power from the NWA flows into the cavity. In this state, the measured Q is  $\frac{1}{2} Q_o$ . In the unloaded state power is weakly coupled into the cavity through an additional capacitive probe near the open end of the cavity. This probe is adjusted for a poor match (majority of incident power is reflected back to the NWA). “Weakly coupled” means that a negligible amount of rf power is coupled into and out of the cavity. A factor of 1000 at both the input and output was found to be sufficient. In this case  $-40$  dB at input and  $-40$  dB at output gave a transmitted signal below  $-80$  dB down from the input. The frequency response curve for the hybrid rf cavity is shown in Figure 84.

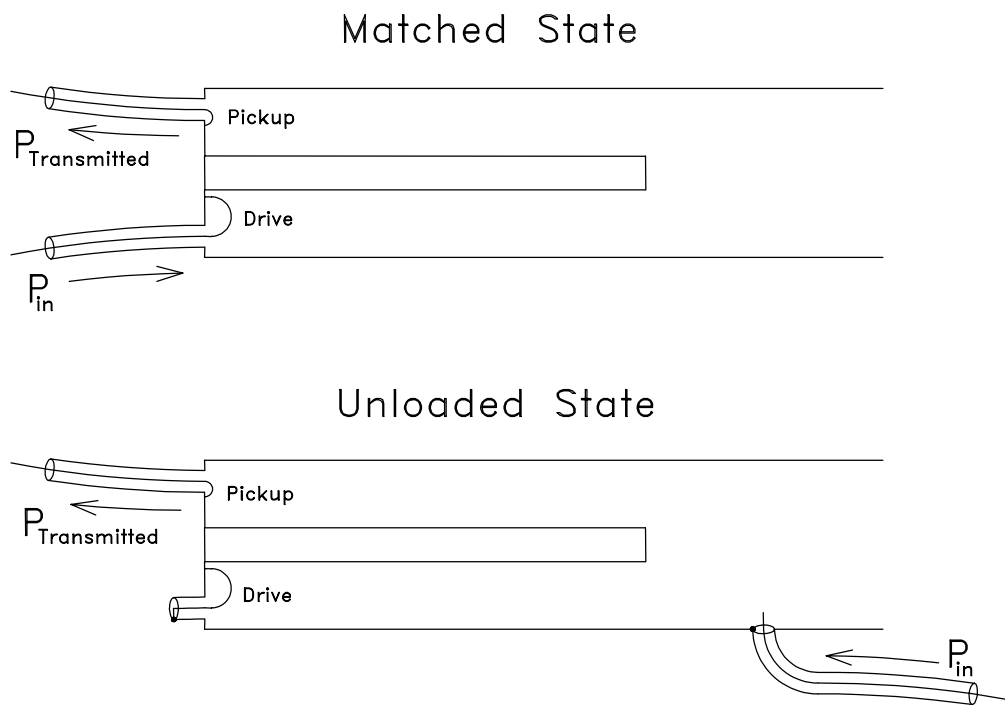


**Figure 83. Schematic drawing of the experimental setup for measurement of Q.**

**The matched state is the condition used when running the cavity at full power and accelerating beam.**

**However, measured Q approaches the true unloaded Q only in the unloaded state.**

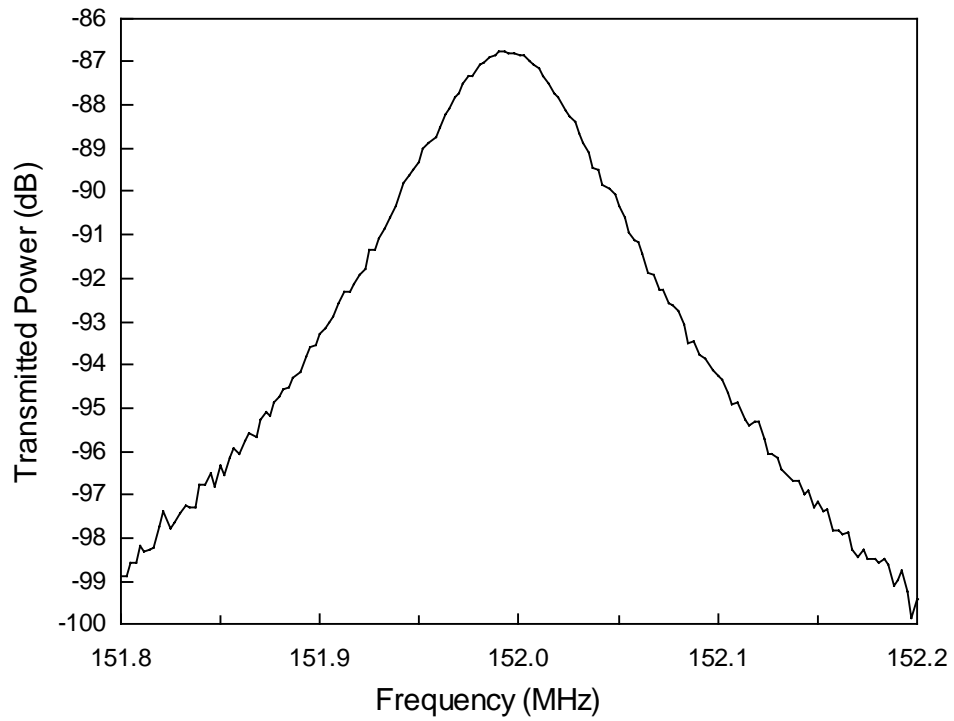
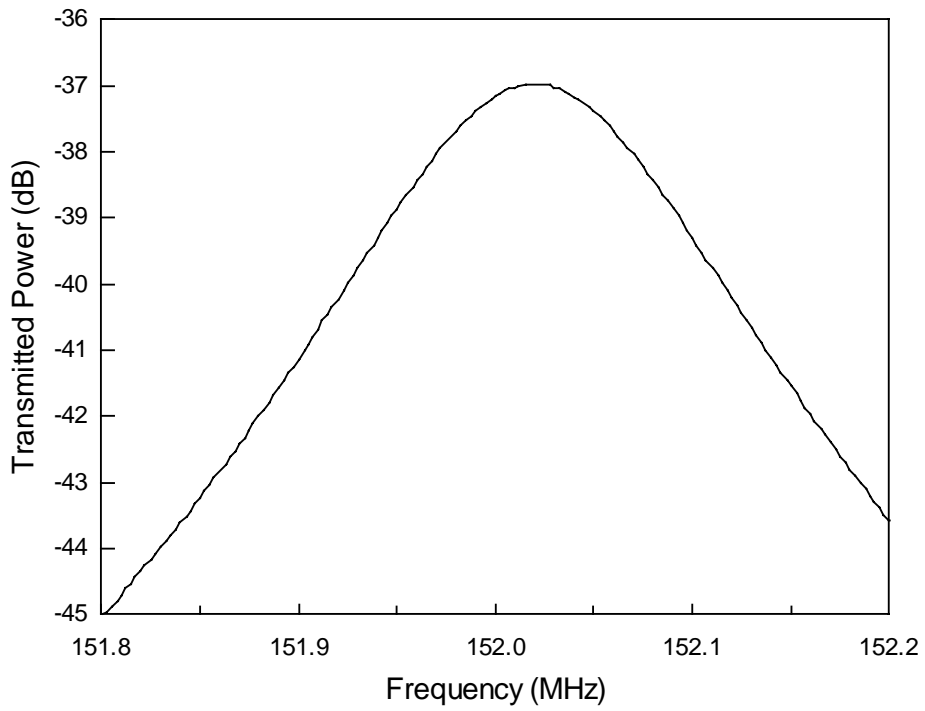


**Figure 84. Transmission frequency response curves used for measurement of the Q.**

**The matched state (top) gives  $f_0/\Delta f = 802$ , and the unloaded state (bottom) gives  $f_0/\Delta f = 1550$**

The measured Q of the hybrid rf cavity is  $Q \cong 1600$ . Therefore, calculation of  $R_s$  gives 41,400 k $\Omega$ , and the cavity voltage for 100 input power is  $V_o = 2880$  V. The results of method 1 are given in Table 8 below.

**Table 8. Results of method 1: Parameters for the hybrid rf cavity.**

Inner conductor radius: $a =$	$\frac{1}{2}$ (0.75") = 0.95 cm
Outer conductor radius: $b =$	$\frac{1}{2}$ (4.5") = 5.72 cm
Length of coaxial section: $\ell =$	9.7 cm
Capacitance of coaxial section: $C_\ell =$	1.5 pF
Capacitance of magnetron section: $C_m =$	39 pF
Resonant frequency: $f_o =$	152.02 MHz
$R_s/Q =$	25.85 $\Omega$
Quality factor: $Q =$	1600
Shunt resistance: $R_s =$	41,400 $\Omega$
Gap voltage (for $P_{in} = 100W$ ): $V_o =$	2,880 V

## **Method 2 (Calibration of Drive and Pickup Loops)**

As in method 1, the purpose here is to determine the gap voltage  $V_o$  for a given input power. The calibration technique of method 2 provides two important measurements. First, the ratio of gap voltage to pickup voltage ( $V_o/V_2$ ) is measured. This calibration factor allows  $V_o$  to be determined from the pickup voltage while the rf cavity is running at full power. Second, the ratio of gap voltage to drive voltage ( $V_o/V_1$ ) is measured. This allows the shunt resistance ( $R_s$ ) to be calculated and therefore is useful for confirming  $V_o$  that was calculated by method 1.

The three experimental conditions used for the calibration method are shown in Figure 85. The matched state is the same configuration that the cavity will run in when accelerating the beam. In this state, the drive loop is matched to the input line so that the impedance of the cavity looks like  $50 \Omega$  and all power flows into the cavity without being reflected. The pickup loop couples to the cavity fields and provides a small voltage signal which is proportional to  $V_o$ . In the forced state, a probe is attached directly across the open end of the cavity so that  $V_o$  can be forced to a known value. In this state either the drive voltage ( $V_1$ ) or the pickup voltage ( $V_2$ ) can be measured to obtain ratios ( $V_o/V_1$ ) and ( $V_o/V_2$ ).

The three configurations in Figure 85 are used to measure three voltage ratios:

( $V_1/V_2$ ) in the matched state

( $V_o/V_2$ ) in the forced state (for the pickup voltage)

( $V_o/V_1$ ) in the forced state (for the drive voltage)

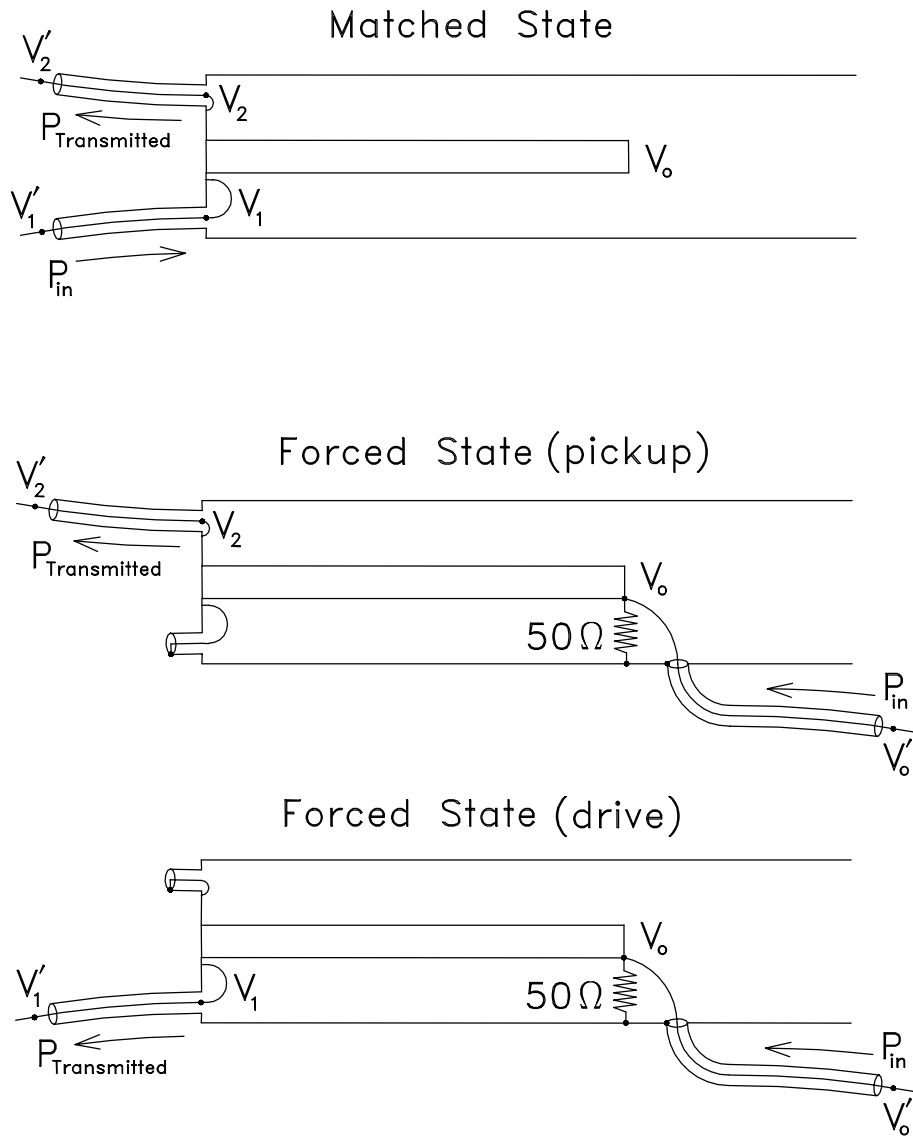


**Figure 85. Experimental setup for the calibration of method 2.**

**$V$  is a voltage at a probe, and  $V'$  is a voltage at the end of a cable.**

Voltage ratios are determined from power ratios measured with the network analyzer, therefore care must be taken to insure that the power can be related to the voltage on the line (i.e. no standing waves). For example, in the matched state, the

voltage at the input loop is known only if the drive loop is matched to the 50  $\Omega$  characteristic impedance of the input cable. In that case the voltage is related to the input power by:  $P_1 = \frac{V_1^2}{2(50\Omega)}$ . Now consider the forced state for measuring  $V_o/V_2$  as shown in Figure 85. The 50  $\Omega$  resistor across the open end of the cavity insures that no reflections occur and allows  $V_o$  to be related to the input power ( $P_o$ ) by:

$$P_o = \frac{V_o^2}{2(50\Omega)}$$

Since power coupled out by the pickup loop ( $P_2$ ) is sent to the transmission port of the NWA,  $P_2$  and  $V_2$  are related in the same way.

$$P_2 = \frac{V_2^2}{2(50\Omega)}$$

Under these conditions the voltage ratio can be calculated directly from the power ratio.

$$\frac{V_o}{V_2} = \sqrt{\frac{P_o}{P_2}}$$

where the power ratio is measured with the NWA in dB. Similarly for the drive ratio ( $V_o/V_1$ ). The three measured voltage ratios (after correcting for cable losses) are given in Table 9 at the end of this section.

When running the accelerator, the cavity will be run in the matched state, therefore we would like to equate  $\frac{V_o}{V_2}$  measured in the forced state with the actual  $\frac{V_o}{V_2}$  in the matched state. However, before making this assumption we must check that the measurements in the forced state did not alter the field profile in the cavity. If the field

profile is unchanged, then the drive to pickup voltage ratio ( $V_1/V_2$ ) measured in each state should agree:

$$\left(\frac{V_1}{V_o}\right)\Bigg|_{\text{forced state}} \left(\frac{V_o}{V_2}\right)\Bigg|_{\text{forced state}} \stackrel{?}{=} \left(\frac{V_1}{V_2}\right)\Bigg|_{\text{matched state}} \quad (4.3)$$

For actual measurements made on the hybrid rf cavity:

the left hand side gives:  $\left(\frac{V_1}{V_o}\right)\Bigg|_{\text{forced state}} \left(\frac{V_o}{V_2}\right)\Bigg|_{\text{forced state}} = \frac{1810}{31.2} = 58.0$

and the right hand side gives:  $\left(\frac{V_1}{V_2}\right)\Bigg|_{\text{matched state}} = 60.4$

The error between these two ratios is 4%, which indicates that measurements in the forced state give good agreement with the actual voltage ratios in the matched state.

Thus we can equate:  $\frac{V_o}{V_2}\Bigg|_{\text{matched state}} = \frac{V_o}{V_2}\Bigg|_{\text{forced state}}$

and:  $\frac{V_o}{V_1}\Bigg|_{\text{matched state}} = \frac{V_o}{V_1}\Bigg|_{\text{forced state}}$

This allows two important conclusions.

1) The first equation allows us to calculate the gap voltage from the pickup voltage when

the cavity is running in the matched state. The measured value of  $\frac{V_o}{V_2}\Bigg|_{\text{forced state}}$  is 1810,

therefore:  $\boxed{V_o = 1810 V_2}$  (4.4)

2) The second equation allows us to calculate  $R_s$  and  $V_o$  and therefore make a comparison with the results of method 1. If the drive loop is matched to  $50 \Omega$  so that no reflections occur, then the power on the input cable is equal to the power which flows into the cavity.

$$P_{\text{line}} = P_{\text{cavity}}$$

Relating power to voltage in the matched state gives:

$$\frac{V_1^2}{2(50\Omega)} = \frac{V_o^2}{2R_s}$$

so that:

$$R_s = 50\Omega \left( \frac{V_o}{V_1} \right)^2 \quad (4.5)$$

The measured value of  $\frac{V_o}{V_1}|_{\text{forced}}$  is 31.2 therefore:

$$R_s = 48,700 \Omega$$

The shunt resistance allows us to calculate the cavity voltage for a given input power using equation 4.1. Results of calibration measurements using method 2 are summarized in Table 9.

**Table 9. Three voltage ratios measured by the low power calibration method.**

Matched State: $V_1/V_2 =$	60.4
Forced State: $V_o/V_1 =$	31.2
Forced State: $V_o/V_2 =$	1810
Shunt resistance: $R_s =$	48,700 $\Omega$
Gap voltage ( $P_{\text{in}} = 100\text{W}$ ): $V_o =$	3,120 V

## Comparison Between Methods 1 and 2

The rf cavity voltage has been indirectly measured by two independent low power methods. The error in  $V_o$  between the two methods is 8%. Table 10 below gives a comparison of the results. The cavity voltage will be calculated using the average between these two methods.

**Table 10. Comparison between low power measurements made by method 1 and method 2.**

	<b>Low Power RF Measurements</b>		
	<b>Method 1</b>	<b>Method 2</b>	<b>Average</b>
$V_o/V_2 =$	1670	1810	1740
$V_o/V_1 =$		31.2	
$R_s/Q =$	25.85 $\Omega$		
$Q =$	1600		
$R_s =$	41,400 $\Omega$	48,700 $\Omega$	45,050 $\Omega$
(for $P_{in}=100W$ ) $V_o =$	2,880 V	3,120 V	3000 V

## High Power Measurements

The two measurement techniques above both use low power signals from a network analyzer. When running the cavity at high power, conditions may change due to rf heating. High power measurements also include errors due to the calibration of the Bird Watt Meter used to measure  $P_1$ , and the oscilloscope used to measure  $V_2$ . When using high power, the cavity is run only in the matched state, therefore the ratio  $V_1/V_2$  is used to make a comparison between high power and low power measurements.

High power measurements in the matched state give:  $\left(\frac{V_1}{V_2}\right)\Bigg|_{\text{High Power}} = 62.2$

The low power matched state results were found previously:  $\left(\frac{V_1}{V_2}\right)\Bigg|_{\text{Low Power}} = 60.4$

The error between low power and high power is 3 %. Since the uncertainty in the low power measurement is greater than 3%, this is considered good agreement. Therefore, the low power measurements summarized in Table 10 will be used to calculate  $V_o$  from the measured pickup voltage ( $V_2$ ).

Finally, it is important to note that while running the cavity at full power, only the pickup voltage should be used to determine  $V_o$ . In cases such as multipactoring, or if the cavity develops an arc, or even if the input signal is off resonance, then losses in the cavity will increase causing a mismatch at the drive loop, therefore some input power will be reflected. In such cases, the gap voltage is not proportional to the drive voltage. However since the pickup voltage couples power only from the actual cavity fields,  $V_2$  is always a reliable indicator of the cavity gap voltage

### 4.3.2 Summary of RF Measurements

Section 4.3.1 covered the experimental methods used to determine the cavity gap voltage ( $V_o$ ) by two independent methods. In method 1 measurements were made of the quality factor ( $Q$ ), the resonant frequency ( $f_o$ ), and the capacitance of the magnetron section ( $C_m$ ), then the capacitance of the coaxial section ( $C_c$ ) was calculated. From these,  $R_s$  was calculated using equation 4.2, so that  $V_o$  is known for a given input power (equation 4.1). Method 2 is a calibration of the pickup and drive loops. The cavity is driven from the open end so that  $V_o$  is known, then the voltages at the drive loop ( $V_1$ ) and the pickup loop ( $V_2$ ) are measured. Measurement of ( $V_o/V_1$ ) allows us to calculate  $R_s$  for comparison with method 1 (equation 4.5). Measurement of ( $V_o/V_2$ ) allows us to calculate the gap voltage from the pickup voltage when operating the accelerator. The error in  $V_o$  between these two low power measurements is 8 %.

High power measurements include additional errors due to rf heating and calibration of the Bird Watt meter and the oscilloscope. The error between high power measurements and low power measurements is 3%. This is good agreement, therefore the average between the two low power results will be used to calculate the gap voltage ( $V_o$ ) from the pickup voltage ( $V_2$ ) during the 50 keV ICRA experiment. Final rf results are summarized in Table 11 below.

**Table 11. Summary of rf cavity measurements.**

$f_o =$	152.02 MHz
$V_o/V_2 =$	1740
$R_s =$	45,050 $\Omega$
(for $P_{in}=100W$ ) $V_o =$	3000 V

#### **4.4 Alignment**

Alignment of the 50 keV ICRA was done in two phases.

- 1) During the initial assembly, all major components of the ICRA were aligned according to design specifications.
- 2) Later, the alignment was adjusted based on measurements of the injected beam.

A brief description of each process is given below.

##### Alignment to Design Specifications

The mounting structure discussed in section 3.2.6 has four pivot points which allow vertical and horizontal motion for positioning the major components (review Figure 80). The rf cavity was aligned with the magnetic axis and centered axially based on the magnetic field mapping results. A surveying scope was then aligned along the axis of the rf cavity by viewing center marks at each end. The scope provided a reference so that each component could be located relative to the magnetic axis. The surface of the lower ion source table (Figure 70) was shimmed to be level with the magnetic axis. A dial indicator standing on this table was used to level the electrostatic bending plates. Cross hairs were attached to the bend plates and the bend was shimmed to meet the z axis by sighting through the scope. Next, a square standing up on the table surface was viewed through the scope and a line was marked on the table directly below the z axis. From this reference line, the angled position of the ion source was plotted on the surface of the lower table, and the upper table of the ion source was aligned with the lines below. Position errors for this alignment process are estimated to be less than 1 mm.

## Alignment Based on Beam Measurements

The design alignment was sufficient for the injected beam to pass through the entire system, however the alignment was improved by making small position adjustments based on beam measurements. The improved alignment is based on two criterion:

- The ion source should be aligned with the local magnetic field line.
- The proton beam orbit should be centered on the axis of the accelerating cavity.

The injected beam contains three different ion species and each ion has a different radius of curvature in the B-field. If the beam extracted from the ion source is parallel with the B-field, then the  $\vec{v} \times \vec{B}$  force is zero and all ions move together in a straight line. However, a misalignment with the B-field causes the beam to split so that three separate beam spots are visible on the injection Faraday cup. By adjusting the angle of the ion source, these three beam spots were brought together into a single beam spot with a diameter of about 1 mm.

Later, computer modeling revealed that even when the beam is extracted directly along a field line, the curvature of the field line causes separation before the beam reaches the injection Faraday cup. The alignment which brings all 3 beam spots together on the injection Faraday cup is actually  $0.5^\circ$  off from parallel with the B-field line. Since all experimental data was taken using this condition, the same alignment has been used in the computer code.

The rf cavity was centered around the  $H^+$  beam by moving the extraction end of the entire rf cavity vertically and horizontally until the beam clips at the entrance plane of the magnetron (review pivot points Figure 80). The bend voltage is increased until the proton beam is just below mirroring so that there is zero axial spacing between turns. The entrance to the magnetron is the narrowest aperture in the system. When the beam clips there, the image observed on the extraction Faraday cup disappears. The process can be described as: up, down, move to center, then left, right, move to center. The result is to center the entrance of the magnetron around the proton orbit, as shown in Figure 86. The smallest resolution in the motion of the magnetron is 0.004", which is less than 1% of the entrance diameter (0.433"). Alignment data also provides a measurement of the beam orbit radius (see section 4.5.3)

The disadvantage of this method is that since the extraction end of the cavity is moved but the injection end is not, the final position of the cavity may be at some small angle to the magnetic axis. For the 50 keV ICRA the magnetron entrance was displaced by 0.063" which creates an angle of 5 mrad or 0.3°. This angle effectively causes a 2% degradation in the exit radius of the magnetron which corresponds to a 4% degradation in the final beam energy. A more complicated procedure can be imagined in which the injection end and the extraction end are both moved iteratively in order to center the cavity vertically and horizontally, while simultaneously keeping the cavity aligned with the magnetic axis. This procedure was not attempted because the degradation in final accelerated beam energy was considered insignificant.

## **4.5 Measurements of the Injected Beam**

The remainder of this chapter covers beam measurements made on the 50 keV ICRA experiment. In this section the goal is to understand the injected beam therefore the accelerating rf voltage is off in all cases. Beam measurements with rf on are covered in section 4.6.

The ion spectrum of the injected beam is studied in section 4.5.1. This is important so that only the proton beam is injected into the acceleration region because other ions can obscure measurements of the accelerated beam in section 4.6. Section 4.5.2 shows several measurements of the proton beam orbit radius which verify that the correct beam has been injected. Section 4.5.3 shows measured mirror curves which can be used to determine the spread in the axial momentum of the beam. 4.5.4 covers the methods used to determine the axial momentum and number of turns through the acceleration region. In section 4.5.5 the mirror curve and arc lengths are each used to estimate the emittance of the injected beam. These two estimates are used to place bounds on the emittance of the injected beam that will be used for computer simulation of the accelerated beam in section 4.6.

### 4.5.1 Ion Spectrum

The purpose of studying the ion spectrum of the injected beam is so that we can block all ions from entrance into the acceleration region except the proton ( $H^+$ ) beam. This is necessary so that extraneous beams do not obscure measurements of the accelerated proton beam made later in section 4.6. This section begins with a summary of the results, then each Figure is discussed in greater detail below.

#### Summary

The full ion spectrum (Figure 87) gives only rough agreement with the theoretical calculations because it is plagued with many complexities that are not accounted for by the theory. Results indicate that ions produced by the source are probably  $Ar^+$ ,  $H_2^+$ , and  $H^+$ , however we cannot draw any definite conclusions. These three ions are also observed visually as three distinct rings on the phosphor screen at the extraction end of the system (Figure 88). Visual observations of the beam are more reliable because they allow the user to see exactly when each ion beam clips. The technique used was to increase the bending voltage until all ion beams have clipped except the innermost proton beam (see Figure 86). Later in section 4.5.2, measurements of the beam radius are used to confirm that this is the proton beam. Figure 89 shows a comparison between the visual observations and an ion spectrum taken with the radial probe. This Figure is important because it allows us to identify at what bending voltage the  $H_2^+$  clips and where the mirror curve begins. The mirror curve is covered in section 4.5.3

### Current vs. Bending Voltage

Recall that both Argon and H<sub>2</sub> gas are leaked into the ion source (section 4.2). Therefore, the most likely constituents in the ion beam are: Ar<sup>+</sup>, Ar<sup>+2</sup>, Ar<sup>+3</sup>... and the ionized molecules: H<sup>+</sup>, H<sub>2</sub><sup>+</sup>, and H<sub>3</sub><sup>+</sup>. However, other common ions such as C<sup>+</sup>, N<sup>+</sup>, O<sup>+</sup>, CO<sup>+</sup>, CO<sub>2</sub><sup>+</sup>, H<sub>2</sub>O<sup>+</sup> and others are also possible.

As explained in section 2.5.4, ions with different charge or mass will have a different momentum, and therefore will orbit with different radius in the magnetic field. According to equation 2.72 the radius of each ion orbit is proportional to the root of its mass to charge ratio:

$$r \propto \sqrt{\frac{m}{q}}$$

Protons have the highest q/m available and therefore will have the smallest orbit radius of all constituents in the beam. As the bending voltage is increased, the radius of all ion beams increases until the outer beams clip on the entrance aperture of the magnetron.

Figure 86 shows the geometry.

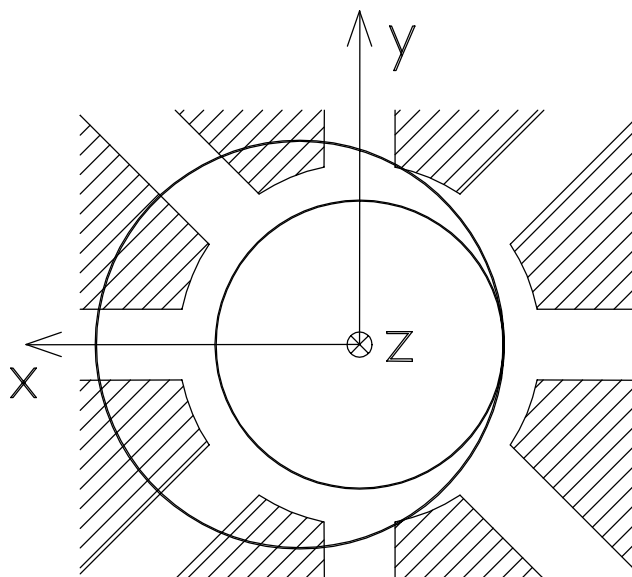


**Figure 86. Geometry of the ion beam as one constituent clips on the entrance to the magnatron. Here the bending voltage is turned high enough that the  $H_2^+$  beam (larger radius) has clipped on the entrance to the magnatron and the beam with the  $H^+$  (smaller radius) is centered on the z axis.**

Figure 87 shows the full ion spectrum taken by scanning over bending voltage and plotting the current on the extraction FC. We would expect the beam current to staircase downward each time an ion beam clips on the entrance of the magnatron. Vertical dotted lines show the theoretical calculation for where each ion should clip (equation 2.73)

Unfortunately the spectrum is plagued with additional complexities which are not described by the theory such as secondary electrons, beam scraping on the bend plate at low bend voltage, and an entrance aperture that is not perfectly round. Furthermore, the accuracy is limited by the fact that the beam is a spiral, so there is some variation in the radius at which the beam actually clips. This spectrum shows only rough agreement with theoretical values. The major constituents of the ion beam appear to be  $Ar^+$ ,  $H_2^+$  and  $H^+$ . However, we cannot draw any definite conclusions from this graph.

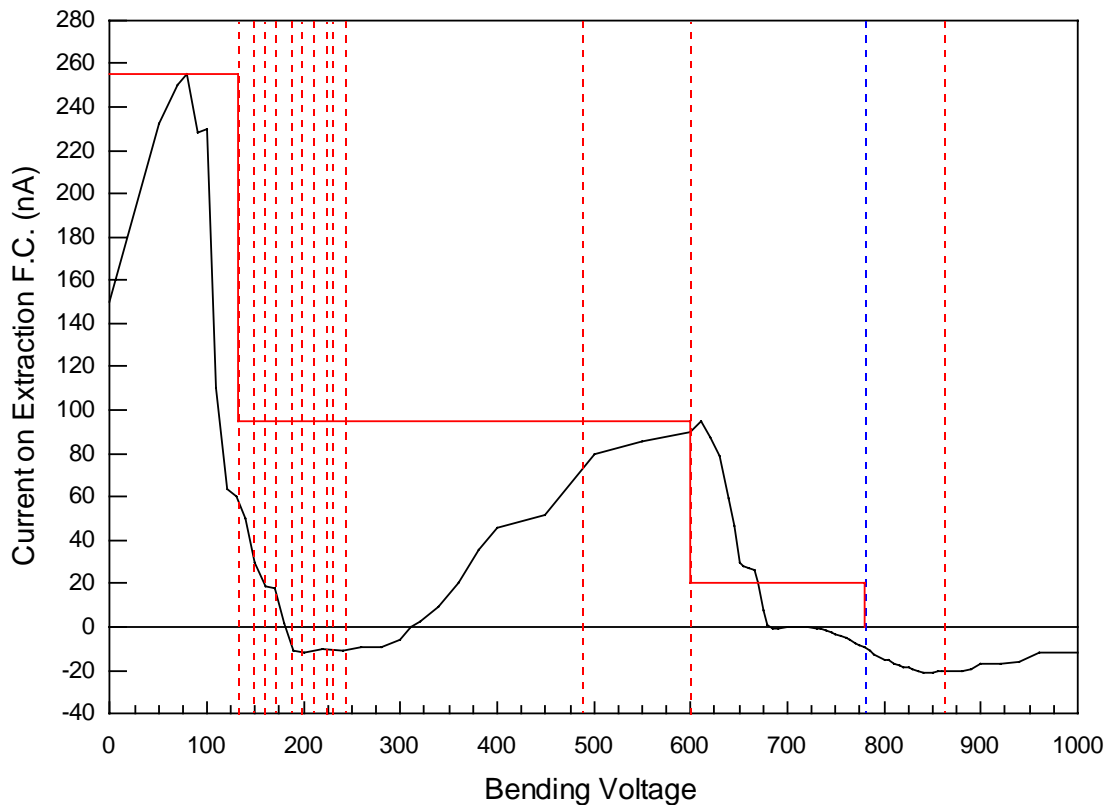


**Figure 87. Ion spectrum taken on the extraction FC. The solid black line shows experimental data. Theoretical values where each ion should clip have been calculated using equation 2.73 and are shown as vertical red dotted lines. From left to right:  $\text{Ar}^+$ ,  $\text{N}_2^+$ ,  $\text{O}_2^+$ ,  $\text{C}_2^+$ ,  $\text{Ar}^{+2}$ ,  $\text{H}_2\text{O}^+$ ,  $\text{N}^+$ ,  $\text{O}^+$ ,  $\text{Ar}^{+3}$ ,  $\text{C}^+$ ,  $\text{H}_3^+$ ,  $\text{H}_2^+$ , and  $\text{H}^+$ . The experimental value at which the  $\text{H}^+$  beam mirrors is shown as a blue dotted line. Using these calculated values, the expected theoretical curve is plotted as a solid red line.**

In theory this technique for analyzing the beam injected into an ICRA should be very useful. However in practice, the method must be improved in order to obtain more convincing results. Since agreement between the ion spectrum and theoretical calculations is so crude, it is necessary to rely on visual observations and on measurements of the beam orbit radius to identify the proton beam.

## Visual observations

Visual observations were important for understanding the ion spectrum. Phosphor coating on the extraction Faraday cup (described in section 3.2.5) produced an image of the beam at the extreme downstream end of the system. Figure 88 shows a drawing of the beam image that was observed. The Argon ring is not shown here because it clips at such a low bending voltage when the image of Figure 88 is still very small. As the bend voltage is increased, the  $H_2^+$  beam eventually clips on the cavity entrance and the outer ring in Figure 88 disappears. If the bend voltage is increased still further, the image of the inner ring eventually fades away as the  $H^+$  beam mirrors. In order to clip the  $H_2^+$  beam before the  $H^+$  mirrors, it was necessary to increase the injection energy from 5keV to 6.4keV. Even at this beam energy, the  $H^+$  beam mirrors before its radius becomes large enough to clip on the cavity entrance.

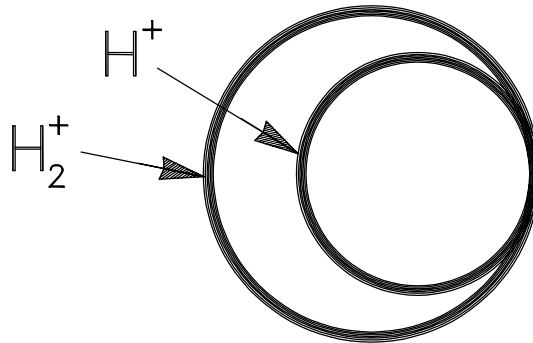


**Figure 88. Drawing of the beam image observed on the extraction Faraday cup. Here the bending voltage is high enough that both ion beams produce a full 360° ring. At lower bend voltages the image observed is less than 360° as will be described in section 4.5.4.**

The arc lengths shown in Figure 88 are greater than  $360^\circ$  because the bend voltage is high (near mirroring), however at lower bending voltages, arc lengths are less than  $360^\circ$ .

Arc

length data is used in section 4.5.4 as a measure of the spread in the axial momentum.

These visual observations can be used together with the radial probe (which has an electron blocker) to obtain a reliable ion spectrum. Figure 89 shows excellent correlation between the visual observations and drops in the beam current measured on the radial probe. This technique shows when the  $H_2^+$  beam has clipped, and therefore allows us to obtain the range of bending voltage for which only the proton beam is injected into the acceleration region. Furthermore, we can identify the region where the proton beam mirrors. The mirror curve is important because it provides information about the axial momentum spread. Section 4.5.3 will concentrate on the “mirror curve” in greater detail.

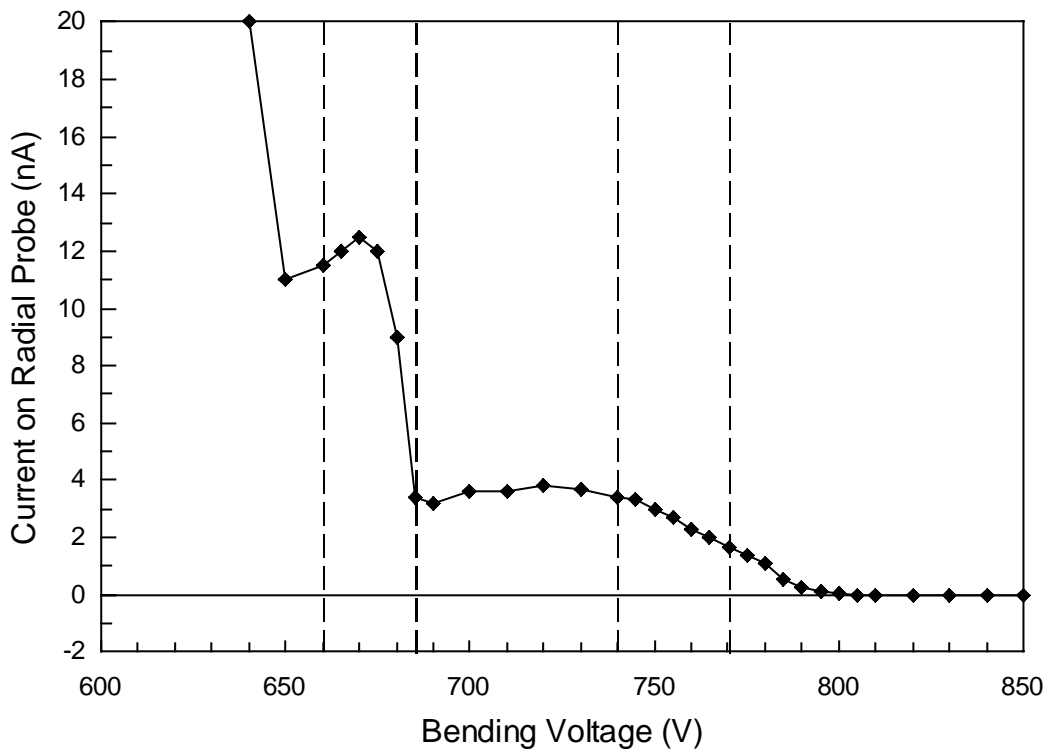


**Figure 89. Experimental data. Black diamonds represent beam current measured on the radial probe which is shielded from electrons showers. Dotted lines mark the range of bend voltage where the  $H_2^+$  beam was observed to clip visually, and where the  $H^+$  beam mirrors**

#### 4.5.2 Radius of Beam Orbit

The radius of the proton beam was measured using three different techniques. These measurements provide confirmation that the innermost ring in the beam image is the proton beam (review Figure 88). The results are summarized in Table 12 below.

**Table 12. Comparison between calculation and experimental data of the  $H^+$  beam orbit radius in the high B-field region. In each case the beam is just below mirroring ( $p_{\perp} \approx p_{total}$ )**

Method	$H^+$ orbit radius	Error relative to calculated
Calculated from known $V_{beam}$ and B-field	4.65 mm	-
Measured using radial probe.	4.5 mm	- 3 %
Measured from alignment data:	4.2 mm	- 10 %
Estimated from size of image on extraction FC	4.3 mm	- 8 %

For comparison, the radius of the  $H_2^+$  beam is calculated to be 6.58 mm. The most accurate measurement of the  $H^+$  orbit radius is done using the radial probe. An example of a radial probe scan is shown in Figures 97 and 98 in section 4.6.1.

#### Spread in beam radius

The radial spread in the injected proton beam ( $\Delta r$ ) was measured using alignment data (distance rf cavity is moved to cut across the beam). The result is.

$$\Delta r = 0.3 \pm 0.1 \text{ mm (at } z = 0\text{)}.$$

### 4.5.3 Mirror Curve

As explained in section 2.6.7, if an injected beam with zero emittance mirrors, then the current will drop to zero at one particular bending voltage. However the real injected beam has some finite emittance which leads to a spread in axial velocity.

Therefore, when the beam mirrors, current will drop over some range of  $V_{\text{bend}}$ . Section 2.6.7 showed that the range of  $V_{\text{bend}}$  is proportional to the spread in the axial velocity of the beam (Figure 62). Therefore, the mirror curve provides information about the emittance of the injected beam. In section 4.5.4 the mirror curve will be used to determine the axial momentum spread, and in section 4.5.5 the mirror curve will be used as a measure of the emittance of the injected beam.

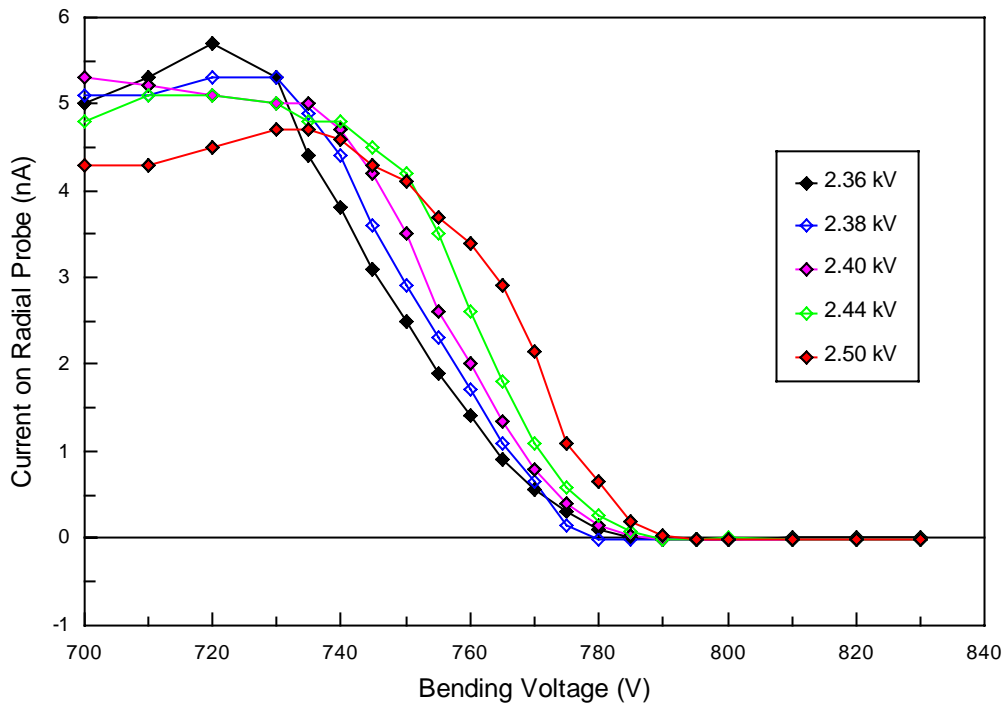


**Figure 90. Experimental mirror curve. Proton beam current on the radial probe vs. bend voltage for several different Einzel lens settings.**

Figure 90 shows a measured mirror curve. Proton beam current vs. bending voltage is plotted for several different Einzel lens settings. The Einzel lens affects the axial velocity spread, because it changes how parallel the beam is to B-field lines in the region before entering the electrostatic bend.

Small changes in the alignment of the ion source cause a significant shift in the mirror voltage. Figure 91 below shows the mirror curve which is relevant to the accelerated beam shown in section 4.6.1. This mirror data will first be used to determine the spread in  $p_z$  and the emittance injected beam in the following two sections.

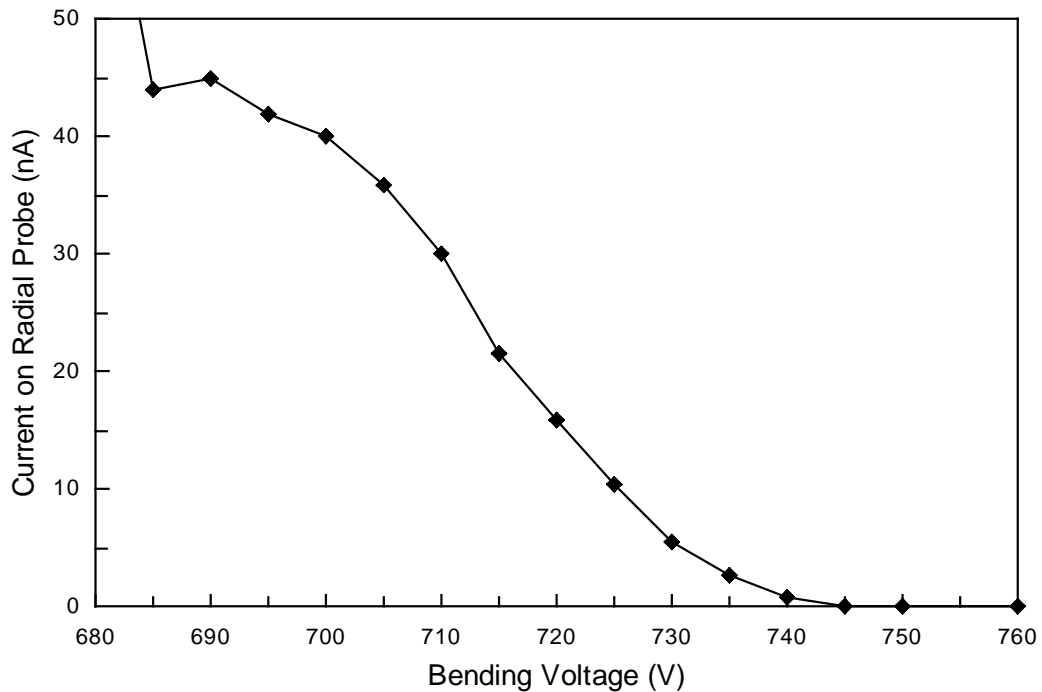


**Figure 91. Experimental data. Proton beam current on the radial probe vs. bend voltage. The Einzel Lens setting is 3.0 kV.**

#### **4.5.4 Number of Turns Through the Acceleration Region**

In this section beam measurements are used to determine how many turns the beam goes through in the acceleration region ( $N_{\text{turns}}$ ). Recall that if  $p_z$  is known then  $N_{\text{turns}}$  is also known (equation 2.75). Again, our purpose is to quantify only the injected beam (i.e. rf is off). Beam measurements have been made which allow two methods of determining  $N_{\text{turns}}$  and two methods of determining the spread in  $N_{\text{turns}}$ .

- 1)  $N_{\text{turns}}$  determined from the mirror curve
- 2)  $\Delta N_{\text{turns}}$  determined from the mirror curve
- 3)  $\Delta N_{\text{turns}}$  determined from the arc length on the extraction Faraday cup
- 4)  $N_{\text{turns}}$  determined from the change in the total # of turns thru the system

These four methods are discussed below.

### $N_{\text{turns}}$ from the Mirror Curve

The number of turns through the acceleration region ( $N_{\text{turns}}$ ) is obviously a function of the bend voltage ( $V_{\text{bend}}$ ). The calculation can be represented conceptually by:

$$V_{\text{bend}} \rightarrow \theta_{\text{bend}} \rightarrow p_z \rightarrow N_{\text{turns}}$$

The first step requires knowledge of the actual mirror voltage. The measured mirror curve of Figure 91 shows that the beam mirrors over a range of  $V_{\text{bend}}$  from 690V to 740V with a center mirror voltage of 715V. The mirror voltage allows the bend angle ( $\theta_{\text{bend}}$ ) to be scaled linearly with  $V_{\text{bend}}$  (equation 2.69). The parallel momentum at the exit of the electrostatic bend is simply  $p_{\parallel} = p_{\text{total}} \cos(\theta_{\text{bend}})$ . The beam then spirals into the high field region where  $p_z$  is given by equation 2.62. Once  $p_z$  is known at  $z = 0$ , equation 2.75 gives  $N_{\text{turns}}$ .

The last step ( $p_z \rightarrow N_{\text{turns}}$ ) is not in question because the magnetic field in the acceleration region is quite flat, and no other assumptions are involved. However, the analytical expressions for the first three steps involve several assumptions, therefore we must question the accuracy in calculating: ( $V_{\text{bend}} \rightarrow \theta_{\text{bend}} \rightarrow p_z$ ).

Figure 92 shows a comparison between  $p_z$  vs.  $V_{\text{bend}}$  calculated analytically and with the computer model. The maximum difference is less than 4% at  $V_{\text{bend}} = 700\text{V}$ . Therefore,  $p_z$  can be calculated analytically from experimental bend voltage. Keep in

mind that Figure 92 is an extrapolation based on the experimental mirror point to obtain  $p_z$  at lower bend voltages.

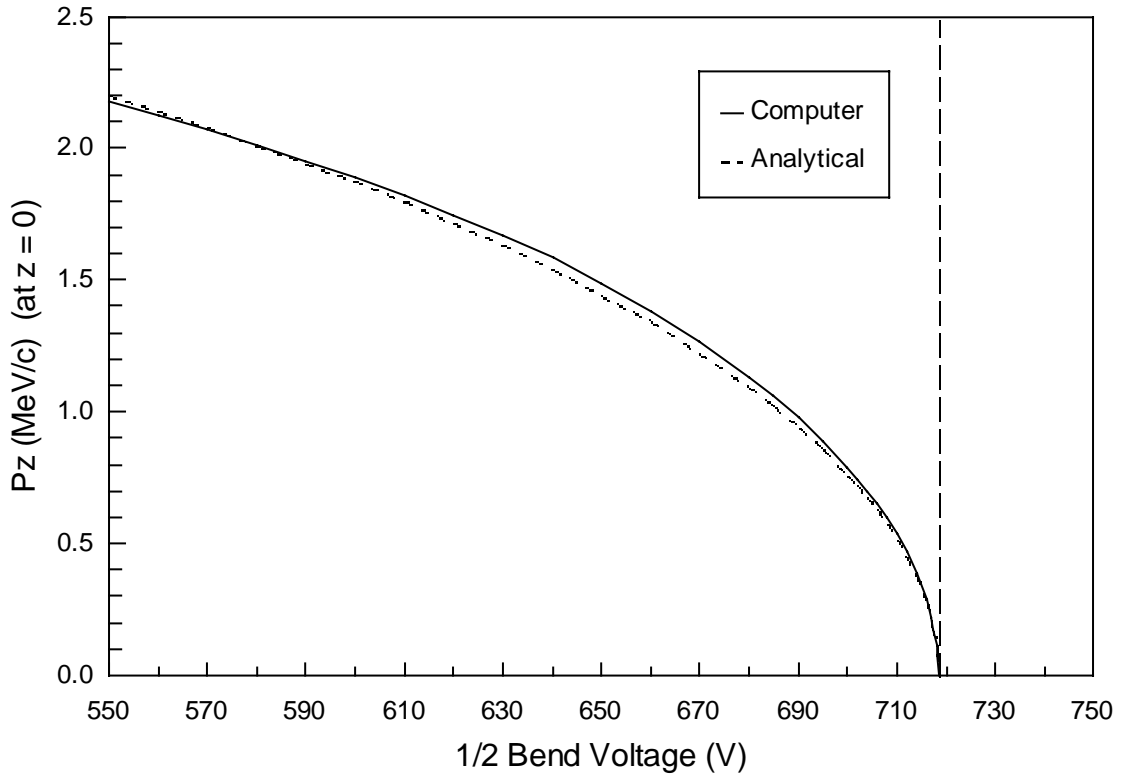


**Figure 92.** Analytical calculation of  $p_z$  vs bend voltage compared with the result from the full computer model. The analytical calculation depends on the mirror voltage, therefore the two curves meet at the mirror point a-priori.

$\Delta N_{\text{turns}}$  from the Mirror Curve

Figure 91 shows that the injected beam mirrors over a range of bend voltages from 690V to 740V. Figure 92 shows that  $V_{\text{mirror}}$  can be used to calculate  $p_z$  analytically for lower bend voltages. Similarly, the spread in  $V_{\text{mirror}}$ , allows us to determine  $\Delta p_z$  for lower bend voltages. Figure 93 shows how simply changing the mirror voltage in the analytical calculation causes a spread in  $p_z$ .

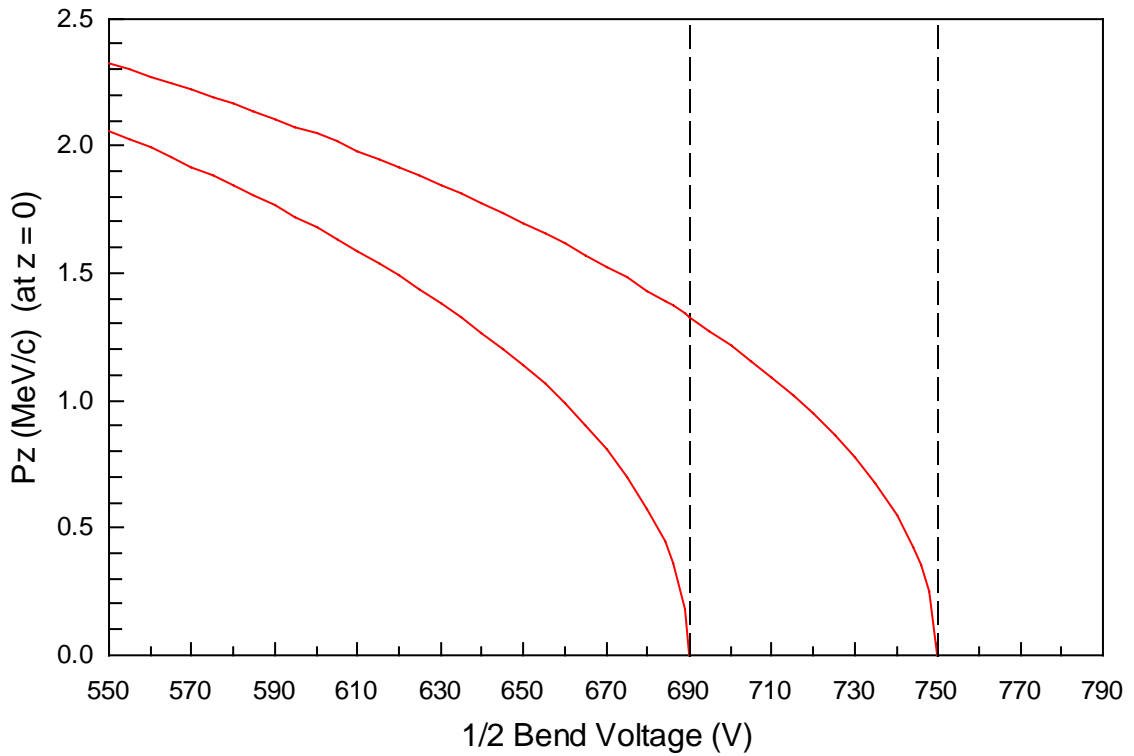


**Figure 93. Analytical calculation of the spread in  $p_z$  vs bend voltage**

This approach involves an approximation. Changing  $V_{\text{mirror}}$  in equation 2.69:

$$\theta_{\text{bend}} = \theta_{\text{mirror}} \left( \frac{V_{\text{bend}}}{V_{\text{mirror}}} \right),$$

effectively changes the length of the bending plates ( $\ell_{\text{eff}}$ ) in equation 2.55. Obviously changing the effectiveness of the bending plates does cause a spread in  $p_z$ . However, the source of the spread will be mostly  $dy/dz$  while the spread in a real beam is due to the full beam emittance which contains spreads in  $(x_s, x'_s, y_s, y'_s)$ . Since section 2.6.7 showed that the mirror voltage is nearly linear with  $p_z$ , regardless of the source of the spread, this approximation is thought to be good.

Figure 93 is useful for visualizing how the spread in  $p_z$  changes with bend voltage. The spreads in  $p_z$  and  $N_{\text{turns}}$  both increase with  $V_{\text{bend}}$ . In the limit that the beam mirrors, the spread in  $N_{\text{turns}}$  becomes infinite, however the spread in  $p_z$  ranges from 0 to  $p_z$ . Table 13 summarizes the calculation of  $p_z$  and  $\Delta p_z$  and gives  $\Delta N_{\text{turns}}$  and  $N_{\text{turns}}$ .

**Table 13.  $p_z$  and  $\Delta p_z$  as well as  $N_{\text{turns}}$  and  $\Delta N_{\text{turns}}$  of the injected beam calculated from experimental mirror data of Figure 91.**

$\frac{1}{2} V_{\text{bend}}$ (V)	$p_z$ (MeV/c)	$\Delta p_z/p_z$ (MeV/c)	$N_{\text{turns}}$	$\Delta N_{\text{turns}}$
650	1.49	38 %	4.0	1.7
660	1.38	45 %	4.3	2.3
670	1.26	57 %	4.7	3.5
680	1.13	76 %	5.3	6.2
690	0.98	100 %	6.1	$\infty$
700	0.79	100 %	7.5	$\infty$
710	0.53	100 %	11.1	$\infty$

$\Delta p_z$  from the Arc Length on the Extraction Faraday cup

The image of the beam shown in Figure 88 has an arc length ( $\Delta\theta$ ) greater than  $360^\circ$  because the bending voltage is high. However at lower bending voltages, the arc length observed is less than  $360^\circ$  as shown in Figure 94. It was shown that the arc length is proportional to the spread in  $p_z$  (section 2.6.7), therefore arc lengths less than  $360^\circ$  can be measured and used to determine  $\Delta p_z$ .

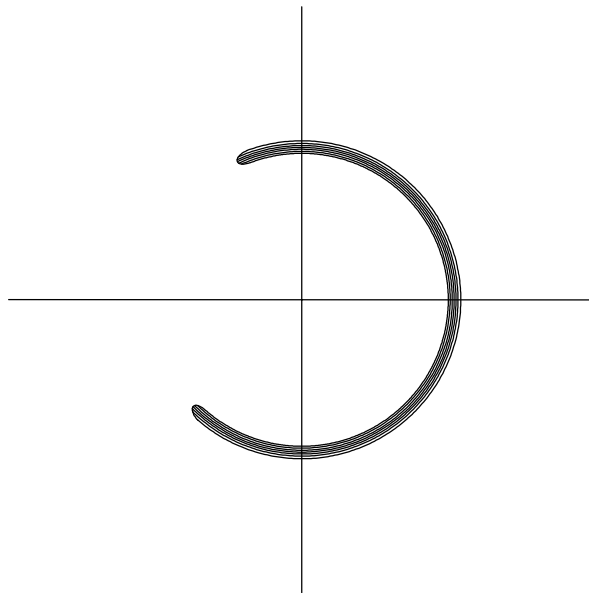


**Figure 94.** Drawing of the proton beam image observed on the extraction Faraday cup

The arc length can only be measured for low bending voltages, where  $\Delta\theta < 360^\circ$ .

For the 50 keV ICRA, the beam mirrors at 690 – 740 V. Operating bend voltages are in the range of 650 to 710 (4 – 11 turns, Table 13), however above 610 V the arc length becomes greater than  $360^\circ$  and therefore cannot be measured.

**Table 14.** Arc lengths observed visually on the extraction Faraday cup ( $V_{\text{Einzel}} = 2.8 \text{ kV}$ )

$\frac{1}{2} V_{\text{bend}}$	$\Delta\theta$
540 V	$120^\circ$
600 V	$180^\circ$
610 V	$360^\circ$

Since  $\Delta\theta$  is greater than  $360^\circ$  at the operating bend voltages, we must measure  $\Delta\theta$  at lower bend voltages and then extrapolate forward to higher  $V_{\text{bend}}$ . The method used here is to choose an emittance which produces an arc length that is consistent with the measured data, then use the computer code to track this emittance at higher bend voltages. This method is used in section 4.5.5.

Measurement of the arc length should be useful for future ICRA designs, particularly if the emittance of the injected beam is small enough (or bend voltage low enough) that arc lengths are less than  $360^\circ$  at the operating bend voltage. This would provide a direct measure of  $\Delta p_z$  without extrapolating.

p<sub>z</sub> from Total Number of Turns Through the System

As the bending voltage increases, the total number of turns through the entire system increases. This means that the image of the beam arc length on the extraction FC will rotate in the same direction that the beam turns (clockwise as viewed along +z). Angular positions of the trailing edge of the image were recorded for several bending voltages. This data provides the rate of change of the final angle vs. bend voltage

$\frac{d\theta_{\text{final}}}{dV_{\text{bend}}}$ , which can be verified using the computer model. The results are shown in

Table 15.

**Table 15. Rate of change of total number of turns (N) through the 50 keV ICRA.**

**Visual observations compared with computer result (using  $V_{\text{mirror}} = 745$  V for trailing edge of image).**

$\frac{1}{2} V_{\text{bend}}$	<b>Experimental Observation</b>	<b>Computer Result</b>
500 V	N	17.2
530 V	N + 0.5	17.2 + 0.70

560 V	N + 1.0	17.2 + 1.43
580 V	N + 1.5	17.2 + 1.92
<b>Average <math>\Delta N =</math></b>	<b>0.5</b>	<b>0.64</b>

The disagreement between observation ( $\Delta N = 0.5$ ) and the computer model ( $\Delta N = 0.64$ ) is small and could easily be attributed to errors in the visual observation. Therefore, this data is taken as confirmation that the computer results of Figure 92 are correct.

#### 4.5.5 Injected Beam Emittance

Section 4.6 will present measurements of the accelerated beam current. In order to compare with theory, an injected beam of finite emittance must be simulated by using the full computer code to track many single particle trajectories. Therefore it is first necessary to determine the emittance of the injected beam.

In section 2.6.6 we saw that the acceptance phase space of the rf driven magnetron is most sensitive to the spread in  $p_\theta$  (or equivalently, the spread in  $p_z$ ). Section 2.6.7 showed that the mirror curve and the arc length are both good measures of the spread in  $p_z$ . Therefore, the method used here is to use the computer model to choose an emittance which is consistent with beam measurements of the mirror curve, and the arc length. In this way, the emittance chosen will be consistent with the  $\Delta p_z$  and therefore will produce a similar accelerated beam current in section 4.6. The model used for the emittance of the injected beam was shown in section 2.6.7.

## Mirror Curve

Figure 95 shows mirror curves generated for several different injected beam emittances using the computer model. The experimental mirror curve (relevant to the accelerated beam in section 4.6) has been normalized to its peak value and is shown in black. The beam with  $0.35\pi$  mm mrad (red) has a much narrower range of mirror voltage than the experimental data. However, the beam with  $3.7\pi$  mm mrad (orange) clearly has a much wider range of mirror voltage than the experimental data. The range from  $0.8\pi$  to  $2.2\pi$  mm mrad gives close agreement with the experimental data.

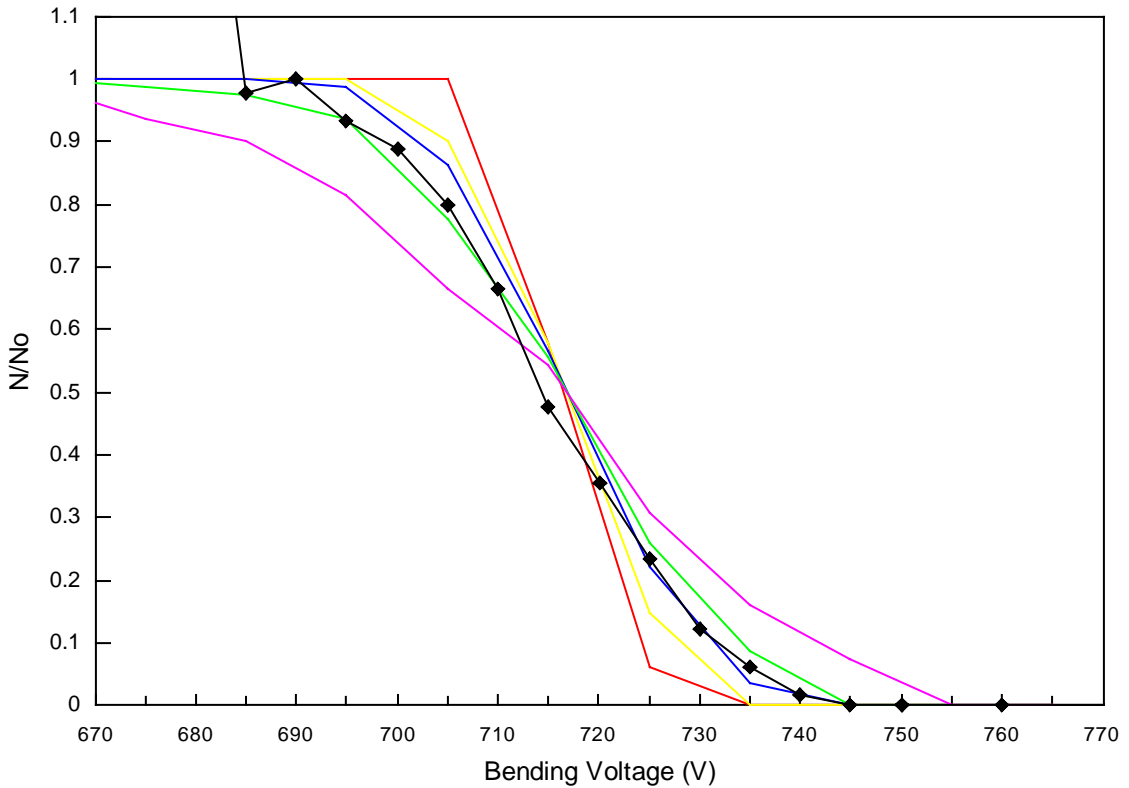
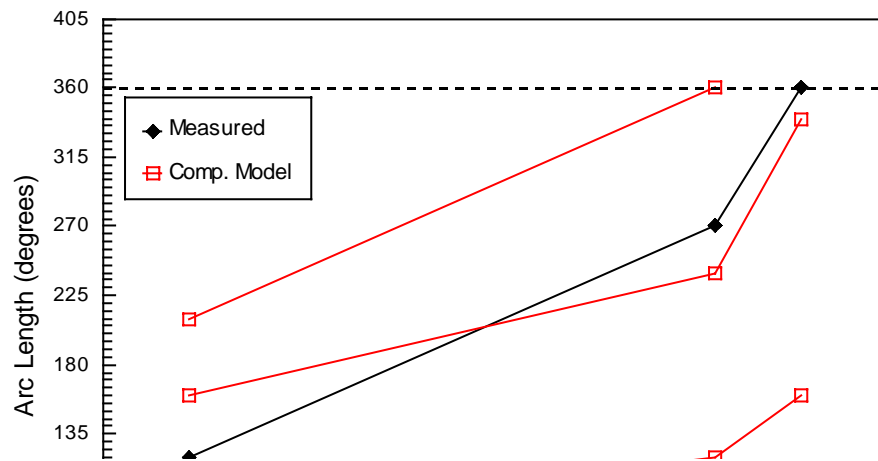


**Figure 95. Comparison between computer generated mirror curves and experimental data. Experimental data (black diamonds) is normalized to its peak value (45 nA). The 5 solid lines represent computer generated mirror curves for 5 different injected emittances.**

## Arc Length

Section 2.6.7 described the how the computer model can be used to reproduce the arclength on the extraction Faraday cup. Experimental measurements of the beam arc lengths were given in Table 14. Figure 96 shows a comparison between experiment and the computer model for three different injected beam emittances. Arc lengths indicate that the injected beam emittance is roughly  $0.35\pi$  mm mrad.

Comparing the results from the mirror curve and the arc length indicates that the emittance of the injected beam is in the range from  $0.35\pi$  to  $2.2\pi$  mm mrad (unnormalized).



$$\varepsilon = 0.8 \pi$$

$$\varepsilon = 0.35 \pi$$

$$\varepsilon = 0.1 \pi$$

**Figure 96. Arc length increases with bend voltage. The experimental data from Table 14 is plotted. The computer model is used to generate arc lengths for three different injected beam emittances:  $0.1\pi$ ,  $0.35\pi$ , and  $0.8\pi$  mm mrad (emittances are un-normalized) .**

#### **4.6 Measurements of the Accelerated Beam**

In the previous section, measurements of the mirror voltage and the arc length were used to place bounds on the injected beam emittance. Section 4.6.1 below shows the measured radial distribution of the beam with rf on and with rf off. The radial distribution is then converted to an energy distribution. An injected beam emittance is selected within the bounded range and used in the computer model to generate energy distribution curves. Computer results for several energy distribution curves are compared with measured data.

Finally, section 4.6.2 shows the measurement of the accelerated beam current while sweeping over the B-field. This “resonance width” is then compared with the theoretical resonance width using the computer model.

#### 4.6.1 Energy Distributions

This section covers the measured radial distribution and energy distributions for the accelerated beam. First, the radial probe data is corrected for errors in order to recover the full beam current at each radial position. Visual data is discussed. Then the energy distribution is calculated from the radial distributions and the result is compared with the results from the computer model.

Figure 97 shows raw experimental data taken on the radial probe with the rf on and off. The beam current which strikes the radial probe is measured as the probe is moved from large radius inward toward  $r = 0$ . When the rf is on, beam current is clearly accelerated to a much larger radius than with rf off.

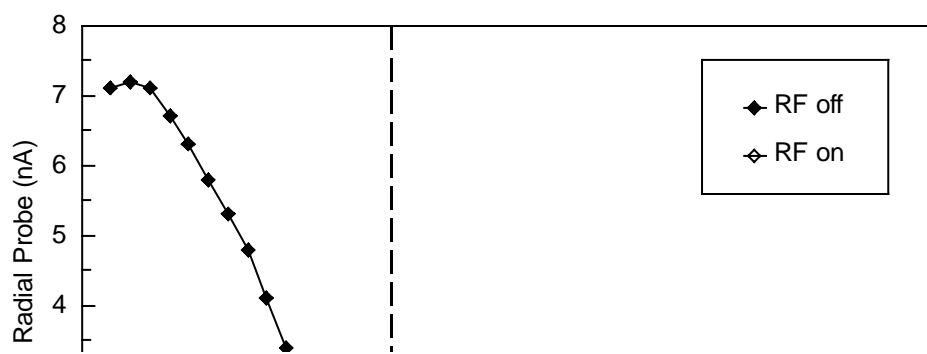


**Figure 97. Measured radial distribution with rf on and off (raw data). Beam current on the radial probe is plotted vs. radial position of the radial probe. Vertical dotted lines mark the calculated radius of the injected beam and maximum radius corresponding to the exit diameter of the magnetron.**

The reader may want to review the design of the radial probe as explained in section 3.2.5 on beam diagnostics. Since the radial probe is designed to capture 100% of the beam when it is moved all the way in to  $r = 0$ , the data is an integrated distribution. In other words, every point on the graph represents the sum of all beam current with radius equal to or greater than the radius read off the graph.

Consider the unaccelerated beam data shown in Figure 97. According to calculations we expect the 6.4 keV proton beam at the radial probe to have an orbit radius of  $r = 7.9$  mm and a radial spread of about  $\Delta r = 0.4$  mm. Thus, we would expect the measured beam current to be zero for any radius above roughly 8 mm, but then rise to 100% and remain constant for all lower radii. This theoretical curve is shown as a solid line in Figure 98 below. The apparent energy spread in the raw data of Figure 97 is caused by the sloped inner edge of the radial probe cutting across the beam orbit radius (refer to Figure 73). This is the first of three effects on the radial probe data which must

be mathematically corrected. Corrections to the radial probe data were explained briefly in section 3.2.5. They are:

- 1) Slope on the inner edge of the probe
- 2) Beam lost on the electron blocker
- 3) Axial turn spacing longer than the probe length

The effects of 1) and 2) are largest for beams with small radius. The effect of 3) is largest for beams with large radius. The rf off data has been corrected for all three effects. The rf on data has been corrected for 2) and 3) only. The effect of 1) on the accelerated data has not been corrected for. The distortion caused by this effect is largest at low radius and goes to zero at 22mm (50 keV field line). Furthermore, the correction would shift

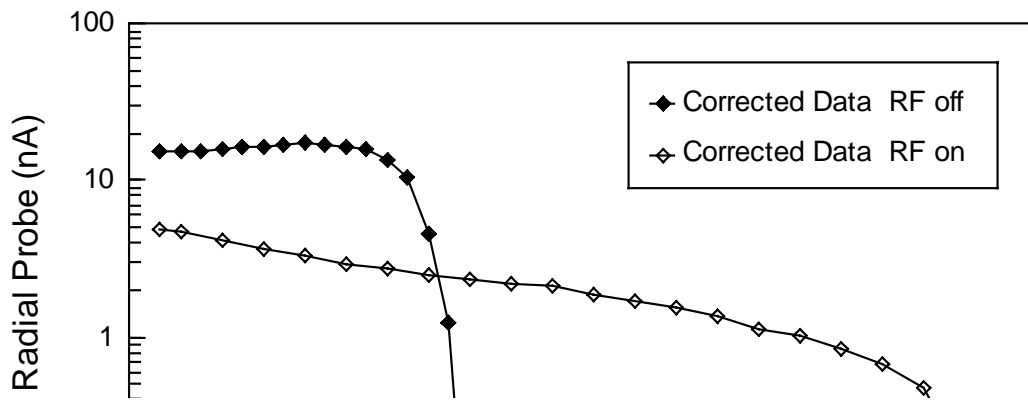
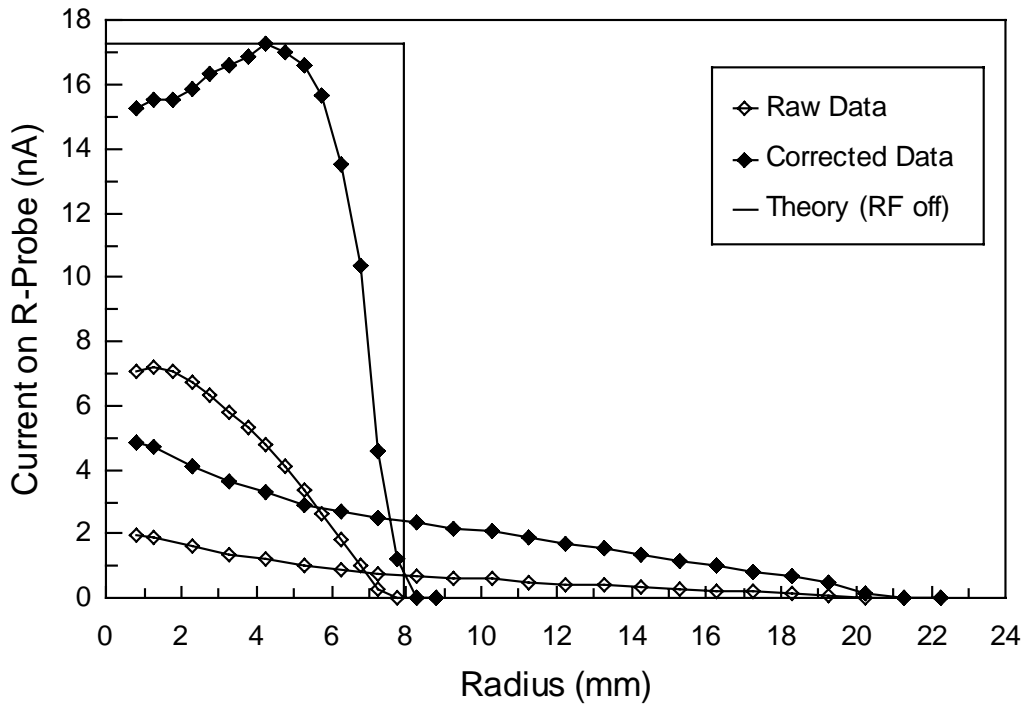


**Figure 98. Top graph: Raw data and corrected data are shown for rf on and off. The solid line shows a theoretical curve for the rf off case only. Bottom graph: The corrected data for rf on and off is shown on a log scale in order to show the accelerated data more clearly.**

beam current toward higher radius, therefore neglecting this correction leads to a conservative energy distribution. Details of the radial probe corrections are given in the Appendix.

In Figure 98 above, the top graph shows raw data, and corrected data from the radial probe (rf on and off). The theoretical curve is shown as a solid line (for rf off only). The lower graph in Figure 98 shows the corrected experimental data on a log scale. The log plot provides a better view of the accelerated beam current and allows one to see at what beam radius the current drops off. The accelerated proton beam current is 0.5 nA (3 %) at 19.3 mm and drops to 0.2 nA (1 %) by 20.3 mm.

The purpose of the radial probe is to obtain an energy distribution (current vs. energy). The radial distribution can be converted to an energy distribution using  $E \propto r^2$ . However before doing this, it is first necessary to consider visual observations which show that this relation is valid.

### Visual observations

We wish to convert radial probe data to beam energy in order to obtain a current vs. energy distribution. However, relating radius to energy by ( $E \propto r^2$ ) assumes that each orbit in the accelerated beam is centered on the z axis. Computer modeling indicates that the extracted beam is centered around the z axis, however we require experimental verification. Visual observation provides this verification.

The ability to observe an image of the beam on the extraction Faraday cup is as useful for understanding the accelerated beam as it was for understanding the injected beam. When the rf power is turned on, the image of the injected beam with narrow  $\Delta r$  (see Figure 88) is observed to bloat up into a large diffuse cloud which can cover nearly the entire extraction Faraday cup. When the radial probe is moved into the accelerated beam, it casts a shadow into this image as shown in Figure 99. The shadow observed is at approximately  $90^\circ$  azimuthal rotation from the orientation of the radial probe. Furthermore, the shadow moves inward as the probe moves in, leaving a circular image in the center undisturbed. These observations are consistent with a spiral trajectory and are taken as evidence that the beam does consist of large orbits centered around the z axis.

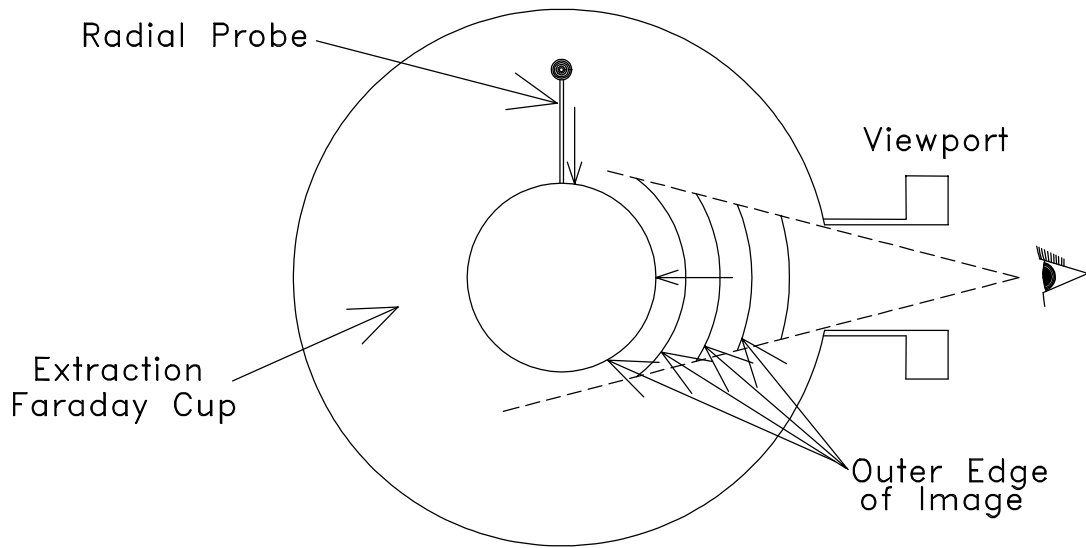


**Figure 99. Drawing of visual observations on the extraction Faraday cup. This axial view shows the extraction Faraday cup which is located  $\approx 7''$  further down stream (into the page) than the radial probe. The radial probe casts a shadow at  $90^\circ$  rotation from the probe. The edge of the shadow moves inward as the radial probe is moved inward.**

### Energy Distribution

When converting the beam orbit radius to energy, the radius must first be transformed back to the exit of the magnetron (equation 2.59) where the momentum is nearly all in the  $\theta$  direction. Then using the known magnetic field,  $p_\theta$  can be calculated (equation 2.1) and converted to the beam energy. This method neglects the axial beam energy at the exit of the magnetron (about 1 keV in this case). Figure 100 below, shows the data from the corrected radial distribution of Figure 98 which has been converted to an energy distribution.



**Figure 100. Measured energy distribution with rf on and off. Data is taken from the corrected radial distribution of Figure 98. Dotted lines mark the injection energy and peak design energy.**

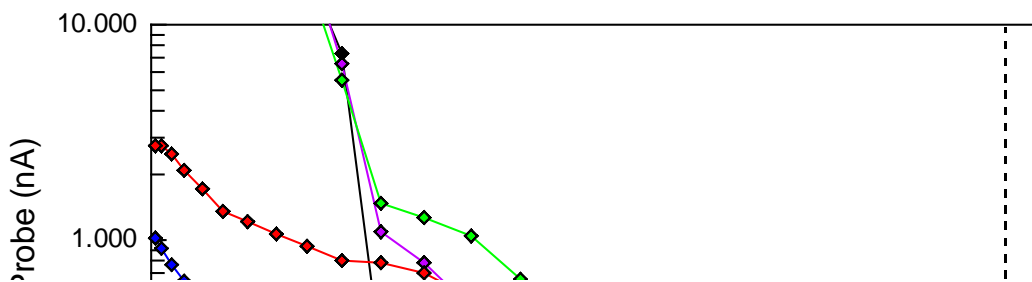
The injected beam energy (6.4 keV), and the energy corresponding to the exit radius of the magnetron (48 keV) are both marked with vertical dotted lines. The accelerated proton beam current is 7 % above 24 keV ( $0.5 E_{\text{design}}$ ), then drops to 1 % above 42 keV ( $\approx 0.9 E_{\text{design}}$ ). A smaller fraction may be accelerated as high as 46 keV.

Figure 101 shows a comparison between experimental data and the computer model. The experimental data has been normalized using the peak value of the unaccelerated beam. In section 4.5.5 measurements of the arclength and mirror curves were used to place bounds on the emittance of the injected beam. An emittance was selected within this range ( $0.35\pi - 2.2\pi$ ) which gives reasonable agreement with the experimental energy distribution. The emittance used in Figure 101 is  $2.2\pi$  mm mrad.



**Figure 101. Comparison between corrected experimental data and the computer generated energy distribution. In each case:  $V_0 = 1.7$  kV,  $\frac{1}{2}V_{\text{bend}} = 740$  V,  $V_{\text{Einzel}} = 2.5$  kV. The computer model uses a  $2.2 \pi$  mm mrad injected beam emittance.**

Figure 102 below shows experimental energy distributions taken for several different bending voltages while  $V_0$  is held constant. This data illustrates two important characteristics. First, at low bend voltages (axial momentum is high so  $N_{\text{turns}}$  is low) the beam is not accelerated to full energy. As the bend voltage is increased (axial momentum decreases so  $N_{\text{turns}}$  increases) the accelerated beam current moves to higher energies. The experimental data of Figure 102 shows the expected trend. The second trend to notice is that when the beam is accelerated to higher energies, (high  $V_{\text{bend}}$ ) the total beam current (above  $E = 0$ ) decreases. This indicates that a significant portion of the beam strikes the wall inside accelerating cavity. This trend was observed in Figure 63.



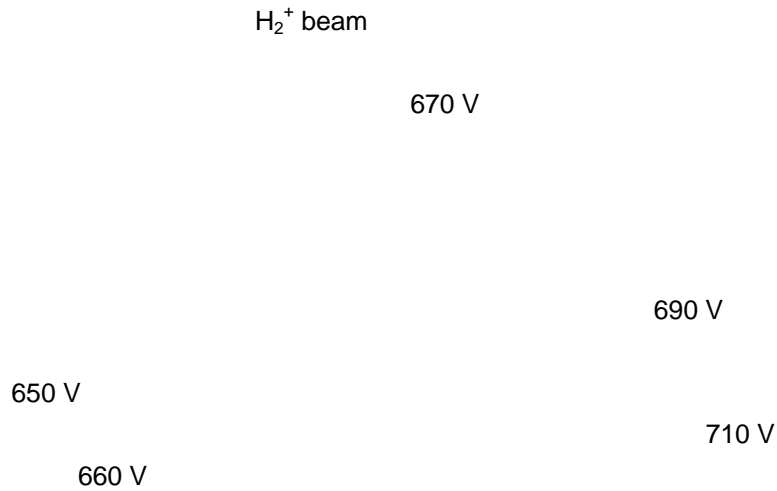
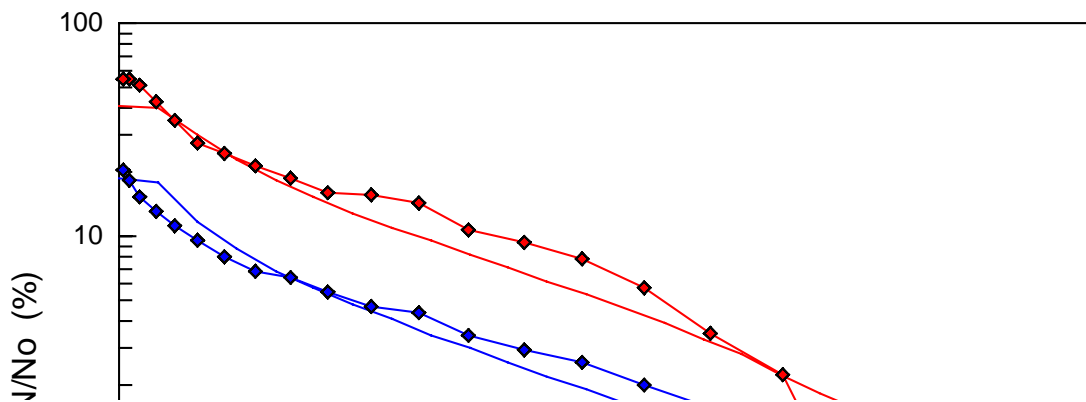


**Figure 102. Measured energy distributions for several bending voltages.**

**Cavity voltage is 1.4 kV,  $V_{\text{Einzel}} = 2.7$  kV, Mirror voltage ranges from 690 – 745 V.**

Finally, notice that for  $V_{\text{bend}} = 650, 660,$  and  $670$  V the  $\text{H}_2^+$  beam is present and shows up as a large increase in beam current at about 12 – 13 keV. The conversion from radial distribution to energy distribution is valid only for the proton beam, therefore this data should be ignored.

Comparison between this experimental data and the computer generated energy distributions shows good correlation at high bend voltages but increasingly worse agreement at lower bending voltages. Figure 103 compares computer with experimental data for bending voltages of 690 V and 710 V. Figure 104 shows the comparison for 650, 660, and 670 V. The emittance used in the computer code is  $2.2 \pi$  mm mrad.

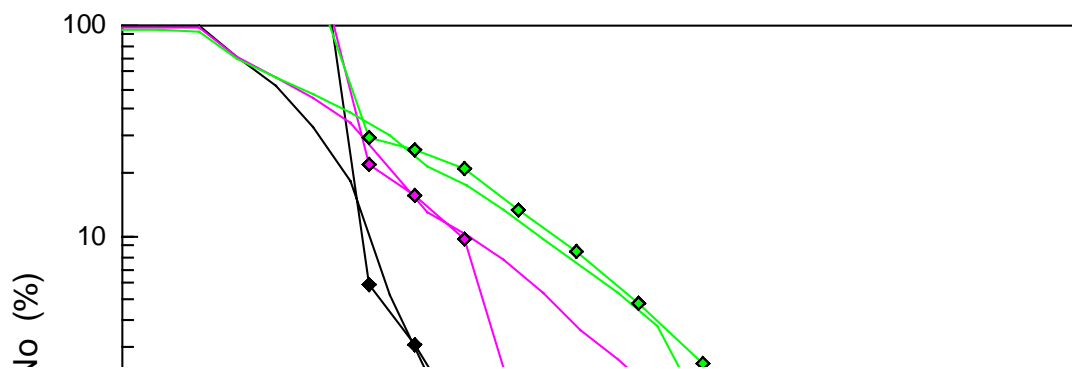
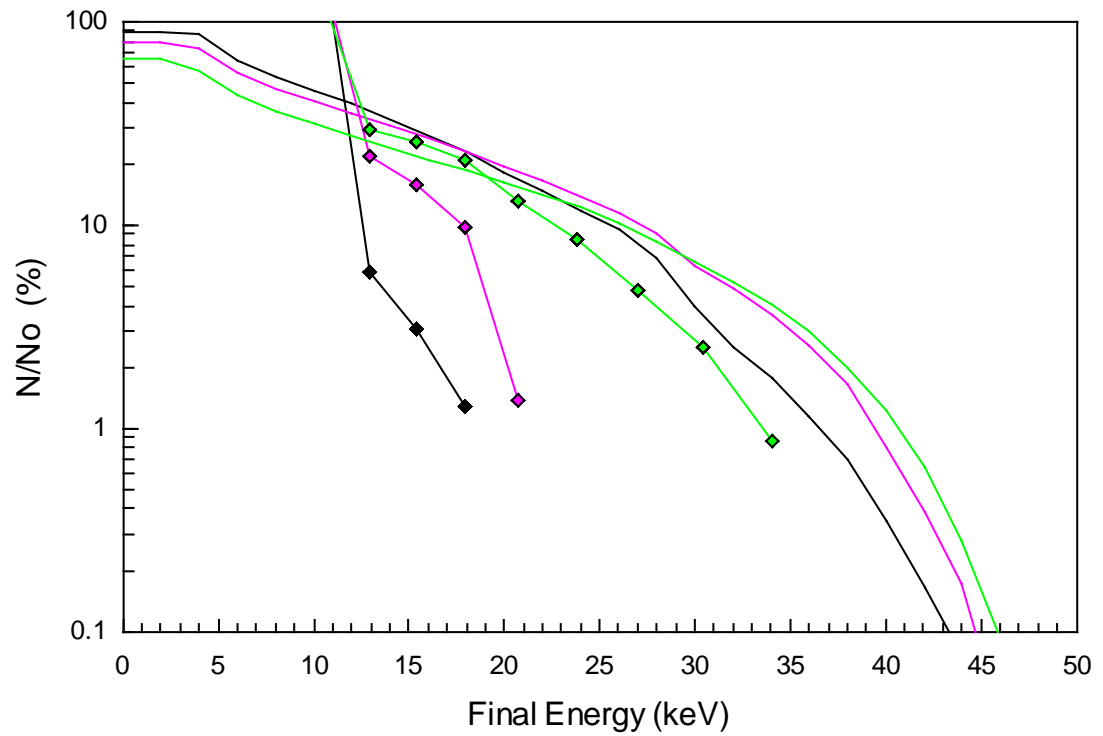


Computer Model  
 $V_{\text{bend}} = 690 \text{ V}$

Measured  
 $V_{\text{bend}} = 710 \text{ V}$

Computer Model  
 $V_{\text{bend}} = 710 \text{ V}$

**Figure 103.** Experimental data from Figure 102 is compared with the computer result. Here, bending voltages of 690 V and 710 V are used in the computer and experiment both.



Measured 660 V  
Computer Model 630 V

Measured  
650 V  
Computer Model  
605 V

**Figure 104. Experimental data from Figure 102 is compared with the computer result. In the top graph the same bend voltage is used for computer and experiment. In the bottom graph, bending voltages in the computer model have been shifted lower to obtain matching energy distributions.**

Figure 104 shows that the energy distributions can be made to match the experimental data, if the bend voltage in the computer code is shifted lower. The maximum discrepancy in bend voltage is 45 volts or 7% of 650V. The reason for this discrepancy is unknown at this time. The most likely cause is an error in the position or the alignment of the ion source.

#### 4.6.2 Resonance Width

Section 2.5.7 explained the phase drift caused by magnetic field detuning only. Using equation 2.85, a beam with  $N_{\text{turns}} = 5$  would experience a phase drift of  $\Delta\phi = 45^\circ$  for a magnetic field error of  $\Delta B/B_0 = 0.6\%$ . Therefore, we would expect a total resonance width of about 1.2% if acceleration through the magnetron does not contribute to the phase change. Experimental measurements of the accelerated beam show a resonance width of approximately 3%. Figure 105 shows the measured data. If the magnetic field is detuned by 1.5% from center, equation 2.85 gives  $\Delta\phi = 108^\circ$  which is clearly not compatible with a beam accelerated over 5 turns.

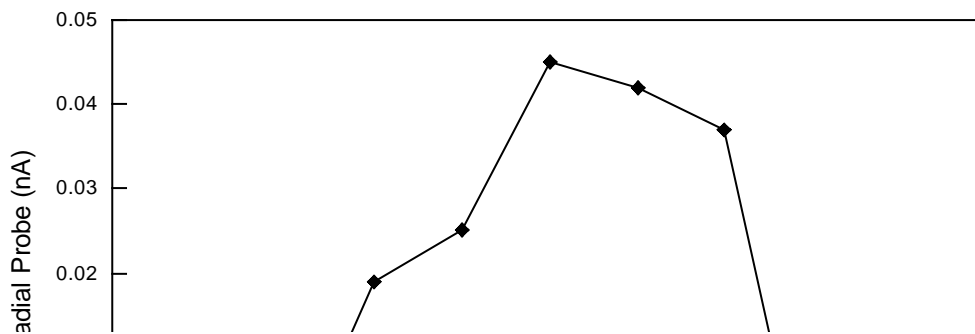


**Figure 105. Experimental data showing the accelerated beam current vs. magnetic field. The position of the radial probe is 19.3 mm ( $E > 38$  keV), and  $\frac{1}{2}V_{\text{bend}} = 683$  V ( $N_{\text{turns}} \approx 5$ ).**

The computer model has been used to simulate acceleration of a full emittance beam. Varying the rf frequency to simulate magnetic field detuning indicates a resonance width of over 4%. Figure 106 shows the comparison between the computer result and the experimental data. This is taken as further evidence that acceleration through the rf driven magnetron does cause phase bunching as discussed in sections 2.62 and 3.1. The ‘wider than expected’ resonance width means a less stringent accuracy in setting the magnetic field, and is therefore a desirable characteristic of the ICRA.

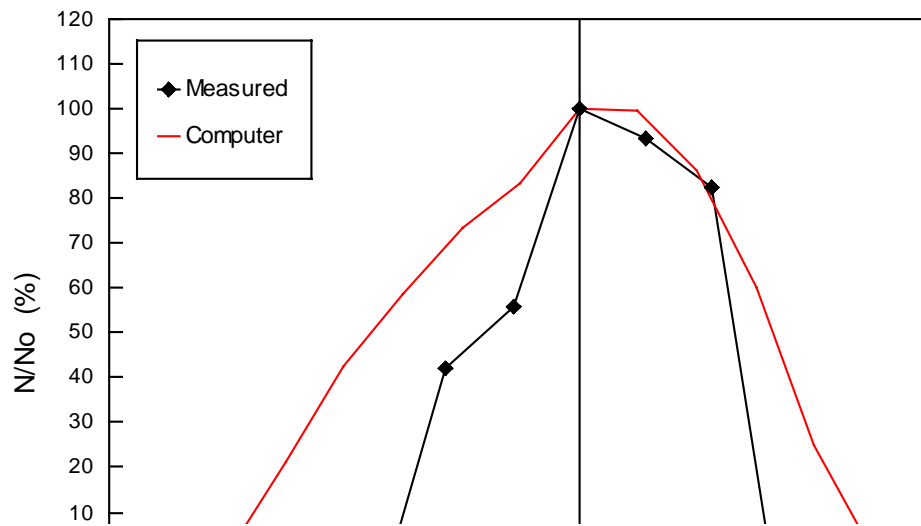


**Figure 106. Comparison between experimental data and the computer generated resonance width.**  
**The computer model uses:  $\frac{1}{2}V_{\text{bend}} = 683 \text{ V}$ ,  $E > 38 \text{ keV}$  (for R-probe at 19.3 mm) and injected beam emittance of  $2.2 \pi \text{ mm mrad}$ .**

**NOT USED**

If one wanted to improve the resolution of the ion spectrum, a moveable beam scraper should be added at a point further upstream. This would allow adjustment of the radius at which the beam clips, and the Faraday cup on the extraction end would be shielded from electron showers created when ions slam into the scraper because electrons would not go forward into the high magnetic field region.

Approximate fractions of the three major constituents in the beam are given in Table X

**Table 10. Rough fractions of the three major constituents in the beam.**

Ar <sup>+</sup>	63 %
H <sub>2</sub> <sup>+</sup>	33 %
H <sup>+</sup>	2 %

As one might suspect, there is some non-linearity in  $\theta_{\text{bend}}$  as a function of  $V_{\text{bend}}$  for small bend angles (bend designed for 20° deflection so plates are tilted 10°). However, for bend voltages above 630V, the maximum error is only XX%.

**Parameters for the hybrid rf cavity for the 50 keV ICRA**

<b>General RF Cavity Parameters</b>	
$\epsilon_0 =$	$8.85 (10^{-12}) \text{ C/Vm}$
$\mu_0 =$	$4\pi(10^{-7}) \text{ Tm/Amp}$
$Z_0 =$	$377 \Omega$
copper: $\sigma_c =$	$58.8 (10^6) (\Omega\text{m})^{-1}$
aluminum: $\sigma_a =$	$38.5 (10^6) (\Omega\text{m})^{-1}$
copper: $\delta_c =$	$5.32 (10^{-6}) \text{ m (for 152 MHz)}$
aluminum: $\delta_a =$	$6.58 (10^{-6}) \text{ m (for 152 MHz)}$
<b>Parameters for the Hybrid Coaxial / Magnetron Cavity</b>	
Inner conductor radius: $a =$	$\frac{1}{2} (0.75'') = 0.95 \text{ cm}$
Outer conductor radius: $b =$	$\frac{1}{2} (4.5'') = 5.72 \text{ cm}$
$b/a =$	6
$\ln(b/a) =$	1.79
Length of coaxial section: $\ell =$	9.7 cm
$C_\ell =$	1.5 pF

$C_m =$	39 pF
$f_o =$	152.02 MHz
$R_s/Q =$	25.85 $\Omega$
$Z_C =$	20.3 $\Omega$
Current on the Short: $I_o =$	147.7 Amps (for $V_o=3kV$ )
$V_o =$	3 kV (for $P_{loss} = 100$ watts)

### Low Power Calibration Measurements (with Cables Subtracted Out)

$P'$  is a measurement of power which includes cable loss (see figure XXX)  
 $P$  without the prime has been corrected for the cable loss.

#### 1) Forced State (Open to Drive Ratio):

measured:  $\left(\frac{P'_1}{P'_o}\right) = -30.51 \text{ dB} \quad \leftarrow \text{correct this for cable loss}$

$$\left(\frac{P_o}{P_1}\right) = \left(\frac{P'_o}{P'_1}\right)\left(\frac{P_o}{P'_o}\right)\left(\frac{P'_1}{P_1}\right) \Rightarrow (+30.51 - 0.15 - 0.481) \text{ dB} = +29.88 \text{ dB}$$

Gives:  $\boxed{\frac{V_o}{V_1} = 31.2}$

#### 2) Forced State (Open to Pickup Ratio):

measured:  $\left(\frac{P'_2}{P'_o}\right) = -66.17 \text{ dB} \quad \leftarrow \text{correct this for cable loss}$

$$\left(\frac{P_o}{P_2}\right) = \left(\frac{P'_o}{P'_2}\right)\left(\frac{P_o}{P'_o}\right)\left(\frac{P'_2}{P_2}\right) \Rightarrow (+66.17 - 0.15 - 0.882) \text{ dB} = +65.14 \text{ dB}$$

Gives:  $\boxed{\frac{V_o}{V_2} = 1807}$

### 3) Matched State:

measured:  $\left(\frac{P'_2}{P'_1}\right) = -36.98 \text{ dB} \quad \leftarrow \text{correct this for cable loss}$

$$\left(\frac{P_1}{P_2}\right) = \left(\frac{P'_1}{P'_2}\right)\left(\frac{P_1}{P'_1}\right)\left(\frac{P'_2}{P_2}\right) \Rightarrow (+36.98 - 0.481 - 0.882) \text{ dB} = +35.62 \text{ dB}$$

Gives:  $\boxed{\frac{V_1}{V_2} = 60.4}$

### Error in Low Power Calibration Measurements

Ultimately the cavity will run in the matched state, with power input at the drive loop ( $P_1$ ) and a small output signal taken from the pickup loop ( $P_2$ ). (see Figure XXX of full power setup). Therefore we need to determine  $V_o$  in the matched state, yet  $V_o$  can only be measured in the forced state (and at low power). For this reason, we must consider whether the forced state measurements caused any change in the field distribution inside the cavity. If not, then the voltage ratios measured in each state should fully agree:

$$\left(\frac{V_1}{V_o}\right)\Bigg|_{\text{Force State}} \left(\frac{V_o}{V_2}\right)\Bigg|_{\text{Forced State}} \stackrel{?}{=} \left(\frac{V_1}{V_2}\right)\Bigg|_{\text{Matched State}}$$

The left hand side gives:  $\left(\frac{V_1}{V_o}\right)\Bigg|_{\text{Forced State}} \left(\frac{V_o}{V_2}\right)\Bigg|_{\text{Forced State}} = \frac{1807}{31.2} = 57.9$

and the right hand side gives:  $\left(\frac{V_1'}{V_2'}\right)\Big|_{\text{Matched State}} = 60.4$

These two measurements agree to within 4%

$$\sigma_1 = \frac{57.9 - 60.4}{60.4} = -4\%$$

Evidently, the error incurred when using forced state measurements to determine  $V_o$  in the matched state is 4%

### **High Power Measurements**

For high power measurements, the ratio of  $V_1/V_2$  is measured using a Bird Watt Meter to measure  $P_1$  and an oscilloscope is used to measure  $V_2$ . High power measurements include any errors due to measuring the input rf power using the Bird Watt Meter, and errors in the voltage calibration of the oscilloscope, as well as any difference between running at high power or low power.

\*\*\*\*\*

However, conditions may change when running the cavity at full power. As an example, for an input power of  $P_1' = 80$  watts read on Bird Watt Meter, a pickup voltage of  $V_2' = 1.23$  V is read on an oscilloscope. After correcting for cable losses we obtain:

$$\left(\frac{V_1}{V_2}\right)\Big|_{\text{High Power}} = 62.2$$

This ratio includes errors in measuring the input rf power using the Bird Watt Meter, and errors in the voltage calibration of the oscilloscope, as well as any difference between running at high power or low power. Comparing this with the low power measurement of the matched state (Table 9):

$$\left( \frac{V_1}{V_2} \right) \Big|_{\text{Low Power}} = 60.4$$

we find an error of 3%. Error in the low power forced state measurements was estimated to be 4% (Table 10). Therefore, the total error in using low power - forced state measurements to calculate  $V_o$  in a high power - matched state, is the addition of these two errors.

$$\sigma = \sigma_1 + \sigma_2 = 7\%$$

\*\*\*\*\*

**My main question here is:**

What I really want is the error in  $(V_o/V_1)$  because that's what I use to calculate the shunt

resistance. 
$$R_s = 50\Omega \left( \frac{V_o}{V_1} \right)^2$$

But we can only find the error in  $(V_1/V_2)$

What does the error in  $V_1/V_2$  tell us about the error in  $(V_o/V_1)$  ????

\*\*\*\*\*

**Table XXX. Parameters for the beam shown in Figure 98.**

	Experimental	Computer Model
$V_o =$	1.7 kV $\pm$ XXX	1.7 kV
$\frac{1}{2} V_{\text{bend}} =$	740 V	740 V

$N_{\text{turns}} =$		
$\epsilon =$	state full range	$2.2 \pi$ mm mrad
Beam Current (RF off) =	17.3 nA	

**Parameters for each Energy Distribution**

	<b>1/28/99 pg (51-52)</b>	<b>2/9/99 pg (88-89)</b>
$V_o =$	1.7 kV	1.4 kV
$\frac{1}{2} V_{\text{bend}} =$	740 V	650, 660, 670, 690. 710 V
Range: $V_{\text{mirror}} =$	(730 – 780) V	(690 – 740) V
Mirror Curve	pg (47 – 48)	pg 99 (or pg 88)
$V_{\text{Einzel}} =$	2.5 kV	2.7 kV
B-field: $I_B =$	89.1 A	88.7 A

## 5. DISCUSSION

### 5.1 Discussion of Results

The Ion Cyclotron Resonance Accelerator uses novel geometry which allows the beam to drift axially while being accelerated in the azimuthal direction. A superconducting magnet provides an axial B-field and an rf driven magnetron provides azimuthal electric fields. This accelerator design is simple, compact and lightweight. A 10 MeV ICRA would be useful for production of radioisotopes or neutron beams.

The objective of this research has been to provide experimental verification of the ICRA acceleration method. This task has two steps:

- 1) Develop analytical theory and a computer model which can be used to predict the fraction of beam accelerated by an ICRA
- 2) Design, build, and test a 50 keV proton ICRA. Then compare the experimental results with theory.

These objectives have been successfully completed. The analytical theory shown here can be used to calculate single trajectories that are centered on the z axis. This analysis is accurate for most design work. The computer model developed for the ICRA can be used to track particle trajectories from ion source to target. Many single particle trajectories have been used to model a full emittance injected beam and predict the fraction of beam current accelerated.

An ICRA has been designed to accelerate protons to 50 keV. The design uses an existing superconducting solenoid. The ion source, vacuum system, accelerating rf

cavity, and beam diagnostics have been built for this experiment. Beam measurements have been made in order to understand both the injected and the accelerated beam.

Figure 107 shows a measured energy distribution. A proton beam was injected at 6.4 keV (rf off). When the rf is on, the beam is accelerated to a distribution ranging from near zero up to near the design energy. 7% of the beam current is accelerated above 24 keV ( $0.5 E_{\text{design}}$ ) and 1 % is accelerated above 42 keV ( $\approx 0.9 E_{\text{design}}$ ). A smaller fraction may be accelerated as high as 46 keV.

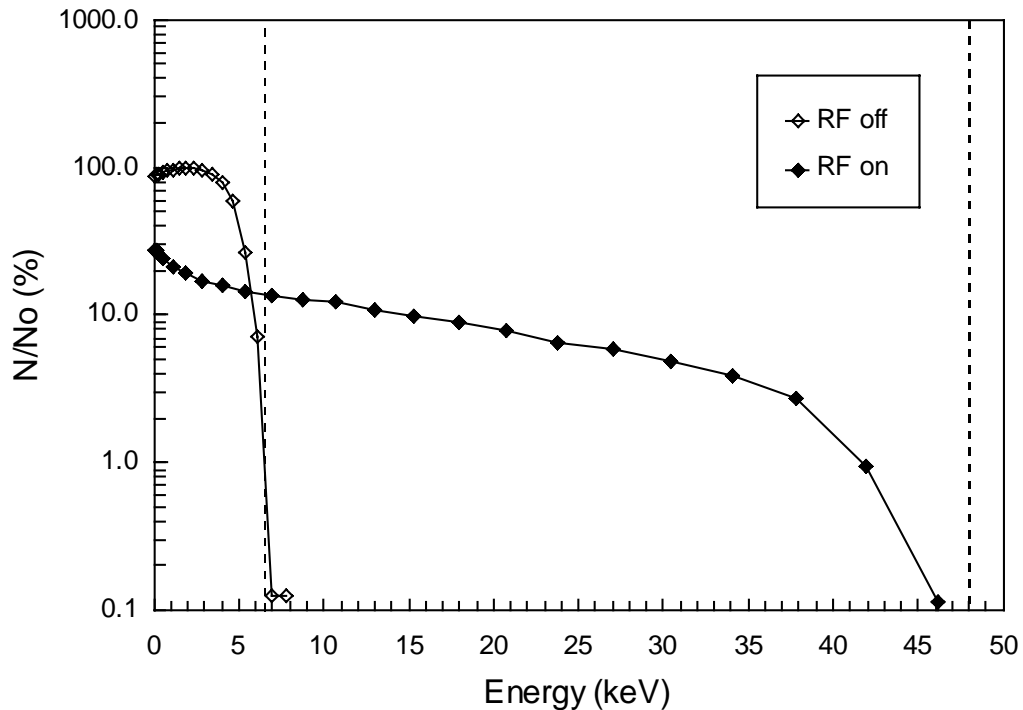


**Figure 107. Measured energy distribution of the proton beam with rf on and with rf off.**

All beam parameters needed for input into the ICRA computer code have been determined from beam measurements, rf cavity measurements, magnetic field mapping, and alignment measurements. These include: cavity gap voltage ( $V_o$ ), bend voltage

( $V_{\text{bend}}$ ), injection energy ( $E_0$ ), B-field profile, and the location of all components.

Beam measurements have been used to estimate a range of emittance of the injected beam. An emittance was selected in this range which gives the best match with the measured energy distributions.

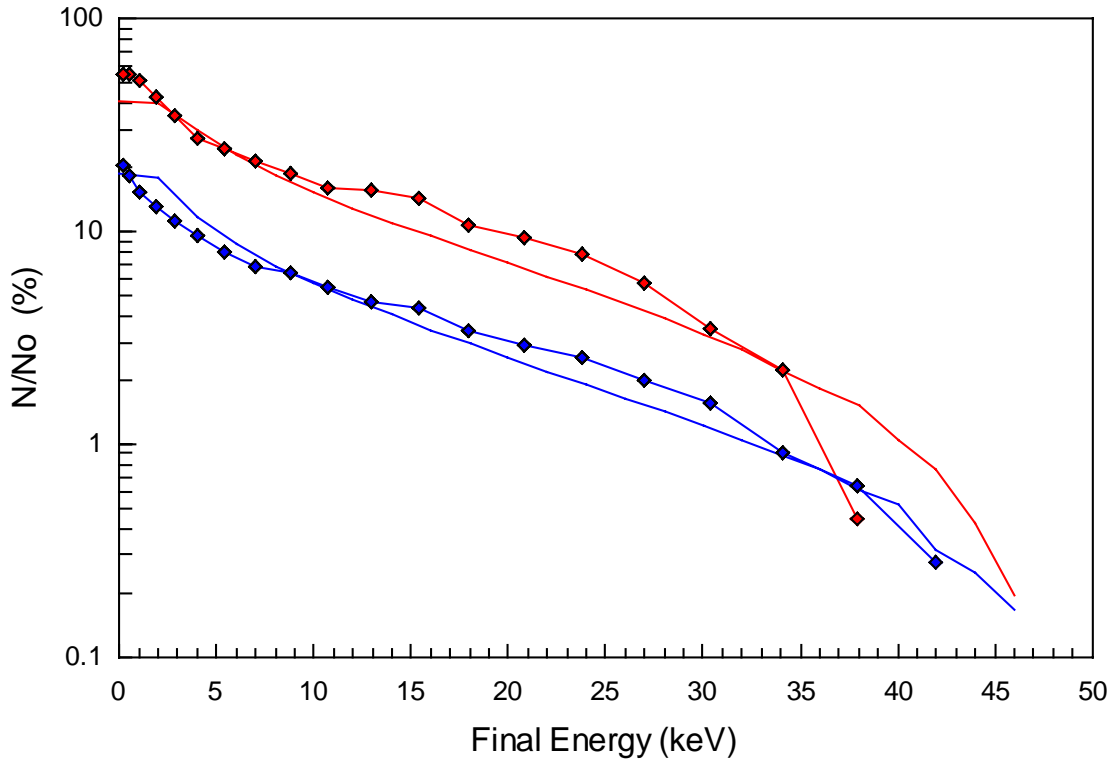


**Figure 108. Comparison between measured energy distributions and computer generated energy distributions for two different bend voltages.**

Using these input parameters, the computer code has been used to reproduce energy distributions for the accelerated beam. Figure 108 shows a comparison between the computer results and measured energy distributions for two different bend voltages. The computer data shows good agreement with the magnitude and shape of the measured energy distributions, and even correctly predicts the drop in beam current caused by the beam striking the inner diameter of the magnetron. With a small correction to  $V_{\text{bend}}$ , the

computer model yields good agreement over a wider range of bend voltages. This agreement indicates that the ICRA computer code can be used to correctly predict the energy distribution of the beam accelerated in an ICRA.

Finally, having benchmarked the ICRA computer model, the code should be a useful tool for designing the next higher energy ICRA. This topic is addressed in section 5.2 below.

## 5.2 The Next Step for the ICRA

The 50 keV ICRA experiment successfully demonstrated the ICRA. The analytical model is adequate for most of the design work. The computer model has been used to estimate the fraction of the accelerated beam current. Clearly, the next step should be to design and build an ICRA which will accelerate beam to useful energies. The final energy was chosen at 10 MeV. Beam currents of 10 – 50  $\mu\text{A}$  in an energy range of  $5 \leq E \leq 10$  MeV would be useful for the applications discussed in section 1.5. The goal here is to optimize the design parameters to obtain a compromise between maximum accelerated beam current and minimum cost of the components. This section presents a scheme for optimization of basic design equations. After which, three 10 MeV proton ICRA designs are presented.

### Magnetic Field Profile

A proton at 10 MeV has a relativistic mass factor of  $\gamma = 1.01$ . Therefore, relativity begins to significantly affect the cyclotron frequency. Since the energy gain in the ICRA trajectory is roughly linear with axial ( $z$ ) position, simply sloping the B-field at a rate of  $\approx 1\%$  over the cavity length will match  $\gamma$  so that the beam remains in phase with the rf. The B-field slope can be obtained by using a Helmholtz coil pair with independent current control, or by simply adding a trim coil to a flat field configuration. The designer should be aware that this slope in the B-field will cause the axial momentum to decrease throughout the acceleration region, which creates the possibility of mirroring the beam inside the acceleration region. This effect should be compensated for by increasing the axial momentum at the cavity entrance.

## Magnetron Taper

Since the energy gain in the ICRA trajectory is roughly linear with  $z$  position, the orbit radius of the beam is roughly proportional to the square root of  $z$ . Thus, if the inner radius of the magnetron increases linearly with  $z$  ( $dR/dz = \text{constant}$ ), the beam will move away from the wall to lower voltage  $V_o \propto (\frac{r}{R})^n$  during the latter part of the acceleration region. This effect is negligible in the 50 keV ICRA; therefore only one linear taper was used. However, the 10 MeV should have at least two different linear tapers as shown in Figure 110. The slopes are chosen to approximate the natural shape of the acceleration trajectory so that the beam remains close to the inner diameter of the accelerating structure.

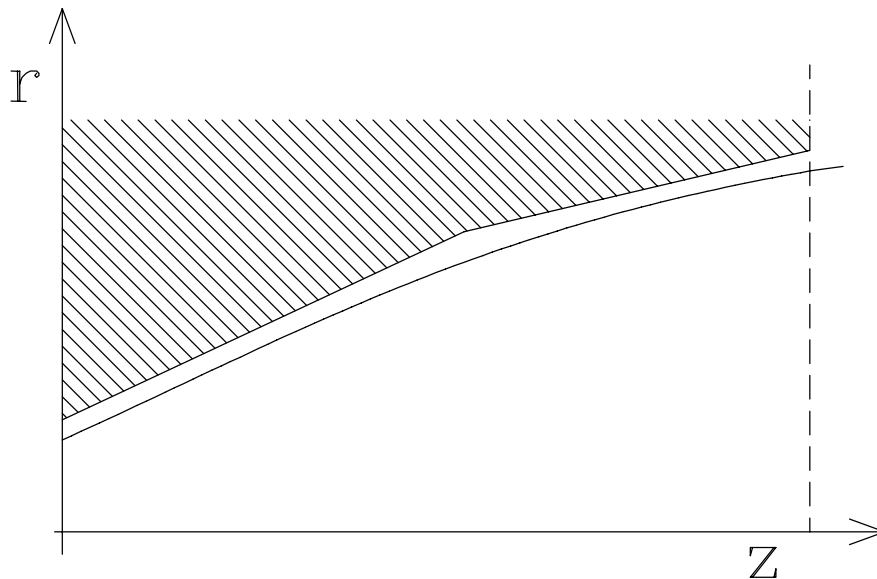


**Figure 110. Cross section of a magnetron with two linear tapers used to approximate the square root shape of the acceleration trajectory.**

## Two Cost Saving Technologies

Ideally, the 10 MeV ICRA should utilize two technological developments which will lead to significant cost savings.

1) Cryogen free superconducting magnets utilize high  $T_c$  current leads in order to minimize heat transfer into the liquid helium. This allows a compact refrigeration system mounted directly on the side of the magnet to produce a closed helium system. Cryogen free magnets such as this would be particularly beneficial in the design of a portable ICRA. Superconducting magnets which use NbTi coils produce magnetic fields up to about 8 Tesla and are relatively inexpensive. The cost scales roughly with the volume of the warm bore. Magnetic fields higher than 8 Tesla, require more advanced superconducting materials (i.e. Nb<sub>3</sub>Sn), therefore the cost rises significantly.

2) Industrial magnetrons at 460 MHz and 950 MHz and output powers in the range of 50 to 100 kW would provide an inexpensive rf power source for the ICRA.

## Energy Spread Caused by Radial Dependence of the Cavity Voltage

One challenge in designing a 10 MeV ICRA is that the radial defocusing discussed in section 2.6.2 will have a larger effect because the induced energy spread depends on the energy gain. This means that a smaller fraction of the beam will be accelerated above the desired cutoff energy for the same injected beam emittance. In order to design an ICRA which will accelerate significant current to the desired energy range, it is important to understand the source of the energy spread, so that we can determine which design parameters affect the spread.

In order to determine the absolute energy spread which will be induced over the entire acceleration trajectory, it is necessary to choose a particular cavity geometry and run computer simulations. However, it is possible to gain some insight into the relative energy spread by considering only the spread induced by an infinitesimal energy gain at the entrance of the cavity.

As the beam spirals through the injection region (toward higher B-field), the ratio of  $\alpha = p_{\perp}/p_{\parallel}$  increases. Assuming that all ions in the injected beam have the same energy but a slightly different angle relative to the local B-field, we have:

$$p_{\text{total}}^2 = p_{\perp}^2 + p_{\parallel}^2$$

Differentiating gives:  $0 = p_{\perp} \delta p_{\perp} + p_{\parallel} \delta p_{\parallel}$

Rearranging yields a convenient expression.

$$\boxed{\frac{\delta p_{\parallel}}{p_{\parallel}} = -\alpha^2 \frac{\delta p_{\perp}}{p_{\perp}}} \quad (5.1)$$

Equation 5.1 is valid through the injection region, up to the cavity entrance, however it is not valid in the acceleration region (where  $\alpha$  increases, yet  $\delta p_{\parallel}/p_{\parallel}$  remains roughly constant). We define  $\alpha_o$  as the ratio of  $p_{\perp}/p_{\parallel}$  at the entrance to the acceleration region. For an ICRA of any reasonable length,  $\alpha_o$  will be greater than 1. Therefore, at the entrance to the acceleration region, the fractional spread in  $p_{\parallel}$  is greater than the fractional spread in  $p_{\perp}$  by a factor of  $\alpha_o^2$ .

Now consider equation 2.79, which gives an analytical expression for the energy gained across a single gap.

$$E_{\text{gap}} = \frac{\pi}{4} q V_o \left( \frac{r}{R} \right)^n$$

Two particles with different orbit radii ( $r$ ) will see two different gap voltages. This leads to a spread in the energy gained. Differentiating with respect to  $r$  gives:

$$\left( \frac{\delta E_{\text{gap}}}{E_{\text{gap}}} \right)_{\perp} = n \left( \frac{\delta r}{r} \right)$$

Since  $p_{\perp} = q B_o r$ , we can write:

$$\left( \frac{\delta E_{\text{gap}}}{E_{\text{gap}}} \right)_{\perp} = n \left( \frac{\delta p_{\perp}}{p_{\perp}} \right) \quad (5.2)$$

Similarly, a spread in the number of kicks ( $N = 2nN_{\text{turns}}$ ) leads to a spread in the energy gain. This can be found using equation 2.80.

$$E_{\text{gain}} = \frac{\pi}{4} q V_o \left\langle \frac{r}{R} \right\rangle^n N$$

Differentiating with respect to  $N$  gives:

$$\left( \frac{\delta E_{\text{gain}}}{E_{\text{gain}}} \right)_{\parallel} = \frac{\delta N}{N}$$

If we take  $N$  to be continuous rather than discrete, then this equation is also true for the energy gain across a single gap.

$$\left( \frac{\delta E_{\text{gap}}}{E_{\text{gap}}} \right)_{\parallel} = \frac{\delta N}{N}$$

since  $p_{\parallel} \propto \frac{1}{N_{\text{kicks}}}$  we can write: 
$$\left( \frac{\delta E_{\text{gap}}}{E_{\text{gap}}} \right)_{\parallel} = -\frac{\delta p_{\parallel}}{p_{\parallel}} \quad (5.3)$$

Since  $r/R$  is constant in equation 2.80, equation 5.3 neglects any variation in  $r/R$  due to variation in  $p_{\parallel}$ . If we neglect this coupling term, the infinitesimal energy spreads caused by spreads in parallel and perpendicular momentum can be added directly.

$$\frac{\delta E_{\text{gap}}}{E_{\text{gap}}} = \left( \frac{\delta E_{\text{gap}}}{E_{\text{gap}}} \right)_{\perp} + \left( \frac{\delta E_{\text{gap}}}{E_{\text{gap}}} \right)_{\parallel}$$

Substituting equations 5.2 and 5.3 leads to:

$$\frac{\delta E_{\text{gap}}}{E_{\text{gap}}} = n \left( \frac{\delta p_{\perp}}{p_{\perp}} \right) + \left( \frac{\delta p_{\parallel}}{p_{\parallel}} \right)$$

This equation is valid for an infinitesimal energy spread at any point in the acceleration region. At the entrance to the cavity  $\delta p_{\parallel}$  and  $\delta p_{\perp}$  are related by equation 5.1. It is convenient to express the energy spread in terms of the perpendicular momentum spread rather than the parallel momentum spread since  $\frac{\delta p_{\perp}}{p_{\perp}}$  remains constant throughout the

injection region, while  $\frac{\delta p_{\parallel}}{p_{\parallel}}$  does not (section 2.5.2).

$$\boxed{\left. \frac{\delta E_{\text{gap}}}{E_{\text{gap}}} \right|_{\text{cavity entrance}}} = (n + \alpha_0^2) \frac{\delta p_{\perp}}{p_{\perp}} \quad (5.4)$$

Equation 5.4 shows that for a particular choice of harmonic number ( $n$ ), this initial energy spread will never go below  $n$ . Figure 111 shows the ratio of  $\frac{\delta E_{\text{gap}} / E_{\text{gap}}}{\delta p_{\perp} / p_{\perp}}$  for several values of  $n$  and for a range of  $\alpha_0$ . For  $\alpha_0$  greater than about 2, the energy spread is dominated by  $\alpha_0$  (or  $\delta p_{\parallel}$ ). While for  $\alpha_0$  less than 2, the spread is dominated by  $n$  (or  $\delta p_{\perp}$ ). Obviously, for high accelerated beam current,  $n$  and  $\alpha_0$  should both be as low as possible. However, it is more important to have low  $\alpha_0$  because the second term in equation 5.4 varies as  $\alpha_0^2$ .

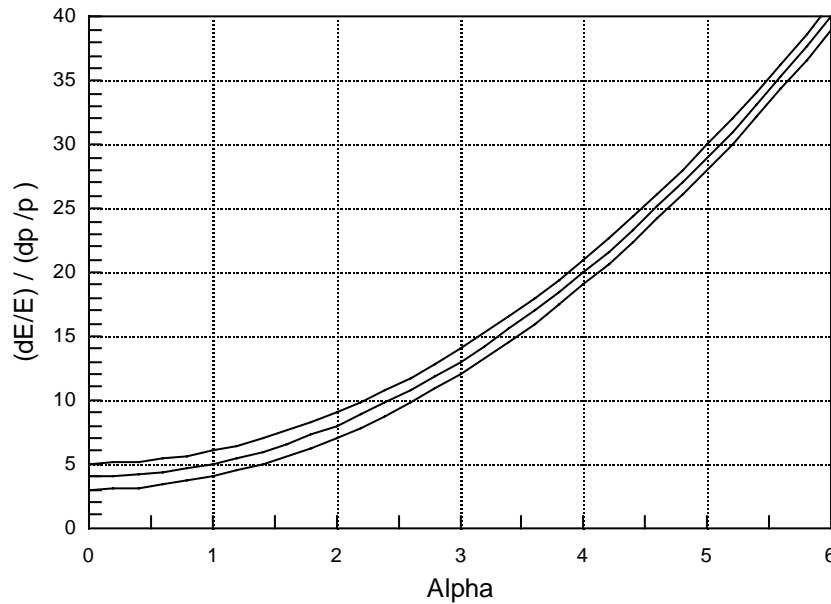


**Figure 111. The infinitesimal energy spread caused by an infinitesimal spread momentum spread is plotted vs.  $\alpha_0$  and for several values of  $n$ .**

## Optimization of ICRA Design Parameters

Optimization of ICRA design parameters requires two criterion.

- 1) Minimize cost
- 2) Maximize the accelerated beam current

The cost can be minimized by: small magnet volume, and low rf power, and by using the cryogen free superconducting magnet as well as an industrial magnetron for an rf power source. High accelerated beam current requires low harmonic number ( $n$ ) and low  $\alpha$  as discussed above.

In the optimization scheme below, the ICRA design parameters have been divided into natural input parameters, and output parameters.

**Input parameters:**  $E_o$ ,  $\alpha$ ,  $B_o$ ,  $n$ ,  $F$ ,  $E_{\text{gain}}$ ,  $\langle r/R \rangle$ ,  $\frac{\delta p_{\perp}}{p_{\perp}}$ ,  $Q$ ,  $\ell_c$

**Output parameters:**  $f_{\text{rf}}$ ,  $V_o$ ,  $\ell_{\text{cav}}$ ,  $r_{\text{beam}}$ ,  $R_{\text{magnetron}}$ ,  $P_{\text{rf}}$ ,

Where  $E_o$  is the injection energy,  $\alpha$  is the ratio of  $p_{\perp}$  to  $p_{\parallel}$  at the cavity entrance,  $B_o$  is the central magnetic field,  $n$  is the harmonic number,  $F$  is the ratio of the rf cavity voltage ( $V_o$ ) to the maximum cavity voltage set by the Kilpatrick criterion for sparking,  $E_{\text{gain}}$  is the total energy gained through the acceleration region ( $E_{\text{gain}} = E_{\text{final}} - E_o$ ).  $\langle r/R \rangle$  is the average radius fraction throughout the acceleration trajectory,  $\frac{\delta p_{\perp}}{p_{\perp}}$  is the spread in the perpendicular momentum of the injected beam,  $Q$  is the quality factor of the rf driven

magnetron, and  $\ell_c$  is the radial length of the capacitor gap in the magnetron (defined in Figure 16, pg 35).

Two input parameters should be ignored or taken as constant because we do not have much choice in their values. For an average trajectory through the acceleration region  $\langle r/R \rangle \cong 0.85$ , and in order to obtain the lowest possible capacitance (and a high  $R_s/Q$ ),  $\ell_c$  should be no more than  $\cong 0.5$  cm.

The output parameters are the rf frequency ( $f_{rf}$ ), and the cavity voltage ( $V_o$ ), the length of the acceleration region ( $\ell_{cav}$ ), the orbit radius of the final accelerated beam ( $r_{beam}$ ), the radial distance needed for the resonators of the magnetron ( $R_{magnetron}$ ), and the rf power needed to run the magnetron ( $P_{rf}$ ). Notice that  $\ell_{cav}$ ,  $r_{beam}$ , and  $R_{magnetron}$  together define the volume of the superconducting magnet, because  $\ell_{cav}$  is also the magnet flat field length, and the diameter of the magnet warm bore is given by  $D = 2(r_{beam} + R_{magnetron})$ .

In an effort to be brief, all design equations have been summarized in Figure 112, and Figure 113. All equations have been presented previously in this dissertation, except the Kilpatrick criterion (below). The equations in Figure 112 deal only with the trajectory through the acceleration region. The equations in Figure 113 deal only with the resonant structure of the magnetron and the rf power required to run the magnetron. The equations represent the simplest analytical approach to relate all design parameters. Only lowest order effects are used. For example, the trajectory equations assume a centered proton orbit, the electric field in the magnetron is represented by first harmonic only, and relativistic effects are neglected.

## Inputs

$E_o$

$$p_{\text{total}} = \sqrt{2mE_o}$$

$$p_{\perp} = p_{\text{total}} \frac{\alpha}{\sqrt{1+\alpha^2}}$$

$\alpha$

$$p_{\parallel} = p_{\text{total}} \frac{1}{\sqrt{1+\alpha^2}}$$

$B_o$

$$r_o = \frac{p_{\perp}}{qB_o}$$

$$R_o = \frac{4}{3}r_o$$

$n$

$$g = \frac{\pi R_o}{2n}$$

$$f_{\text{rf}} = n \left( \frac{qB_o}{2\pi m} \right)$$

$F$

$$V_o = F 4\pi \frac{m_p}{e} (f_{\text{rf}} g)^2$$

$E_{\text{gain}}$

$$N_{\text{turns}} = \frac{E_{\text{gain}}}{\frac{\pi}{2} V_o n \left\langle \frac{r}{R} \right\rangle^n}$$

$\left\langle \frac{r}{R} \right\rangle$

$$\ell_{\text{cav}} = 2\pi \left( \frac{p_{\parallel}}{qB_o} \right) N_{\text{turns}}$$

**Figure 112.** A graphical map of the basic design equations for the acceleration trajectory of the ICRA. Input parameters are  $E_o$ ,  $\alpha$ ,  $B_o$ ,  $n$ ,  $F$ ,  $E_{\text{gain}}$ , and the average radius fraction  $(r/R)$ .

From  
Figure 112

$g$

$l_c$

$f_{rf}$

$l_{cav}$

$n$

$Q$

$V_o$

$$r_L = \frac{1}{2} \left( \frac{c}{2\pi f_{rf}} \right) \sqrt{\frac{g}{\pi l_c}}$$

$$C = \epsilon_o \left( \frac{l_c l_{cav}}{g} \right)$$

$$R_{magnetron} = l_c + 2r_L$$

$$R_s = \frac{1}{2n} \left( \frac{Q}{2\pi f_{rf} C} \right)$$

$$P_{rf} = \frac{V_o^2}{2R_s}$$

**Figure 113. Design equations for the resonant structure of the rf driven magnetron. Input parameters are:  $l_c$ ,  $n$ , and  $Q$ . Parameters taken from Figure 112 are:  $g$ ,  $l_{cav}$ ,  $f_{rf}$ , and  $V_o$ .**

Using the equations of Figure 112, we see that choosing  $E_o$  and  $\alpha$  defines  $p_{\perp}$  and  $p_{\parallel}$  at the cavity entrance. Choosing  $B_o$  sets the beam orbit radius at the cavity entrance ( $r_o$ ). The beam should enter the magnetron at an initial radius fraction of about  $r_o/R_o = 0.75$ , therefore choosing  $B_o$  also sets the initial radius of the magnetron ( $R_o$ ). The width of a gap is limited by the circumference of the magnetron at its entrance. A good assumption is to divide the circumference equally among  $2n$  gaps and  $2n$  vanes. Choosing the harmonic number defines the gap width ( $g$ ) and the rf frequency ( $f_{rf}$ ). Using the Kilpatrick criterion for vacuum sparking, the maximum cavity voltage ( $V_o$ ) depends on  $f_{rf}$  but also on the gap width [Kilpatrick, Humphries]. The actual cavity voltage should be set to some fraction ( $F$ ) of the Kilpatrick voltage ( $V_o = FV_K$ ) to allow for field enhancement and a safety margin. Once  $V_o$  is known, choosing  $E_{gain}$  sets the number of turns through the acceleration region ( $N_{turns}$ ). Finally, the flat field length ( $\ell_{cav}$ ) is known from  $N_{turns}$ ,  $p_{\parallel}$ , and  $B_o$ .

In Figure 113, the capacitance of the magnetron ( $C$ ) is calculated from geometry (review Figure 16). Once  $C$ ,  $f_{rf}$ ,  $n$ , and the  $Q$  of the cavity are known, we can calculate the shunt resistance ( $R_s$ ). The rf power required to run the magnetron is then calculated from  $V_o$  and  $R_s$ . Since the capacitance and  $f_{rf}$  are both known, the radius of the required inductor ( $r_L$ ) can be calculated. This simple geometry assumes a round hole for the inductor (Figure 16), However, the inductor can always be deformed to reduce its radial extent, therefore the equation for  $r_L$  assumes a reduction by a factor of  $1/2$ . Finally, the radial distance needed for the magnetron oscillators ( $R_{magnetron}$ ) can be calculated from  $\ell_c$  and  $r_L$ . As mentioned above, the magnet diameter required is simply

$$D = 2(r_{beam} + R_{magnetron}).$$

Using the equations in Figure 112 and 113, it is straightforward to derive expressions for each output parameter in terms of only input parameters and constants. This allows us to look at the effect of each input parameter on the output parameters.

$$f_{\text{rf}} = n \left( \frac{qB_o}{2\pi m} \right)$$

$$V_o = F \frac{8\pi}{9} \frac{E_o}{e} \frac{\alpha^2}{1 + \alpha^2}$$

$$\ell_{\text{cav}} = \frac{9}{2\pi} \frac{1}{F} \frac{\sqrt{2m}}{B_o n \langle r/R \rangle^n} \frac{E_{\text{gain}}}{\sqrt{E_o}} \frac{\sqrt{1 + \alpha^2}}{\alpha^2}$$

$$r_{\text{beam}} = \frac{\sqrt{2mE_{\text{final}}}}{qB_o}$$

$$R_{\text{magnetron}} = \ell_c + mc \sqrt{\frac{2}{3}} \frac{1}{\sqrt{\ell_c}} \frac{(2mE_o)^{1/4}}{(enB_o)^{3/2}} \frac{\sqrt{\alpha}}{(1 + \alpha^2)^{1/4}}$$

$$P_{\text{rf}} = \frac{16}{3} \frac{\epsilon_o}{m} F E_o E_{\text{gain}} B_o \frac{n^2}{\langle r/R \rangle^n} \frac{\ell_c}{Q} \frac{\alpha}{1 + \alpha^2}$$

$$\frac{\delta E}{E} = (n + \alpha^2) \frac{\delta p_{\perp}}{p_{\perp}}$$

We want  $\ell_{\text{cav}}$  and  $R_{\text{magnet}}$  both small to reduce the cost of the superconducting magnet. Similarly, the rf power should be low to reduce the cost of the rf power system. And the energy spread should be low in order to maximize the accelerated beam current.

From these equations we can make several useful observations about the effect of each input parameter. For this example,  $E_{\text{gain}} \cong 10 \text{ MeV}$  has been chosen because it is a useful beam energy for the applications discussed in chapter 1. As stated previously,  $\langle r/R \rangle \cong 0.85$ , and in order to obtain a high  $R_s/Q$  without causing an unreasonably low capacitance we require  $\ell_c \cong 0.5 \text{ cm}$ . No claims about the  $Q$  of the magnetron structure will be made until rf after measurements are done. If an estimate of the rf power is needed, then a conservative value for the  $Q$  would be 2000. Furthermore,  $\frac{\delta p_{\perp}}{p_{\perp}}$  is the result of the injected beam emittance and the electrostatic bend. Again, if an estimate is needed, then the value from the 50 keV ICRA could be used  $\frac{\delta p_{\perp}}{p_{\perp}} \cong 8.7\%$ .

This leaves only 5 input parameters:  $E_o$ ,  $B_o$ ,  $F$ ,  $n$ , and  $\alpha$ . The effect of these 5 input parameters is summarized below.

#### Effect of Injection Energy ( $E_o$ )

- 1) High  $E_o$  causes shorter  $\ell_{\text{cav}}$  (cheaper magnet)
- 2) High  $E_o$  causes smaller injected beam emittance (higher accelerated beam current)
- 3) High  $E_o$  allows larger gaps and higher  $V_o$  (potentially higher rf power). However we can still choose  $F$  low to counteract this effect.

#### Effect of Magnetic Field ( $B_o$ )

- 4) High  $B_o$  causes shorter  $\ell_{\text{cav}}$  (cheaper magnet).

- 5) High  $B_o$  causes smaller  $r_{\text{beam}}$  (cheaper magnet).
- 6) High  $B_o$  causes higher rf frequency / smaller  $R_{\text{magnetron}}$  (cheaper magnet).
- 7) High  $B_o$  causes higher rf power.
- 8) High  $B_o$  may require smaller injected beam size.

#### Effect of Cavity Voltage Fraction (F)

- 9) High F causes high  $V_o$  (high rf power).
- 10) High F causes shorter  $\ell_{\text{cav}}$  (cheaper magnet).

#### Effect of Harmonic Number (n)

- 11) High n requires higher rf power ( $P_{\text{rf}} \sim n^2$  because  $R_s \sim n^{-2}$ ).
- 12) High n causes a larger energy spread (lower accelerated beam current).
- 13) High n causes higher rf frequency and a smaller  $R_{\text{magnetron}}$  (cheaper magnet).
- 14) High n causes shorter  $\ell_{\text{cav}}$  (cheaper magnet).

#### Effect of Alpha ( $\alpha$ )

- 15) High  $\alpha$  causes a larger energy spread (lower accelerated beam current)
- 16) High  $\alpha$  causes a shorter  $\ell_{\text{cav}}$  (cheaper magnet)
- 17) High  $\alpha$  lowers the rf power.

Using the observations listed above we are now in a position to choose some input parameters. It is obvious from points 1-3 that  $E_0$  should be as high as is convenient. We choose  $E_0 = 100$  keV. Similarly,  $B_0$  should be as high as possible without inducing excessive cost. Current NbTi technology allows  $B_0 = 8$  Tesla. Above this level the cost rises steeply. Therefore, we choose  $B_0 = 8$  Tesla. The harmonic number  $n$  should be low for a high beam quality, however we want  $n$  high so that the magnetron fits inside the magnet bore. The choice of  $n = 4$  gives  $f_{rf} = 488$  MHz which allows the use of an industrial magnetron as the rf power source. Furthermore,  $f_{rf} = 488$  MHz makes the radius of the magnetron resonators less than 2 inches. Together with the final beam diameter, this leads to a warm bore of roughly 8 inches which is a convenient size. Figure 114 shows the magnet bore diameter as a function of magnetic field for  $n = 4$ .

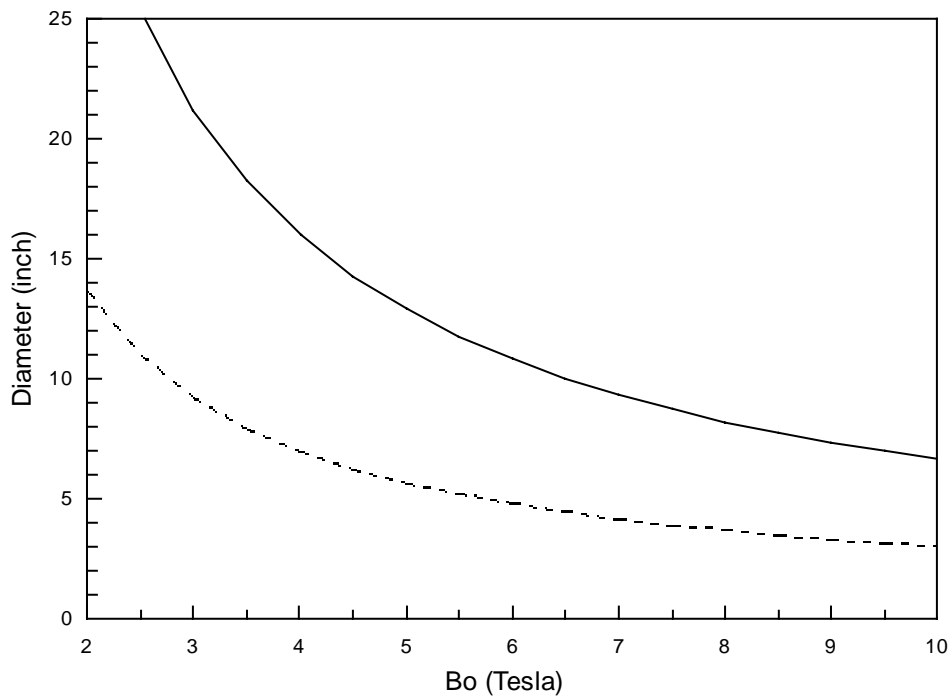


**Figure 114.** The dotted line shows the diameter required for resonators of the magnetron ( $n=4$ ) as a function of magnetic field. The solid line shows total diameter  $D = 2(r_{\text{beam}} + R_{\text{magnetron}})$  (for a 10 MeV beam) needed for the warm bore of the superconducting magnet.

The two remaining input parameters are  $F$  and  $\alpha$ . Since the beam quality has already been pushed low by using  $n = 4$ , it is important to have  $\alpha$  as low as possible. However, low  $\alpha$  causes a long cavity length. Since high  $F$  will lower  $\ell_{cav}$ , and  $F$  is the only parameter left to adjust, we should choose  $F$  as high as possible so that we can choose  $\alpha$  as low as possible and yet still obtain a reasonable cavity length. Choosing  $F$  high requires higher rf power, therefore  $F$  controls the trade off between rf power and cavity length. The highest possible voltage fraction is  $F = 0.25$  (0.5 for field enhancement, and 0.5 for a safety factor). Table 16 below shows the resulting three designs with  $\alpha = 2, 4, \text{ and } 8$ .

**Table 16. Three different 10 MeV ICRA designs with  $\alpha = 2,4,8$ .**

$\alpha$	2	4	8
ion	proton	proton	proton
$E_{\text{final}}$	10 MeV	10 MeV	10 MeV
$E_o$	100 keV	100 keV	100 keV
$B_o$	8 Tesla	8 Tesla	8 Tesla
n	4	4	4
$N_{\text{gaps}}$	8	8	8
$f_c$	122 MHz	122 MHz	122 MHz
$f_{\text{rf}}$	488 MHz	488 MHz	488 MHz
g	2.7 mm	2.9 mm	3.0 mm
F	0.25	0.25	0.25
$V_o$	56 kV	66 kV	69 kV
$N_{\text{turns}}$	54	46	44
$r_o$	0.51 cm	0.55 cm	0.57 cm
$R_o$	0.68 cm	0.74 cm	0.76 cm
$r_{\text{exit}}$	5.7 cm	5.7 cm	5.7 cm
$R_{\text{exit}}$	6.0 cm	6.0 cm	6.0 cm
$l_{\text{cav}}$	34 inches	16 inches	8 inches
C	14 pF	6 pF	3pF
L	$7 \times 10^{-9}$ Henry	$2 \times 10^{-8}$ Henry	$4 \times 10^{-8}$ Henry
$R_s/Q$	3 $\Omega$	7 $\Omega$	14 $\Omega$
Q	2000	2000	2000
$R_s$	5.7 k $\Omega$	13.3 k $\Omega$	28.0 k $\Omega$
$P_{\text{rf}}$	270 kW	160 kW	84 kW
$l_c$	0.5 cm	0.5 cm	0.5 cm
$r_L$	2.02 cm	2.10 cm	2.13 cm
$R_{\text{magnetron}}$	4.5 cm	4.7 cm	4.8 cm
Magnet ID	8.3 inches	8.4 inches	8.5 inches
$n + \alpha^2$	8	20	68

## Discussion

The three ICRA designs presented in Table 16 all use an 8 Tesla central field, 4<sup>th</sup> harmonic, and an injection energy of 100 keV. Varying  $\alpha = 2, 4, 8$  controls the trade off between cavity length and quality of the accelerated beam. Each design has a magnet bore of reasonable diameter (ID  $\approx 8$ " ). However, the  $\alpha = 2$  design requires a flat field length of 34" while the  $\alpha = 8$  design fits into a very reasonable 8" length. The  $\alpha = 2$  design will certainly accelerate higher beam current because  $(n + \alpha^2) = 8$ , while the  $\alpha = 8$  design will accelerate much lower beam current since  $(n + \alpha^2) = 68$ . The longer cavity design also requires significantly more rf power because of the increased capacitance of the accelerating cavity.

It is useful to compare these results with a previous 10 MeV design which was computer modeled, but not put through this optimization process [1]. This design also used an 8 Tesla B-field,  $n = 4$ , for a 488 MHz magnetron, and had  $\alpha = 4.1$ . However the injection energy was 54 keV, and the fraction of Kilpatrick voltage was  $F = 0.5$  which caused a cavity length of only 10 inches. Computer modeling results showed  $13\mu\text{A}$  (0.67 %) of the beam accelerated to the range from 5 to 10 MeV, assuming an injected proton beam of 2 mA in an emittance of  $2\pi$  mm mrad (unnormalized) [1, 26].

The  $\alpha = 4$  design in Table 16 should do better than the previous 10 MeV results for several reasons. The factors which control the energy spread ( $n$ ,  $\alpha$ , and  $E_{\text{gain}}$ ) are the same in both designs. However, the optimized design in Table 16 has a higher injection energy, which causes a lower beam emittance at injection. Also the previous 10 MeV results were obtained for a condition where the beam is not scraping the wall. Experience

from the 50 keV ICRA experiment shows that peak accelerated beam current is obtained for a condition such that the beam current is scraping the wall (section 2.6.8).

Furthermore, the analysis of the acceptance phase space in section 2.6.6 showed that the acceptance is independent of azimuthal ( $\theta$ ) position. This leaves open the option of using multiple ion sources at different azimuthal positions, or a single source with multiple extraction apertures.

As a conservative goal, if the  $\alpha = 4$  design in Table 16 accelerated only 2% of the beam current to an energy distribution between 5 – 10 MeV, this would produce a 40  $\mu$ A beam which would be useful for applications. The  $\alpha = 2$  design would accelerate higher current and the  $\alpha = 8$  design would accelerate less.

All three designs in Table 16 have the distinct advantage of being able to utilize an existing industrial magnetron for the rf power source. If a cryogen free magnet is also used, this combination would lead to an inexpensive accelerator. At this point, the main question is how much current each design will accelerate. In order to answer this question, the ICRA computer code (section 2.6) should be used to model a full emittance beam through each of the three designs. In this way a proper analysis can be made between cost vs. accelerated beam current. This task is recommended as future research.

## 6. CONCLUSION

This experimental study of a 50 keV Ion Cyclotron Resonance Accelerator (ICRA) has successfully demonstrated ion acceleration using the same axial drift geometry that is characteristic of gyrotrons. Although, cyclotron resonance acceleration has been previously demonstrated using electrons [5], this experiment marks the first time that this geometry has been used to accelerate an ion beam.

An rf driven magnetron operating at 152 MHz was mounted in 2.5 Tesla axial magnetic field supplied by a superconducting solenoid. A 6.4 keV proton beam was injected into the high magnetic field region such that the beam spirals around magnetic field lines while continuing to drift axially through the acceleration region. RF electric fields of the magnetron accelerated the beam in the azimuthal direction. Measurements of the accelerated beam show an energy distribution with 7% of the beam current above 24 keV and 1% above 42 keV.

Measurements of the injected beam were used to determine the radius of the proton orbit ( $r$ ) and the number of turns through the acceleration region ( $N_{\text{turns}}$ ) as well as the spreads in  $r$  and  $N_{\text{turns}}$ . Beam measurements have also been used to estimate the emittance of the injected beam between  $0.35\pi$  and  $2.2\pi$  mm mrad (unnormalized).

Analytical theory and a complete computer model have been developed for the ICRA. A full emittance injected beam has been simulated using the computer model to track many single particle trajectories. The computer model was used to obtain energy distributions of the accelerated beam.

Computer generated energy distributions show reasonable agreement with the experimental energy distributions. After a small correction of the bend voltage the

computer model gives good agreement with the magnitude and shape of the experimental data over a range of turn number.

The agreement between the computer model and experiment is considered a benchmark of the ICRA computer code. Therefore the code will be a useful tool for designing a higher energy ICRA.

A scheme for optimizing an ICRA design has been given. Design parameters which minimize cost and maximize the accelerated beam current have been identified. Three different 10 MeV designs have been proposed which offer a range of the trade off between cost vs. accelerated beam current. A full cost analysis and prediction of the accelerated beam current using the ICRA computer code for each design is suggested as future research.

# APPENDIX

## Radial Probe Corrections

Ideally the radial probe should block all of the beam current above a certain radius and read an integrated current vs radius. Errors in the radial probe data were explained in section 3.2.5. Three mathematical corrections are needed to correct the radial probe data:

**1) Account for the slope on the inner edge of the probe**

**2) Account for beam lost on the electron blocker**

**3) Account for axial turn lengths which are longer than the probe length**

The slope on the inner edge of the radial probe matches the slope of the B-field for the 50 keV orbit radius. At any smaller radius, the slope on the probe induces an apparent energy spread in the measured data. Corrections for the electron blocker and for the axial turn spacing both depend on the beam energy. Therefore, correction 1) must be made before 2) or 3). The order of 2) and 3) does not matter.

## Slope on the Inner Edge

The slope on the inner edge of the radial probe matches the slope of the B-field for the 50 keV orbit radius only. At any radius smaller than this, the slope of the field line is less than the slope of the probe. Thus the probe induces an energy spread on the measured data. Unaccelerated beam data can be corrected using the simple thin shell model. Accelerated beam data can only be corrected using the thick shell model.



Therefore, the measured beam current as a function of  $r_m$  becomes:

$$I_m = I_o \left( \frac{r_o - r_m}{m_p \ell} \right)$$

Solving for  $I_o$  gives a formula to recover the actual beam current from the measured data.

$$I_o = I_m \left( \frac{m_p \ell}{r_o - r_m} \right) \quad \text{for } \Delta z \leq \ell \quad (\text{A.2})$$

If the B-field is not constant, but the field line has slope  $m_B$ , then the length intercepted by the probe ( $\Delta \ell$ ) is more complicated.

$$\Delta \ell = \sqrt{\Delta z^2 + (m_B \Delta z)^2} \quad \text{where} \quad \Delta z = \left( \frac{r_o - r_m}{m_p - m_B} \right)$$

Therefore:

$$\boxed{I_o = \frac{I_m}{\sqrt{1 + m_B^2}} \frac{(m_p - m_B) \ell}{(r_o - r_m)}} \quad \text{for } \Delta z \leq \ell \quad (\text{A.3})$$

This formula can be applied directly to the measured data ( $I_m$  vs.  $r_m$ ).

### Thick Shell Model

Radial distributions of the accelerated beam have not been corrected for the distortion caused by the slope on the inner edge of the radial probe. The distortion is largest in the lower energy portion of the distribution and goes to zero at 50 keV. Correcting for this effect would shift current toward higher energies, therefore neglecting this correction leads to conservative energy distributions. Furthermore, some of the beam is never picked up at the low end of the energy spectrum (0 – 5 keV), therefore not enough information is known to correctly perform the correction. For completeness, the effect is explained below.

The accelerated beam is not concentrated at one radius, but rather is spread out in a radial distribution which ranges from near  $r = 0$  to the radius of the maximum energy. Therefore, correcting accelerated data for the effect of the probe slope requires a thick shell model.

As an example, assume that the B-field is constant (horizontal field lines) and the beam current is distributed over a range from  $r = (0 - 20)$  mm. The radial probe is moved inward in 2mm steps. As the probe moves from  $r_m = 6$  mm to  $r_m = 4$  mm, a 2 mm wide strip along the sloped inner edge of the probe picks up some additional beam current ( $\Delta I_4 = I_4 - I_6$ ). Although this measured current has been recorded at  $r_m = 4$  mm, the slope on the inner edge of the radial probe has cut across shells with radius 6,8,10,12,and 14mm. Therefore the proper correction must take a fraction of the current measured at low radius, and redistribute it to higher radii.

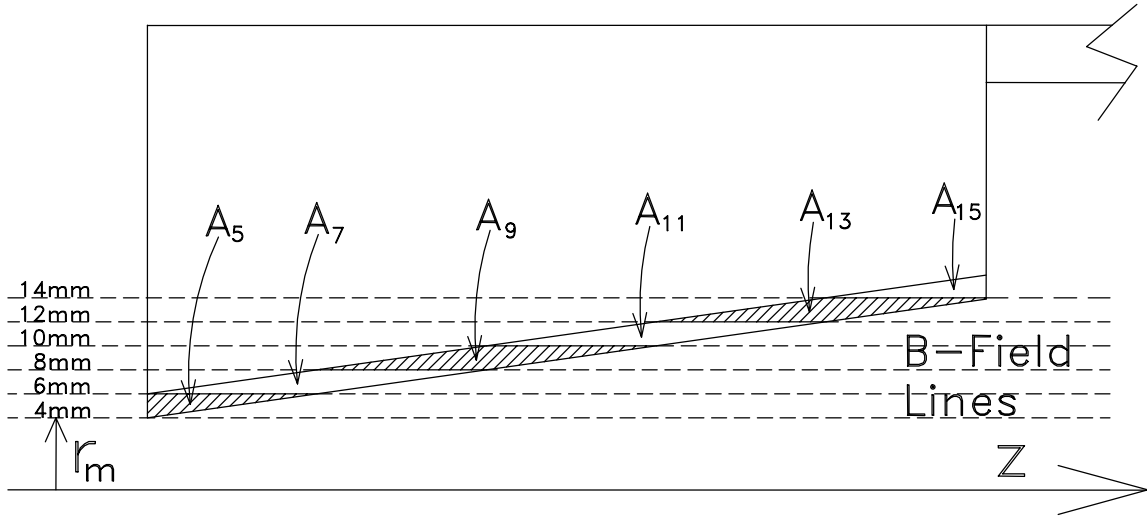


**Figure A2. The slope on the inner edge of the radial probe cuts across shells at several radius.**

The probe is shown here as it moves from  $r_m = 6\text{mm}$  to  $4\text{mm}$ .

For each radial step, the additional current measured ( $\Delta I_i$ ) can be decomposed into the contribution from each shell. The contribution from each shell is the area times the current density of that shell ( $A_i J_i$ ).

$$\Delta I_2 = A_3 J_3 + A_5 J_5 + A_7 J_7 + A_9 J_9 + \dots$$

$$\Delta I_4 = 0 + A_5 J_5 + A_7 J_7 + A_9 J_9 + \dots$$

$$\Delta I_6 = 0 + 0 + A_7 J_7 + A_9 J_9 + \dots$$

Thus, the transformation is a matrix equation.

$$\Delta I_i = A_{ij} J_j$$

If the total number of radial steps taken is “n”, then  $A_{ij}$  is an  $n \times n$  matrix with zeros below the diagonal.  $J_j$  is the actual current density in each radial shell and  $\Delta I_i$  is the measured increase in current in going from  $r = i+2$  to  $i$ .

The actual beam current can be recovered by inverting this matrix equation:

$$J_i = A_{ij}^{-1} \Delta I_j$$

The distortion in the measured radial distribution is less for the actual B-field than for the constant magnetic field case illustrated in Figure A2. In reality the slope of the radial probe matches the 50 keV field line, therefore the distortion goes to zero at full energy. Figure A3 shows the range of energies that are mixed.

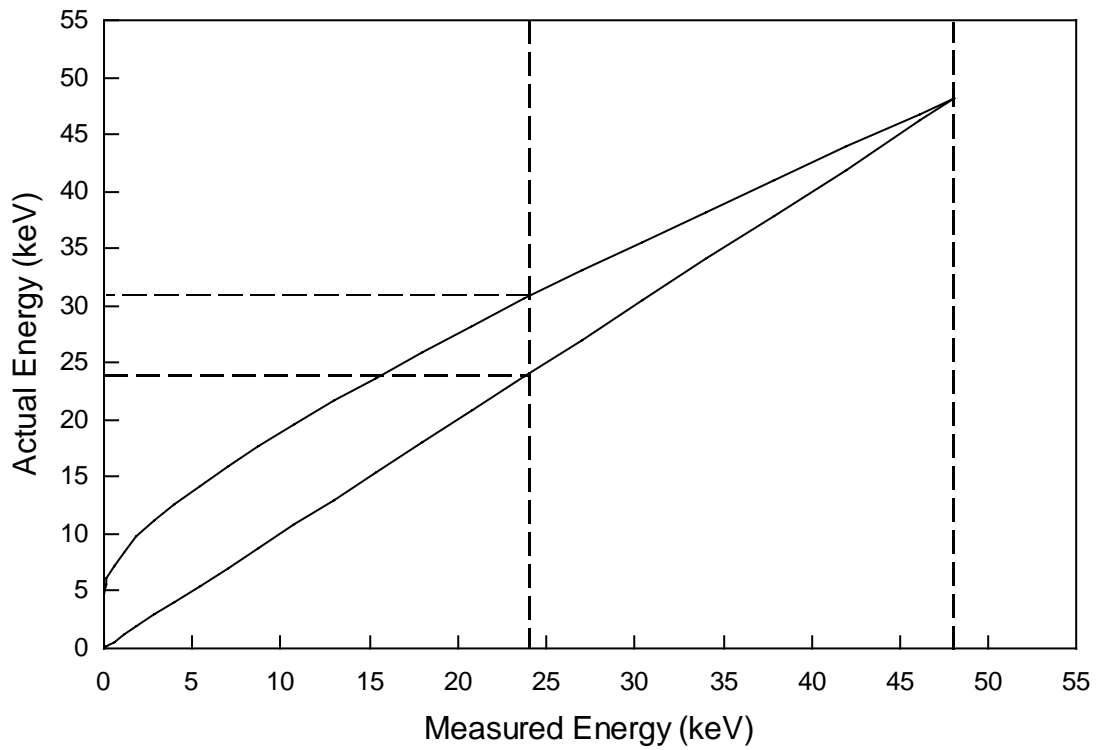


**Figure A3.** The measured beam current at a particular energy actually contains a spread in beam energies bounded by the two lines shown here. For example, the beam current measured at 24 keV actually contains energies ranging from 24 keV to 31 keV. The spread goes to zero at 50 keV. Vertical dotted lines mark the injected beam, half maximum, and the full the beam energy (48 keV)

### Beam Lost on the Electron Blocker

The electron blocker is mounted along the upstream edge of the radial probe as shown in Figure A4. Since electrons are trapped on magnetic field lines, the electron blocker casts a shadow over the Faraday cup portion of the probe that electrons cannot reach. On the other hand, ions orbit around the z axis with large radius therefore they can pass behind the electron blocker and strike the Faraday cup.

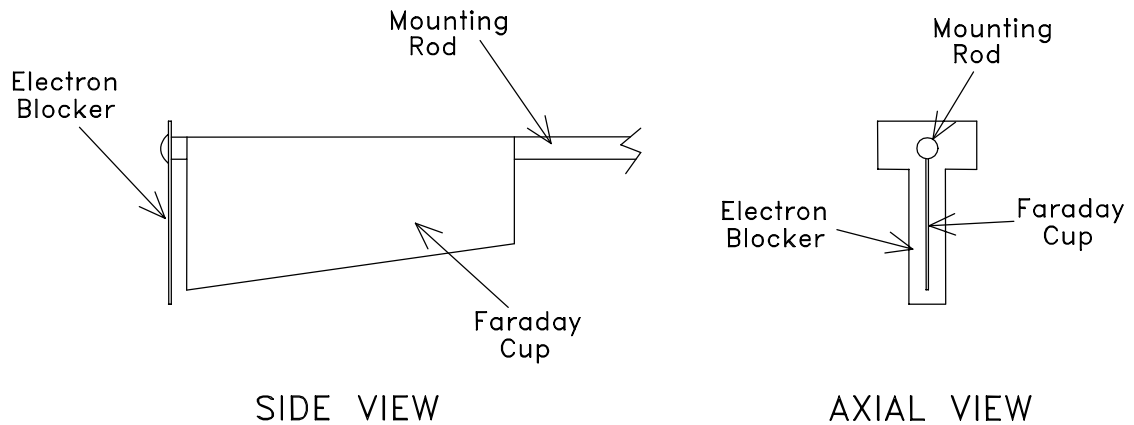


**Figure A4. Geometry of the radial probe and the electron blocker.**

Since the ion beam moves forward in z as it rotates azimuthally, a small portion of the ion beam will be intercepted by the electron blocker. Figure A5 shows the geometry. The fraction (f) of the beam that is lost is just the arc length across the width of the blocker divided by the circumference of the entire orbit ( $f = s/2\pi r = \theta/2\pi$ ). Since the width of the blocker is constant, error induced will be largest for beams with small diameter. If the e- blocker has width (w) and the beam has radius (r) then:

$$\frac{1}{2}w = r \sin\left(\frac{\theta}{2}\right)$$

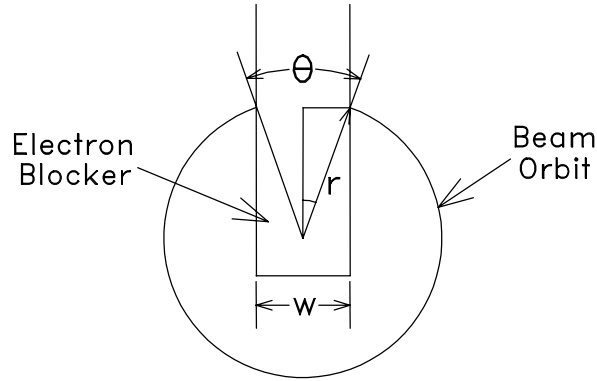


**Figure A5. Geometry showing the fraction of an ion orbit circumference which is intercepted by the electron blocker.**

So the fraction ( $f$ ) of the orbit that is blocked is

$$f = \frac{1}{\pi} \sin^{-1} \left( \frac{w}{2r} \right) \quad (\text{A.4})$$

The measured current ( $I_m$ ) is reduced from the actual current ( $I_o$ ) by:

$$I_m = I_o (1 - f)$$

Therefore the corrected beam current is:

$$I_o = \frac{I_m}{(1 - f)} \quad (\text{A.5})$$

Notice that this correction depends on knowing the radius of the beam correctly.

Therefore, the energy spread caused by the slope on the leading edge of the probe must be corrected for before the electron blocker correction is applied.

The electron blocker correction must be applied only to the current at a particular radius. Therefore, since data taken with the radial probe is an integrated distribution, the currents must first be unstacked to recover the actual beam current at each radius

( $\Delta I_i = I_i - I_{i+1}$ ) then correction factor is applied, then data is resummed ( $I_i = I_{i+1} + \Delta I_i$ ).

### Axial Turn Length

In the extraction region, the axial momentum of the beam ( $p_z$ ) increases as the magnetic field drops off. The axial length between turns ( $\Delta z_{\text{turn}}$ ) is proportional to  $p_z$ . This relation was derived in section 2.5.8. Furthermore, the increase in  $\Delta z_{\text{turn}}$  depends on the energy of the beam upon exit from the acceleration region. Section 2.5.8 showed that  $\Delta z_{\text{turn}}$  is approximately linear with the beam orbit radius in the extraction region.

If the axial turn length is longer than the axial length of the radial probe ( $\ell$ ), then the Faraday cup on the radial probe will intercept only a fraction of the total beam current ( $I_o$ ). The measured beam current ( $I_m$ ) is simply:

$$I_m = I_o \frac{\ell}{\Delta z_{\text{turn}}}$$

Therefore the corrected beam current is:

$$I_o = I_m \frac{\Delta z_{\text{turn}}}{\ell} \quad (\text{A.6})$$

where  $\Delta z_{\text{turn}}$  must be calculated for each beam energy in the distribution using equations 2.62 and 2.88. Since  $\Delta z_{\text{turn}}$  increases with beam energy, this correction effects mostly the upper energy portion of the radial distribution.

This correction depends on knowing the radius of the beam correctly. Therefore, the energy spread caused by the slope on the leading edge of the probe must be corrected for before correcting for the axial turn spacing. Correction for the axial turn spacing must be applied only to the current at a particular radius. Therefore, since data taken with the radial probe is an integrated distribution, the currents must first be unstacked to recover the actual beam current at each radius ( $\Delta I_i = I_i - I_{i+1}$ ) then correction factor is applied, then data is resummed ( $I_i = I_{i+1} + \Delta I_i$ ).

## REFERENCES

1. T.L. Grimm, C.T. Ramsell and R.C. York, *Ion Cyclotron Resonance Accelerator*, Proc. of 1997 IEEE Particle Accelerator Conf., Vancouver (1997)
2. C.T. Ramsell, T.L. Grimm and R.C. York, *Experimental Study of an Ion Cyclotron Resonance Accelerator*, Proc. of 1999 IEEE Particle Accelerator Conf., New York (1999)
3. J. Benford and J. Swegle, *High Power Microwaves*, Artech House Inc. (1992)
4. A.S. Gilmour Jr., *Microwave Tubes*, Artech House Inc. (1986)
5. H.R. Jory and A.W Trivelpiece, *Charged Particle Motion in Large-Amplitude Electromagnetic*, J. of Applied Physics, **39**, 7, p3053-3060 (1968)
6. R.S.H. Boulding, *The Resonant Cavity Magnetron*, D. Van Nostrand Co. Inc. (1952)
7. J.J.Coupling (a pseudonym for J.R. Pierce) Article in *Astounding Science Fiction* Street & Smith Publ. (Feb.1948)
8. G.B. Collins, *Microwave Magnetrons*, McGraw Hill Inc. (1948)
9. J.T.Coleman, *Microwave Devices*, Reston Publishing Co. (1982)
10. A.P Wolf, *Cyclotrons, Radionuclides, Precursors, and Demand for Routine versus Research Compounds*, Ann Neurol 15(suppl) S19-S24, (1984)
11. B.W. Wieland, R.R Highfill and P.H. King, *Proton Accelerator Targets for the Production of  $^{11}\text{C}$ ,  $^{13}\text{N}$ ,  $^{15}\text{O}$ , and  $^{18}\text{F}$* , IEEE Transactions on Nuclear Science, Vol. NS-26, No.1, (Feb. 1979)
12. J.D. Jackson, *Classical Electrodynamics*, 2<sup>nd</sup> ed. John Wiley & Sons Inc. (1975)
13. D.J. Griffiths, *Introduction to Electrodynamics*, Prentice-Hall Inc. (1989)
14. *RF Engineering for Particle Accelerators*, Proc. of the CERN Accelerator School, Exeter College, Oxford, UK, Vol 2, April 3-10 (1991)

15. W.D. Callister, *Materials Science and Engineering – An Introduction*, 2<sup>nd</sup> ed. John Wiley & Sons Inc. (1991)
16. E.L. Ginzton, *Microwave Measurements*, McGraw-Hill Inc. (1957)
17. J.H. Moore, C.C. Davis, and M.A. Coplan, *Building Scientific Apparatus*, Ch 3. Addison-Wesley Publishing Co. (1989)
18. G. Schmidt, *Physics of High Temperature Plasmas*, 2<sup>nd</sup> ed. Academic Press, New York (1979)
19. M.A. Lieberman and A.J. Lichtenberg, *Principles of Plasma Discharges and Materials Processing*, John Wiley & Sons Inc. (1994)
20. Z3CYCLONE version 4.0 Instruction Manual, MSU-NSCL Accelerator Group, (March 2, 1993)
21. S.L. Snyder and F. Marti, *Study and Redesign of the NSCL K500 Central Region*, Proc. of the 1995 IEEE Particle Accelerator Conference, (1995) p. 375-377
22. D. Johnson, *Circular Coil Program*, NSCL internal document
23. B.T. Smith, *Mistic Program for Computation of the Magnetic Field of a Circular Current*, Masters Thesis, MSU Cyclotron Project, Dept. of Physics (Nov. 1960)
24. C.J. Kost and F.W. Jones, *RELAX3D User's Guide and Reference Manual, Version 3.0*, TRIUMF 404 Wesbrook Mall, Vancouver, B.C. Canada, (Jan. 1992)
25. W.D. Kilpatrick, *A Criterion for Vacuum Sparking Designed to Include Both RF and DC.*, University of California Radiation Laboratory, UCRL – 2321, (Sept. 4, 1953)
26. T.J. Dolan, *Fusion Research - Volume 1 Principles*, Pergamon Press (1982)
27. A.B. El-Kareh and J.C.J. El-Kareh, *Electron Beams, Lenses and Optics*, Academic Press, New York (1970)